DOCTOR OF PHILOSOPHY

Solar cells based on the nc-TiO semiconducting polymer heterojunction

Al-Dmour, Hmoud

Award date:
2007

Awarding institution:
University of Wales, Bangor

Solar Cells Based on the nc-TiO_2 Semiconducting Polymer Heterojunction

By

Hmoud Al-Dmour

A Thesis Submitted for the Degree of
Doctor of Philosophy
in the College of Physical and Applied Sciences
University of Wales, Bangor

December 2007

Contents

Chapter 3: Metal Oxide Solar Cells (MOSCs)

Chapter4: Materials and Methodology

Chapter 5: Characteristics of nc-TiO_2 Films

Acknowledgments

I would like to thank Prof. Martin Taylor for his guidance, encouragement and supports throughout the period of this research. His patience gives me energy and strength to complete this thesis.

Many thanks to the Solaronix Co. for helpful advice on the sintering of the TiO_2 sol-gel, Dr N. C. Greenham and H. Clubb (Cambridge University) for undertaking the EQE measurements, the OpTIC Technium for the TGA data and the Higher Education Funding Council for Wales for financial support of this CAFMaD project.

I would also like to thank Dr.Paul Sayer for his helps during device fabrication in the cleanroom. I am also very much grateful to John Cambridge for his help in an AFM measurement. I am also thankful to the people in the Chemistry Department, University of Wales, Bangor for helping in XRD measurements.

Throughout these years, I also had the memorable time meeting and working with my group colleagues, Maria, Penny, Paco, Yara, James, Janet and David who made the research work less stressful.

I would like to thank my Mum and Dad for the love, encouragement and understanding. I am really indebt to my brother (Nidal) and sister (Asma) for their moral support during these years.

Abstract

We compare the performance of heterojunction solar cells formed from p-type organic semiconductor poly (3-hexylthiophene), P3HT, and sintered nano-crystalline titanium dioxide (nc-TiO_2) films. The solar cells were from two batches (A and B) of sol-gel materials and some were sensitized with a ruthenium dye. Atomic force microscopy shows that the RMS roughness of the nc-TiO_2 layers films was 12.7 to 20.5 nm with corresponding mean particle height ranging from 60 to 90 nm. Scanning electron microscopy reveals that these different topographies are linked to differences in the morphology of the sintered nc-TiO_2 layers. Thermogravimetric analysis suggests that these structural differences may arise from differences in solvent concentration in the nominally identical sol-gel solutions used for preparing the nc-TiO_2 layer. The best solar cell performance, achieved with films showing the highest RMS roughness and a 'columnar' morphology, displayed the highest external quantum efficiencies (EQE) reported for this combination of materials: 11%<EQE<16% for the wavelength range 580-380 nm. However, the lower turn-on voltage for the dark, forward current in these devices leads to a reduction of ~0.2V in open-circuit voltage compared with the smoother films of nc-TiO_2.

We have also investigated the properties of the P3HT/nc-TiO_2 interface and the effect of ambient conditions on the parameters of our solar cells. Good rectification was achieved in the air in the dark. The capacitance of the devices increased with increase of the applied voltage for the sensitized (batch A) TLSCs and non-sensitized (batch A, B) DLSCs devices. This change in the capacitance indicates the existence of band bending and the presence of a depletion region at the interface between P3HT and nc-TiO_2. Therefore, the junction capacitance is dominated by the depletion capacitance. However, different results were obtained in the vacuum: 1) there was a significant decrease of the dark-current and the loss of rectification, 2) under illumination, the open circuit voltage was zero and the photocurrent larger than in air, and 3) the capacitance was not affected by varying the applied voltage because there is a decrease in the band bending at interface between P3HT and nc-TiO_2 and a disappearance of the depletion region at the interface. The sensitized devices from batch B TLSCs exhibit solar cells characteristics both in vacuum and in air with Voc of ~0.8V. The capacitance remained constant when the voltage increased.

Contributions to Published Literature

Parts of this thesis have been accepted for published as follow

- "Effect of Nanocrystalline-TiO_2 Morphology on the Performance of Polymer Heterojunction Solar Cell", H. A. Al-Dmour, D. M. Taylor and J. A. Cambridge, *Journal of Physics D: Applied Physics*, **40,** 5034, (2007).
- "Morphology of Nanocrystalline TiO_2 for Improved Heterojunction Solar Cell Performance", H. A. Al-Dmour, D. M. Taylor and J. A. Cambridge, International Conference on Organic Electronics (ICOE), 04 - 07 June 2007, Eindhoven, The Netherlands. (oral presentation)
- "Nano-crystalline TiO_2-Semiconducting Polymer Solar Cells", D. M. Taylor and H. A. Al-Dmour, Symposium O: Hybrid Organic/Inorganic/Metallic Electronic and Optical Devices, April, 2006, San Francisco, USA. (poster presentation)
- "Ambient Effect on nc-TiO_2/P3HT Solar Cells Performance", H. A. Al-Dmour, D. M. Taylor, International Conference on Organic Electronics (ICOE), June 2006, Eindhoven, The Netherlands.(poster presentation).

Chapter 1

Introduction

1.1 Introduction

This chapter gives an introduction to the basic elements underlying the work presented in this thesis regarding energy sources and organic semiconductors. It also presents the motivation for and outline of this thesis.

1.2 Energy Sources

Fossil fuels are the major source of energy for heating, cooking, lighting, and transport. Fossil fuels are not renewable and need a long time in order to be formed. Also, the burning of fossil fuels is accompanied by the release of CO_2 gas which is dumped in the atmosphere. CO_2 gas is considered to be an important factor in global warming (green house problem) [1]. Unfortunately, human demand for energy has increased with the increase of our reliance on technology, leading to an increasing use of fossil fuel.

An alternative source of energy that avoids the CO_2 problem is nuclear energy. Nuclear power stations contribute some 8% of the energy used on the Earth but carry the risk of radioactive contamination from waste material [2]. The growing realization of the risks posed by global warming and the risk of using nuclear stations led to an agreement, the Kyoto Protocol, among countries to reduce the emission of CO_2 gas and so reduce global warming. The agreement also aims to avoid the shortage of fossil fuel in 2050 by using renewable energy [3].

The main sources for renewable energy are from wind, sun, and tide. These sources are friendly to the environment and are available to varying extents also around the Earth. However, there is a big gap between the costs of energy produced from fossil fuel in comparison with renewable energy. Therefore, finding low–cost methods for extracting energy from renewable sources has attracted the interests of researchers world wide.

Solar energy can provide us with our needs for electricity. For example, figure 1.1 shows an area of hot desert with two red squares. The larger red square shows an area of 254 km × 254 km [4]. This area if it is covered with concentrating solar power plants, would provide electricity equivalent to the current electricity consumption of the whole world. The smaller square shown in the figure (110 km × 110 km) would provide electricity equivalent to the current electricity consumption of the European Union.

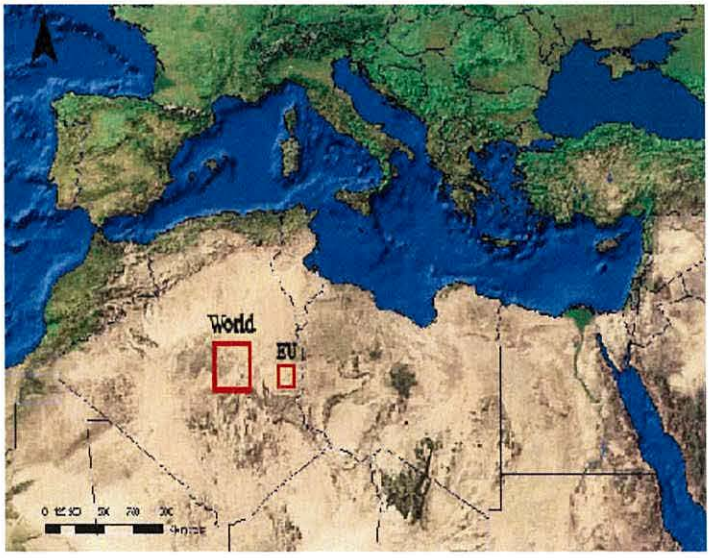

Figure 1.1 *A map showing part of the world with hot deserts. The squares indicate the area needed to capture solar power for current world and EU consumption* [4].

Solar Cells (Photovoltaic Cells) are devices used to convert sunlight to electricity. In 1839, Edmund Bequeral was the first person to report the photovoltaic effect [5, 6]. He observed the generation of a current through the action of light on a silver coated platinum electrode immersed in an electrolyte. The work of Bequeral was followed by attempts to fabricate solar cells made from different materials such as copper–copper oxide. The photovoltaic effect in such devices was dependent on the barrier between the metal and the oxide. In 1930s, this was explained by the Schottky effect [6, 7, 8].

The first silicon solar cells with power conversion efficiency of 6% were produced by Chapin in 1954 [9]. These silicon solar cells proved to be reliable for use as power sources for satellites; they were active for much longer times than could be achieved using normal batteries. However, the ambition was to use solar cells for power generation, but the fabrication of solar cells at that time was very expensive (the cost of generation was $200/W using one solar cell). The high cost of producing silicon solar cells was a major factor for not using this technology for several decades. However, there were benefits from using these solar cells to provide energy to remote areas away from civilization such as Africa or oil companies which work in deserts [10]. In 1973, stopping oil supplies to the West played an important role in reducing the reliance of the West on the oil from the Middle East by finding alternative energy sources. Consequently, there has been significant investment in solar cell research. Solar cell scientists have investigated different materials and various techniques to fabricate solar cells with high efficiency and low costs. Organic semiconductors are examples of materials for fabricating solar cells whose properties have the potential to compete with silicon and at a much reduced cost.

1.3 Organic Semiconductors

Organic materials were considered to be good insulators until 1977, when Shirakawa and Ikeda [11] managed to increase the conductivity of the unsaturated conjugated polymer so that it showed metallic-like conductivity. This change in the conductivity of polyacetylene was achieved by doping the polymer with bromine, iodine or chlorine. This has led to the use of organic materials in electrical applications such as light emitting diodes and solar cells.

Figure 1.2 shows the chemical structure of trans–polyacetylene as a simple example of an organic semiconductor. It is composed of a backbone of carbon atoms connected together by alternating double and single bonds, the defining character of a conjugated polymer. The single bond is referred to as a σ bond and the double bond is referred to as a π bond. These bonds are formed by the hybridization of electron energy levels of the carbon atoms in C-C and C-H bonds.

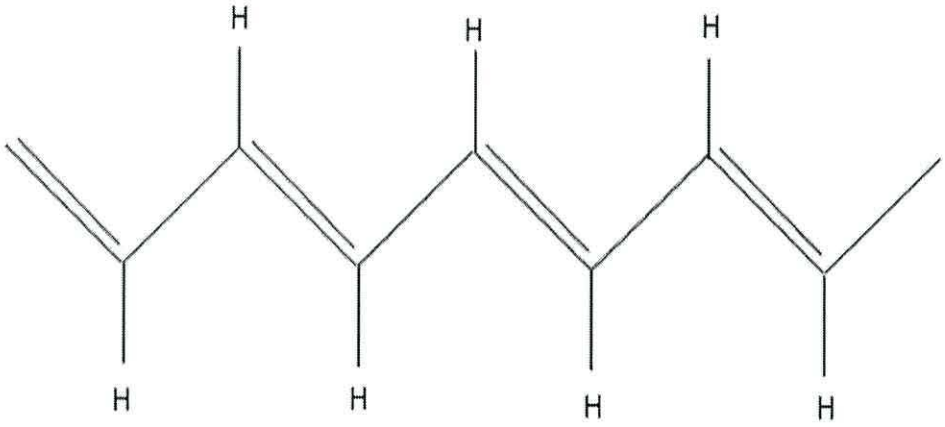

Figure 1.2 *The backbone of polyacetylene with double and single bonds.*

The ground state of a carbon atom is $1s^2 2s^2 2p^2$. Electrons in the 1s orbitals are core electrons where as the electrons in the $2s^2 2p^2$ orbitals are valence electrons. However, the hybridization of the orbitals (2s and 2p(x,y)) occurs leading to the formation of three sp^2 orbitals aligned at 120° to each one (Figure 1.3(a)). This leaves one 2p(z) orbital of each carbon atom unchanged and directed perpendicular to the three sp^2 orbitals of carbon atoms in the polymer chain. Two of the sp^2 orbitals overlap with adjacent carbon atoms while the third overlaps with the 1s orbital of hydrogen atoms, both forming σ bonds. This is the skeleton of the polymer chain. The electrons participating in forming σ bonds (σ electrons) are usually localized and do not contribute to any electrical conductivity in organic semiconductors. π bonds are formed through overlapping of the remaining 2p(z) orbitals of adjacent carbon atoms (Figure 1.3(b)). The electrons in π orbitals are delocalized so that electrons in these orbitals move easily along the polymer chains. Thus, π electrons can contribute significantly to the electrical conductivity of organic semiconductors. They respond

to an external influence by re-distributing the charges across the polymer chain and hence affect its conductivity.

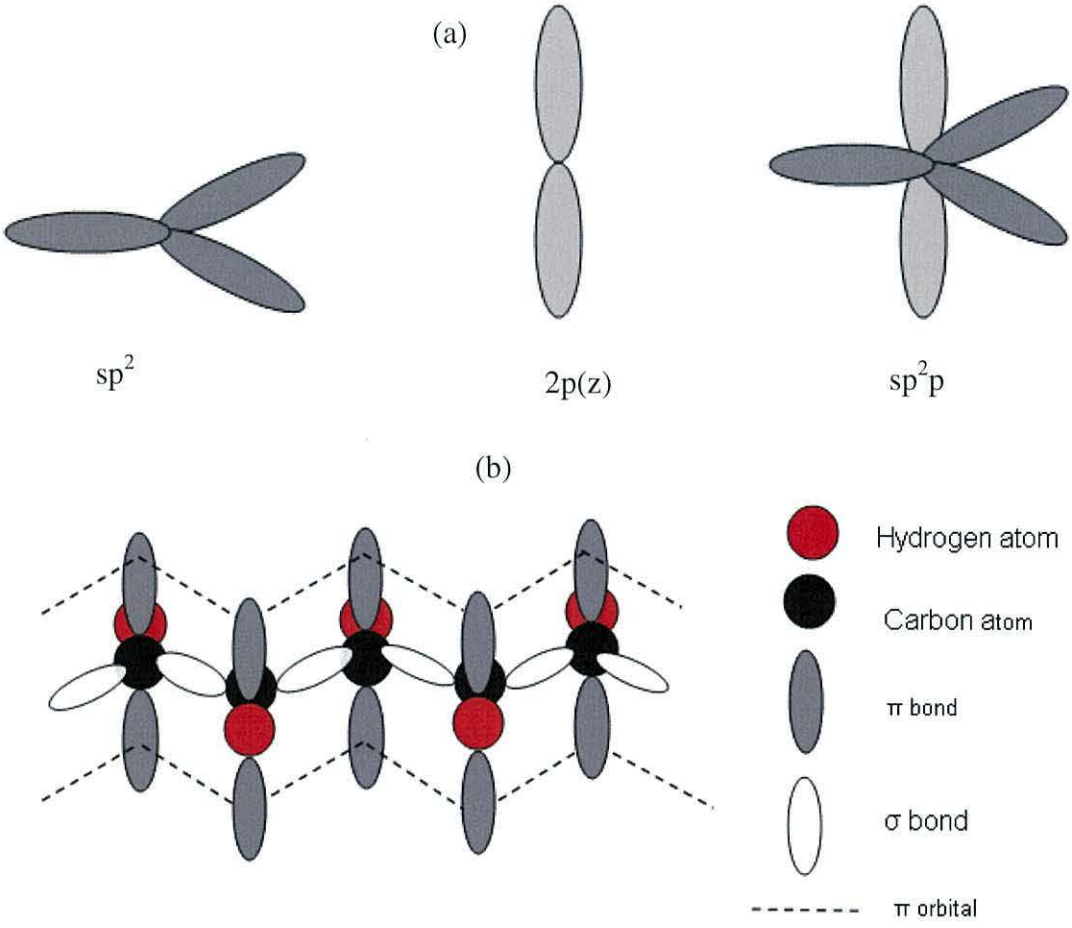

Figure 1.3 a) *The atomic orbitals of p ,sp^2 ,sp^2p orbitals, b) orbital structure showing the π-bonding orbitals of trans- polyacetylene.*

The energy levels in organic semiconductors are represented by the molecular orbitals used to form σ and π bonds. They form two separated orbitals groups equivalent to energy bands in inorganic materials. The lowest energy levels of the polymer chain are denoted bonding molecular orbitals (σ and π) and the highest energy levels of organic semiconductors are denoted anti-bonding molecular orbitals (σ^* an π^*) (figure 1.4(a)). However, the number of bonding and anti-bonding molecular orbitals depends on the number of carbon and hydrogen atoms in organic semiconductors. In conjugated polymers where there are many repeating units of carbon and hydrogen atoms, the group of anti-bonding π^* molecular orbitals and group of π bonding molecular orbitals form an energy band called the Lowest Un-occupied Molecular Orbilats (LUMO) and Highest Occupied Molecular Orbitals

(HOMO) respectively The LUMO and HOMO are separated and create an energy gap [12] which determines the intrinsic conductivity of the organic polymer. The LUMOs are not filled with electrons and act as the conduction band in inorganic solar cells. The HOMOs are filled with electrons and act as the valence band in inorganic solar cells (Figure 1.4(b)).

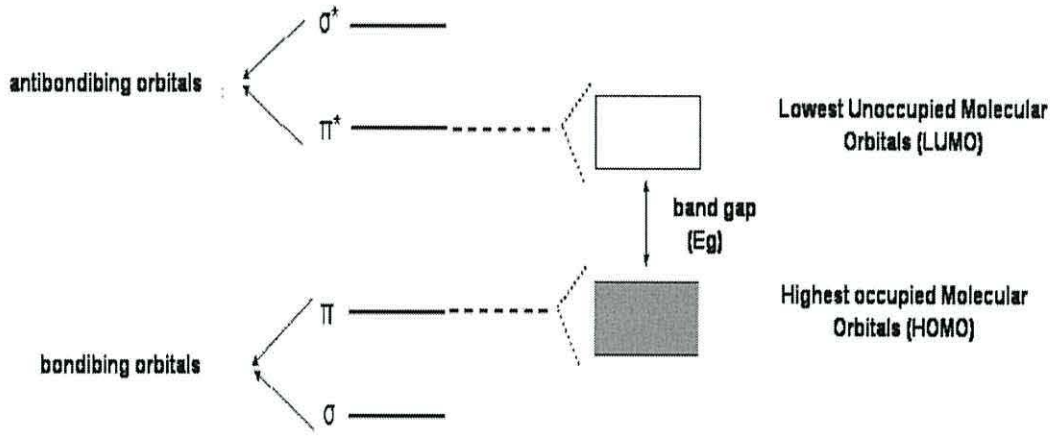

Figure 1.4 *Energy levels of bands for a) monomer of conjugated polymer b) conjugated polymer.*

Organic semiconductors usually have an energy gap of ~2eV which increases the possibility of electron promotion from HOMO to LUMO compared to organic insulator where the gap is larger. The lower band gap also means that the free charge concentration can readily be changed by charge injection from the electrodes or by photoexcitation. Most importantly they may be doped. This occurs when acceptors dopant is introduced into the polymer and electrons are removed from π bonds generating holes in the polymer. The polymer undergoes a change in its configuration around the hole, to the higher energy quinoid arrangement. The induced structural changes associated with the holes are known as polarons (Figure 1.5(a)). As the acceptor concentration increases, additional polarons are formed. When the doping density is increased further, bi-polaron formation may occur and new energy levels are introduced into the energy gap (Figure 1.5(b)).

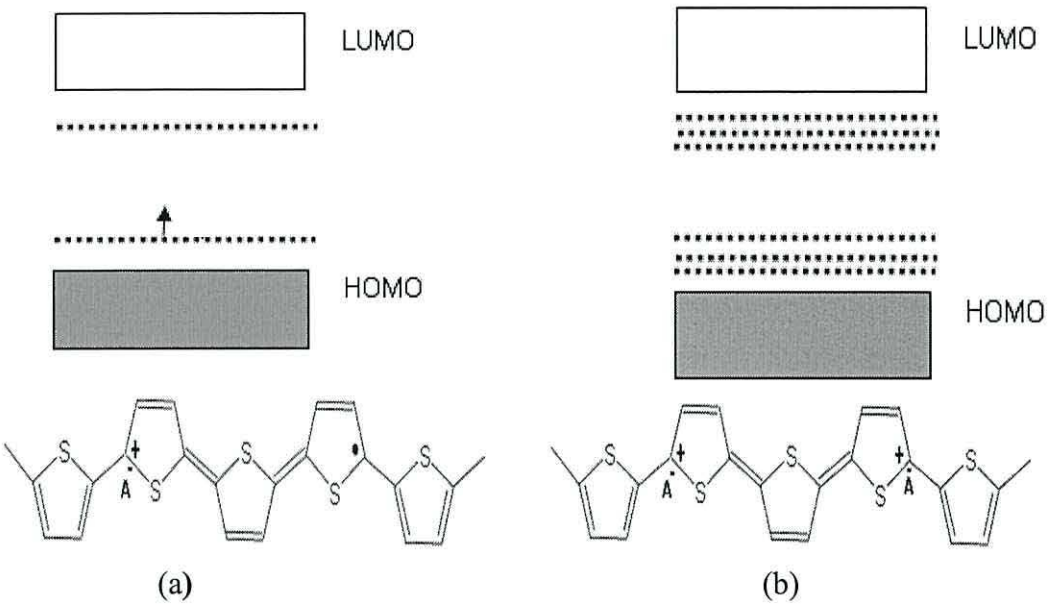

Figure 1.5 *Energy band and chemical structure of P3HT after formation of a) polaron and b) bi-polaron.*

1.4 Organic Solar Cells

Much work has been undertaken to produce organic solar cells with high efficiency. Organic solar cells are characterized by high optical absorption coefficient (usually $\geq 10^5$ cm $^{-1}$), low cost of the basic material, the formation of a large interface area, compatible with a flexible substrate, and a good response to high temperature and low light intensities [13, 14, 15] .

The simplest configuration of an organic solar cell is to have the organic material sandwiched between two electrodes of different work functions [8, 10]. This device exhibits the characteristics of an ideal diode due either to the difference in the work functions of the metals (un-doped semiconductor) or to Schottky barrier formation at the interface between one electrode and the doped-organic material. In either case an interface electric field is created sufficiently large to separate the excitons. Figure 1.6 shows the energy diagram of a single layer solar cell with a Schottky contact at the interface between the aluminum electrode and the polymer.

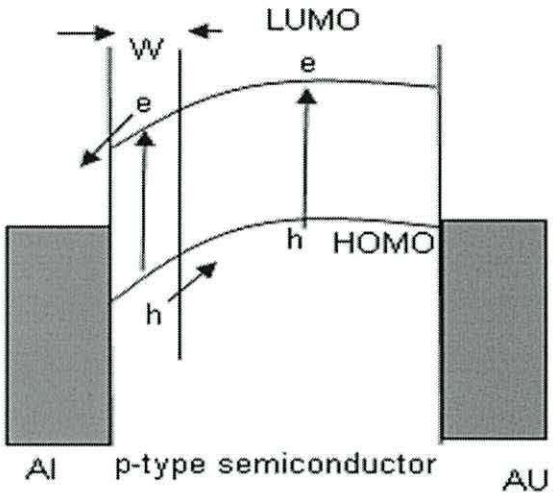

Figure 1.6 *Energy diagram of a Schottky barrier –single layer solar cell. The Schottky barrier is formed at the aluminum electrode.*

The dissociation of excitons in single layer solar cells occurs at the interface between the Schottky contact and the polymer. The efficiency of the process depends on the diffusion length of excitons in organic material which is less than 10 nm. It has been found that single–layer solar cells respond poorly to light and exhibit a very low Fill Factor (FF), 0.25, or less [16]. This is attributed to the high series resistance of the organic material which limits the transport of charge carriers [17].

To overcome the low performance of single-layer solar cells, two organic materials have been used to fabricate bi-layer solar cells. These organic materials have different properties regarding their electron affinity, and ionization potential (i.e. different HOMO and LUMO levels) [18]. The dissociation of excitons in bi-layer solar cells occurs mainly at the interface region between the two organic materials. This is followed by the transport of electrons into the first organic material (acceptor material) leaving holes in the second organic material (donor material). The transport of charge carriers across the junction occurs if the electron affinity of the acceptor material (LUMO) is lower than the electron affinity of donor material. In such a case, recombination of excitons is reduced, resulting in increased efficiency compared with single layer solar cells. The advantage of bi-layer solar cells composed of two organic materials is that one of the organic materials has a high electron mobility and the other has a high hole mobility. Unlike single layer solar

cells, there are no electrons trapped in bi-layer solar cells [18, 10]. Additionally, bi-layer solar cells increase the absorption range of the incident light because of the difference in energy gaps of the organic materials. In some cases, the photovoltaic effect in bi-layer solar cells depends on the existence of a depletion region at the interface between the doped donor and acceptor materials. When a depletion region is present, excitons are dissociated by the electric field created across the depletion region [19]. When the donor and acceptor materials in bi-layer solar cells are un-doped, the photovoltaic effect depends on the ionization potential of the acceptor, electron affinity of the donor, and the work function of the electrodes [20, 21]. For example, C. W. Tang [21] in 1986 fabricated one of first types of bi-layer solar cells composed of two organic materials. An efficiency of 1% was achieved. Figure 1.7 shows the energy diagram of bi-layer solar cell for donor and acceptor materials where the exciton dissociation occurs at the interface.

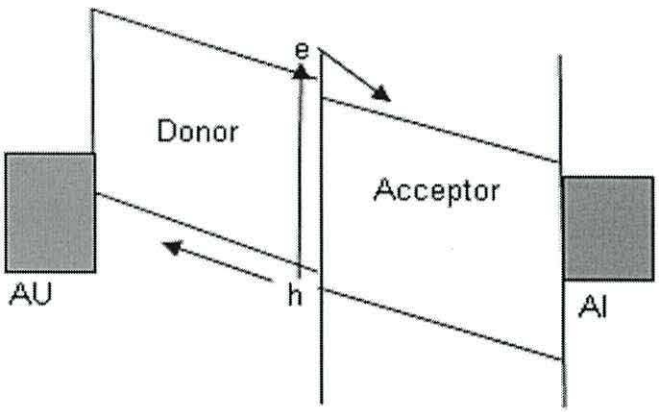

Figure 1.7 *Schematic diagrams of bi-layer solar cells.*

However, when the two organic layer are planar, for example when spin coated, bi-layer solar cells have a small interfacial area between donor and acceptor materials. This limits the dissociation of excitons which only occurs within ~ 10nm of the interface. In order to improve the efficiency in such cells, the layer thickness should be small to reduce resistance losses. The better approach is to increase the interfacial area for exciton dissociation. Polymers generally act as donor materials and have very different mobility e.g. P3HT and MEH-PPV. The most popular electron acceptor materials are the (C_{60}) buckminsterfullerene and nano-particles of TiO_2 and are discussed in Chapters 2 and 3 [19, 22].

To increase interfacial area, donors and acceptors were mixed with each other instead of spin coating. This type of solar cell is called a bulk heterojunction solar cell and shows good performance compared to spin-coated bi-layer solar cells, a direct consequence of the enhancement in interfacial area in the bulk region to provide large area to dissociate excitons. Polymer blends are increasingly being investigated where phase separation of a mixture is used to create the high area interface [23]. This imposed light harvesting coupled to increased exciton dissociation leads to an increase in the short circuit current in the device and an increase in efficiency to 5% [24]. A number of factors affect the performance of bulk heterojunction solar cells, for example, the concentration of materials composing the solar cells, the type of solvent used, and the work functions of bottom electrode which affect on the open circuit voltage (Voc) [25, 26, 27]. Additionally, the interfacial area of bulk heterojunction solar cells could be modified by annealing the device [25]. Figure 1.8 shows the energy diagram of bulk heterojunction solar cells.

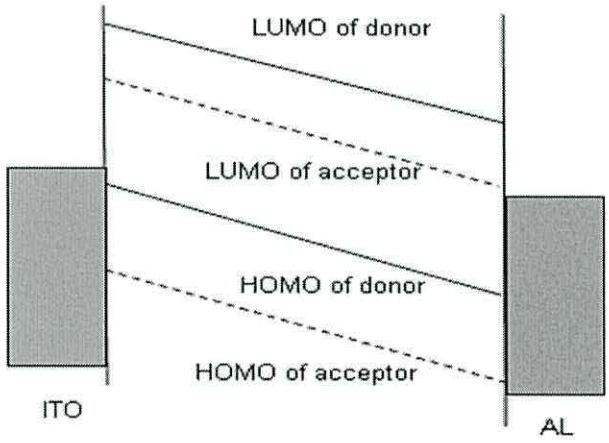

Figure 1.8 *Energy diagrams of bulk heterojunction solar cells.*

Research has been conducted to increase further the performance of organic solar cells by inserting a dye layer between the acceptor and donor materials [28]. Examples of acceptor materials are again nano-particles of TiO_2 and carbon nanotubes. The donor material is spin coated on top of these nano-particle semiconductors. These acceptor materials were also used with donor materials to produce double-layer solar cells as well as the three layer solar cells incorporating a

dye. The double layer solar cells and three layer solar cells are at the centre of our work in this thesis.

Finally, the key challenge facing organic solar cells in order to be used commercially to improve their low efficiency compared to silicon solar cells. Figure 1.9 shows the difference in efficiencies for organic and silicon solar cells. The goal of increasing the efficiency of organic solar cells is the motivation for many researchers around the world who are seeking synthetic organic materials from which to fabricate solar cells that compete with silicon at a fraction of the cost.

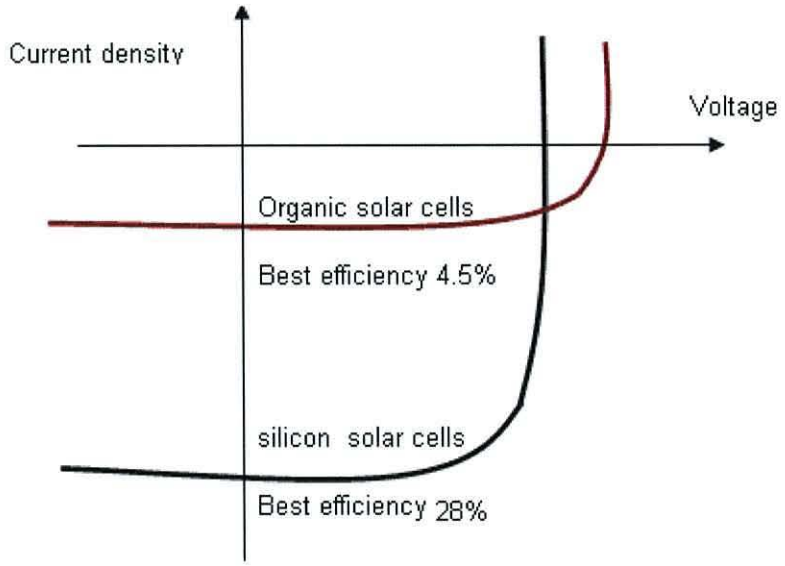

Figure 1.9 *I-V plots contrasting the efficiency of organic and silicon solar cells.*

1.5 Motivation

There has been much interest in replacing the electrolyte of the dye-sensitized Grätzel cell with a polymeric hole transporting layer [29, 30]. Considerable progress has been made in improving the power conversion efficiencies of cells based on dye-sensitized, mesoporous films of nanocrystalline TiO_2 (nc-TiO_2). For example, Mende [31] reported 4% power conversion efficiency for the AM1.5 solar spectrum. This was achieved by optimizing the thickness of the TiO_2 layer to ensure good light harvesting and employing a doped spirobifluorene derivative as an efficient hole

conductor. A previous report [32] had advocated the use of silver complexation of the dye to the TiO_2, although this approach apparently had a detrimental effect in this later work. It was suggested as early as 1999 [33] that the ability to control the pore size, thickness and interfacial surface area was important for increasing solar cell efficiency. Such effects were investigated by Breeze [34] who concluded that an order of magnitude increase in external quantum efficiencies (EQE) to ~6% at ~500 nm became possible by combining a thin, high mobility hole conductor with a rough TiO_2 surface. More recently, Coakley and McGehee [35] achieved EQEs rising to ~10% at 514 nm by controlling the thickness and porosity of the TiO_2 film in a cell using poly(3-hexylthiophene), (P3HT), as the hole conductor. In the present contribution, we show that markedly different results can be obtained depending on the morphology of the nanocrystalline particles, which in turn depends on the composition of the starting sol-gel.

The second part of this thesis was motivated by the on-going discussion about the existence of band bending between the hole conductor and nano-crystalline TiO_2. Some researchers [36] claim or argue that there is no band bending at the interface between the hole conductor and the nc-TiO_2 because the particles in TiO_2 are very small. Therefore, the existence of band bending at the interface is not necessary to dissociate excitons. The most common model applied in TiO_2/polmer solar cells to interpret the internal field was employed by Grätzel. It depends mainly on the difference between the LUMO of hole conductor or and work function of the top electrode and the conduction band of nc-TiO_2 [33]. Scanning tunneling spectroscopy (STS) has been used to study the surface band gap and band bending of nc-TiO_2 when the dye was attached on the surface [37]. In the present work, one of our objectives was to investigate the junction at the nc-TiO_2/polymer interface by using admittance measurements. In a comparative study, devices with and without dye-sensitization were investigated.

The third part of the thesis was motivated by the effect of atmospheric contaminants on the electrical properties of solar cells fabricated from nc-TiO_2 and semiconductor polymer. It was suggested in [38] that the influence of oxygen and water vapor in the atmosphere play an important role in forming defects on the surface of porous TiO_2. It is also known that semiconducting polymer devices are sensitive to the ambient conditions as reported by Rep in 2003 [39] and Taylor et al

in 1991 [40]. Therefore, the atmospheric effect on polymer/nc-TiO_2 and polymer/dye/nc- TiO_2 was studied using both DC and AC measurements.

1.6 Thesis Outlines

An introduction to organic solar cells is given in Chapter 2. We illustrate the essential elements in the operation of organic solar cells: coupling of photons, light absorption and exciton generation, exciton migration, exciton dissociation, charge transport and collection at the electrode. We also present the characterization of solar cell devices.

Chapter 3 presents an analysis of the metal oxide-solar cells mentioned in the literature. We discuss the properties of nc- TiO_2 and its application in organic solar cells and the basic operation of Dye Sensitized Solar Sells (DSSCs) – the Grätzel Cell.

Chapter 4 illustrates the materials and techniques used to fabricate Double layer Solar Cells (DLSCs) and Three Layer Solar Cells (TLSCs). It presents the equipment used for studying electronic properties, physical properties, and morphology of the nc-TiO2 films.

Chapter 5 shows the characteristics of nc-TiO_2 films derived from two different batches (A and B). The characteristics were studied using: Atomic Force Microscopy (AFM), Scanning Electronic Microscopy (SEM), Scanning Tunneling Microscope (STM), and Thermo- Gravimetric Analysis (TGA).

Chapter 6 shows the electrical characteristics of DLSCs, including the vacuum effect on DLSC performance. The DLSCs were fabricated from the two batches: A and B. Chapter 7 shows the electrical characteristics of TLSCs from batches A and B, including the vacuum effect on TLSC performance. Chapter 8 presents the admittance measurements of DLSC and TLSC in vacuum and air. Finally, in chapter 9 we present some conclusions and discuss future work.

1.7 References

1. United Nations Environments Programmer, *Climate Change.* http://www.unep.org/geo/geo3/english/pdfs/chapter2-7_atmosphere.pdf
2. World Nuclear Association, http://www.world-nuclear.org/info/inf103.html.
3. Hatfield, C. Bond, *Nature*, **387**, 6629, (1997).
4. Tran-Mediterranean Renewable Energy Cooperation (TREC), http://www.desertec.org/.
5. A. E. Becquerel, *Comptes Rendus*, **9**, 561, (1983).
6. Jenny Nelson, *The Physics of Solar Cells,* Imperial College press, (2003).
7. W. Schottky, *Naturwiss,* **26**, 843, (1938).
8. S. M. Sze, *Physics of Semiconductor Devices*, Wiley, *(*1969).
9. D. M. Chapin, C. S. Fuller, and G. L. Pearson, *Journal of Applied Physics,* **25**, 676, (1954).
10. S. S. Sun, N. S. Sariciftic, *Organic Photovoltaic Mechanism, Material and Devices*, Taylor and Francis, (2005).
11. Shirakawa, F. J. Louis, A.G. MacDiarmid, C. K. Chiang, A.J. Heeger, *Journal of the Chemical Society Chemical Communications,* **578**, (1977).
12. A. Moschwitzr, clarendon. *Semiconductor Devices, Circuits and Systems*, Oxford, (1991).
13. M. A. Ibrahim, H. K Roth, and S. Sensfuss, *Applied Physics Letters,* **85**, 1481, (2004).
14. C. J. Brabec, N. S. Sariciftic, and J. C. Hummelen, *Advance Function Materials* , **11**, 15, (2001).
15. J.Nelson, *Mater*, **5**, 20, (2002).
16. A. J. Breeze, Z. Schlesinger, and S. A. Carter, *Physical Reviews B*, **64**, 125205, (2000).
17. P. W. M. Blom, M. J. M. de Jong, and J. J. M. Vleggaar, *Applied Physics Letters,* **68**. 3308, (1996).
18. M. Onado, K. Tada, *Current Applied Physics*, **3**, 141, (2003).
19. A. Watanabe, A. Kasuya, *Thin Solid Fi*lms, **483**, 358, (2005).
20. C. M. Ramsdale, J. A. Barker, A. C. Arias, J. D. MacKenzie, R. H. Friend, N. C. Greenham, *Journal of Applied Physics*, **92**, 4266, (2002).

21. C. W. Tang, *Applied Physics Letters,* **48**, 183, (1986).
22. U. Mengesha, T.Yohannes, *Solar Energy Materials and Solar Cells*, **90**, 3508, (2006).
23. G. Yu. and A. J. Heeger, *Journal of Applied Physics,* **94**, 6849, (2003).
24. M. R. Reyes, K. Kinm, and D. Carroll, *Applied Physics Letters*, **87**, 083506. (2005).
25. G. Li, V. Shrotriya, Y.Yao, and Y. Yang, *Applied Physics Letters*, **98**, 043704, (2005).
26. C. Y. Kwong, A. B. Djuri, P. C. Chui, K. W. Cheng , and W. K. Chan, *Chemical Physics Letters*, **384**, 372. (2004).
27. V. D. Mihailetchi, P. W. M. Blom, J. C. Hummelen, and M. T. Rispens, *Journal of Applied Physics* , **94**, 6849, (2003).
28. B. O'Regan and M. Grätzel, *Nature*, **353**, 737, (1991).
29. D. Gebeyehu, C. J. Brabec, F. Padinger, T. Fromherz, S. Spiekermann, N. Vlachopoulos,F. Kienberger, H. Schindler and N. S. Sariciftci, *Synthetic Metals*, **121**, 1549 (2001).
30. Q. Fan, B. McQuillin, D. D. C. Bradley, S. Whitelegg and A. D. Seddon, *Chemical Physics Letters* , **347**, 325 (2001).
31. L. S.Mende, S. M. Zakeeruddin and M. Grätzel, *Applied Physics Letters* , **86**, 013504, (2005).
32. . J. Krüger, R. Plass, M. Grätzel and H.-J. Matthieu, *Applied Physics Letters,* **81**, 367 (2002).
33. A. C. Arango, S. A. Carter and P. J. Brock, *Applied Physics Letters,* **74**, 1698. (1999).
34. J. Breeze, Z. Schlesinger, S. A. Carter and P. J. Brock, *Physical Reviews B,* **64**, 125205, (2001).
35. K. M. Coakley and M. D. McGehee, *Applied Physics Letters*. **83**, 3380 (2003).
36. D. Cahen, G. Hodes, M. Grätzel, J. F. Guillemoles, I. Riess, *Journal of Physical Chemistry B*, **104**, 2053, (2000).
37. A. R. Kumarasinghe, and W. R. Flavell, *Physica E: Low Dimentional Systems and Nanostructure,* **14**, 224, (2002).

38. A. L. Linsebigler, G. Lu, and J. T. Yates, *Chemical Reviews*, **95**, 735, (1995).
39. D.B.A. Rep, A.F. Morpurgo, and T. M. Klapwijk. *Organic Electronics,* **4**, 201, (2003).
40. D. M. Taylor, H. L. Gomes, A. E. Underhill, S. Edge, and P. I .Clemenson, *Journal of Physics. D: Applied. Physics.* **24**, 2032, (1991).

Chapter 2

Review of Organic Solar Cells

2.1 Introduction

The performance of organic solar cells is investigated in this chapter by studying the current-voltage properties of solar cell devices under both illumination and in the dark. We introduce the single-layer Schottky barrier solar cells as a simple structure and review its DC properties. AC measurements on single-layer Schottky barrier solar cells will be explained and the influence of diffusion and depletion capacitance discussed.

2.2 The Operation of Organic Solar Cells

In general, solar cells are devices that have the ability to convert incident sunlight (Solar Irradiation) into electrical energy. This section is intended to explain the essential elements in the operation of organic solar cells. Five processes occur to generate photocharges as follows [1]:

1- In -Coupling of photons to the cell.

2- Photon absorption and exciton generation.

3- Exciton migration.

4- Exciton dissociation.

5- Charge transport and collection at the electrode.

The power conversion efficiency of solar cells depends on the efficiency at each of the steps outlined above. In 1995 [2], Yuelal reported that the total external quantum efficiency (η) could be described by

$$\eta = (1-R)\eta_{AB}\eta_{ED}\eta_{CT}\eta_{CC} \qquad (2.1)$$

where η_{AB} is the efficiency of the light absorption in the active layer, η_{ED} is the efficiency of exciton migration to the interface, η_{CT} is the efficiency of charge dissociation at the interface and transport to the electrodes, η_{CC} is the efficiency of the charge collection, and R is the reflectivity of the substrate at the air interface.

2.2.1 Intensity of Solar Irradiation on the Earth

The main source of the light in nature comes from the Sun and is produced through nuclear fusion [3] reactions occurring at its centre. The temperature of the Sun's core is 13,600,000K and the temperature of the sun's outer visible layer (photosphere) is 5800K. The spectrum of the Sun is usually emitted from the photosphere and is similar to the spectrum of a black body. The photosphere layer emits radiation which spreads across space until it decays or strike an object in its way. When the Sun's radiation hits an object, energy is transferred to that object. The intensity of the sunlight measured just outside the earth atmosphere is ~1.353 K W/m^2.

The intensity of the light falling on the Earth's surface depends on the location and the time of the year. Because the Earth is approximately spherical, the distance from the Earth to the Sun differs from one place to another on Earth's surface. The loss of radiation passing through the atmosphere is due to the following reasons [4].

1- Rayleigh scattering by dust particles and water droplets for short wavelength of sunlight.

2- Part of the infrared and ultraviolet regions of the Sun's spectrum is lost due to absorption by water vapor, carbon dioxide, and ozone.

The Air Mass (AM) term is used to describe the spectral distribution of the Sun's irradiation reaching the Earth's surface. It is defined as the ratio (X) of the actual

path length (L_A) of the Sunlight falling on the Earth's surface to the path length (L_M) if the sun was directly overhead [4].

$$X = \frac{1}{\cos\phi} = \frac{L_A}{L_M}. \tag{2.2}$$

Thus, X ranges from 1 at the equator to ∞ near the poles. For the purpose of studying the performance of the solar cells, the AM1.5 solar spectrum is taken as the standard value and corresponds to an angle of 48.7^o between the actual path of the radiation and the sun directly overhead (Figure 2.1). Figure 2.2 presents the typical distribution of the incident power of sunlight reaching the Earth's surface under the AM1.5 condition [5]. It also reveals that the maximum peak of spectral irradiation intensity is observed at ~500nm. The dips in the spectrum come from absorption in the atmosphere.

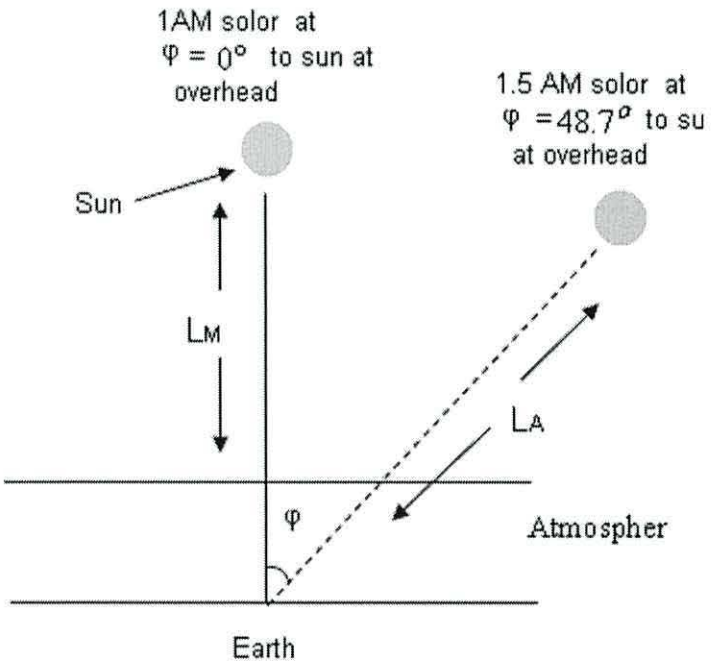

Figure 2.1 *Diagram to explain solar AM conditions.*

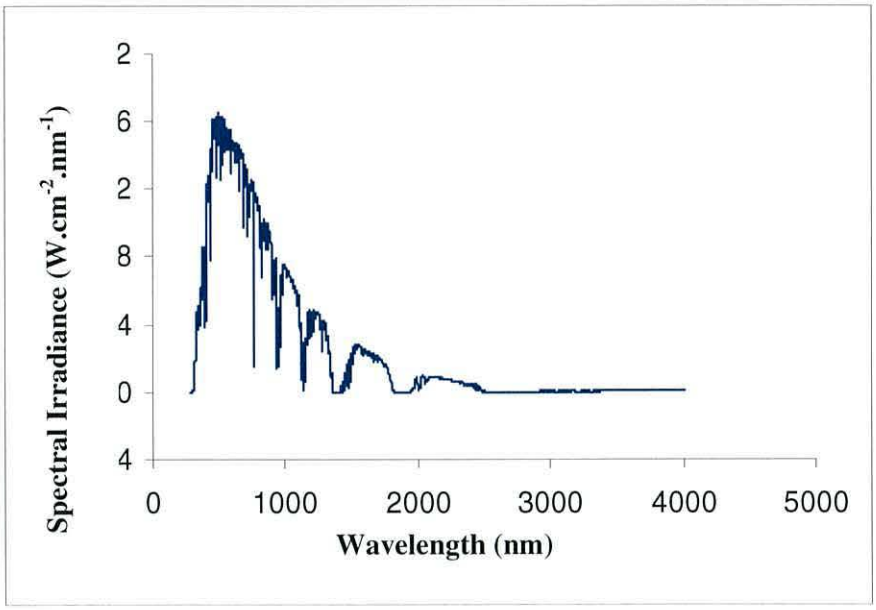

Figure 2.2 *Spectral distribution of solar radiation intensity under different conditions.*

2.2.2 In-coupling of the Light

Solar cells are usually manufactured on substrates such a glass or quartz. For high efficiency, the materials used to fabricate devices should be highly transparent to light until it reaches the active region. However, solar cells are constructed from multiple layer of different materials. When light is incident on the interface between two different materials, it is partially reflected and partially refracted. On passing through a particular material it will be absorbed. Losses due to reflection and absorption depend on layer thickness and the complex refractive index of each layer. Thus, solar cell performance will be affected by geometric factors as well as the optical properties of materials. For example, Bach [6] reported that conducting glass (SnO_2:F) absorb 15% of the light falling on the device. Consequently, many research groups are trying to fabricate solar cells of specific geometries to increase light harvesting e.g. devices including downward pointing pyramid shapes [7]. To reduce absorption losses, layer thickness are kept thin and improvements in the transparency of conducting glass are being worked on.

2.2.3 Light Absorption and Exciton Generation

Figure 2.3 shows the first step in the photocurrent generation process in donor-acceptor solar cells which is common to solar cells with different configurations. Photons are absorbed in the active layer when their energy just exceeds close to the energy gap of the active layer. The efficiency of absorption depends on the absorption coefficient of the active layer which varies from one material to the other. The light absorption may be assumed to follow the Beer-Lambert equation, so that the light intensity (I_X) after passing through a thickness x of material is given by

$$I_X = I_0 e^{-\alpha x} \tag{2.3}$$

where I_0 is the incident light intensity, α is the absorption coefficient. For high efficiency, the materials used to construct solar cells should have a high absorption coefficient.

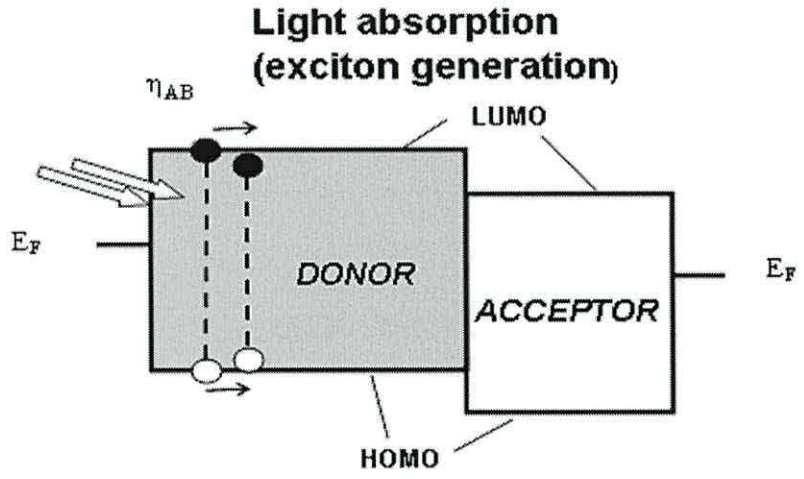

Figure 2.3 *Photon absorption in the active layer of solar cells to generate excitons.*

Photons absorbed in the active layer generally have sufficient energy to promote electrons from the HOMO to LUMO levels of the donor material. Each electron-hole pair (exciton) is bound by Coulomb attraction with an energy that ranges from 0.1eV to 2eV [8, 9, 10]. The exciton is electrically neutral and remains associated with the polymer chain in which it was created occupying an excited state in the energy gap. To extract electrical energy from the solar cells, the exciton must be separated. This is generally achieved at an interface between the light absorbing

material and an electron acceptor (see figure 2.3). Most organic materials have the ability to absorb visible light (wavelength ranges from 400 nm to 700 nm) corresponding to their energy gap which ranges from 2.2eV down to1.5eV [11].

2.2.4 Exciton Migration

Excitons remain on molecules of the active material until the electrons and holes are either separated or recombined. This depends on the diffusion length, the lifetime of the exciton and the structure of the device. In organic solar cells, the diffusion length of excitons is limited to ~ 5-20 nm [12, 13, 14, 15] and their lifetime is hundreds of picoseconds [16, 17]. Therefore, an exciton, formed far away from the interface at a distance longer than its diffusion length, will recombine either radiatively or non-radiatively. Under zero bias conditions, therefore, the efficiency of exciton migration (η_{ED}) is governed by the thickness of the active layer (d) and the exciton diffusion length (L_D) and is given by

$$\eta_{ED} = \exp(\frac{-d}{L_D}). \qquad (2.4)$$

The decay of excitons will be decreased when excitons are generated close to i.e. within a diffusion length of dissociation sites at the interface of double-layer solar cells. This process is depicted in figure 2.4 where the exciton is shown diffusing toward the donor/acceptor interface.

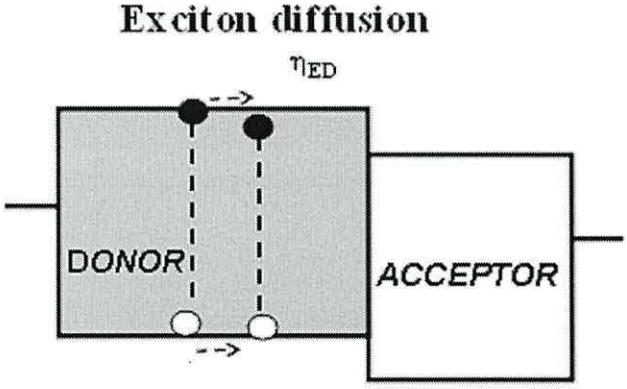

Figure 2.4 *Exciton diffusion in the active layer of solar cells.*

2.2.5 Exciton Dissociation

Excitons created in the active layer must be dissociated at an interface to generate free charge carriers in solar cells. So far, the best efficiency obtained for exciton dissociation has been reported donor/acceptor (D/A) interfaces of solar cells [18, 14, 19]. Such an interface is formed when energy levels of two un-doped organic materials are brought together. The two materials (donor and acceptor) form a heterojunction at the interface. For example, fullerene(C_{60}) and nano-crystalline titanium dioxide (nc-TiO_2) are electron acceptors and both have been used to produce double layer solar cells with PPV as the electron donor [19, 14].

The separation force experienced by an exciton depends on the difference between the ionization energy (I_P) of the donor material and the electron affinity (E_A) of the acceptor material. After excitons are created in the active layer, they diffuse to a dissociation site at the interface between donor and acceptor. Figure 2.5 shows the energy level diagram for a donor-acceptor heterojunction solar cell. Excitons are formed in the donor material following the scheme

$$D + h\nu \longrightarrow D^* \qquad (2.5)$$

where D represents the donor material, and D^* is the excited state of the donor following photon absorption in the material, h is Planck's constant, and ν is the frequency of the light falling on the device. The electron transfer to the LUMO level of the acceptor layer leaves behind a hole in the donor i.e.

$$D^* + A \longrightarrow D^+ + A^-. \qquad (2.6)$$

However, for dissociation to occur, the energy of the exciton must exceed the energy difference between the ionization potential of the donor and the electron affinity of the acceptor, i.e. I_P-E_A. If the exciton energy is less than I_P-E_A dissociation does not occur [20].

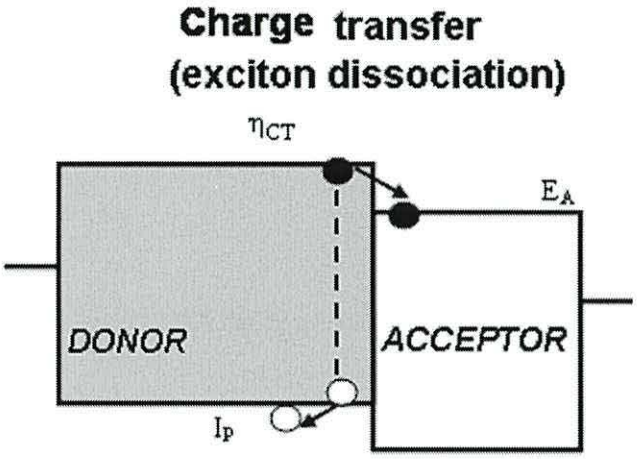

Figure 2.5 *Exciton dissociation occurs at the interface between donor and acceptor materials.*

The most popular type of acceptor materials in organic solar cells are Buckminsterfullerene (C_{60}) and its derivatives and titanium dioxide (TiO_2). A photo-electric study of C_{60}/PPV was reported for the first time by Sariciftci and co-workers [21]. They obtained interesting results in terms of ultrafast, reversible, and metastable photo-induced electron transfer from the PPV to C_{60}. The dissociation of excitons at the C_{60}/PPV interface occurs within a few hundred femto-seconds with an upper limit of 300 fs. This is shorter than the time needed to recombine holes and electrons by approximately three orders of magnitude. Therefore, exciton dissociation efficiency could reach 100% for such devices, thus improving the quantum efficiency over that achieved in single layer solar cells. Unlike the bi-layer devices fabricated by Sariciftci, the single layer solar cells suffers from a recombination efficiency of excitons of 90 % .

The donor/acceptor solar cells composed of polymer with fullerene (C_{60}) were constructed either as bi-layer or bulk heterojunction solar cells. In bi-layer solar cells, the dissociation process occurs only at the contact between the donor and acceptor materials. The bulk region in solar cells makes no contribution to the dissociation process. Despite the improvement in the efficiency, the efficiency of bi-layer solar cells remains low because of the small area of electrical contact between the donor and acceptor materials.

Bulk heterojunction solar cells are fabricated by spin-coating a solution containing PPV and C_{60} onto the bottom of the electrode. Thus, the interface area between the donor and acceptor materials increases substantially and is present throughout the whole bulk of the device. This reduces the limiting effect of exciton diffusion length and increases the power conversion efficiency to 4 %. Devices constructed using nano crystalline titanium dioxide as the acceptor are introduced in Chapter 3.

2.2.6 Charge Transport and Collection

The free charge carriers formed by exciton dissociation must flow to the electrodes in order to generate an external current from the solar cells. Electrons and holes (in the form of polarons) flow in the acceptor and donor material respectively. In organic materials, charge transport is likely to occur via hopping through a density of states. Such transport is characterized by relatively low mobilites and charge trapping, both of which will reduce solar cells efficiency. To reduce this problem, the electrical path length must be kept as low as possible by using thin layer of materials. After optimizing, the efficiency of exciton generation/dissociation and charge transport in solar cells will be high. The final problem to consider is the contacting electrodes. Ideally, the electrodes should form ohmic contacts that present no barrier to carrier transport out of the cell.

Under illumination, the free charges resulting from exciton dissociation drift in the electric field to the respective electrode. These free charge carriers could also diffuse to electrodes responding to a gradient of carrier concentration (Figure 2.6). To avoid the loss of generated charges, the work function of electrodes should be higher than the electron affinity of the acceptor material in order to transport electrons from the material to the electrode ($\varphi_m > E_A$). Similarly, the work function of the counter electrode should be lower than the ionization potential of the donor material, ($\varphi_m < I_p$) to transport holes from the donor material.

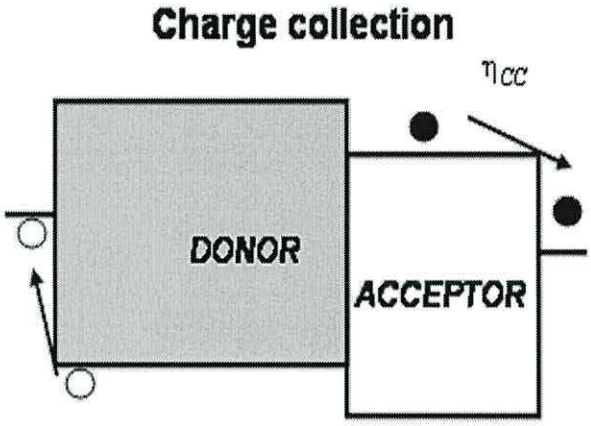

Figure 2.6 Charge *collection in bi- layer solar cells under illumination.*

Finally, for organic solar cells, there has been considerable debate about the factors which determine the value of Voc reported which are as follows:

- For single layer solar cells: In a Schottky–type device, the upper limit of Voc is determined by the difference in the work functions of the electrode metal and semiconductor used to fabricate the solar cells. This is an equal to built-in potential formed at interface between metal and semiconductor. If electrode materials are chosen so that their Fermi levels align with the HOMO and LUMO of an undoped semiconductor then, based an the MIM model, Voc is determined by the difference in the work functions of electrodes. However, this model does not apply if a Schottky barrier is formed between the electrode and semiconductor [22].
- For two layer solar cells: Less is known about the Voc in solar cells fabricated from un-doped semiconductors. It has been suggested [23, 24] that the difference between the electron affinity of acceptor material (LUMO) and ionization potential of donor material (HOMO) determine the maximum value of Voc**.** The authors of [25] suggested that the difference in the work functions of the electrode determines the value of Voc for bulk heterojunction solar cells. This may be a coincidence since the work functions of the electrodes were chosen to be close to the LUMO and HOMO of the donor and acceptor materials respectively. For solar cells fabricated form doped semiconductors, the p-n junction model that is applied is similar to the Schottky barrier mentioned in single layer solar cells.

2.3 Characterization of organic solar cells

2.3.1 Equivalent Circuit of Organic Solar Cells

Organic solar cells have been fabricated using various different architectures and organic materials, yielding different efficiencies. These devices are characterized using the same model as that applied in inorganic solar cells although there are differences in some aspects from organic solar cells. An Equivalent Circuit Diagram (ECD) for solar cells is shown in figure 2.7.

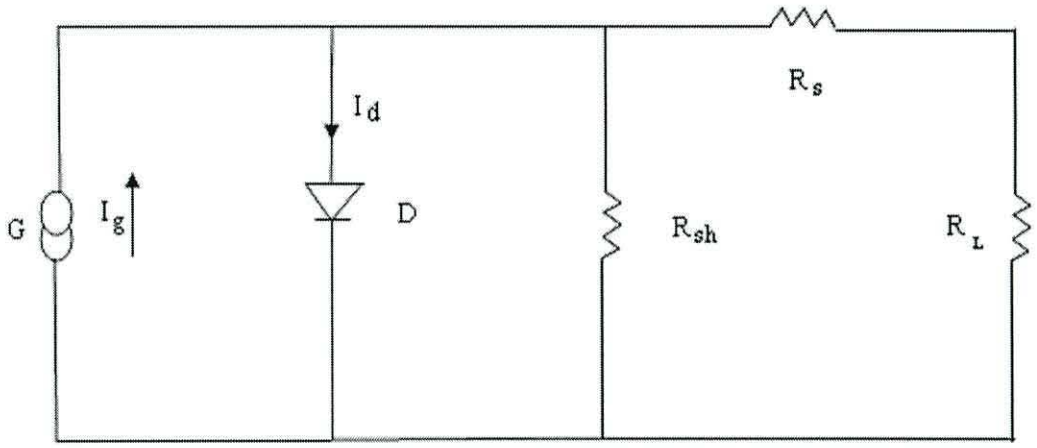

Figure 2.7 *Equivalent circuit diagram of a solar cell.*

The ECD consists of photocurrent generator (G), diode (D), load resistance (R_L), series resistance (R_s), and shunt resistance (R_{sh}). The origin of the components is as follow

- G: The photocurrent generator represents exciton dissociation at the interface which provides I_g. After dissociation, electrons and holes move toward the electrodes to be collected and generate the external current.
- D: The diode represents the dark current (I_d)-voltage (V) characteristic of the solar cells and is controlled either by the metal-semiconductor interface or by the donor /acceptor interface. The turn–on voltage of the diode sets an upper limit on Voc.

- R_L : Load resistance is the external load in which the power generated by the solar cells is usefully dissipated. When measuring the device properties in the present work this is a Keithley instrument source measure unit (SMU).
- R_s : The series resistance represents the total resistance through which the useful photocurrent must flow before reaching the load. It includes the bulk resistance of the semiconductor and contact interfaces at the electrode. The most serious limitation of solar cells performance is the bulk resistance of the semiconductor which arises from the thickness and carrier mobility of materials used in the fabrication of solar cells. The front and back contact should be Ohmic contacts to reduce losses.
- Rsh: The shunt resistance represents the loss of photogenerated current internally. One component arises from the recombination of photo generated hole-electron pairs. The second contribution is related to defect sites at the interface providing current pathway through the junction.

Thus, the ECD can be used to interpret the IV characteristics of organic and inorganic solar cells. In the following section, a single- layer Schottky barrier solar cell is considered as a simple example to explain the DC and AC characteristics of solar cells.

2.3.2 DC Characteristics of Single-Layer Schottky Barrier Solar Cells

The existence of a Schottky barrier at the interface between a metal and semiconductor depends on the value of the built-in potential which should be bigger than 0.3eV. Under this condition, a rectifying contact is formed which allows the flow of charge carriers in one direction only. A Schottky barrier is formed when the work function of the metal is higher than the work function of an n-type semiconductor ($\Phi_m > \Phi_{Sn}$) or when the work function of the metal is lower than work function of a p-type semiconductor ($\Phi_m < \Phi_{Sp}$).

Figure 2.8 shows the Schottky contact created between aluminum (Al) with a work function of 4.2eV and P3HT (p-type semiconductor) with a work function of 5eV. The built-in potential at the interface is formed from the diffusion of holes (majority carriers) from P3HT to aluminum until the Fermi levels of the two

materials are aligned. This process leads to bending of the bands edges of P3HT due to the space–charge of uncompensated negative acceptor ions present at the interface. The space–charge or depletion region at the interface gives rise to an electric field. Excitons generated in the depletion region or within ~10 nm of the diffusion edge can dissociate into free electrons and holes.

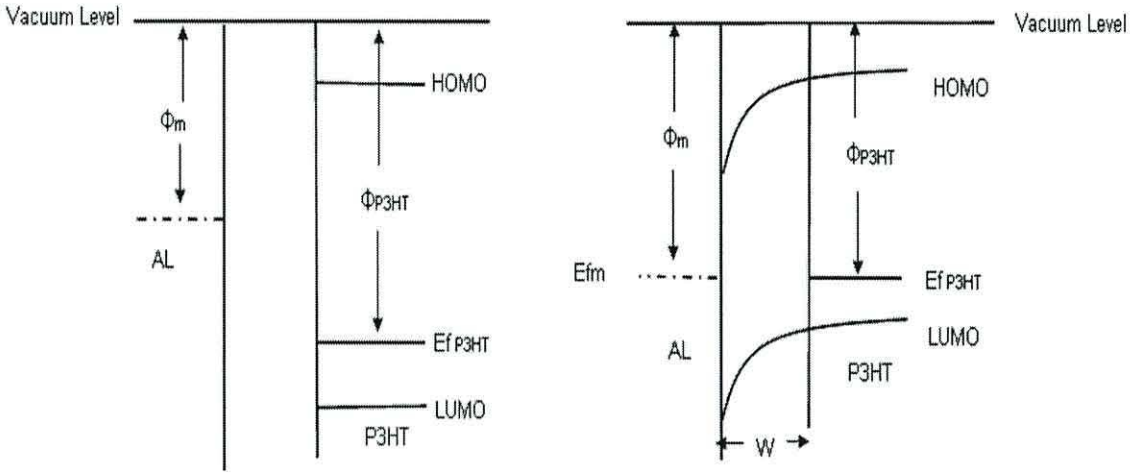

Figure 2.8 *Schottky barrier formed at the interface between P3HT as the p-type semiconductor and aluminum.*

Under dark conditions, the current-voltage characteristics of Schottky barrier solar cells can be described by

$$I_{dark} = I_o (\exp(\frac{qV}{kT}) - 1) \qquad (2.7)$$

where I_o is the reverse saturation current, k is Boltzman constant, I_{dark} is the dark current, q the electron charge, T the absolute temperature, and V is the bias voltage.

Under illumination, a photo generated current (I_g) flows in a direction that opposes the forward current of the diode. Therefore, the net current flow (I_{net}) is given by:

$$I_{net} = I_g - I_o (\exp(\frac{qV}{kT}) - 1) . \qquad (2.8)$$

Under open circuit voltage conditions, $I_{net} = 0$ which occurs when the dark diode current is equal and opposite to the photo-generated current (I_g). Therefore, the externally generated voltage (Voc) under these conditions is given by

$$V_{oc} = \frac{kT}{q}\ln(\frac{I_g}{I_o}+1), \tag{2.9}$$

When $R_s = 0$ and $R_{sh} = \infty$, then the short circuit current (I_{sc}) measured externally is given by

$$I_{sc} = I_g \ . \tag{2.10}$$

Therefore, to maximize the power delivered to an external load, the photogenerated current (I_g) must be maximized by optimizing light absorption and exciton generation and dissociation efficiencies.

In real devices, both R_s and R_{sh} have values determined by the properties of the materials forming the devices as well as by the nature of the interfaces. R_{sh} must be as large as possible so as to minimize the loss of current internally while R_s needs to be as small as possible to reduce the loss of voltage internally. When the effect of R_s and R_{sh} are taken in account, the relation between output current, I_{out}, and output voltage , V_{out}, becomes:

$$I_{out} = I_g - I_o(\exp(\frac{qV}{kT})-1) - \frac{V}{R_{sh}} \tag{2.11}$$

where

$$V = V_{out} + I_{out} R_s . \tag{2.12}$$

Under this condition, the open circuit voltage (Voc) is obtained when $I_{out} = 0$, and described by

$$V_{oc} = \frac{kT}{q}\ln(\frac{I_g}{I_o}+1-\frac{V_{oc}}{I_o R_{sh}}) \tag{2.13}$$

When $R_{sh}=\infty$, we recover equation (2.9). However, when R_{sh} decreases so does V_{oc}. The short circuit current is obtained when $V_{out}=0$ i.e.

$$I_{sc}=\frac{kT}{qR_s}\ln\left(\frac{I_g}{I_o}+1-\frac{Isc}{I_o}\left(1+\frac{R_s}{R_{sh}}\right)\right) \tag{2.14}$$

Increasing R_s decreases I_{sc}. Decreasing R_{sh} will also produce a small reduction in I_{sc}. This influence of R_s and R_{sh} on the current–voltage characteristics of solar cells will be discussed further after considering the parameters that define solar cells performance.

Figure 2.9 shows a typical IV characteristic for a solar cell under illumination. The important parameters indicated on the curve are: short circuit current (I_{sc}), open circuit voltage (V_{oc}), and the maximum output power (P_{max}). These parameters are used to determine a Fill Factor which indicates the quality of the solar cells. Fill Factor is defined as the ratio of the areas of rectangles representing the maximum output power (P_{max}) and the product I_{sc} V_{oc} and is given by

$$FF=\frac{P_{max}}{I_{sc}V_{oc}}=\frac{I_mV_m}{I_{sc}V_{oc}}. \tag{2.15}$$

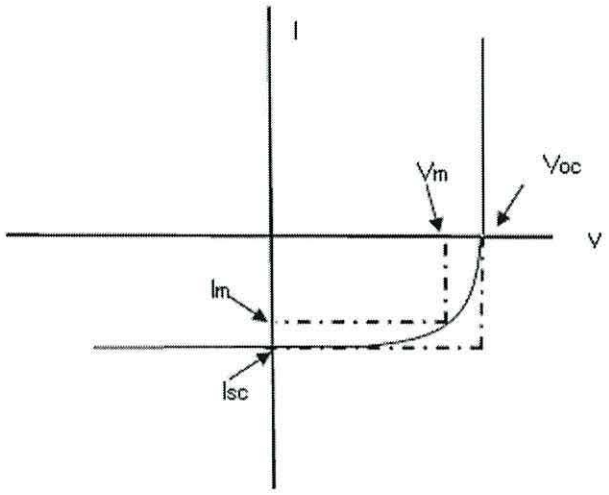

Figure 2.9 *I-V curve of an ideal single- layer Schottky barrier solar cell under illumination*

The Fill Factor for solar cells are usually in range from 0.25 to 1. This depends on properties of the materials used to fabricate solar cells and the quality of the interface. Solar cells with a high Fill Factor close to 1 indicate that the solar cells have high efficiency. Fill factor of low value (~ 0.25) indicates that the solar cells have low efficiency.

The power conversion efficiency (η) of solar cells is the ratio of the maximum output power to the power of the incident light (P_{Light}) and given by

$$\eta = \frac{P_{max}}{P_{light}} = \frac{I_m V_m}{P_{light}}. \tag{2.16}$$

Substituting for $I_m V_m$ from equation (2.15) above yields:

$$\eta = \frac{I_{sc} V_{oc} FF}{P_{light}}. \tag{2.17}$$

The light source used for measuring the efficiency of solar cells should have a similar spectrum to sunlight. This can be achieved by using a solar simulator with appropriate filters. Unfortunately, such a system was not available for the present work. As reported by several laboratories, a tungsten halogen lamp was used instead with appropriate changes made to the light intensity to compensate partially for the difference in spectral output. In a separate approach, the efficiency-under solar illumination- can be calculated from the External Quantum Efficiency (EQE) of the device as a function of wavelength. EQE is defined as the number of electrons collected ($N_{electrons}$) per incident photon ($N_{photons}$) so that

$$EQE = \frac{N_{electrons}}{N_{photons}}. \tag{2.18}$$

The number of electrons flowing in the external current circuit in time Δt under short circuit conditions is given by

$$I_{sc} = \frac{qN_{electrons}}{\Delta t}. \tag{2.19}$$

The number of photons incident in time Δt may be determined from the relationship for incident power, $P(\lambda)$ i.e.

$$P(\lambda) = \frac{N_{photons} E_{photon}}{\Delta t}. \quad (2.20)$$

where E_{photon} is the energy of the incident photons of wavelength λ. Hence, the EQE can be calculated by measuring the power of light of a particular wavelength and the corresponding short circuit current produced by the incident photons. Thus EQE may be written as

$$EQE = \frac{E_{photon}}{q} \times \frac{I_{sc}}{P(\lambda)} \quad (2.21)$$

or

$$EQE = \frac{hc}{q\lambda} \times \frac{J_{sc}}{P(\lambda)} = \frac{1.2 \times 10^{-6}}{\lambda} \times \frac{J_{sc}(mA/cm^2)}{P(\lambda)(mW/cm^2)} \quad (2.22)$$

Once the EQE has been determined as a function of wavelength it may be combined with the AM1.5 solar spectrum $\phi(\lambda)$ to estimate the short circuit current density (J_{SC}) that could be expected from the solar cells under solar irradiation. Thus, J_{SC} may be calculated by using equation 2.23.

$$J_{sc} = q \int_{\lambda 2}^{\lambda 1} EQE(\lambda)\phi(\lambda).d\lambda . \quad (2.23)$$

The integral is taken over the useful response range of the device. In addition to the intrinsic properties of the materials used for constructing the solar cells, parameters such as R_S and R_{sh} are also affected by external factors in particular the device temperature. While the direct dependence on T in equation (2.13) and (2.14) suggest that both Voc and Jsc should increase proportionally with temperature, other temperature dependent parameters mitigate against this. R_{sh} decreases with increasing temperature leading to a reduction in Voc. In contrast, the reduction in R_S leads to an increase in Jsc (equation 2.14). However, both effects will be dominated

by the exponential dependence of I_0 on temperature which will reduce both Voc and J_{sc}.

Figure 2.10 illustrates the effect of decreasing R_S and R_{sh} on the current-voltage properties of single-layer Schottky barrier solar cells. It appears that the Voc and Jsc are high when R_s is small and R_{sh} is high. Additionally, the maximum output power decreases with the increase of R_s and the decrease of R_{sh}. Therefore, the Fill factor and power conversion efficiency of solar cells will be affected.

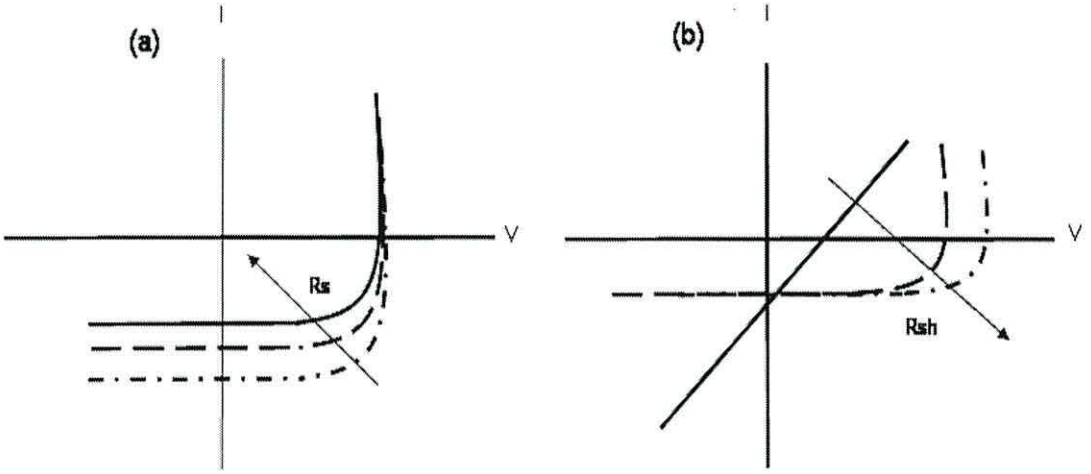

Figure 2.10 The effect of Rs and Rsh on IV curve of solar cells was a) when the series resistance was high (solid curve (——)) and low (- - - -) (see equation (2.14)) b)when the Rsh was low *(solid line——) and high (dash line* . - - - -) (see equation 2.13).

2.3.3 AC Characteristics of Single- Layer Schottky Barrier Solar Cells

The depletion region of single-layer Schottky barrier solar cells is composed of a uniform density of fixed charge Qsc (Figure2.11). The width (W_d) of the depletion region is related through Poisson equation to the charge density and the potential Vs appearing across the layer i.e.

$$V_s = \frac{Q_{sc} W_d^{\,2}}{2\varepsilon\varepsilon_o} \tag{2.24}$$

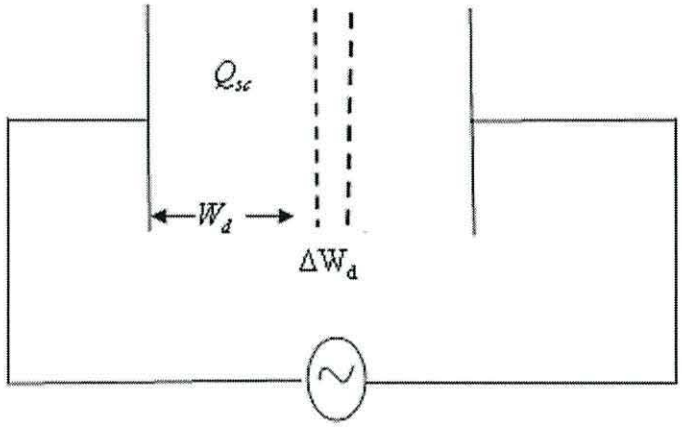

Figure 2.11 *Schematic diagram of the depletion region in a Schottky diode under small AC voltage.*

When a small signal voltage, v, is applied across the structure, majority carriers at the boundary of the depletion region respond by modulating the thickness of the depletion region. The resulting change in charge ($A\Delta W_d Q_{sc}$) at the depletion region edge is equivalent to the presence of a capacitor (C_d).

$$C_d = \frac{dQ}{dV} = \frac{q_{sc}}{v} = \frac{A\Delta W_d Q_{sc}}{v} \tag{2.25}$$

where q_{sc} is the small signal change in charge.

The depletion region behaves as parallel plate capacitor i.e.

$$C_d = \frac{A\varepsilon\varepsilon_o}{W_d}. \tag{2.26}$$

Applying a bias voltage (V) across the device changes the depletion region width (W_d). The depletion capacitance for an ideal diode will exhibit the well-known Mott-Schottky dependence,

$$C_d^{-2} = \frac{2}{N_a q\varepsilon\varepsilon_o A^2}[V_{bi} - V - \frac{kT}{q}] \tag{2.27}$$

where N_a is the density of ionized acceptors in the depletion region of a p-type semiconductor and V_{bi} is the built - in potential.

The diffusion capacitance (C_{diff}) contributes to the total capacitance when the diode is in forward bias. It results from the injection of minority charge carriers across the junction forming a neutral zone close to the interface. This capacitance depends on the forward current and thus increases exponentially with the voltage applied on the device.

It may be shown that the admittance Y_{diff} arising from minority carrier diffusion is given by

$$Y_{diff} = \frac{qI}{kT}[1 + j\omega\tau]^{1/2} \tag{2.28}$$

where τ is the minority carrier lifetime.

At low frequency ($\omega\tau << 1$)

$$Y_{diff} \approx \frac{qI}{kT}[1 + \frac{j\omega\tau}{2}] \tag{2.29}$$

so that the capacitance and conductance may be written as

$$C_{diff} = \frac{qI}{2kT}\tau \tag{2.30}$$

$$\frac{1}{R} = G_{diff} = \frac{qI}{kT}. \tag{2.31}$$

At high frequency ($\omega\tau >> 1$),

$$Y_{diff} = \frac{qI}{kT}[\frac{j\omega\tau}{2}]^{1/2} \quad . \tag{2.32}$$

which readily gives the capacitance and conductance

$$C_{diff} = \frac{qI}{kT}(\frac{\tau}{2\omega})^{1/2} \tag{2.33}$$

$$G_{diff} = \frac{qI}{kT}(\frac{\omega\tau}{2})^{1/2} \quad . \tag{2.34}$$

The total capacitance C_j at the interface of the junction in a singe layer–Schottky solar cells is then the sum of the depletion and diffusion capacitances i.e.

$$C_j = C_d + C_{diff} \tag{2.35}$$

For a single layer-Schottky barrier solar cells, the AC equivalent circuit may be represented as shown in figure 2.12. We have already shown that the depletion region at the interface between polymer and metal may be represented by a parallel plate capacitor C_d. In parallel with this capacitance is R_d to account for the small leakage current through the depletion region. The change in concentration of minority charge carriers at high forward bias is represent by C_{diff}, while the conductance associated with these carriers is represented by R_{diff}. The bulk region of the device is represented by the parallel combination of C_b and R_b. In general terms, we may associate R_b with R_S and R_d and R_{sh} in the DC equivalent circuit of the solar cells. However, care is required in this analogy since R_{sh} also represents the effect of recombination of photogenerated electrons and holes.

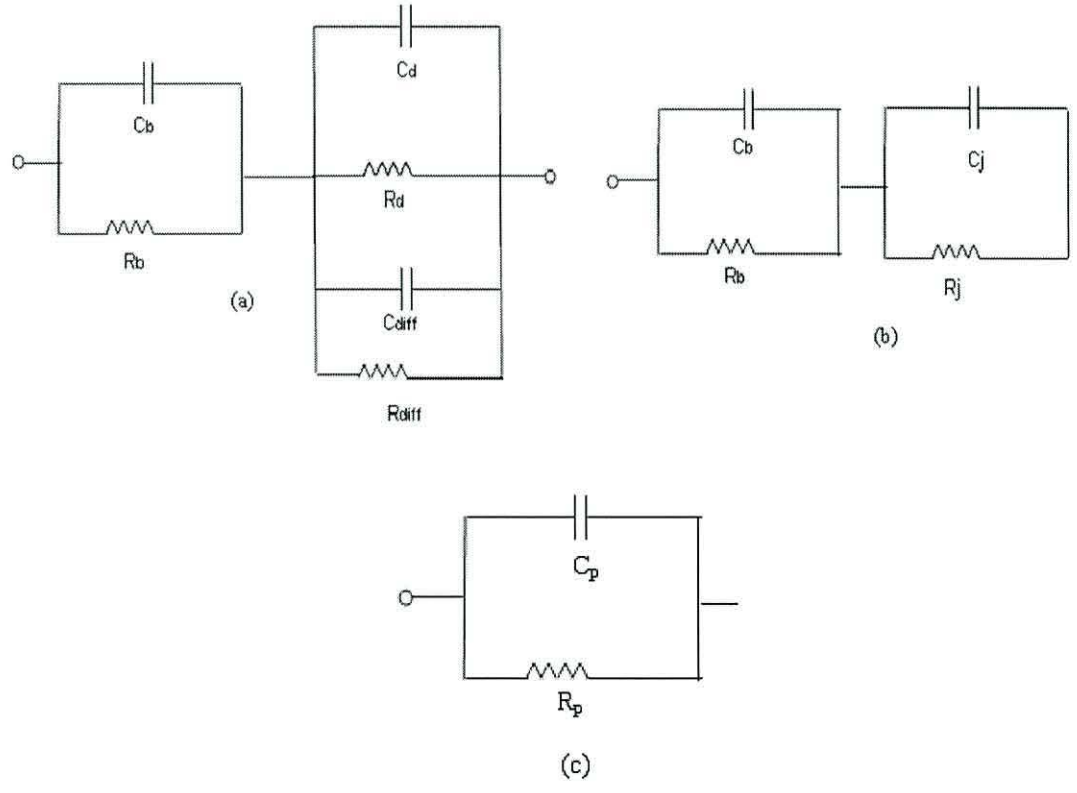

Figure 2.12 a) *Equivalent circuit to model the AC behavior of a Schottky barrier solar cell and b) the same circuit with capacitance and conductance combined and (c) the circuit observed by the bridge.*

The equivalent circuit in figure 2.12(a) may be reduced to the simple form in figure 2.12(b) where $C_j = C_d + C_{diff}$ is the total junction capacitance and $R_j (= \frac{R_d + R_{diff}}{R_d R_{diff}})$ is the resistance of the junction itself. The total admittance of the device may now be written

$$Y_p = G_p + j\omega C_p \tag{2.36}$$

where G_p and C_p are equivalent parallel-conductance and capacitance respectively (Figure 2.12 (c). They are both frequency-and voltage-dependent. At high requencies above the relaxation frequency, the measured capacitance is approximately C_b since the total capacitance (C_P) observed by bridge is the series sum of C_b and C_j and $C_b << C_j$. At high forward voltage ($R_b << R_j$), the measured capacitance is equal to C_j which is approximately C_d (C_{diff} =0).

At low frequency, the bulk region capacitance is shunted by R_b and the measured capacitance increases and is equal to the junction capacitance. The junction capacitance has contributions from diffusion and depletion capacitances which have the following properties.

1. C_{diff} decreases with increasing frequency and increases exponentially with increasing applied voltage. Thus, at low frequency under high forward bias the junction capacitance is dominated by the diffusion capacitance.
2. Under reverse and zero bias, there is no diffusion capacitance at the junction only a depletion capacitance which decreases with increasing reverse bias. Therefore, at low frequency the measured capacitance is dominated by the depletion region.

2.4 References

1. S. S. Sun, N, S, Sariciftic, *Organic Photovoltaic Mechanism, Material, and Devices*, Taylor and Francis, (2005).
2. G. Yu, J. C. Hummelen, F. Wudl, and A. J. Heeger, *Science*, **270**, 1789, (1995).
3. J. Beer, W. Mende, and R. Stelmacher, Quaternary *Science Reviews*, **19**, 403, (2000).
4. M. A. Green, Solar cells, *Operating principles, Technology and System Application*, Prentice Hall, (1982).
5. R. H. B. Exell,. *http://www.jgsee.kmutt.ac.th/exell/Solar/Intensity.html* King Mongkut's University of Technology Thonburi, (2000).
6. U. Bach, D. Lupo, P. Comte, J. E. Moser, F. Weissortel, J. Salbeck, H.Spreitzer, and M. Gratäzel, *Letters to Nature*, **385**, 583, (1998).
7. H. L. Chen, W. Fan, C.C.Cheng, C. H. Lin, and K. T. Hiang, *Journal of the Electrochemical Society.* **153**, 802, (2006).
8. I. G. Hill, A. Kahn, Z. G. Soos, and R. A. Pascal, Jr, *Chemical Physics Letters*, **327**, 181, (2000).
9. S. F. Alvarado, P. F. Seidler, D. G. Lidzey, and D. D. C. Bradley, *Physics Review Letters,* **81,** 1082, (1998).
10. R. Kersting, U. Lemmer, M. Deussen, H. J. Bakker, R. F. Mahrt H. Kurz, V. I. Arkhipov, H. Bässler, and E. O. Göbe. *Physics Review Letters,* **73**, 1440, (1994).
11. M. Al-Ibrahim, H. K. Roth, M. Schroedner, A. Konkin, U. Zhokhavets, G. Gobasch, P. Scharff, and S. Sensfuss, *Organic Electronics*, **6**, 56, (2005)
12. S.R. Scully and M.D. McGehee, *Journal of Applied Physics.* **100,** 034907, (2006).
13. J. J. M. Halls, K. Pichler, R. H. Friend, S. C. Moratti and A. B. Holmes, *Synthetic Metals*, **68**, 3120, (1996).
14. L. A. Pettersson, L. S. Roman, and O. Inganäs, *Journal of Applied Phy*sics, **86**, 487, (1999).
15. T. J. Savenije, J.M. Warman, and A. Goossensm, *Chemical Physics Letters*, **148,** 287, (1998).

16. N. C. Greenham, I. D. W. Samuel, G. R. Haves, R. T. Phillips, Y. A. R. Kessenet, S. C. Moratti, A. B. Hplmed, and R. H. Friend, *Chemical Physics Letters,* **89,** 241, (1995).
17. S. S. Harilal, C. V. Bindhu, V. P. N. Nampoori, and C. P. G. Vallabhan,. *Journal of Physics: D Applied Physics,* **86**, 1388, (1996).
18. D. Chirvase, Z. Chiguvare, M. Knipper, J. Parisi, V, Dyakonov, J. C. Hummelen, *Synthetic Metals*, **138**, 299, (2003).
19. T. J. Savenije, J. M. Warman, A. Goossens, *Chemical Physics Letters*, **148**, (1998).
20. P. Peumans, A. Yakimov, and S.R.Forrest, *Journal of Applied Physics*, **93**, 3693, (2003).
21. N. S. Sariciftci, L. Smilowitz, A. J. Heeger, and F.wudl, *Science*, **258**, 1474.(1992).
22. H. Hoppe, and N. S. Sariciftci, *Journal of Materials Research*, **19**, 1924, (2004).
23. W.Mammo, S. A dmassie, A. Gadisa, F. Zhang, O. Inganäs, and M. Andersson, *Solar Enegry Materials and Solar cells*, **91**, 1010, (2007).
24. B. P. Rand, D. P. Burk, S. R. Forrest, *Physical Reviews,* **75.**15327, (2007).
25. C. M. Ramsdale, J. A. barker, A.C. Arias, J. D. Mackenzie, R. H. Friend, *Journal of Applied Physics* , **92**, 4266, (2002).
26. Jenny Nelson, *The Physics of Solar Cells,* Imperial College press, (2003).
27. K. Feldrapp, R. Horbelb, R. Aure, and R. Brendel, *Progress in Photovoltaic: Research and Application*, **11**, 105, (2003).

Chapter 3

Metal Oxide-solar cells (MOSCs)

3.1 Introduction

This chapter reviews the properties of Metal-Oxide Solar Cells (MOSCs). It describes the materials used, the structure of the solar cells and their electro-optical behavior.

3.2 Components of Metal Oxide-Solar cells

Much work has been undertaken to find easy techniques for producing MOSCs with high efficiency. Fabricated MOSCs have been fabricated from 2, 3, and 4 layers sandwiched between electrodes. Each layer of a MOSC has a certain task to perform in the process of converting solar energy into electrical energy [1, 2, 3]. This section explains the various components of MOSCs which are: Transparent Conducting

Oxide (TCO), Metal Oxide Materials, Sensitizer Layer, Hole Conductor, and top electrode.

3.2.1 Transparent Conducting Oxide Substrate

There are different kinds of substrates used in fabricating solar cells. This is due to the increase of demand to produce solar cells with certain properties (e.g. flexibility and reduction of preparation cost) [4]. Examples of substrates are polymer foil substrates and a glass substrate. Thus, for the production of plastic solar cells on an industrial scale polymer foil substrates are preferred. They are easier to handle e.g. processing steps like cutting of large entities into smaller individual modules, and laminating. However, polymer foils have a disadvantage by reducing the light transmission to the active layer in solar cells. For solar cells which use polymer foils the light should enter through the top electrode instead of bottom electrode.

For MOSCs, two kinds of Transparent Conducting Oxide (TCO) are used as glass substrates: fluorine–doped tin dioxide (SnO_2:F) and indium tin oxide (ITO) [5,6]. These materials can withstand the high temperature between 450 to 550 °C needed to prepare the nc-oxide film. SnO_2:F substrate is now becoming more widely used in MOSCs, because when heated to high temperature indium might diffuse into the cells causing short circuit [6]. Additionally, the work function of ITO can change depending upon the cleaning process [7]. SnO_2:F also forms Ohmic contact with TiO_2 which is important for achieving good Voc. A high Voc of 0.65V was reported for MOSCs composed of SnO_2:F where it was 0.5V for devices composed of ITO [8]. In both cases, it is preferable to coat the transparent electrode with a thin compact layer of TiO_2 before coating with a porous nanocrystalline TiO_2 ($nc\text{-}TiO_2$) to reduce the possibility of short circuits between the hole conductor and the TCO in MOSCs.

3.2.2 Metal Oxide Materials

In inorganic–organic solar cells, an oxide material is used as the layer for transmitting the light and acting as the electron acceptor. It is also used as a substrate surface to be coated with a dye layer and the hole conductor. The oxide materials are usually n-type semiconductors with enhanced electron mobility e.g. CeO_2, $nc\text{-}TiO_2$, ZnO, SnO_2 [9]. They can be used as a layer deposited directly onto the TCO or mixed with a hole conductor for improving the solar cells efficiency [10, 11].

Additionally, the morphology of metal oxides can be modified to increase the efficiency of solar cells. The best performance of MOSCs has been reported for solar cells composed of nc-TiO_2. Thus, nc-TiO_2 materials have attracted the attention of many research groups for fabricating solar cells commercially compared with other metal oxides [12]. We aim in this section to discuss the different aspects of nc-TiO_2 which are relevant to the fabrication of solar cells described in this thesis.

History of Titanium Dioxide

Titanium dioxide (TiO_2) is an important inorganic compound that is widely used. It was discovered in 1791 by William Gregor [13] and attracted the attention of many researchers due to its unique physical, chemical, and electronic properties. It is a white pigment used in plastics, paints, rubbers and paper. Additionally, TiO_2 is considered to be a non-toxic material and available naturally at low cost. It is composed of 59.94 % titanium and 40.06 % oxygen. In 1972, the photocatalytic characteristics of titanium oxide were discovered by Fujishima and Hond [14]. This led to the establishment of a new area in heterogeneous photocatalysts to overcome problems such as pollution [15]. Another important application of nc-TiO_2 was reported first time in 1990 when Grtäzel used it in the fabrication of dye sensitized solar cells with high efficiency [16].

Crystalline forms of Titanium Dioxide

Titanium dioxide film can be obtained by various methods: spray pyrolysis, colloidal suspension and a sol–gel procedure. The films prepared by all of these methods contain either nano-crystals or micro-crystals of TiO_2. The size of nano-crystals depends on the temperature of annealing and the content of the materials used to form the TiO_2. Three crystalline phases of TiO_2 exist based on their crystal structure: Anatase, Rutile, and Brookite [17]. The three crystalline phases have been used in different applications.

Anatase TiO_2 was first found in the Buckwheat Dolomite by W. B. Thomas and was later reported by Frondel.. It has different forms: black opaque, blue, and yellow transparent crystals and is mainly used in catalysis, photocatalysis and solar cells applications. Figure 3.1 shows the crystal structure of anatase TiO_2 which looks

like tetragonal pyramids. It exhibits perfect cleavage along certain planes such as the 101 and 200. Therefore, anatase TiO_2 could be defined by determining the type of planes which form its structure using X-Ray Diffraction (XRD). Figure 3.2 shows the XRD pattern of anatase TiO_2 [19]. Clear peaks were observed at different values of 2θ ($2\theta = 25.3^{\circ}, 38^{\circ}, 48^{\circ}, 54^{\circ}$). The distance between two Ti atoms is 3.79 $\mathring{A}$ and the distance between oxygen and Ti atoms is 1.934 $\mathring{A}$.

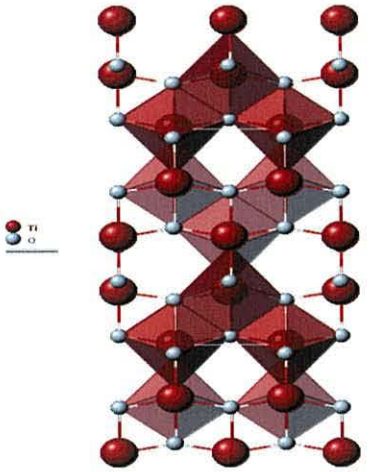

Figure 3.1 *Crystal structure of anatase crystalline TiO_2 (image adopted from reference[18]).*

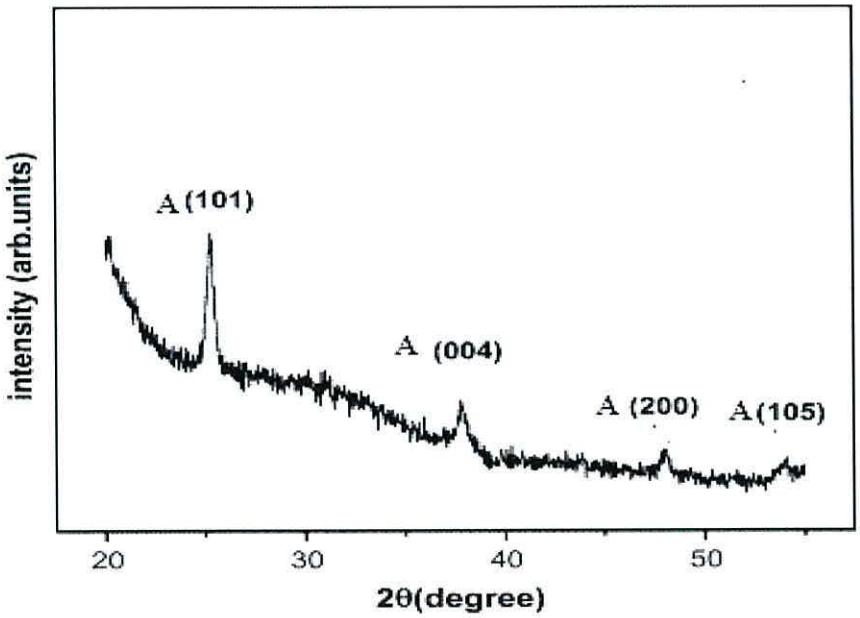

Figure 3.2 *XRD patterns of the standard anatase crystalline- TiO_2 (image adopted from reference[19].*

The second form of TiO_2 is rutile which was synthesized in 1947. Rutile TiO_2 is prepared at high temperature. Thus, it exists sometime in rocks around volcanoes and is brownish yellow, brown red or violet in colour. Figure 3.3 shows the crystal structure of rutile TiO_2 which appears as needle like crystals.

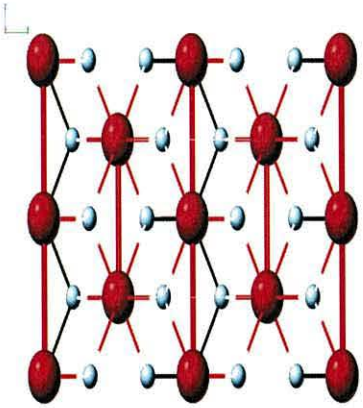

Figure 3.3 *Crystal structure of rutile crystalline TiO_2.(image adopted From reference[18]).*

Rutile TiO_2 differs from antese TiO_2 in the following ways:

- Rutile TiO_2 is commonly used as a white pigment in paints unlike the anatase form. It scatters white light more efficiently.
- Rutile TiO_2 can be distinguished from anatase TiO_2 using XRD. Figure 3.4 [20] shows the XRD pattern of rutile TiO_2. Peak intensities occur when 2θ is approximately (2θ = 27°,36°,43°,$53^{\circ}57^{\circ}$) representing planes in Rutile TiO_2 which do not exist in Anatase TiO_2 e.g. 110.
- The distance between two Ti atoms in rutile TiO_2 (2.96 $\mathring{A}$) is shorter than the distance in anatase TiO_2. Also, the distance between Ti and O atoms are greater than in anatase TiO_2 .
- Anatase TiO_2 is usually formed by sintering at 350 to $450^{\circ}C$. Once the temperature of sintering increases above $450^{\circ}C$, the TiO_2 phase changes from anatase to rutile.

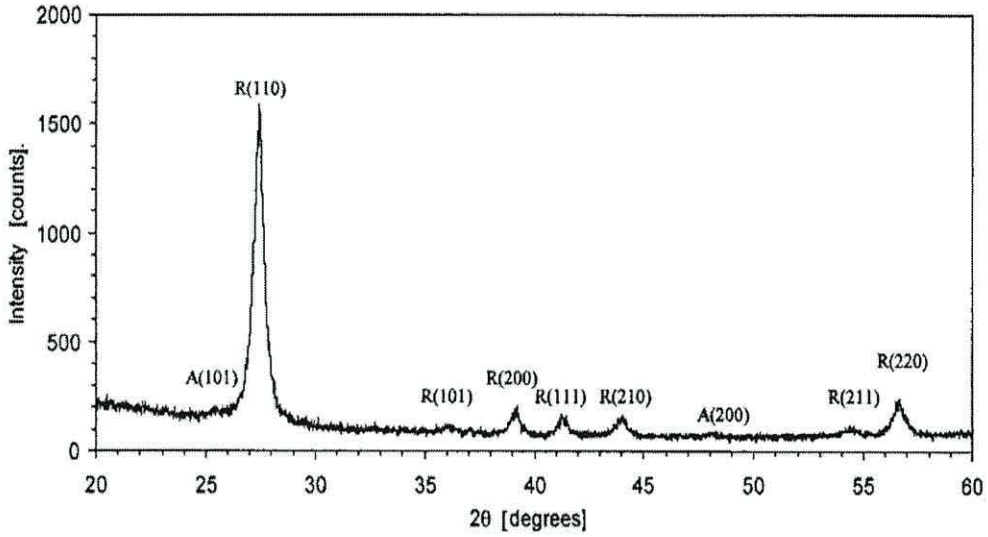

Figure 3.4 *XRD patterns of rutile crystalline TiO_2. (Image adopted From reference[20]).*

The third phase of TiO_2 is brookite which has little application. It is brown, light brown, dark brown or dark reddish brown in colour. It is distinguished by its 120 crystal plane .

Properties of Titanium Dioxide

Titanium dioxide is widely used as a catalyst in gas sensors and photoelectrodes in solar cells. It was found that the catalytic action of TiO_2 depended mainly on the ambient gas composition in air (oxygen, water) [22]. This effect was observed through studying the electrical transport properties of nano-porous TiO_2 films in laboratory air and in a dry nitrogen ambient [23]. The dark current was found to be higher in air compared to the dark current in dry N_2 gas. The authors [24] found that the receptivity of porous nc-TiO_2 was in the range between $10^9 - 10^{10}$ Ωm in the vacuum and $10^6 - 10^8$ Ωm in air. Water vapor adsorbed on the surface and in the bulk region of TiO_2 at room temperature. This causes the formation of protons, and hydroxyl ions resulting in the formation of Ti^{3+} states which come from the reaction of H_2O with bridging oxygen atom to form two OH. These defects sites (OH and Ti^{3+}) play an important role in the conductivity of TiO_2 which is low in vacuum and but high in air.

The density of states in the band gap of TiO_2 arises from oxygen vacancies and extrinsic impurities (Ti^{3+}) which affects the conductivity of TiO_2. Oxygen vacancies are formed on the TiO_2 surface when the nc-TiO_2 is sintered at high temperature. Their concentration is high for TiO_2 sintered in vacuum compared to air. Oxygen molecules in the air react with TiO_2. They capture electrons from the donor states and from the conduction band. This reduces the conductivity of TiO_2. However, the change in TiO_2 dark conductivity was dominated by adsorbed water because of the hydrophilicity of the TiO_2. Thus, the effect of oxygen on the conductivity of TiO_2 will be minor in comparison with the effect of water [24]. This also depends on the thickness, porosity, pressure, and preparation conditions of TiO_2 films [19].

Under illumination and in vacuum, the photoconductivity of TiO_2 was dominated by the reduction of oxygen molecules. In the air, the oxygen molecules capture electrons generated by the light and reduce the photocurrent. Thus, oxygen molecules act as electron scavengers. Electrons are also trapped at other surface defects Ti^{+3} which are formed close to the oxygen deficiency. In vacuum, the photocurrent was higher than in air because the concentration of oxygen molecules and other defects is less. Consequently, the concentration of traps and the scavengers on nc-TiO_2 surface are less and easily filled by electrons during the early stages of illumination leading to an increased photocurrent in vacuum. These defects and oxygen should cause a change in band bending of nc-TiO_2 in dark. Masakazu Anop and his team studied the effect of oxygen molecules on band bending of TiO_2 and ZnO [25].

As mentioned before, TiO_2 is widely used for fabricating solar cells generally forming a hole conductor/electron acceptor (p-n) junction with a p-type semiconductor to fabricate double layer solar cells. Also, the nc-TiO_2 allows the adsorption of a-dye coating on its surface to fabricate three layer solar cells and acting as an electron acceptor in this device [1]. It has already been reported that a depletion region exists at the interface between TiO_2 film and the p-type semiconductor which improves exciton dissociation at the interface and reduces the recombination rate in double layer solar cells [26]. Recently, it has been found that a depletion region forms when nc- TiO_2 is in contact with p-type semiconductor [27].

Various configurations of double layer TiO_2 solar cells have been produced by blending TiO_2 with hole conductors [28]. Such solar cells are referred to as bulk heterojunction solar cells and have the potential to compete with fullerene polymer bulk heterojunction solar cells. Additionally, the modification of TiO_2 morphology increases the efficiency of TiO_2 double layer solar cell. In 2003, Coakley and Mcgehee produced mrsoporous TiO_2 film while allowed improved infiltration of P3H through it [6]. This led to a 3-fold increase in the short circuit current density of mesoporous TiO_2/P3HT solar cells three times more compared to nonporous TiO_2/P3HT solar cells.

For three-layer dye-sensitized solar cells, the nano-crystalline TiO_2 provides a large area for the adsorption of the dye. Not surprisingly the efficiency of dye solar cells was influenced by the morphology of the surface between the dye/TiO_2 and hole conductor. This was achieved by controlling the size of particle and the thickness of nc-TiO_2 film [29]. Also, the pore size and porosity of nc-TiO_2 play an important role in increasing the penetration of the hole conductor into the nc-TiO_2 thus improving solar cells efficiency.

3.2.3 Sensitizer Layer

The efficiency of MOSCs incorporating a dye layer depends on the type of dye sensitizer in which the TiO_2 substrate is soaked. Ideally, the dye layer in the MOSCs should absorb visible light in the range between 450 nm and 650 nm. The energy states of the dye used in a MOSCs should be close to the conduction band of nc-TiO_2 and the LUMO of the hole conductors so as to inject electrons into the oxide material and transfer holes to the hole conductor. The injection of electrons in a MOSCs can be made several orders of magnitude faster than the life time of the excited state of the dye layer. Thus, the recombination of charge carrier in these devices is low so that high short circuit currents can be expected.

To produce a dye-sensitized MOSCs with dye for commercial applications, the dye layer should remain stable in order to regenerate the electrons current and to withstand the ambient conditions. Thus, it is vital that dye solar cells have at least a life time of 20 years with 10^8 redox cycle to be used commercially and compete

with silicon solar cells [30]. Additionally, the dye layer should withstand the high temperature of sunlight since solar cells while in operation.

Ruthenium dyes are one of the most extensively studied transition metal complexes in photochemistry. This is due to their chemical stability, excited state reactivity, luminescence, and long excited state life time. In early polymer/dye/TiO2 solar cells, the efficiency was low due to the low quality of dye used. Jiarg and his co-workers introduced a new sensitized layer based on a ruthenium complex [30]. They presented nc- TiO_2/conjugated polymer solar cells incorporating a ruthenium complex achieving a maximum power conversion efficiency of 2.6%. Figure 3.6 shows the molecular structure of ruthenium 535 bis-TBA cisis (isothiocyanato) bis (2,2'-bipyridyl-4,4'-dicarboxylato)-ruthenium(II) bis-tetrabutylammoniu). This dye is widely used in this field as sensitizer with TiO_2 and hole conductors and is sold by Solarnix in the form of solid material. We used it for fabricating our solar cells in our work.

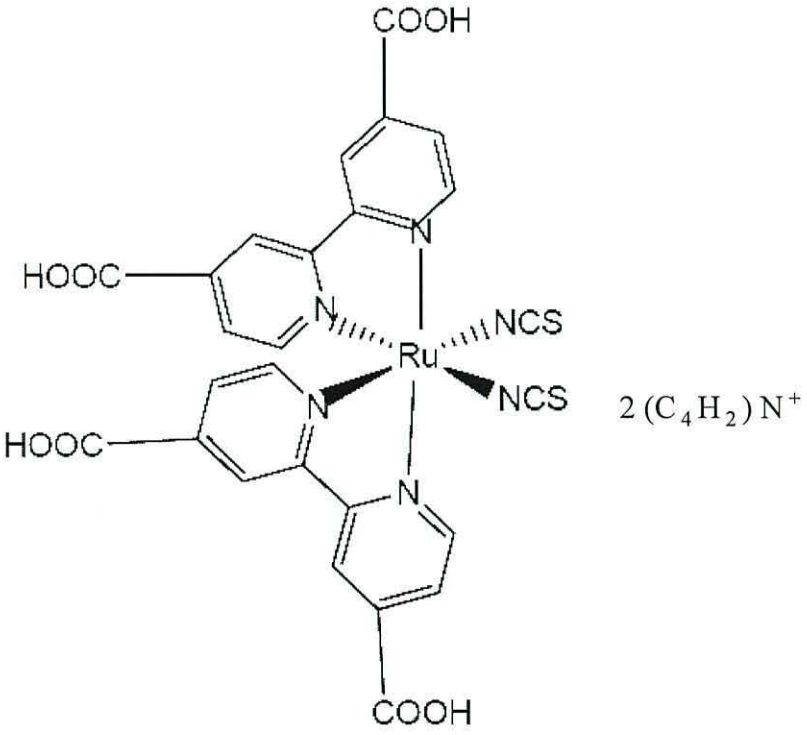

Figure 3.5 *chemical structure of Ruthenium 535-bisTBA. (Image adapted from reference [31].*

3.2.4 Hole Conductor

The common hole conductor used in fabricating dye–sensitized MOSCs is an electrolyte composed of an iodine couple dissolved in an organic solvent. This device has produced high efficiency ~ 11% [16]. However, there are few problems with using electrolyte as the hole conductor. For example, it should be sealed sufficiently well that no leakage occurs for long period of time. This is a serious limitation and to overcome this problem, solid state materials are being investigated as the hole conductor instead of the electrolyte. So far the efficiency of solid state solar cells is lower than the Grätzel cell.

3.2.5 Top Electrode

The top electrode of a MOSC (whether dye–sensitized or not) is important for collecting holes generated from dissociation of excitons at the interface. The top electrode should form an Ohmic contact with the hole conductor to achieve solar cells of good performance. Thus, the work function of the top electrode should be equal or close to the work function of the hole conductor in order to form an Ohmic contact. The existence of a potential barrier between the top electrode and the hole conductor decreases Voc for solar cells. Gold and platinum are preferred as top electrodes because of their high work function.

Thermal evaporation and sputtering techniques are generally used to deposit the top electrode on the hole conductor. The thickness of the electrode should be measured and carefully controlled as it affects the solar cell performance.

3.3 Basic Operation of MOSCs

The properties of the materials used to construct a MOSC determine its ability to achieve high conversion efficiency. One of these properties is the energy levels of each material since they influence Voc. For double layer cells, its operation was similar to double layer solar cells mentioned in Chapter 2. Unlike p-n junction solar cells, dye-sensitized MOSCs do not require an electrical field in order to separate the excitons generated as in p-n junction solar cells. The difference between the LUMO of nc-TiO2 and HOMO of holes or work function of cathode conductor determine

the maxmuim value of Voc as in double layer organic solar cells. The dye layer coated on nc-TiO_2 surface affects the value Voc of dye-senstized solar cells[32].

Figure 3.7 shows the energy level diagram and the process of charge generation of dye-sensitized MOSCs. The photo-current is generated when photons are absorbed by the dye layer. This promotes electrons to the LUMO leaving holes in the HOMO of the dye layer. Because the LUMO of the dye is higher than the conduction band of TiO_2 electrons are injected into the conduction band of nc-TiO_2. The holes left in the HOMO are transported through the hole conductor which has a lower energy than the HOMO of the dye [33].

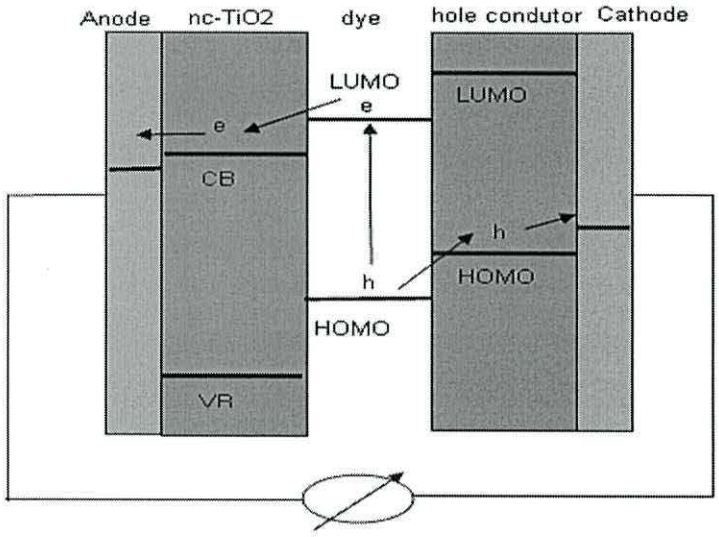

Figure 3.6 *Principle of operation and energy level diagram of solid state –dye solar cells.*

The mechanism of exciton generation in dye layer is summarized by the following:

$$h\nu + \text{dye}(Ru(L_2(NCS)_2) \longrightarrow \text{dye}\ (RuL_2(NCS)_2)^*$$

$$\text{dye}(RuL_2(NCS)_2)^* \longrightarrow \text{dye}\ (RuL_2(NCS)_2)^+ + [\text{nc-}TiO_2]^-$$

$$\text{dye}RuL_2(NCS)_2)^+ + HC \longrightarrow \text{dye}\ (RuL_2(NCS)_2) + HC^+$$

The symbols in the above equations are as follows:

- Dye $(RuL_2\ (NCS)_2)^*$: Presence of exciton in the dye layer state.

- Dye (RuL_2 $(NCS)_2)^+$: Formation of holes in the HOMO of the after electron transfer to conduction band of nc-TiO_2
- [[nc-TiO_2] $^-$: Electron in the conduction band of nc-TiO_2.
- HC $^+$: Hole in the HOMO of hole conductor after it transferred from the HOMO of dye

3.4 References

1. Wang, K. Yang, X. Wang, R. Nagarajan, L. A. Samuelson, and J. Kumar, *Organic Electronics*, **7**, 456, (2006).
2. A. J. Breeze, Z. Schelsinger, S. A. Carter, and P. J. Brock, *Physical Reviews B*, **64**, 125205, (2001).
3. A. J. Mozer, Y.Wada, K. J. Jiang, N. Masaki, and S.Yangida, *Applied Physics Letters,* **89**, 043509, (2006).
4. C.Lungenschmied, G. Dennler, H, Neugebauer, S. N, Sariciftic, M. Glatthaar, T. Meyer, and A. Meryer. *Solar Energy Materials and Solar Cells,* **91**, 379, (2007).
5. D. Gebeyehu, C. J. Brabec, F. Padinger, T. Fromherz, *Synthetic Metals*, **121**, 1549, (2001).
6. K. M. Coakely, and M. D, McGhee, *Applied Physics Letters*, **83**, 3380, (2003).
7. A. Andersson, N. Johansson, P. Bröms, N. Yu, D. Lupo and W.R. Salaneck, *Advance Materials.* **10,** 859**,** (1998).
8. Q. Qiao, J, Beck, R. Lumpkin, J. Pretko, and J. T. Mcleskey, *Solar Energy Materials and Solar Cells*, **90**, 1034, (2006).
9. M. L. Cantu, F. C. Krebs, *Solar Energy Materials and Solar Cells,* **90**, 2076 (2006).
10. W. J. Beek, M. Martijn, and R. A. Janssen, *Advance Materials.* **16**, 1009, (2004).
11. N. Kudo, Y. Shimazki, H, Ohkita, M. Ohoka, and S. Ito, *Solar Energy Materials and Solar Cells*, **91,** 1243, (2007).
12. G. E. Tulloch, *Journal of Photochemistry and Photobiology A: Chemistry,* **164**, 209, (2004).
13. C. Leyens, M. Peters, *Titanium and Titanium Alloys; Fundamental and Application*, Wiley.VCH. (2003).
14. A. Fujishima, and K. Honda. *Nature,* **37,** 238, (1972).
15. M. Bekbolet, M. Lindner, D. Weichgrebe, and D. W. Bahnemann, *Solar Energy*, **77**, 455, (2004).
16. B. O'Regan, M. Grätzel, *Nature*, **353**, 373, (1991).
17. U. Diebold, *Surface Science Reports*, **48**, 53, (2003).

18. Mindat.org, *the mineral and locality database,* http://www.mindat.org/index.php.
19. K. Pomoni, A. Vomas, and C. Trapalis, *Thin Solid Film*, 479, **160**, (2005).
20. A. Rothschild, F. Edelman, Y. Komem, F. Cosandey, *Sensor and Actuators*, **67**, 282, (2002).
21. M. R. Hoffmann, S. T, Martin, W. Choi, and D. W. Bahnemann, *Chemical Reviews.* **95**, 69, (1995).
22. R. Konenkamp, I. Rieck, *Material Science and Engineering* , **519**, 69, (2000).
23. A. M. Eppler, I. M. Ballard, J. Nelson, *Physica E.* **14**, 197, (2002).
24. M. Anope, K.Chiba, M. Tomonar, S, Coluccia, *Bulletin of the Chemical Society of Japan,* **64**, 543, (1991).
25. Q. Fan, B. McQuillin, D. D. C. Bradley, S. Whitelegg and A. B. Seddon, *Chemical Physics Letters* **, 347**, 325, (2001).
26. A, K, Mallick, PhD Thesis, University of Manchester, 2006.
27. C. Y. Kwong, A. B. Djurisic, P. C. Chui, K. W. Chenf, W. K. Chan, *Chemical Physics Letters.* **384**, 372, (2004).
28. Y. Saito, S. Kambe, T. Kitmura, Y. Wada, S. Yanagida, *Solar Energy Materials and Solar Cells*, **83**, 1, (2004).
29. K. Westermark, *Dye/Semiconductor Interface*, UPPSALA, 2001.
30. J. KRruger PhD thesis, University of Heidelberg.
31. H. J. Snaith, L. S. Mende, and M. Grätzel, *Physical Reviews.***74**, 045306, (2006).
32. U. Bach, Y. Tachibana, J.E. Moser, S. A. Haque, J. R. Durrant, M. Grätzel, and D. R. Klug, *Journal of the American Chemical Society Home.* **121,** 7445, (1999).

Chapter 4

Materials and Methodology

4.1 Introduction

This chapter describes the various experimental methods and techniques used during this work. It is divided into two parts. The first part describes the materials and techniques used to fabricate solar cells, all the steps of which were conducted in a class 1000 clean room to minimize atmospheric contamination. The second part outlines the equipment used for studying the electrical properties of the solar cells and the physical properties and morphology of the nc-TiO_2 films.

4.2 Materials

Solar cells were fabricated using nano-crystalline titanium dioxide (nc-TiO_2) as the n-type semiconductor and regio-regular poly (3-hexylthiophene) (P3HT) as the electron donor/hole transporter and light absorber. In a comparative study, one set of

cells also included a layer of the dye ruthenium 535-bisTBA inserted at the interface between P3HT and nc-TiO_2 to produce a polymer/dye/ nc-TiO_2 solar cell.

Substrates were purchased from Solaronix SA and comprised of glass slides coated in a transparent conducting layer of fluorine-doped tin dioxide (SnO_2:F) covered with a layer of compact TiO_2 ~ 500 nm thick prepared by spray pyrolysis [1]. This compact layer of nc-TiO_2 prevented the P3HT from connecting directly to the bottom electrode and short circuiting the device. The SnO_2:F electrode is preferred over indium tin oxide (ITO) because out-diffusion of indium occurs from the ITO. P3HT was purchased from Sigma-Aldrich in the form of a solid (Figure 4.1). These materials were stored in the clean room at room temperature and kept away from light.

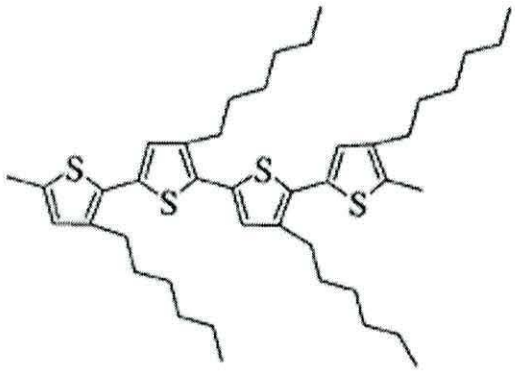

Figure **4.1** *Molecular structure of P3HT.*

4.2.1 Substrate Preparation

The dimensions of the glass substrates were 5cm x 5cm with a thickness of ~1mm. The resistance of the SnO_2:F film was around 10 Ω/sq according to the supplier. Before proceeding with fabricating the solar cells, the substrate was cut into small pieces with dimensions of 2.5cm x 2cm and rinsed in ultrapure and hot water. Cotton wool wetted with Decon 90® (Scientific Service Ltd. UK) was used to rub the surface of the compact TiO_2 layer to remove any trace of organic materials on its surface. After this moment, the substrates were handled using tweezers to keep the

surface clean. Then, they were held under the ultrapure water for about two minutes followed by hot water for two minutes. The slides were held under a stream of warmed air for three minutes followed by a further three minutes under ethanol. Then, they were dried for five minutes using a stream of warm air to make sure that there was no water or ethanol left on the surface.

4.2.2 Nano-crystalline Titanium Dioxide (nc-TiO_2) Films

Chapter 3 presented the structure, preparation, and commercial applications of nano-crystalline titanium oxide (nc-TiO_2) films. We showed that there are three different types of nc-TiO_2 based on its crystalline structure: 1) rutile, 2) anatase, and 3) brookite. However, the anatase structure of nc-TiO_2 is considered to be the best crystalline structure for producing dye sensitized solar cells with good efficiency [2]. In previous work, nc-TiO_2 films were prepared using: 1) a doctor blade technique [3], 2) spray pyrolysis [4] 3) chemical vapor deposition [5], and 4) dip and spin coating technique [6,7]. The work presented in this thesis employed the doctor blade technique.

Porous nc-TiO_2 films were readily prepared by spreading a TiO_2 sol-gel over the substrate surface and sintering at high temperature. Two batches of TiO_2 sol-gel (Ti-Nanoxide T) were purchased from Solaronix SA. According to the supplier, these batches differed from each other only in terms of age. The two batches were labeled batch A and batch B in order to distinguish the films. Prior to use, the TiO_2 sol-gel was stirred using a clean glass rod for 1 minute. To define the area of substrate to be coated with TiO_2 sol-gel, we used 3M Scotch Magic tape. It had a thickness of 50μm and is easily removed from the substrate without leaving traces of adhesive material. The amount of TiO_2 sol-gel initially used depends on the substrate area to be coated. Following the procedures in the literature [8], we used around 50μL of TiO_2 sol gel to coat 5 cm^2 area of substrate surface. The 50 μL of TiO_2 sol gel was deposited on the edge of the substrate using a micropipette. A cleaned glass rod was used to spread the sol gel over the substrate area defined by the tape (Figure 4.2). Then, the film was left in air for 10 minutes to dry until its milky colour disappeared.

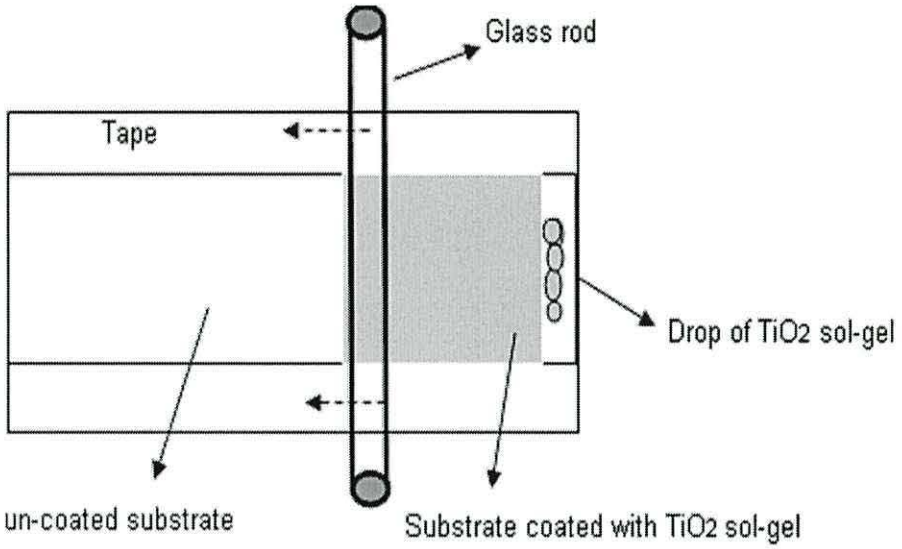

Figure 4.2 *Scheme of doctor blade technique applied to coat TiO_2sol-gel on substrate.*

The tape was then removed and the substrate placed on a hot plate preheated between 75 to 100 °C limited by the accuracy of the dial setting for 30 minutes. The substrate was left on the hot plate for 110 minutes during which time the temperature was increased from ~ 75 °C to 450 °C in 4 steps. Initially the substrate was heated for 15 minutes at 100 °C. Then, the temperature was increased from 100 to 150 °C for a further 15 minutes. Then, the temperature increased to 250 °C and again held for 15 minutes. This is followed by a further increase to 350 °C but this time for 30 minutes. Subsequently, the temperature was increased to 450 °C for 30 minutes to complete the process. Finally, the hot plate was turned off and the temperature allowed to fall naturally to ~70 °C at which point the substrate was recovered. Figure 4.3 [9] illustrates the temperature profile used in this sintering process. Afterwards, the sintered nc-TiO_2 film was rinsed for two minutes under ethanol to remove water so as to improve contact with the hole conductor or dye on the surface. Then, the film was dried using a stream of warmed air for 3 minutes.

.

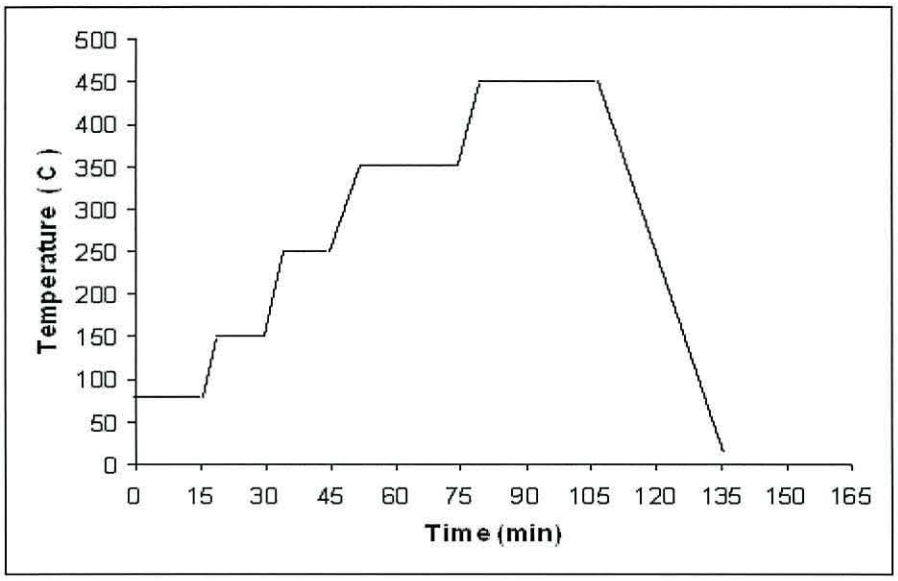

Figure 4.3 A *typical temperature profile of the hot plate during the sintering of the nc – TiO_2 film.*

4.2.3 Ruthenium Dye-Solution

Prior to preparing the dye solution, a vial was cleaned with Decon 90® and rinsed in hot water and the ultrapure water, and dried under a stream of warm air for five minutes. 10 mg of Ru dye was placed inside the vial and dissolved in 50ml of ethanol. The nc-TiO_2 films were placed inside a second vial and the dye–ethanol solution poured over it. The nc-TiO_2 substrate was left for two days to absorb the dye. During this time the container was covered with aluminum foil to prevent light from bleaching the dye. The substrate was removed from the solution using tweezers and rinsed in ethanol immediately. Finally, the dye/nc-TiO_2 film was dried under a nitrogen flow for three minutes.

4.2.4 Poly (3-hexylthiophene)

A solution of the Poly (3-hexylthiophene) (P3HT) was prepared by dissolving 0.03g of P3HT in 2 ml of chloroform (Sigma Aldrich) in a 20ml glass vial yielding a concentration of 1% w/w. The vial was placed inside an ultrasonic bath at a temperature of 50°C for 30 minutes to increase the solubility of P3HT in the chloroform. Finally, the solution was syringed through a 0.2μm PTFE filter into a

second clean vial to remove any un-dissolved particles. To apply P3HT solution, the substrate was placed on the vacuum chuck of an Electronic Micro Systems Ltd. Model 4000 Photoresist Spinner. A pre-cleaned glass pipette was used to place 5 ml of the P3HT solution onto the nc-TiO_2 substrate. Within a few seconds, the spinner was switched on at a spin speed of 1000 rpm for 60 seconds. The substrate was removed and kept in the dark until a gold electrode was deposited onto the P3HT layer. The gold source was a 10 cm length of wire cleaned by rubbing with Decon 90 and rinsed in hot water and then in ultrapure water. After drying in a stream of warm air, it was placed inside a tungsten boat in an Edwards AUTO 306 Turbo Evaporation System. A shadow mask was placed on the substrate which was then put in the Edwards system above the tungsten boat. After pumping to ~10^{-6} torr, a gold film, 50 nm thick, was deposited through the shadow mask to form circular electrodes of ~ 3 mm^2 in area. The double layer cells were constructed by following the same procedures except for the omission of the dye layer. The final device structure is shown in figure 4.4.

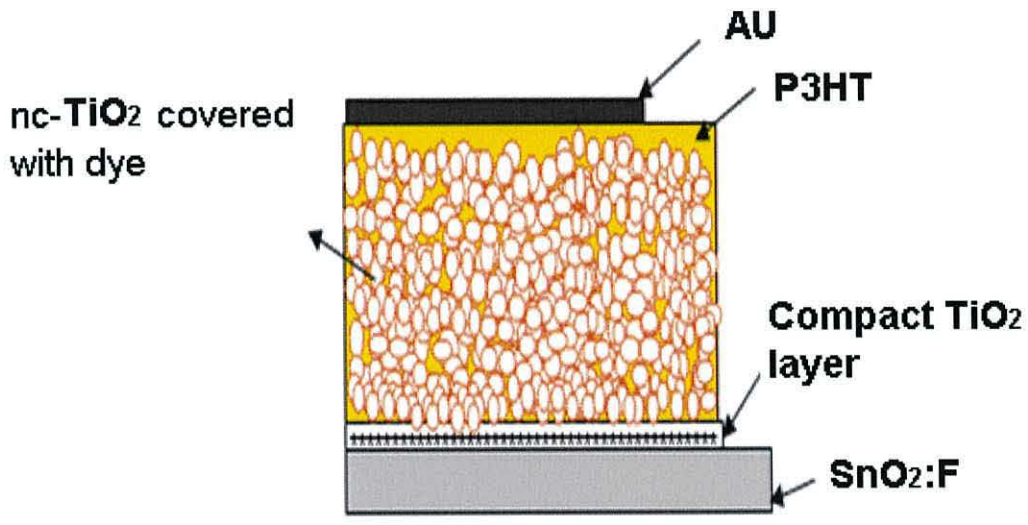

Figure 4.4 *Schematic diagrams of AU/P3HT/dye/nc-TiO_2/compact TiO_2 /SnO_2:F solar cells. Ideally, the P3HT penetrates the whole of nc-TiO_2*

4.3 Electrical Characterization

In this thesis, we have undertaken AC and DC electrical measurements on the solar cells both in the dark and under illumination. Measurements were conducted in air and under vacuum over a range of temperature and light intensity. Current-voltage (I-V) characteristics were measured using a Keithley model 4200 source-measure unit. The optical response of the solar cells was obtained using a tungsten halogen lamp (50W). This light was focused through a window onto the transparent SnO_2:F electrode. Although a slight difference in the spectrum exists between the tungsten lamp and the AM 1.5 solar simulator, a tungsten lamp has been used by many researchers in the solar cell field and provides a reasonable light for comparison [11,12]

To limit the light to the region defined by the gold top electrode, a mask with identical holes (size and distribution of holes are fixed) was placed against the glass substrate. This was done to prevent the generation of photo-charges outside the designated area (Figure 4.5).

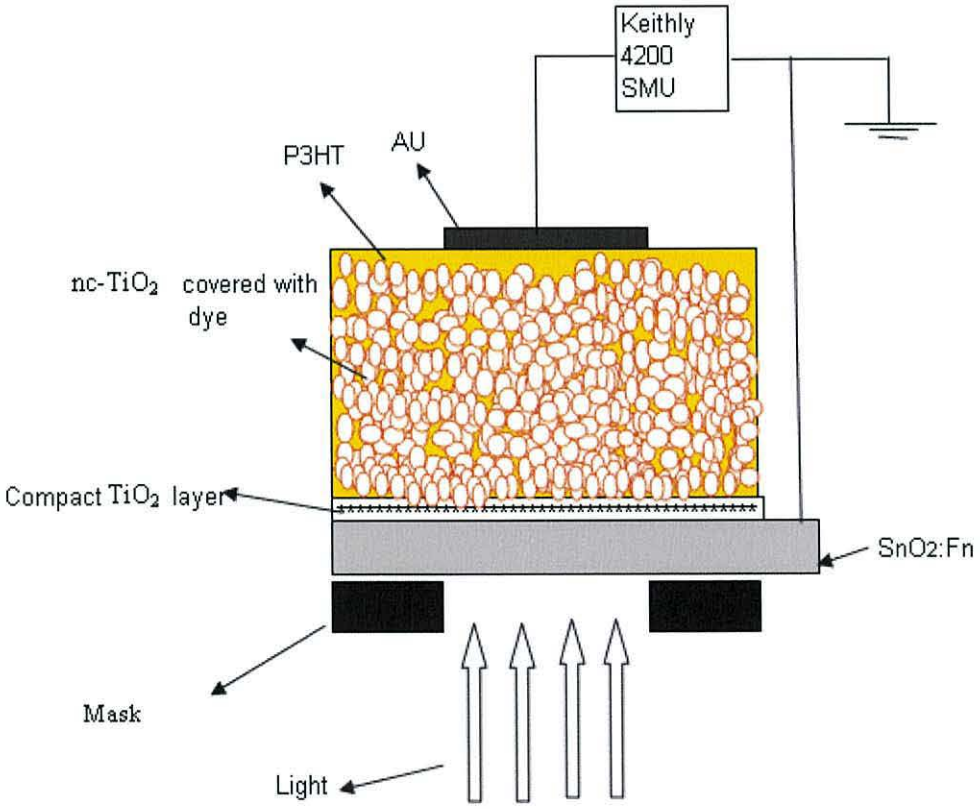

Figure 4.5 *Schematic representation of the solar cell structure tested under illumination.*

The intensity of the light falling on the device could be varied from ~1 to 230 mW/cm^2 by moving the light source toward or away from the test sample. The light intensity was measured using a light intensity meter. A light intensity equivalent to AM1.5 radiation from the halogen lamp was set using an AM1.5 calibrated Si solar cells supplied from Solaronix SA. The external quantum efficiency (EQE) was measured using a system in Cambridge University. The system consisted of a Bentham IL1 illuminator with a halogen lamp, beam-splitter, Keithley 237 Source Measure Unit, and a Thorlabs silicon photodiode as a reference.

The AC measurements were carried out using a Solartron 1260 Frequency Response Analyzer. The capacitance/conductance versus voltage (C/G-V) characteristics of the solar cells was measured as function of frequency (10 KHz and 1 Hz) using a test signal of 100mV. Additionally, capacitance/conductance versus frequency (C/G-F) was measured at a fixed voltage over the frequency range from 1Hz to 0.1 MHz. Table 4.1 provides information on the measurements settings for the DC and AC analysis of the solar cells. For DC measurements, the voltage was applied to the Au electrode. For AC measurements, the voltage was applied to the SnO_2 : F electrode .

Measurement setting	**For DC measurements**	**For AC measurements**
Start Voltage(V)	+1	+1
Stop voltage (V)	-1	-1
Step voltage (V)	0.025	0.025
Step delay time (s)	1	1

Table 4.1 *Common DC/AC measurements parameter for P3HT/dye/nc – TiO_2 solar cells.*

Figure 4.6 shows the vacuum system in which the solar cells were mounted on a copper stage. Measurements on solar cells were done in air and under a high vacuum of 10^{-5} torr. The vacuum system was composed of a steel chamber connected to a rotary pump and a silicone oil diffusion pump. For electrical measurements, contact was made to the solar cells using fine gold wire and silver paste. The gold wire was connected to sockets in the lid of the chamber. The temperature of the solar cells could be varied from room temperature to 120 °C by means of resistance heater mounted in the back of the copper stage. Temperature control was achieved using a Eurotherm 91e Temperature Controller connected to a power supply.

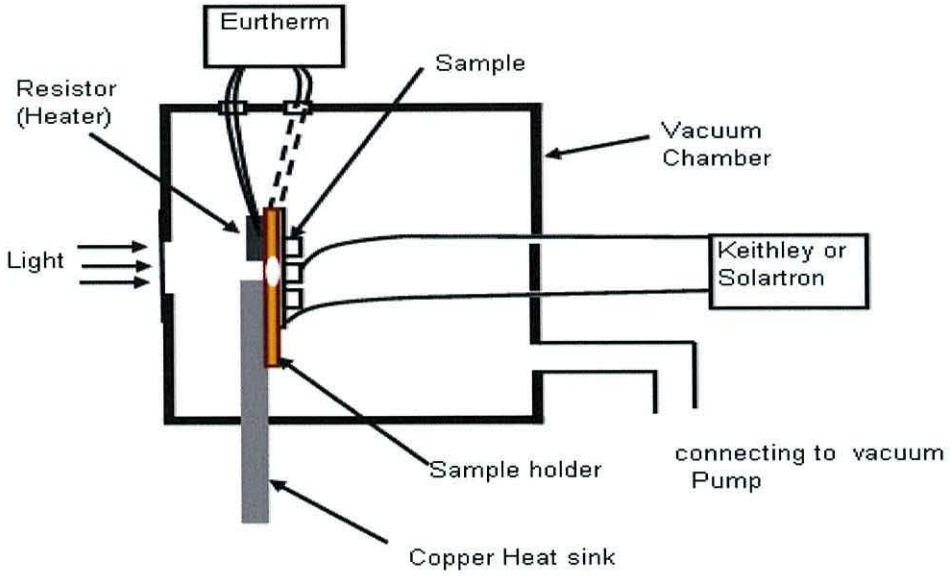

Figure 4.6 *Schematic representation of the vacuum system and sample holder used in this work.*

4.4 Thermo Gravimetric Analysis

Thermo Gravimetric Analysis (TGA) was undertaken using a Pyris 1 Thermo Gravimetric Analyzer at OpTIC Technium St. Asaph. The sol-gel sample was put inside the container and held for 2 minutes at a temperature of 20 °C. Then, the temperature was increased from 20 °C to 600 °C at a rate of 5 °C /min.

4.5 Atomic Force Microscopy

Atomic Force Microscopy (AFM) is a powerful tool for investigating the topography of $nc-TiO_2$ and semiconductor polymer films. In this study, we used a Digital Instruments Nanoscope 3A multimode instrument which also allowed operation as a Scanning Tunnelling Microscope (STM) for Scanning Tunnelling Spectroscopy (STS) measurements. For topographical investigation, the AFM tapping mode was used (Figure 4.7). This is a non–contacting mode where the cantilever probe is driven into resonance (~ 200KHz) with the tip positioned above the surface of the sample. When the sample was raised, Van der Waals forces interact with the tip reducing the amplitude of oscillation. This is detected using a solid state laser reflecting off the back of the cantilever into a quadrant photo-detector. Images are readily obtained using a feed back loop to maintain a constant tip–surface distance (constant amplitude) while scanning over the sample surface. The raw images were enhanced and analyzed using off-line software (Nanoscope version 4.1 sofware). The maximum resolution of the AFM is a few nanometers.

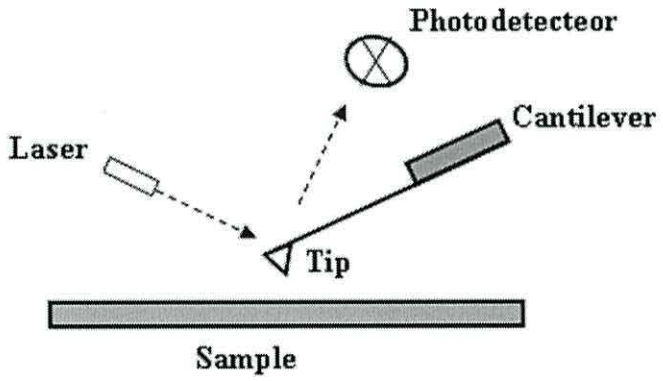

Figure 4.7 *Schematic representation of an AFM showing the key components*

4.6 Scanning Tunneling Spectroscopy

Scanning Tunneling Spectroscopy (STS) was undertaken to determine the electronic properties of the nc-TiO_2 surface. It is conducted by applying a voltage between the tip and the surface of the sample allowing electrons to tunnel from the tip to the surface of the semiconductor (metal) and vice versa. This generates a small current

across the gap which depends on the height between the tip and sample surface, bias voltage and the properties of sample surface (Fgure 4.8). In STS, we are concerned with measuring the onset of electron emission from the tip into the semiconductor LUMO level in negative bias and from the semiconductor HOMO level to the tip in positive bias.

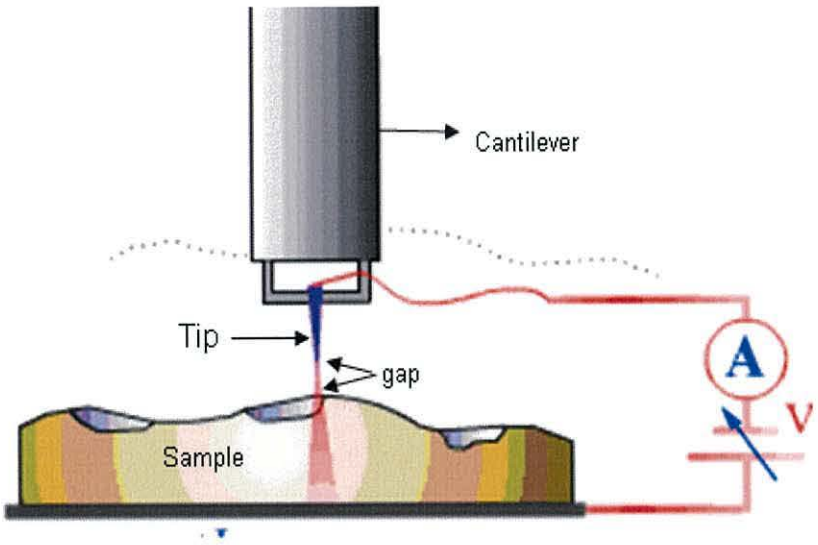

Figure 4.8 *Schematic illustration of the scanning tunnelling spectroscopy (Image adopted from reference (13)).*

4.7 Scanning Electron Microscopy

Sample topography, morphology, and composition were also studied by Scanning Electron Microscopy (SEM). Samples were mounted on metal stubs and coated with a thin layer of gold in a vacuum evaporator. Micrographs of the sample were obtained using an International Scientifics Instrument (ISI-40) scanning electronic microscope with digital image capture. A block diagram of the instrument is shown in figure 4.9(a). An electron beam is generated using an electron gun under vacuum. Accelerating voltages up to 20keV allow the beam to be focused to a diameter of ~10nm using condenser lenses and an objective lens. Electromagnetic deflection coils move the electron beam in raster fashion over the sample's surface to extract an image of whole sample. The primary electrons interact with atoms of the sample's surface and undergo both elastic and inelastic scattering producing secondary electrons and X-rays from the sampled surface (Figure 4.9 (b)). The Secondary electrons are collected by a scintillation detector which converts the incident

electrons into a flash of light. The light is collected by a photomultiplier tube and amplified. The resulting output current is fed via the video amplifier to the grid of a cathode ray tube scanning synchronously with the beam so as to generate an optical image of the surface .

Elemental analysis of the devices using energy dispersive X- ray analysis (EDAX) was undertaken by interfacing a Link System 860 series 2, X-Ray analyser with the SEM. This works by collecting the X-rays emitted from the irradiated sample's surface. The energy of the X-rays emitted depends on the atoms available in the sample. A beryllium window covered a lithium-doped silicon semiconductor detector that absorbs the X-rays emitted from the sample, exciting K-shell electrons in the silicon. This provides a histogram of X-ray counts (concentration of the element in the sample) as a function of x-ray energy (atomic weight of the element).

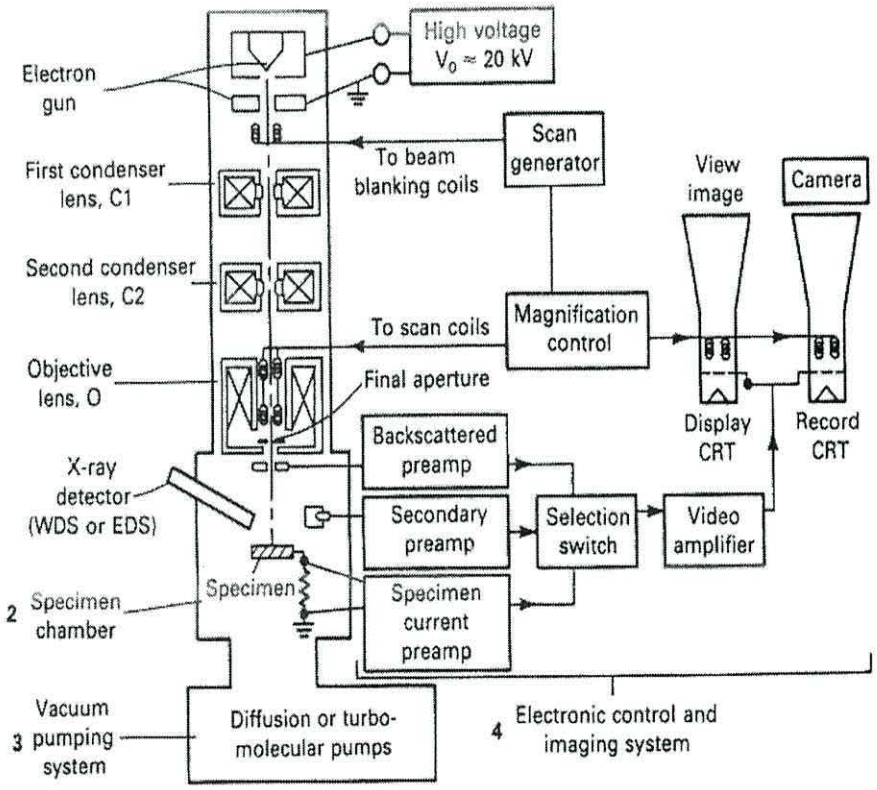

Figure 4.9(a) *the basic components of the scanning electron microscopy Image adopted from reference (14)*

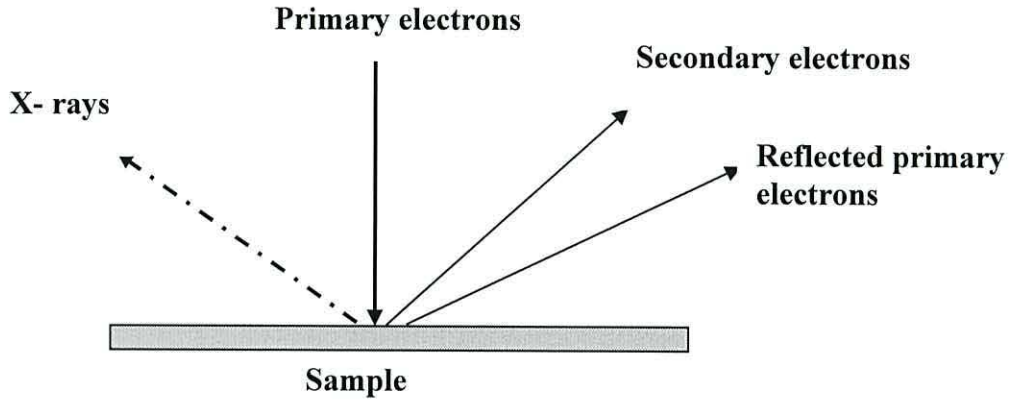

Figure 4.9(b) *The interaction of primary electron with atoms of the sample's surface*

4.8 Ultra-violet/visible Spectroscopy

The UV-visible absorption spectra of the various materials used in the construction of the solar cells were obtained using a Hitachi Model U-2000 Double Beam Ultra-Violet/Visible (UV/VIS) spectrophotometer. The primary light beam was emitted from a deuterium discharge lamp. This beam passed through a half-silvered mirror beam splitter with one beam passing through the sample while the other acted as a reference. The wavelength range was ~190 nm to 1100 nm with a wavelength resolution of 1nm (Figure 4.10)

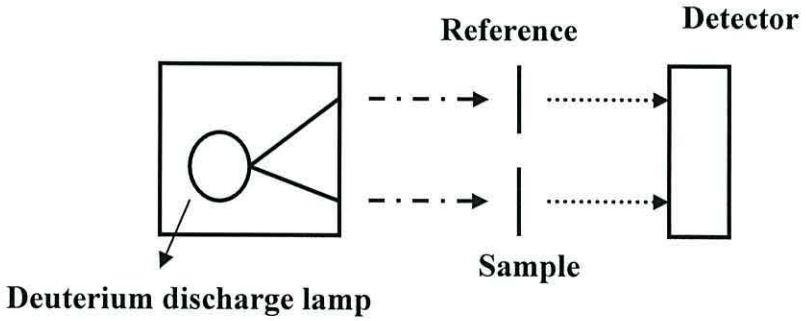

Figure 4.10 *The basic components of the ultra Violet/Visible (UV/VIS) spectrophotometer.*

4.9 X-Ray Diffraction Experiments

The crystal structure of nc-TiO_2 film was investigated using a Philips W3830 X-Ray Meter located in the Chemistry Department, Bangor University. The copper target in this instrument emits X–rays of wavelength ~15.4 nm after filtering using a nicked sheet. Diffraction from lattice planes leads to peaks of reflected intensity which satisfy Bragg's law (equation 4.1)

$$2d_{hki}\text{Sin }\theta = n\lambda \qquad (4.1)$$

where λ is the X-Ray wavelength, d_{hkl} is the spacing of the corresponding (hkl) lattice planes, and is the Bragg angle (the angle between the lattice plane and the surface. Crystalline materials are usually composed of microscopic crystalline (grains) separated from each other by grain boundaries. The grain size is calculated from the Scherrer equation [15]:

$$GS = \frac{k\lambda}{\beta\cos\theta} \qquad (4.2)$$

where GS is the grain size and β is the full width at half maximum of the diffraction peak. Therefore, it becomes possible to investigate the effect of sintering on the nanostructure of the nc-TiO_2 layer.

4.10 References

1. The Spray pyrolysis was done in Solarnix *SA Company* http://www.solaronix.ch/.
2. N. G. Park. J. V. D. Lagemaat, and A. J. Frank, *Journal of Physical Chemistry B,* **104** , 8989 , (2000).
3. N. Fukuri, N. Masaki, T. Kitmaura, Y. Wada, and S. Yangagida, *Journal of Physical Chemistry B.* **110,** 25251, (2006).
4. M. Okuya, K. Nalada, D. Osa, T. Nakano, G. R. A. Kumara, and S. Kaneko, *Journal of Photochemistry and Photobiology A: Chemistry*, **164**, 167, (2004).
5. T. J. Savenuje, J. M Warmerm and A, Goossens, *Chemical Physical Letters,* **287**, 148, (1998).
6. Q. Fan, B. McQuillin, D. D. C. Bradley, S. Whitelegg and A. B. Seddon, *Chemical Physical Letters* **, 347**, 325, (2001)**.**
7. Y. J. lin, L. Wang, W.Y. Chiu, *Thin Solid Films*, **511**, 199, (2006).
8. D. Gebeyehu, C. J. Brabec, F. Padinger, T. Fromherz, *Synthetic Metals*, **121**, 1549, (2001).
9. The sintering process of nc-TiO_2 film is provided from Solaronix. Co.
10. H. P. Deshmukh, P.S. Shinde, and P.S. Patil, *Material Science and Enginerring* . B. **130**, 220, (2006).
11. E. L. Willams, and G. E. Jabbour, *Applied Physics Letters*, **87**, 223504, (2005).
12. W. J. E. Beek, M. M. Wienk and R. A. J. Janssen, *Advanced Materials*, **16**, 1009, (2004).
13. http://www.ntmdt.com
14. 14.http://nhml.com
15. B. D. Cullity, *Eelments of X-Ray diffraction*, Wesley Educational Publishers. US, (1956).

Chapter 5

Characteristics of nc-TiO_2 Films

5.1 Introduction

This chapter presents the characteristics of the nc-TiO_2 films derived from the two different batches of sol gel obtained from Solaronix. The characteristics were studied using various techniques. Morphology and roughness of the nc-TiO_2 films were observed using Atomic Force Microscopy (AFM). Additionally, cross sections of solar cells were obtained using Scanning Electron Microscopy (SEM).

Spectroscopic analysis of the nc-TiO_2 film was conducted to study the elemental composition, optical properties, and the crystallographic nature of the nc-TiO_2 films. Additionally, we determine the surface electronic properties of nc-TiO_2 film using Scanning Tunneling Microscopy (STM). Finally, Thermo Gravimetric Analysis (TGA) was used to study the weight loss of TiO_2 sol-gel as a function of temperature

5.2 Microscopic Analysis

5.2.1 Atomic Force Microscopy

Figures 5.1 and 5.2 show the AFM images of nc-TiO_2 films produced from batch A and batch B sol gel using the procedures described in section 4.2.2. The scan area in both cases is $25\,\mu m^2$. The two films consist of nano-particles partially interconnected with each other. However, there are differences between them in terms of the Root Mean Square (RMS) roughness, average diameter, and shape of $nc-TiO_2$ particles.

For batch A nc-TiO_2 films:

1. The roughness of the film surface was estimated to be around 20.5 nm and its sample surface area was 28.9 μm^2 (c.f. image area = 25 μm^2).
2. The small particles have aggregated together to form larger particles ranging from ~120 nm to 150 nm in size and distributed randomly over the surface of the nc-TiO_2 film.

For batch B nc-TiO_2 films:

1. The roughness of film surface was estimated to be around 12 nm and its sample surface area was 25.6 μm^2 (c.f. image area = 25 μm^2).
2. The small particles have also formed larger particles but with their size ranging from 200 nm to 225 nm. Unlike the film produced from batch A, the particles are distributed uniformly over the sample area.

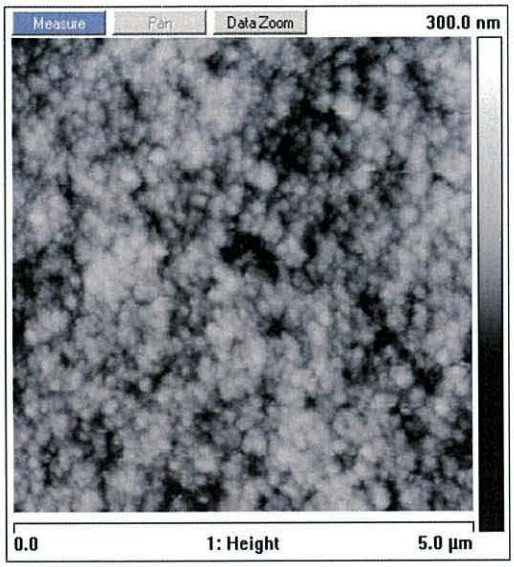

Figure 5.1 *AFM topography of nc-TiO_2 film produced from Batch A.*

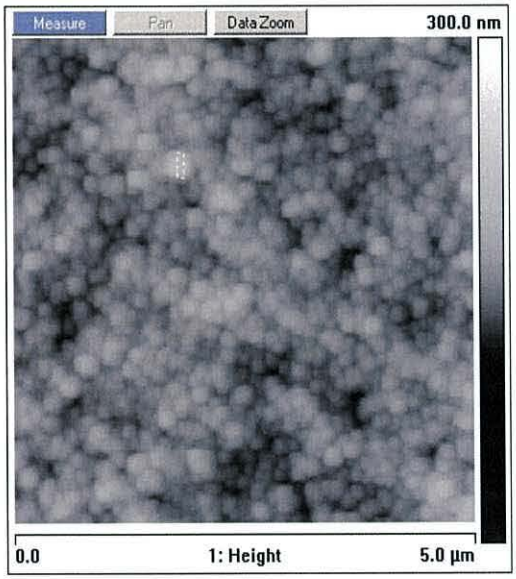

Figure 5.2 *AFM topography of nc-TiO_2 film produced from Batch B.*

The batch A nc-TiO_2 films appear to have a large number of pin-holes in the surface compared with batch B TiO_2 films. This difference may be illustrated by extracting a profile of the particles across the film. Figure 5.3 shows a profile for particles and pin-holes in the batch A nc-TiO_2 film. The figure reveals several gaps between the nano-particles with the depth of the gap ranging from 80nm to100nm.

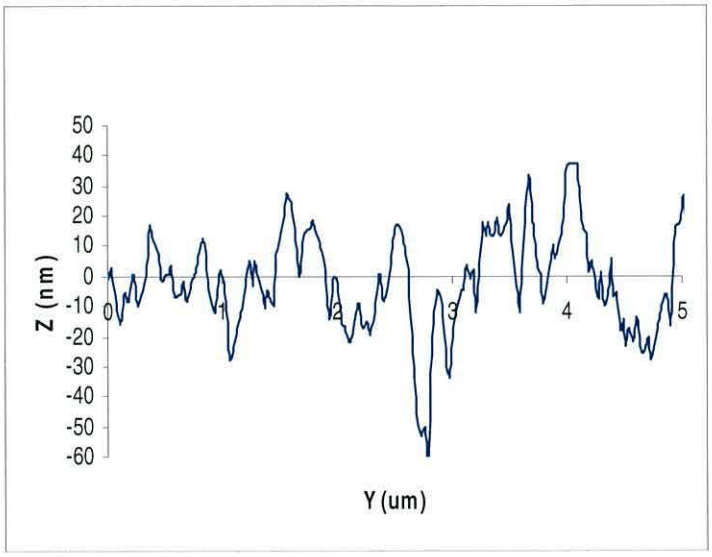

Figure 5.3 *A profile of particles and pin-holes on surface of nc-TiO_2 film produced from batch A.*

Figure 5.4 shows a different profile for the batch B nc-TiO_2 film. The number of pin-holes was less than in batch A nc-TiO_2 films produced from. The figure shows the existence of gaps between nano particles which range in depth from 10 nm to 30 nm and so much smaller than in the batch A nc-TiO_2 film.

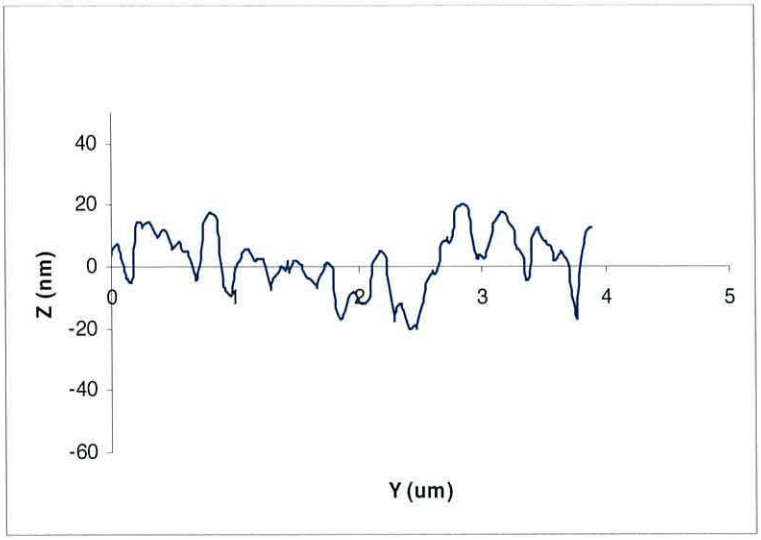

Figure 5.4 A *profile of particles and pin-holes on surface nc-TiO_2 film produced from batch B.*

This difference in surface roughness is clearly seen in the 3D images in figures 5.5 and 5.6. The particles of nc-TiO_2 film produced from batch A (Figure 5.5) have sharply pointed features while those from batch B are smoother (Figure5.6). It is this difference in particle shape that leads to the larger sample area in batch A compared to batch B (28.9 μm^2 compared with 25.6 μm^2).

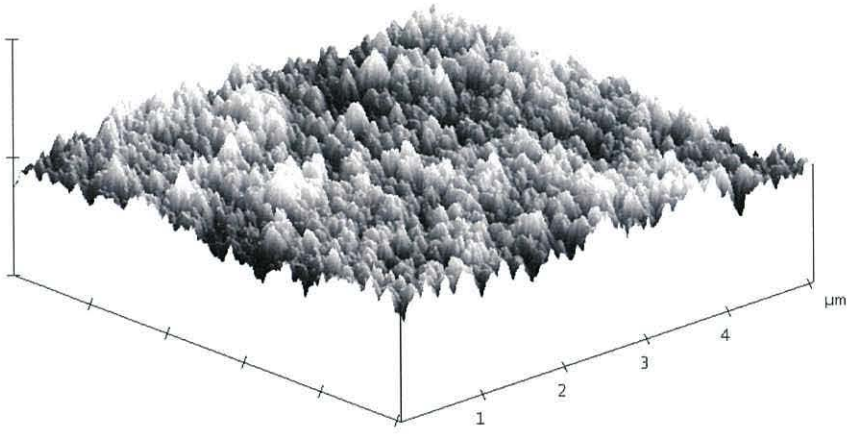

Figure 5.5 *AFM image of nc-TiO_2 produced from batch A.*

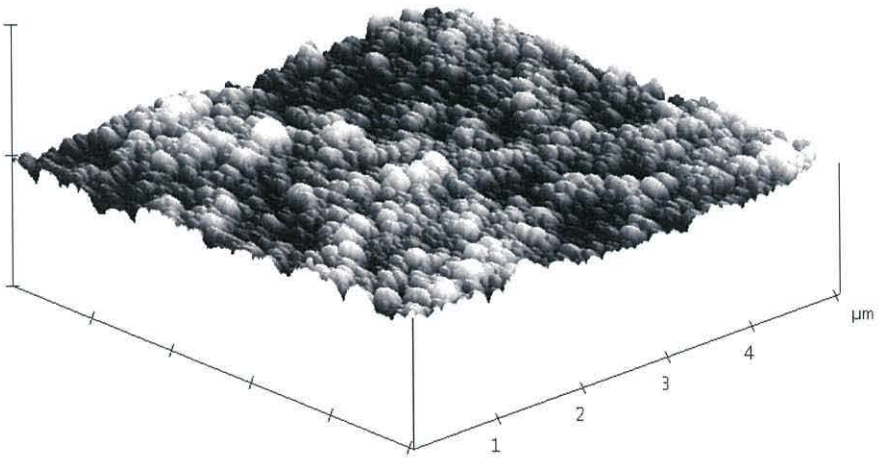

Figure 5.6 *AFM image of nc-TiO_2 produced from batch B.*

Following Arabatzis et al. [1], these differences can also be demonstrated using the particle height analysis capability of the AFM. Figure 5.7 shows a histogram of particle heights over the batch A nc-TiO_2 surface for an area of 5 μm^2, The mean height of particles ranges from 90 to 100 nm. Figure 5.8 shows the corresponding histogram of particle height for batch B nc-TiO_2 surface. Here, the mean height ranges from 50 to 60 nm and so much lower than for batch A.

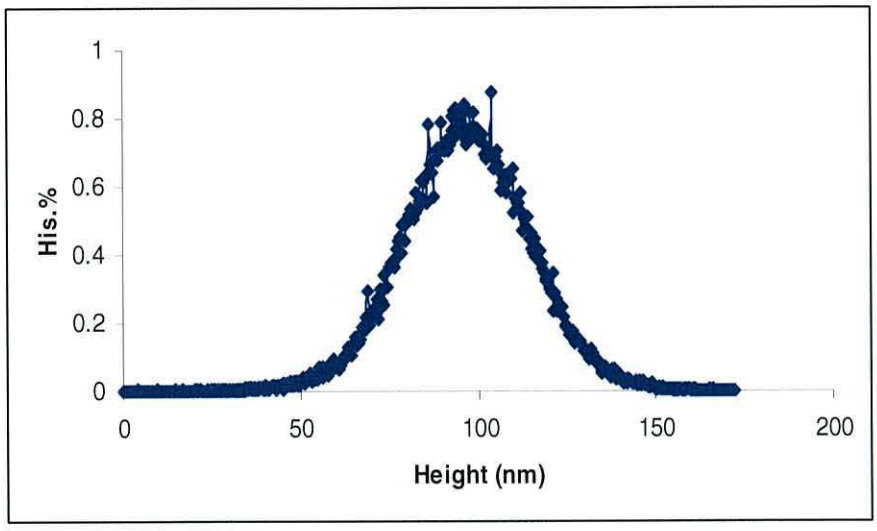

Figure 5.7 *Distribution of particle height of nc-TiO_2 film produced from batch A.*

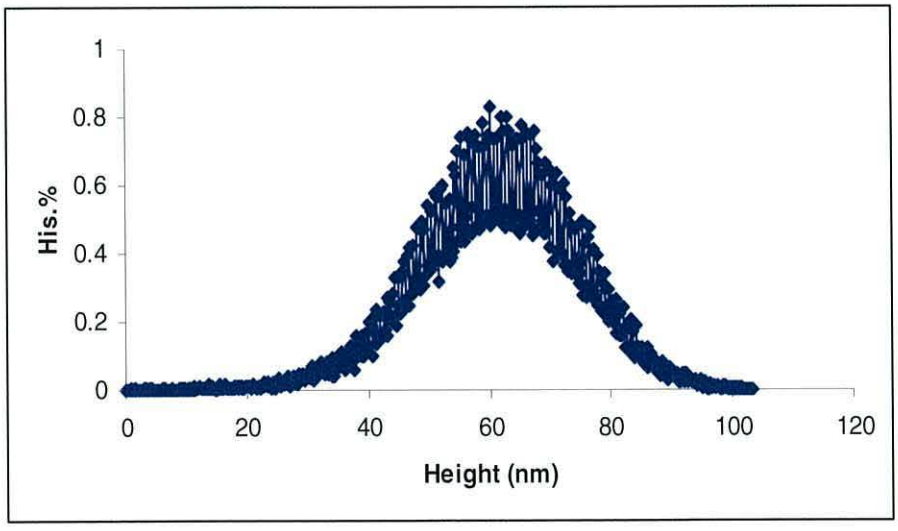

Figure 5.8 *Distribution of particle height for nc-TiO_2 film produced from batch B.*

In comparison to the rough surface of nc-TiO_2 layers, the compact TiO_2 layer deposited by spray pyrolysis on the SnO_2:F substrate is very smooth. Figure 5.9 is the topography a 5 μm×5μm area of the compact layer where there is no evidence for particle formation and the RMS roughness was less than 1 nm.

.

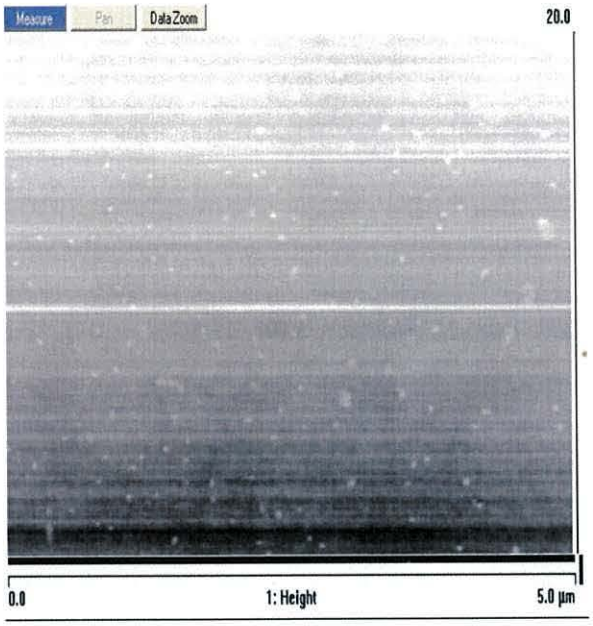

(a)

Figure 5.9 *AFM topography of the compact TiO_2 layer.*

Figures 5.10 and 5.11 show the topography and histogram of particle heights for the batch A nc-TiO_2 coated with P3HT. The RMS roughness was ~18 nm with mean particle height ~103 nm. Figures 5.12 and 5.13 show the topography and histogram of particle heights for batch B nc-TiO_2 film coated with P3HT. Here, the RMS roughness was ~10nm with a mean height of ~ 40nm. These relatively small changes in topography resulting from the additional P3HT layer, suggest that the latter is quite thin.

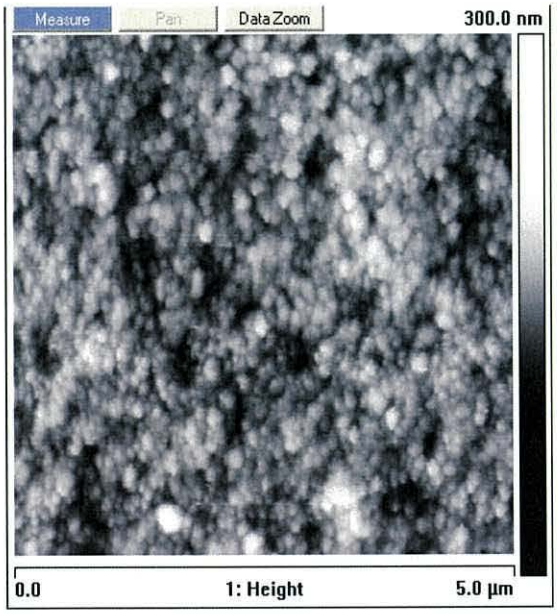

Figure 5.10 *AFM images of nc-TiO_2* produced *from batch A coated with a P3HT layer.*

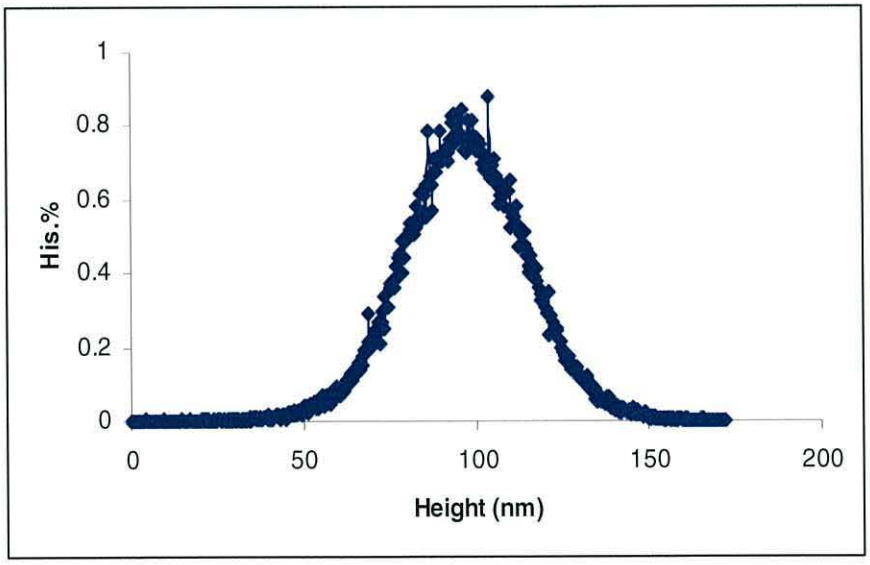

Figure 5.11 *Distribution of particle height for a nc-TiO_2* film *produced from batch A coated with P3HT layer.*

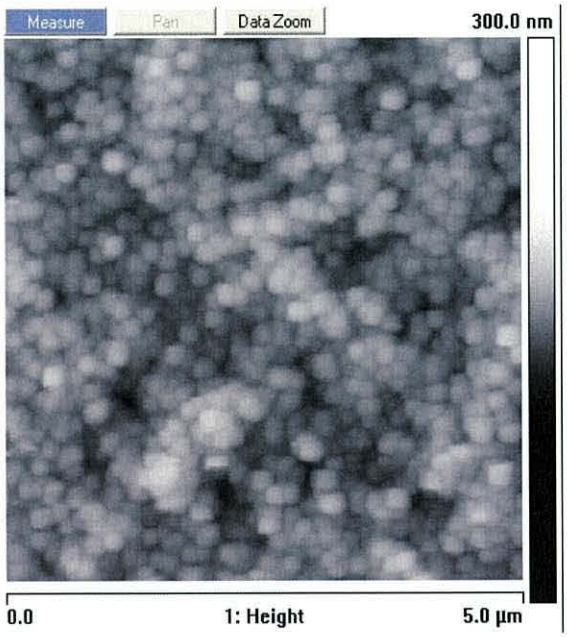

Figure 5.12: *AFM images of nc-TiO_2 produced from batch B coated with P3HT layer.*

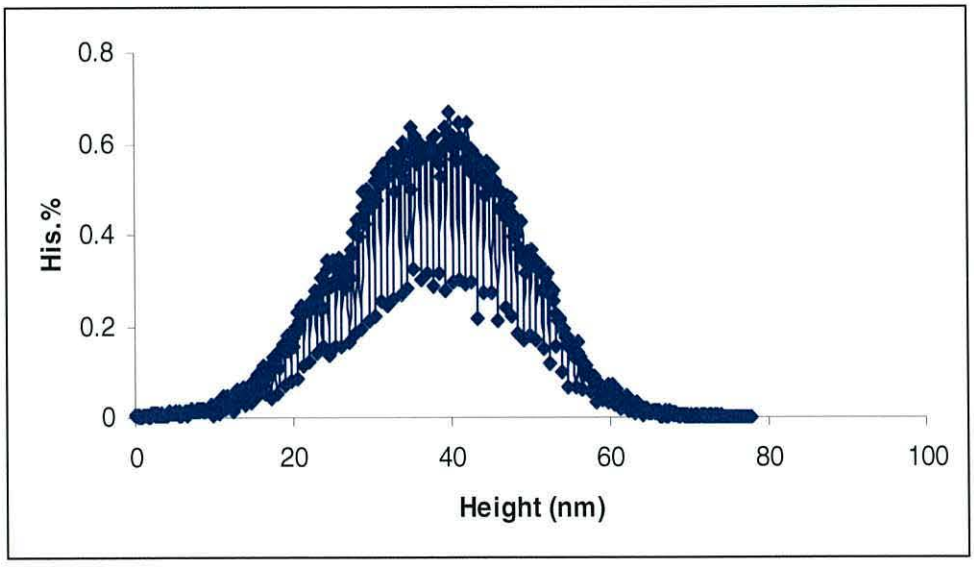

Figure 5.13 *Distribution of particle height for nc-TiO_2 film produced from batch B coated with a P3HT layer.*

Table 5.1 summarizes the important topographical information deduced from the AFM studies of the various layers of the solar cells fabricated in this study. Clearly, there is a major difference between the nc-TiO_2 particles using the two different batches of TiO_2 sol-gel.

Material Surface	**RMS(nm)**	**Maximum height(nm)**	**Particles diameter (nm)**	**Number of pin holes in nc-TiO_2 surface**
nc-TiO_2 film (A)	21	100	150	High
nc-TiO_2 film (B)	12	60	250	Low
P3HT/c-TiO_2 film	18	103	150	High
P3HT/nc nc – TiO_2 film (B)	10	39	200	Low
Compact TiO_2 layer	1.4	-	-	-

Table 5.1 *Roughness, maximum height (nm), particle diameter (nm), and number of pin-holes on surface for coated and uncoated nc-TiO_2 films with P3HT.*

5.2.2 Scanning Electron Microscopy

Scanning Electron Microscopy (SEM) was used to determine whether the difference in the topography of the nc-TiO_2 resulted in differences in morphology throughout the film. To achieve this, a glass-cutter was used to score the underside of the glass substrate which was then snapped to reveal the cross section. The cut piece was mounted on a small stub with the newly exposed surface uppermost and coated with a thin film of gold prior to insertion in the instrument.

Figure 5.14 shows the cross section of the P3HT/nc-TiO_2/compact TiO_2layer /SnO_2:F device where the nc-TiO_2 was produced from batch A. The figure shows that two layers dominate the thickness of the device: the thicker nc-TiO_2 film and the thinner compact TiO_2. From the image, the nc-TiO_2 layer is estimated to be ~1.9 μm

while the SnO_2:F with the compact TiO_2 is ~ 600nm thick. The figure also shows that during the sintering process, the nano-particles were fused together in a manner consistent with the formation of channels from bottom to top during sintering

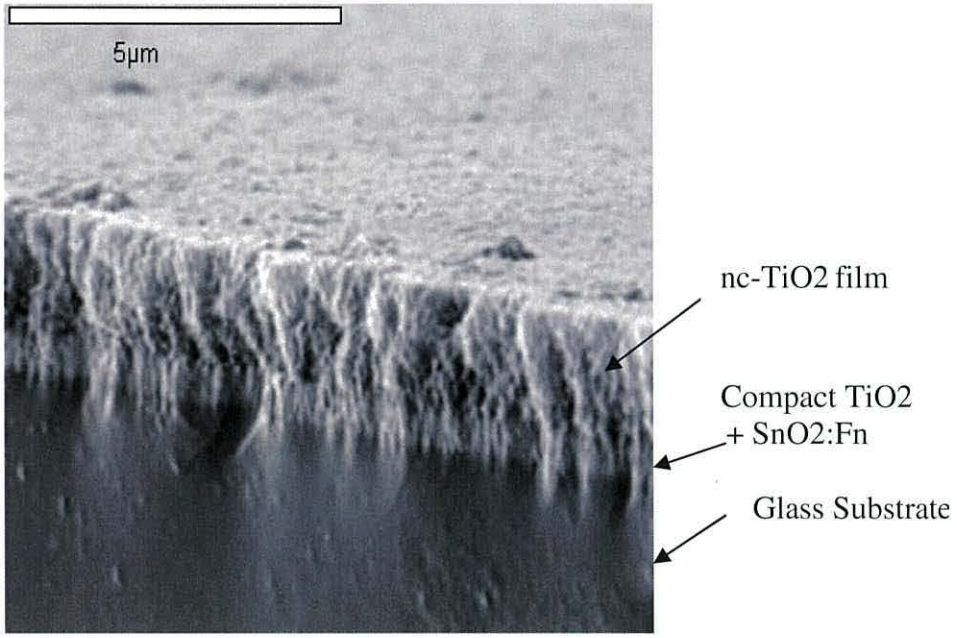

Figure 5.14 *SEM image of the cross section of a AU/P3HT/ nc-TiO_2 /compact TiO_2/SnO_2:F from batch A.*

The cross section of a device from batch B is shown in figure 5.15. It shows that the whole thickness of the device is also dominated by nc-TiO_2 and SnO_2:F /compact TiO_2 layers. The thickness of the nc-TiO_2 layer was 2.1μm and the underlying SnO_2:F/nc-TiO_2 film was ~ 700 nm. In this case, though the cross section shows a more random structure in which the nano-particles have retained their structure. Furthermore, the interface between the nc-TiO_2 layer and the compact layer is better –defined suggesting a less intimate contact has been formed compared to batch A.

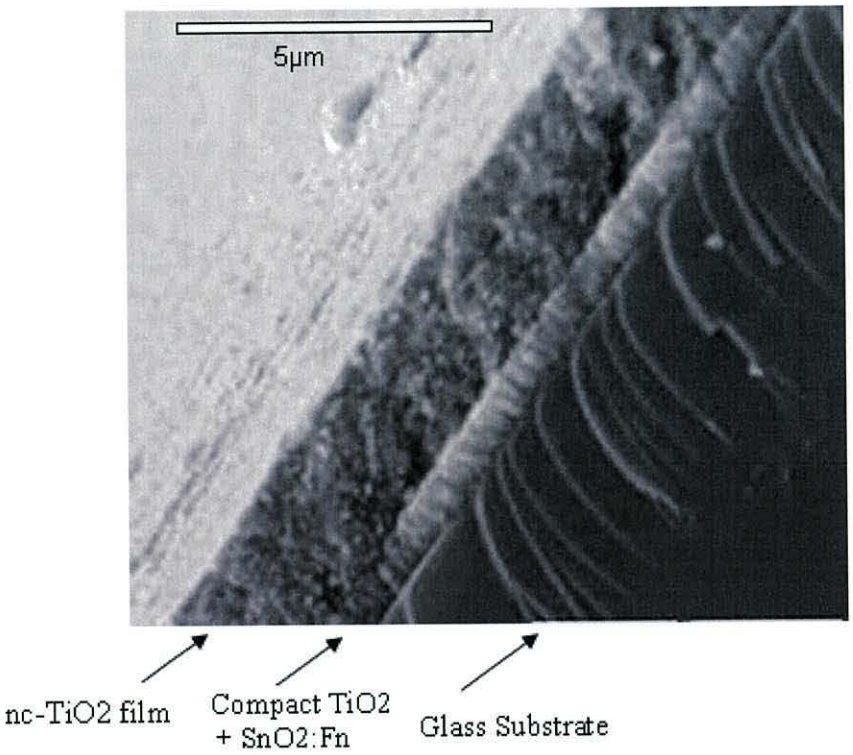

Figure 5.15 *SEM image of the cross section of a AU/P3HT/ nc-TiO_2/cmpact-TiO_2 / SnO_2:F from batch B.*

To confirm that the thinner of the two layers in figure 5.14 and 5.15 was indeed the compact TiO_2/ SnO_2:F layer SEM images were obtained of the cross–section of un-coated substrates. This is shown in figure 5.16 and yield an estimated thickness of 500 to 600 nm confirming the interpretation of figure 5.14 and 5.15.

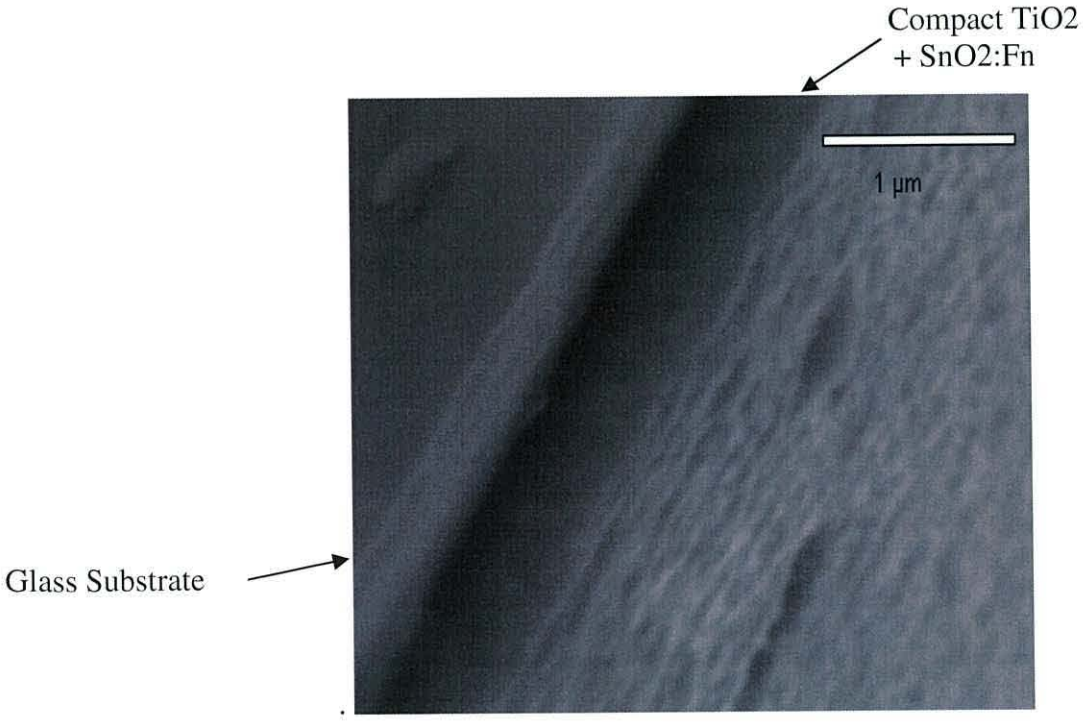

Figure 5.16. *SEM image of the cross section of a compact TiO_2/ SnO_2:F substrate.*

5.3 Spectroscopic Analysis

5.3.1 Energy Dispersive X-Ray Analysis

Energy Dispersive X- Ray Spectroscopy (EDAX) was use to collect information about the elements which exist in the layers of our solar cells. The samples tested were the same samples mentioned in section 5.2.2. They were constructed from five layers one on top of the other on the glass substrate i.e. Au/P3HT/ nc-TiO_2 /compact TiO_2 /SnO_2 /glass substrate. The electron beam was focused over the cross section of each of our samples from the bottom to the top in three stages. Before illustrating our results, it is important to mention that there is no guarantee that the EDAX technique will detect every element in the layers. The EDAX spectrometer depends on the energy of the electrons in the beam as well as the concentration of the elements in the layers of our samples. Figure 5.17 shows the EDAX spectrum for the bottom of our sample which is composed of the glass substrate and SnO_2:F electrode.

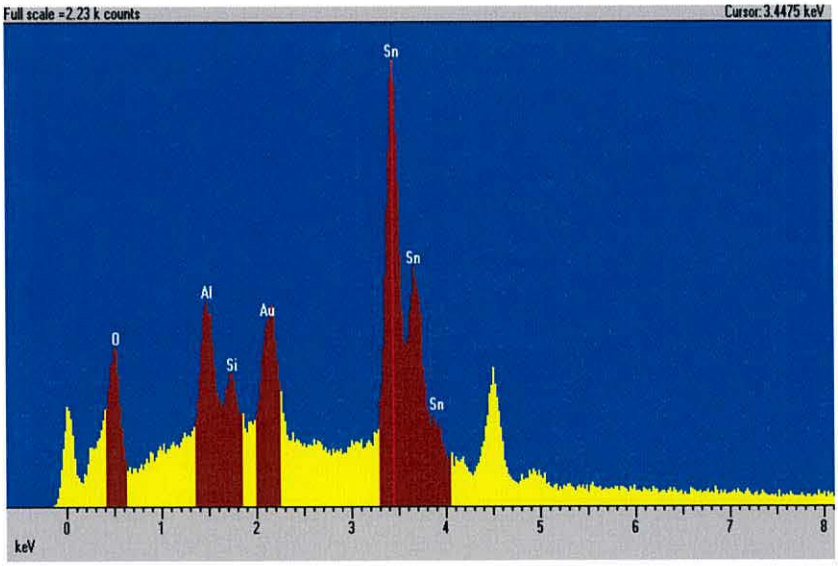

Figure 5.17 *EDAX analysis of the bottom of region of a batch A solar cell.*

The peaks labeled by Al and Si originated from the glass substrate. The Au peak is due to the conductive coating evaporated on top of the sample. The strongest peak was Sn from the SnO_2:F electrode. There is also one small Ti peak. Figure 5.18 shows the EDAX spectrum when the beam was located in the middle of the nc-TiO_2 film. As can be seen, the Al, Si and Sn signals are now reduced while the Ti and O

signal are much larger. One motivation for undertaking the EDAX study was to see whether information could be obtained on the penetration of P3HT into the nc-TiO_2 layer. Unfortunately, no sulphur signal was detected. When the electron beam was moved to the device surface, the spectrum obtained is shown in figure 5.19 . The only significant change in figure 5.19 is the larger Au signal due to X-ray emission from the gold on the top surface as well as from the thin coating over the cross-section. Adjacent to the Au peak, some evidence for suphur is obtained at 2.25KeV.

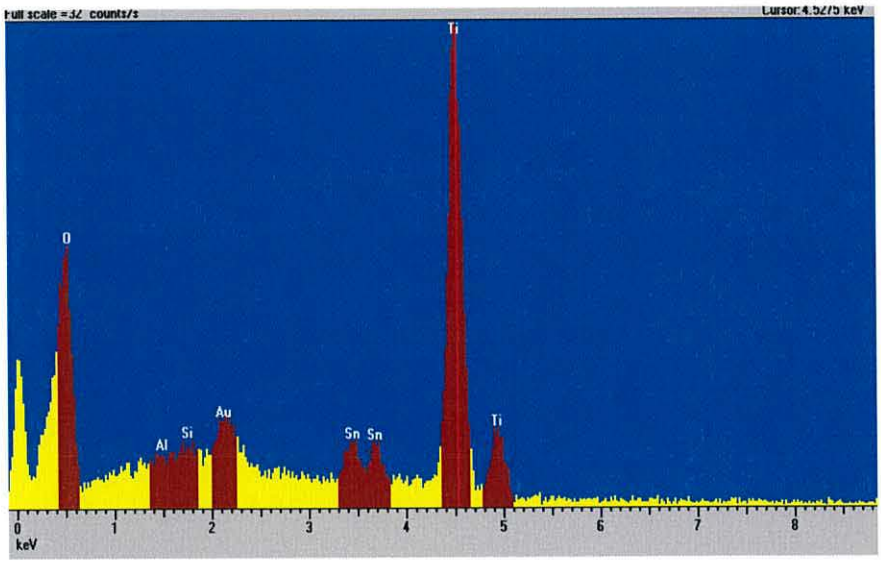

Figure 5.18 *EDAX analysis of the bottom of sample coated on a glass substrate.*

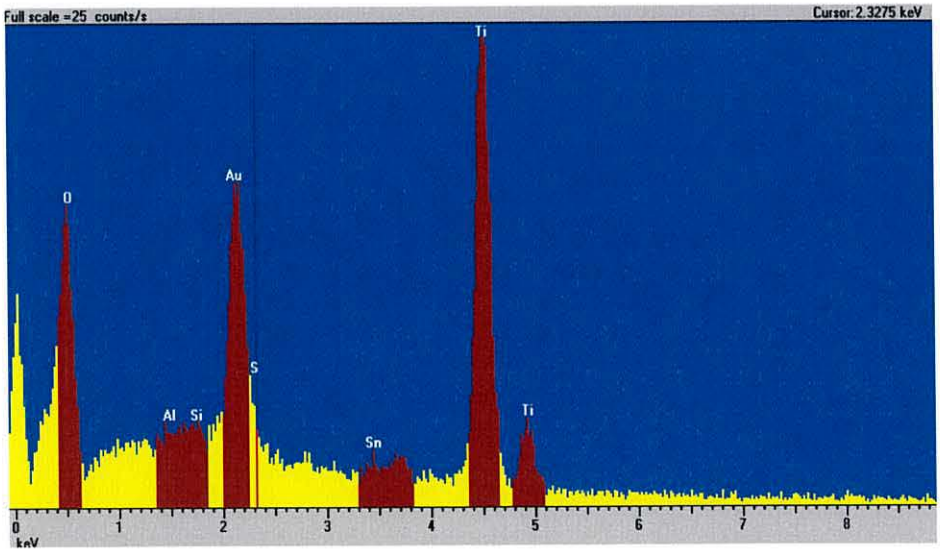

Figure 5.19 *EDAX analysis of the surface of sample coated* on a *glass substrate.*

A similar investigation was undertaken with a device from batch A but showed no significant difference. Table5.2 provides the energy and nature of the X-ray emission from the sample.

Energy (Kev)	**EDAX spectral Assignment**
1.49	Al(kα1)
1.74	Si (kα1)
3.69	Ca(kα1)
4.51	Ti (kα1)
4.95	Ti (kβ1)
2.12	Ai(Mα1]

Table 5.2 *EDAX spectral assignments*

5.3.2 X–Ray Diffraction

For this study, the TiO_2 films were deposited onto glass substrates by following the procedures mentioned in Chapter 4. Section 5.2.1 showed a clear difference in the surface morphology of films produced from the two batches. In this section, we report a further investigation into the crystallinity, particle orientation, and particle size in the nc-TiO_2 using X-Ray Diffraction (XRD). Figure 5.20 shows the XRD signal of nc-TiO_2 films produced from batch A. We observed a strong diffraction peak which occurred at a Bragg angle of $2\theta \sim 25^{\circ}$, while smaller peaks were observed near 38° ,48° and 54° and corresponded to reflections from the 101, 004, 200, and 105 lattice planes of the particles. These lattice planes occur in a tetragonal system and correspond to the anatase phase of TiO_2 (see section 3.2.2).

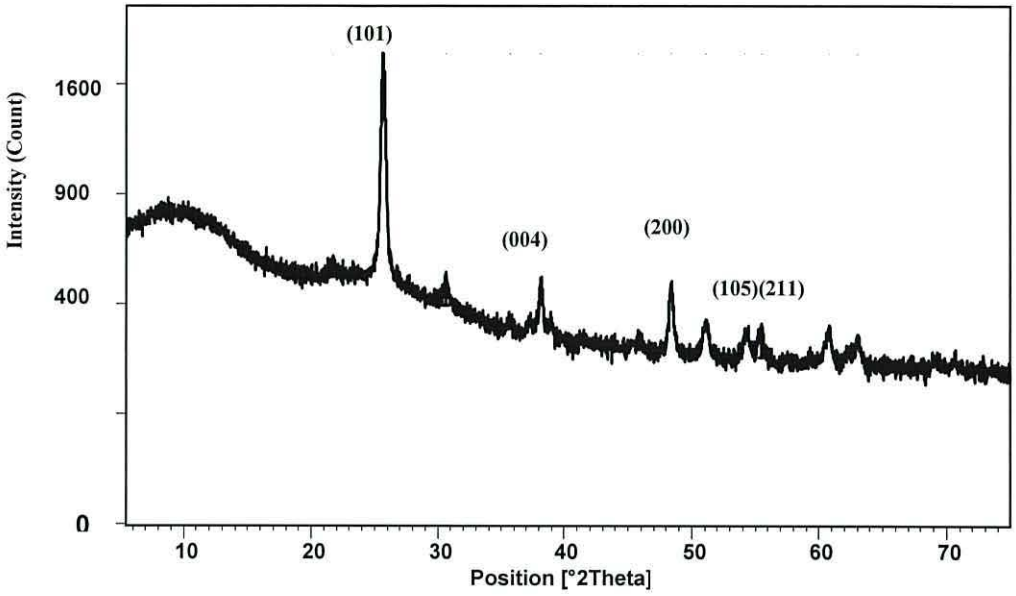

Figure 5.20 *XRD pattern of nanoparticle nc – TiO_2 for batch A.*

In table 5.3 are given the values of the various parameters describing the difference peaks in figure 5.20. These can be used to determine the grain size by applying the Schreer equation (4.2) to the largest diffraction peak i.e the peak occurring at $2\theta = 25.6987^{\circ}$ for the reflection from the 101 lattice plane. Substituting the following values in equation (4.2). 1: β =0.00584 radians, $\cos 12.85^{\circ} = 0.96$, and K = 0.96, the grain size is estimated to be 25.6 nm.

Pos. [°2θ.]	Height [cts]	β [°2Th.]	d-spacing [Å]	Rel. Int. [%]	Lattice index
25.6987	1279.44	0.3346	3.47	100	(101)
38.1801	198.41	0.1673	2.36	15.5	(004)
48.3831	221.22	0.3346	1.88	17.3	(200)
54.1584	65.25	0.4684	1.69	5.1	(105)
55.5089	94.76	0.4015	1.66	7.41	(211)

Table 5.3 *The parameters of the lattice planes extracted from XRD nc-TiO_2 film from batch A.*

Figure 5.21 shows the XRD pattern of nc-TiO_2 from batch B. The strongest diffraction peak again appears at $2\theta \sim 25.6987^{\circ}$, with weaker peaks appearing near 38°,48°, and 54°. Again , the presence of these peaks indicates the existence of the anatase phase in the nc-TiO_2 film produced from batch B (similar to nc-TiO_2 produced from batch A).

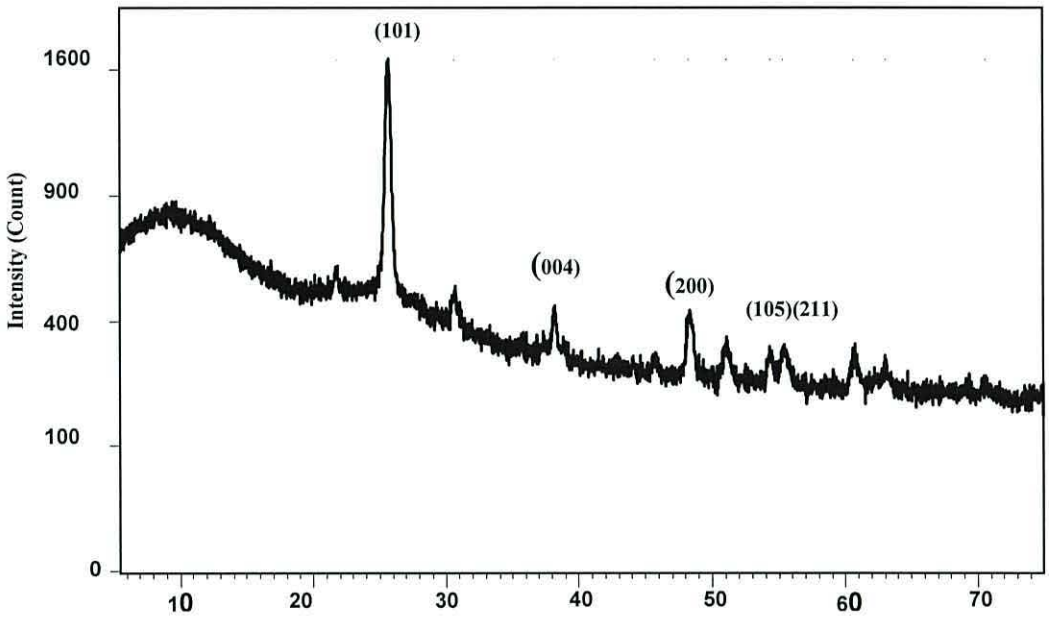

Figure 5.21 *XRD pattern of nano particles nc-TiO_2 film for batch B.*

In table 5.4 shows the lattice parameters of the nc-TiO_2 film produced from batch B extracted from the XRD spectrum in figure 5.21 from which we see a difference regarding the intensity of the peaks and the full width at half maximum (β) between nc-TiO_2 films produced from batches A and B. By comparing tables 5.4 and 5,3, we note that the intensities of the diffraction peaks for nc-TiO_2 from batch A are higher than from batch B. However, the value of β for the nc-TiO_2 from batch B is larger than that from batch A. Therefore, the nc-TiO_2 films produced from batches A and B will have different grain sizes. The lattice parameters from table 5.4 for the strongest diffraction peak ($2\theta = 25.6949^{\circ}$) for the 101 lattice plane are K=0.94, λ=0.154nm, FWHM= 0.00759 radians, cos(12.8493)=0.96, yielding a grain size of 19 nm for the nc-TiO_2 film of batch B. Thus the grain size of nc-TiO_2 produced from batch A is bigger than batch B. It is known that differences in grain size are

important in determining the optical and electronic properties of nc-TiO_2 films [2] and it is expected that the larger grain size should lead to a higher conductivity.

Pos. [°2θ]	Height [cts]	β [°2Th.]	d-spacing [Å]	Rel. Int. [%]	Lattice index
25.6949	1141.37	0.4349	3.47	100	(101)
38.2623	124.41	0.3346	2.35	10.9	(004)
48.3112	165.11	0.5353	1.88	14.47	(200)
54.398	83.93	0.4015	1.69	7.35	(105)
55.3813	89.52	0.3346	1.66	7.84	(211)

Table 5.4 *Lattice parameters extracted from XRD of nc-TiO_2 film produced from batch B.*

5.3.3 Scanning Tunneling Spectroscopy

Scanning Tunneling Microscopy/Spectroscopy (STM/S) was used to study the surface electronic properties of the nc-TiO_2 films. This technique has been used to show that the age of the nc-TiO_2 film as well as the type of material attached to the nc-TiO_2 surface affects the electronic properties of the film [3]. In the present study, two nc-TiO_2 films were studied, one produced from batch A and one from batch B. Figure 5.22 gives the tunneling current as a function of voltage for the batch A film. At -0.7 V, the current flowing is referred to as the anodic tunneling current while the current flowing at 2.6eV referred to as the cathodic current. When the tunneling current is zero in the region that separates the cathodic and the anodic currents this corresponds to the band gap of the sample.

Figure 5.23 shows the conduction spectrum (dI /dv) versus voltage (V) of the batch A nc-TiO_2 obtained by numerical differentiation of the I-V relation. This reveals an increase in conductance for positive voltage influenced by the valence band and negative voltage influenced by the conductive band of nc-TiO_2 film. Therefore, the surface band gap energy for the batch A nc-TiO_2 film is estimated to be ~3.3eV based on conductance results .

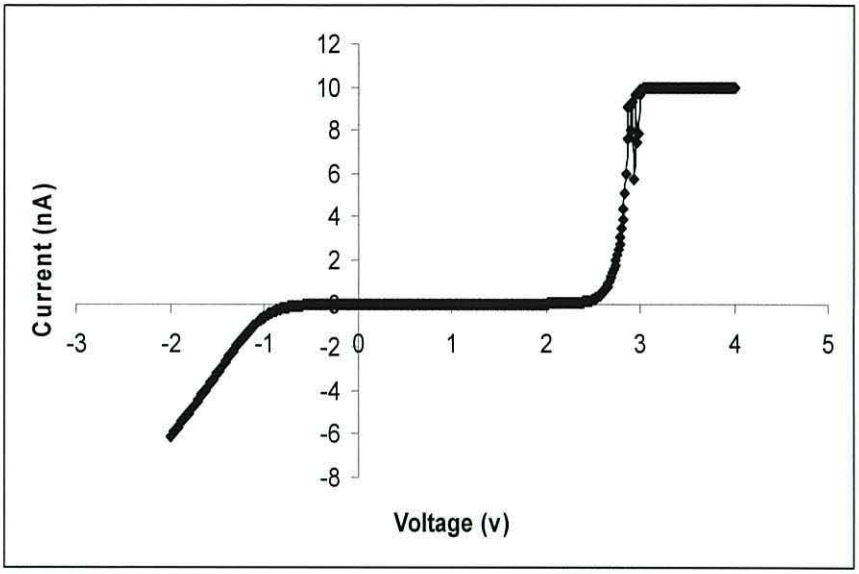

Figure 5.22 *STS I-V characteristics of batch A nc-TiO_2 film.*

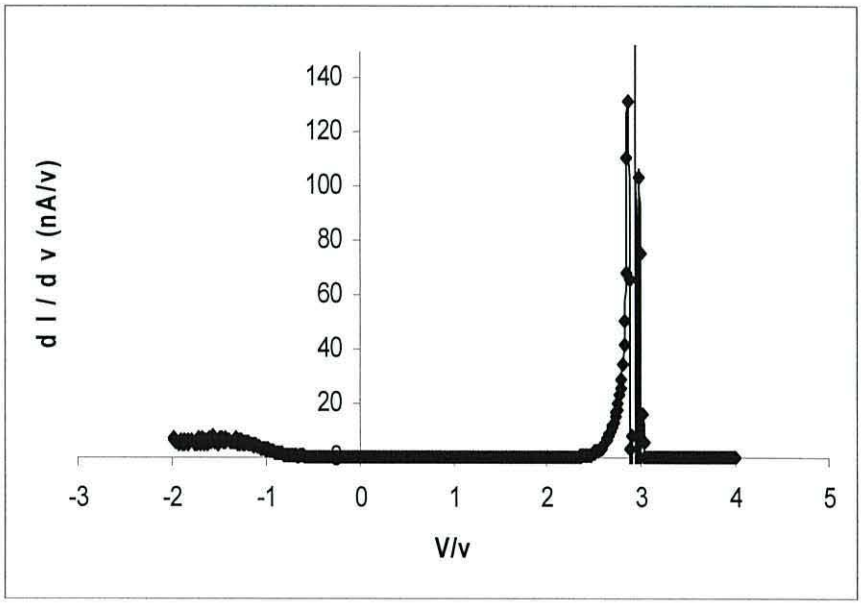

Figure 5.23 *STS dI-dV characteristics of batch A nc-TiO_2 film.*

Figures 5.24 and 5.25 show the corresponding tunnelling current and conductance plots for nc-TiO_2 film produced from batch B. The onset voltage for anodic and cathodic tunneling currents were ~ -0.8V and 1.8V respectively. For batch B nc-TiO_2, there is a reduction, therefore, in the surface bandgap energy from ~3.3eV to ~2.6 eV. While batch A material gave a band gap energy similar to report

in the literature [4]. The lower value for batch B corresponds to values obtained in films kept in air for long period the reduction is attributed to the formation of surface defects in nc-TiO_2. In the present case, samples were prepared on the day of the STS measurements so that the difference in the band gap probably indicates differences in the storage condition of the nc-TiO_2 particles in the storage sol gel.

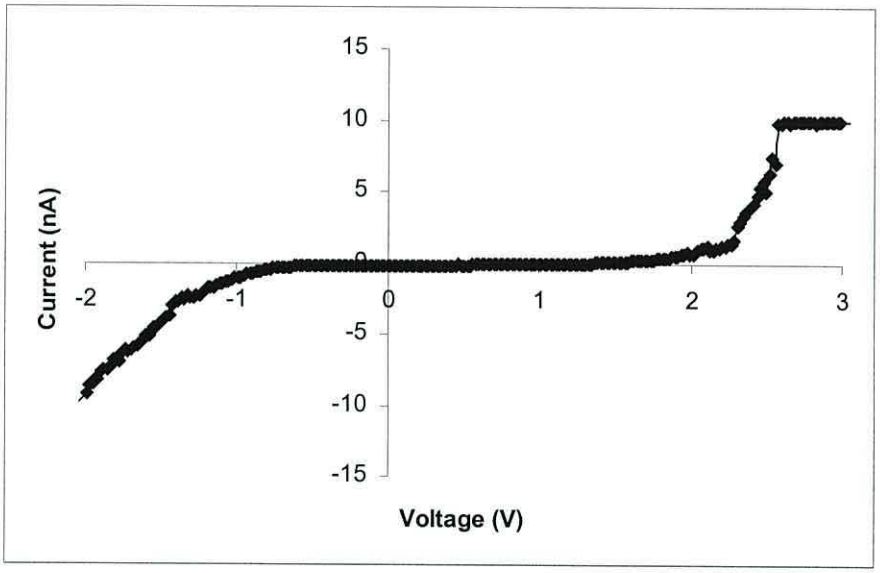

Figure 5.24 *STS I-V characteristics of batch B nc-TiO_2 film.*

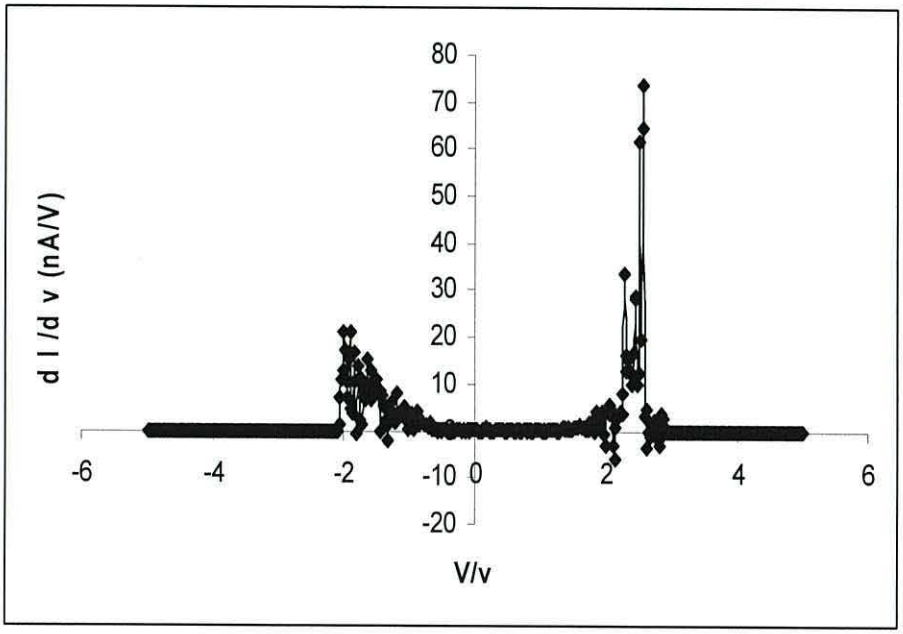

Figure 5.25 *STS dI-dV characteristics of batch B nc-TiO_2.*

5.3.4 Optical Properties of the nc-TiO_2 Films

The optical transmittance spectra (Figure 5.26) were measured for nc-TiO_2 films produced from batches A and B using the procedures described in section [4.2.2]. The thickness of nc-TiO_2 films would be similar to the values extracted from SEM images ~2 μm. The figure reveals that the light transmission of the two nc-TiO_2 films was high for wavelength ranging from 720 nm to 500 nm. Below 350 nm, transmission was very poor in keeping with the optical band gap of the films [5]. Thus, nc-TiO_2 film is an attractive material to be used in solar cell fabrication since it allows visible light to pass through it with relatively little absorption. The slight difference of transmittance between the two samples is probably related to differences in thickness and degree of light scattering from the different morphologies.

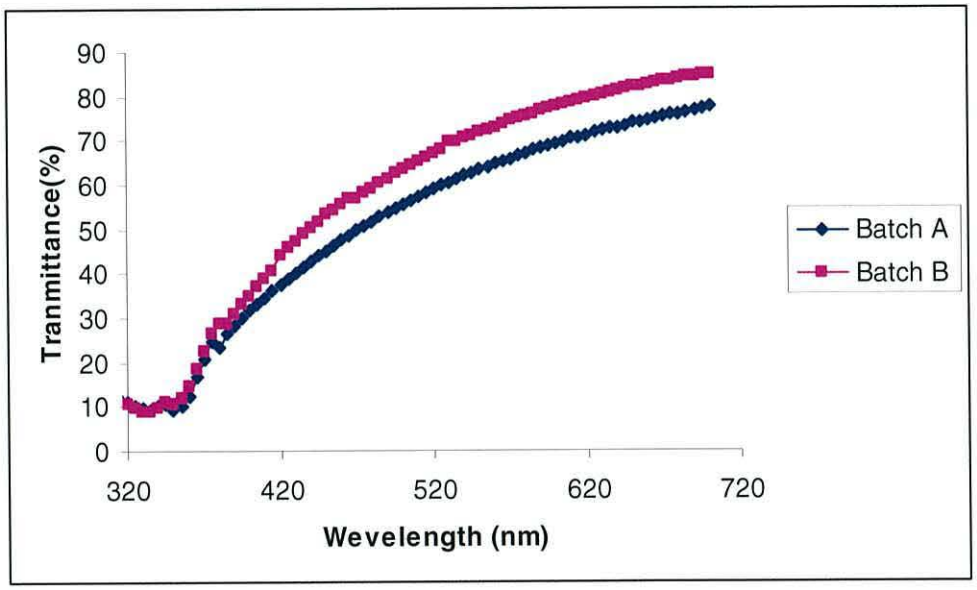

Figure 5.26 *Transmittance spectra of the TiO_2 film from batches A and B.*

5.4 Thermo Gravimetric Analysis

The batches of sol-gel from the supplier were nominally identical. The procedures for producing the nc-TiO_2 films were also identical, so there is no obvious reason for the difference in morphology in films produced from the two batches. According to the supplier the sol-gel was composed of titanium oxide, water, ethanol, and polyethylene oxide (PEO). A small amount of nitric acid (HNO_3) is added to control

the pH. The concentration of each material was not provided. The effect of sol-gel composition on the resulting nc-TiO_2 film has been studied by a number of authors. For example, Que et al [5] found that the concentration of solvent could affect both the structure and thickness of the nc-TiO_2 film. Also the binder, PEO or polyethylene glycol (PEG), and the pH have been shown to play an important role in the performance of solar cells [6-7]. In order to confirm that the sol-gel composition was indeed the same, samples from two batches were subjected to Thermo-Gravimetric Analysis (TGA). Figures 5.27 shows the weight loss of the two batches of TiO_2 sol-gel as a function of temperature in the range from 20 °C to 600°C. Four steps were observed in the TGA curves :

1- **20 to 100 °C**: the weight loss during this range is due to the removal of the residual water and ethanol.
2- **100 to 300 °C**: The weight loss during this range is due to the expulsion of organics that are trapped inside the pores and removal of chemisorbed water [9].
3- **300 to 380 °C**: The weight loss during this range is due to the removal of structural hydroxyls and organic residues. This will increase the number of bridging oxygen and thus the monolithic nature of the sol gel [8, 9].
4- **380 to 600 °C**: Region of small weight loss-the residue is virtually all nc-TiO_2.

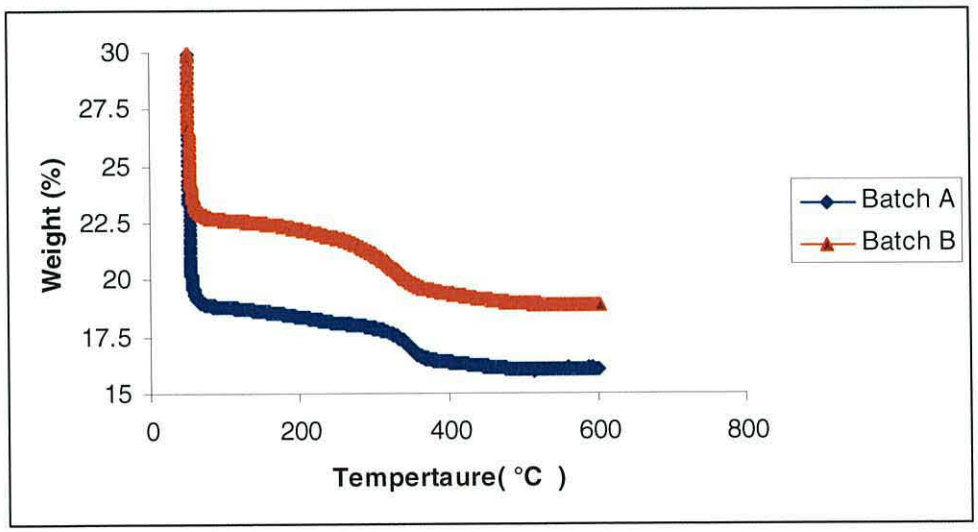

Figur 5.27 *TGA curve of TiO_2 sol-gel from batch A and B.*

In spite of the resemblance in the weight loss for the two batches, the following differences occur:

- The concentration of solvent material (water and ethanol) in batch A is higher than in batch B.
- The concentration of solid material in batch A is lower than in batch B.
- In the temperature range 290 °C to 330 °C, there is a difference in the rate of weight loss in the batches. This suggest possible differences in pH see reference [9].

Table 5.5 shows percentage weight loss of solvent from the starting sol-gels after heating to 100 °C and the weight percent of solid residue at 450 °C. Also, the table shows the thicknesses of the sintered nc-TiO2 layers estimated from the SEM micrographs in section 5.2.2.

Content in sol-gel	**Batch A**	**Batch B**
Weight % solvent	81.2	77.4
Weight % solid residue	16.2	19.1
nc-TiO2 layer thickness (μm)	1.9	2.1

Table 5.5 *Solvent and TiO_2 content of the two TiO_2 sol-gel sol batches.*

The TGA analysis shows difference in the two sol-gel batches. The main difference appears to be high water/ethanol concentration and lower solid residue in batch A. This would be expected to lead to the thinner nc-TiO_2 film observed in practice. The difference in solvent concentration coupled with difference in PEO and acid concentration (these cause the change between 290 to 330 °C) we presume the origin of the different morphologies.

5.5 Summary

The morphology of nc-TiO_2 films prepared by the doctor blade and spray pyrolysis techniques have been studied using AFM and SEM. The surface of nc-TiO_2 film produced from batch A was found to be rougher than the surface of nc-TiO_2 film produced from batch B over a 5 μm x 5 μm sample area. Additionally, their particles were distinguished in terms of height and shape. The particles of nc-TiO_2 produced from batch A have a spiky shape and with a mean particle height ~100nm. The particles of nc-TiO_2 produced from batch B have an elliptical shape and with a mean particle height ~60nm.The compact TiO_2 layer coating on the SnO_2 : F /glass substrate, however, was smooth with RMS roughness ~6nm. Spin coating P3HT onto the films provided a small decrease in the roughness (~2nm) in comparison with the un-coated nc-TiO_2 films. The thickness of devices tested in this work was estimated to be ~1.9 μm for nc-TiO_2 solar cells produced from batch A and 2.1 μm produced from batch B. These values were extracted from SEM images of the cross-section of a completed device. The SEM images also revealed interesting features for nc-TiO_2 films. In batch A, the nc-TiO_2 particles, appeared to have fused together in vertical features, whereas those from batch B have small particles attached together in different shapes. The cross-section of images also show that the thickness of the compact TiO_2/SnO_2 : F layer deposited on the glass substrate, ranged from ~400 nm to ~700 nm.

EDAX analysis confirmed the presence of the elements expected to be present. The optical resolution of the beam was too poor and the sulphur signal too weak to allow the penetration of P3HT into the nc-TiO_2 film to be determined. XRD measurements confirmed that the sintered nc-TiO_2 films of batches were in the anatase crystal phase. Applying the Scherrer equation to the (101) diffraction peak indicated that the grain size in batch A , ~ 25 nm was larger than in batch B, ~ 19 nm. STS measurements were undertaken to study the electronic properties of the nc-TiO_2 surface. The surface band gap energy for batch A was estimated to be 3.3 eV while for batch B it was 2.6 eV. The former value is close to the optical absorption edge (3.4eV) of the nc-TiO_2 films as determined from the transmission spectra. The surface band gap for batch B is much lower and may indicate a higher defect concentration at the particles surface in batch B film. The transmittance of the nc-

TiO_2 films is relatively high for wavelengths greater than ~ 500nm i.e. in the range corresponding to the highest solar irradiance. The slight difference in transmittance between the batches may be attributed to the differences in thickness and/or difference in morphology.

Finally, using the TGA technique, we have shown that differences in composition exist between the nominally identical batches of sol-gel. The principle difference is the higher ethanol/water content in batch A which results is reduced TiO_2 concentration. The TGA plots also suggest a difference in PEO/acid concentration which manifest themselves in the range 290-330°C. Since the morphology has been shown by other to depend on the sol-gel composition, we conclude that the differences seen between batch A and batch B in the AFM and SEM micrographs have their origin in the different compositions exposed by TGA.

5.6 References

1. M. Arabatzis,S.Antonaraki, T. Stergiopoulos, A. Hiskia, E. Papaconstantinou, M. C. Bernard and P. Falaras, *Journal of Photochemistry and Photobiology A: Chemistry*, **149**, 237, (2002).
2. T. G. lei, H. H. Bo, S. J. Da, *Chinies Physics Letter, **22** ,* 1787 (2005).
3. A. R. Kumarasingher, W. R. Flavel, *Phsics.E,14*. 224, (2002).
4. Y, lin, R.Lin, W. Wang, X. Xiao, *Appied surface science.* 143, 169,(1999).
5. W. Que, A.Uddin, X. HU, *Journal of Power Sources, 159, 353*, (2006).
6. B. Li, X. Wang, M. Yan, and L. Li, *Materials Chemistry and Physics,* **78**,184, (2003).
7. B.Guo, Z.Liu, L. Hong, and H. Jiang, *Surface and Coatings Technology*, **198**, 24, (2005).
8. B. Guo, Z. Liu, L. Homg, H. Jiang, and J. Y. Lee, *Thin Solid Films,* **479,** 310, (2004).
9. C. P. Sibu, S. R. Kumar, P. Mukundan, and K.G. k. Warrier, *Nanosized Titanium Oxide Chemistry of Materials,* **14**, 2876, (2002).

Chapter 6
Electrical Characteristics of Double Layer P3HT/ nc-TiO_2 Solar Cells (DLSCs)

6.1 Introduction

The Double Layer P3HT/nc-TiO_2 Solar Cells (DLSCs) were fabricated using an organic semiconductor instead of the electrolyte and the dye in DSSC [1]. Twenty DLSCs were fabricated from the two batches: A and B. The current density–voltage (J-V) characteristics for these devices were measured in the dark and under illumination with a halogen lamp. The external quantum efficiency of DLSCs (produced from batch A) was measured to extract the conversion efficiency at

AM1.5. The effect of vacuum on the solar cell parameters was observed and compared with the results obtained from experimenting in the air.

6.2 Electrical Measurements in the Air

6.2.1 DC Characteristics of DSLCs

The current density-voltage (J-V) characteristics of a typical DLSC produced from batch A are shown in linear and semilog form in figures 6.1 and 6.2 respectively. In the dark, the devices displayed good diode characteristics. In the present case, the forward current turned on at ~0.63V and by 0.8V had risen to ~10mA/cm^2. The reverse current at -0.8V was ~0.001 mA/cm^2 giving a rectification ratio of 10^4. Under illumination with the halogen lamp (72mW/cm^2), the device produced an open circuit voltage, Voc, ~ 0.68V, short-circuit current density, Jsc,~0.22mA/cm^2 with fill factor of ~46% yielding a power conversion efficiency of 0.09%.

The spread in these values for 10 different cells fabricated on different substrate gave 0.1<Jsc<0.22mA/cm^2 and 0.65V<Voc<0.68V. These results especially for Voc are similar to values reported previously for cells of this type [2, 3], and are believed to arise from the presence of a built-in electric field at the interface between the nc-TiO_2 and the P3HT. Interestingly, Jsc for these devices were similar to generally reported values [3, 4], but are still low compared to dye-sensitized solar cells and polymer/fullerene bulk heterojunction solar cells.

Under high forward bias, the present devices exhibit a higher current under illumination in comparison with the dark current at the same condition, around 3mA/cm^2 at V=0.8. This suggests that photoconductivity is occurring in the bulk semiconductor region of device.

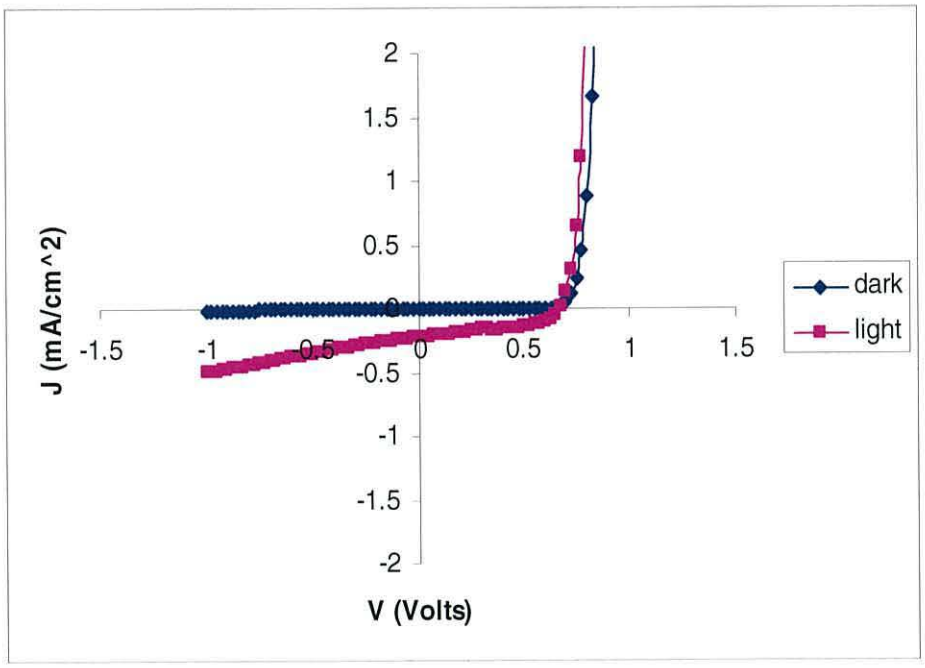

Figure 6.1 *J-V characteristics of a typical DSLC produced from batch A under Halogen lamp illumination and in the dark.*

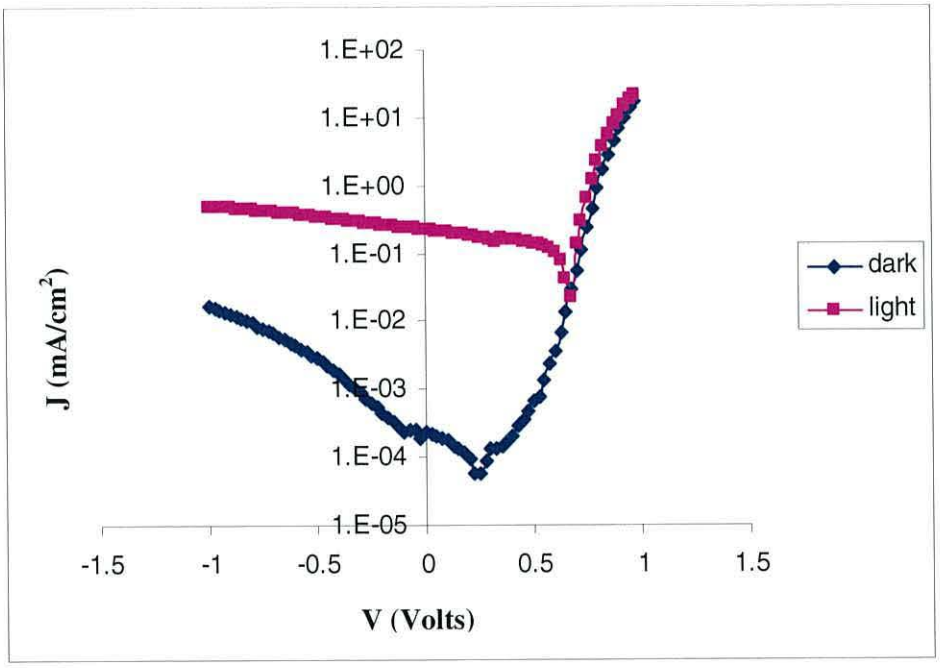

Figure 6.2 *J-V characteristics from figure 6.1 replotted in semilogarithmic form. For negative currents only the modulus is plotted so that the sharp minimum correspond to a sign sharp.*

The J-V characteristics of a DLSC from batch B are shown in linear and semilog form in figures 6.3 and 6.4 respectively. In the dark, the turn-on voltage was 0.75V with the current rising to ~0.1mA/cm^2 at 1V and 4.5×10^{-3} mA/cm^2 at -1V giving a rectification ratio of ~700. While batch B devices demonstrated a higher turn-on voltage, the dark currents were significantly lower in both polarities. Under illumination this device gave a Jsc ~0.03mA/cm^2, Voc~0.83V, and a fill factor of ~ 47% yielding a power conversion efficiency of 0.019% i.e. almost an order magnitude lower than for the batch A device.

The spread in values for 10 devices from different substrates were as follows: 0.02mA/cm^2<Jsc<0.04mA/cm^2 and 0.78V>Voc>0.83V. At high forward bias, there was little difference between the dark current and that under illumination, suggesting that photoconductivity is very small. This is attributed to the presence of a high resistance in the bulk semiconductor and poor contact between nc-TiO_2 and P3HT.

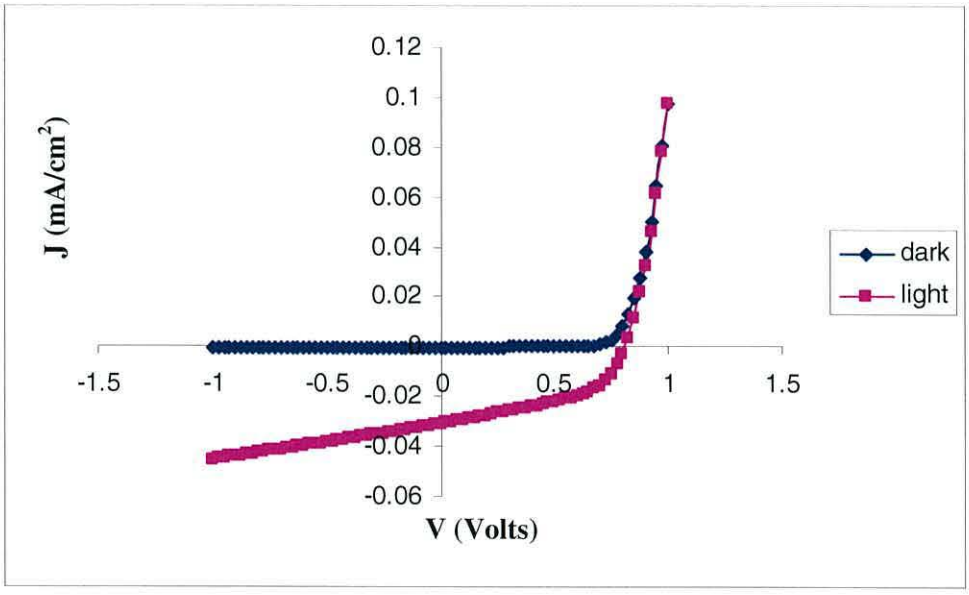

Figure 6.3 *J-V characteristics of DLSCs produced from batch B.*

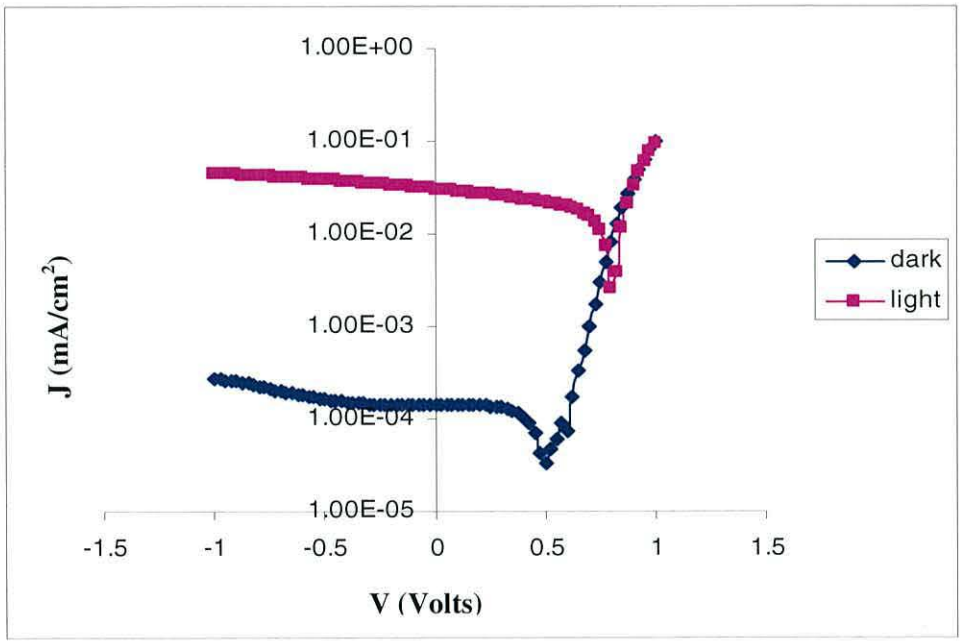

Figure 6.4 *The data of figure 6.3 for the batch B DLSCs is repotted here in semilogarithmic form.*

Table 6.1 provides key comparative data obtained from randomly chosen pixels from a number of substrates produced at different times for P3HT/nc-TiO_2 DLSCs.

Parameter	Batch A	Batch B
J_{SC} (mA/cm^2)	0.223.±0.006	0.03±0.0006
V_{OC} (V)	0.675±0.02	0.825±0.18
FF (%)	46±3.8	47 ±4.4
η_e (%)	0.09±0.01	0.02 ±0.001

Table 6.1 *Mean and standard deviations of the short circuit current density, J_{SC},, V_{OC},, FF,, η_e for the devices produced from batches A and B when illuminated by the halogen lamp (72mW/cm^2).*

In figure 6.4, we note that the dark current for these DLSC devices changed polarity at a non-zero voltage. This arises due to the generation of a displacement current I_d which is described by

$$I_d = C\frac{dV}{dt} \tag{6.1}$$

where C is the device capacitance, and $\frac{dV}{dt}$ the sweep rate of the applied voltage. This is confirmed in figure 6.5 where characteristics obtained from a DLSC from batch B are shown for two different sweep rates i.e. 25mV/s and 2.5mV/s. Sweeping the applied voltage at a slower rate reduces both the zero–bias current and the voltage at which current changes sign i.e. from ~0.5V to ~0.1V.

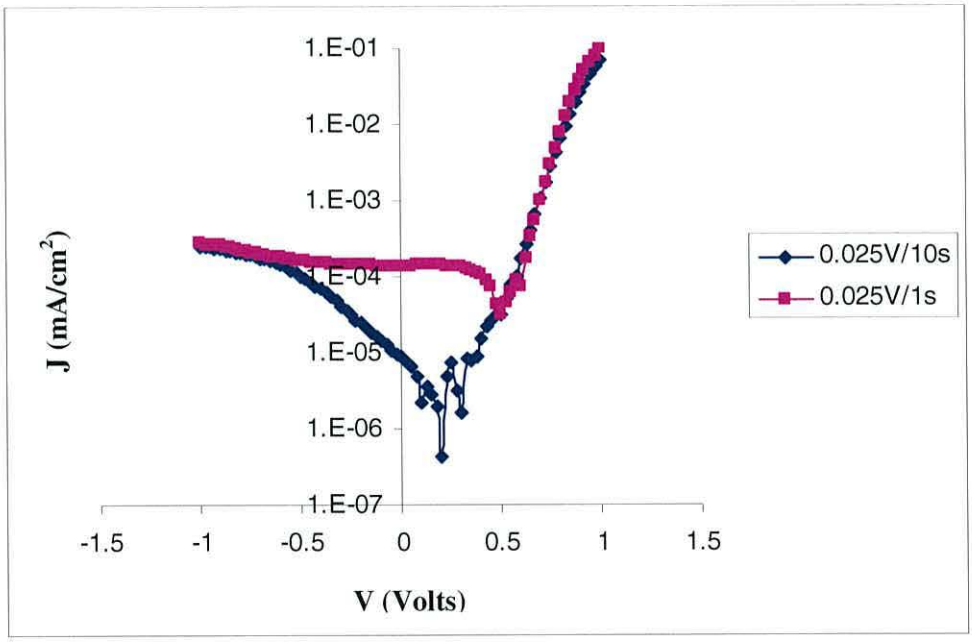

Figure 6.5 *J-V characteristics of DLSCs obtained at two different sweep rates for batch B device in the dark.*

Figure 6.6 shows the UV–visible absorption spectra of the materials used for constructing batch A DLSCs. The P3HT sample was prepared by spin-coating a layer ~130nm onto a glass substrate. The observed spectrum is close to that reported

by others [5] with an absorption edge at 650nm (1.9eV) and a peak absorption at 520nm (2.39eV). For nc-TiO_2, the absorption edge is ~420 nm (2.9eV) with peak absorption at 370nm (3.35 ev). When the nc-TiO_2 is coated in P3HT, the absorption edge shifts to ~650nm with a peak occurring at 520nm as a result of absorption in the P3HT. However, there is a reduction in the coefficient of absorption of the combined nc-TiO_2/P3HT layer in comparison with the P3HT film suggesting that the concentration and/or thickness of the P3HT film in the former is less than in the latter.

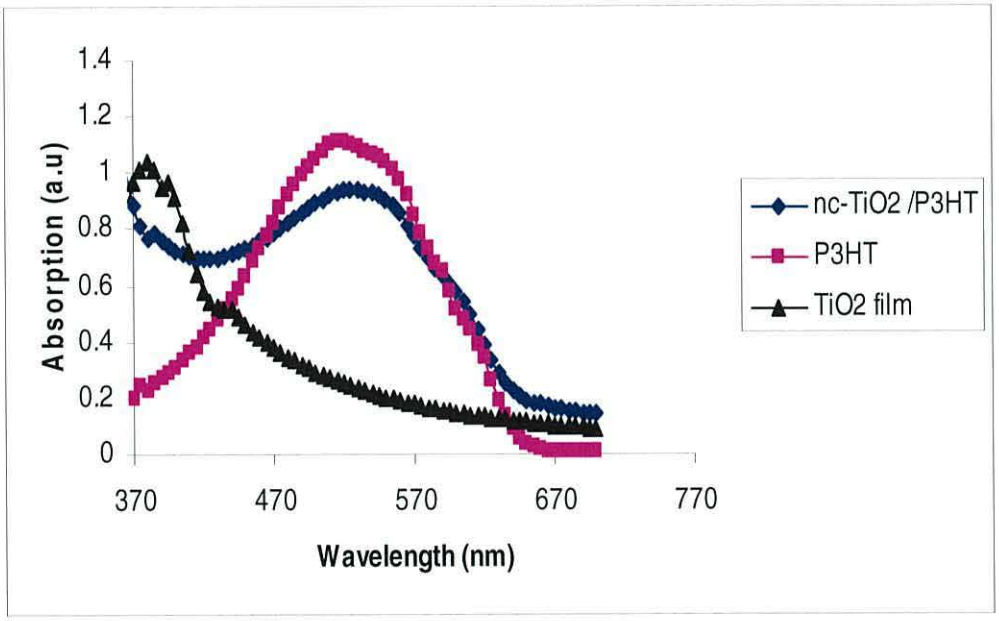

Figure 6.6 *Optical absorption spectra of a P3HT film on glass and ncTiO_2 and P3HT-coated / nc-TiO_2 films on SnO_2:F glass substrate.*

Figure 6.7 shows the External Quantum Efficiency (EQE) for a typical batch A DLSC obtained from the zero-bias photocurrent as a function of wavelength (λ). The value of EQE varied between 2% and 2.5% for the wavelength range from 400nm to 580nm.The wavelength dependence of the EQE and absorption spectrum curves of the DLSC were similar and result from the absorption of the light in the P3HT close to the junction between P3HT and nc-TiO_2. Additionally, there was a small contribution of light absorption in the nc-TiO_2 layer. The value of EQE is reasonable for a non-dye-senstized TiO_2 / polymer solar cell although it is lower than for solar cells utilizing a polymer with hole mobility [6]

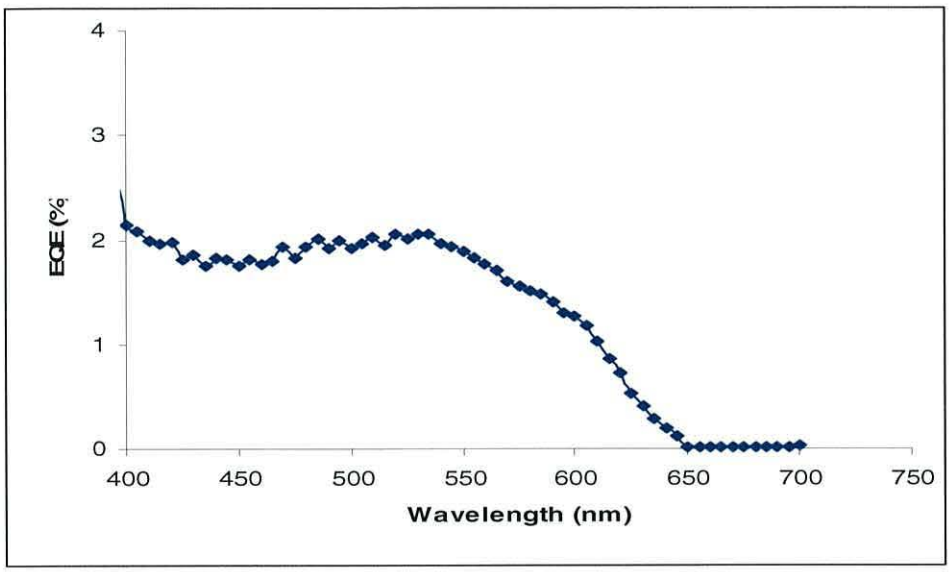

Figure 6.7 *External quantum efficiency of DLSC.*

By integrating the external quantum efficiency spectrum of the DLSC in figure 6.7 with the solar spectrum, the short circuit current density under AM1.5 (1sun) of 0.25 mA/cm^2 was estimated using equation (2.23). Figure 6.8 shows the contribuition of Jsc (λ) to the total current at each wavelength. The area enclosed in this plot is equal to ~ 0.25mA/ mA/cm^2. Thus, we estimated the AM1.5 power conversion efficiency by multiplying this estimated J_{SC} of 0.25 mA/cm^2 by V_{OC} of 0.675V and the Fill Factor of 0.46 arriving at a mean value for efficiency of ~0.093 % under simulated solar conditions. This value of 0.093% is reasonable for a double layer solar cell composed of nc-TiO_2 and a polymeric hole conductor.

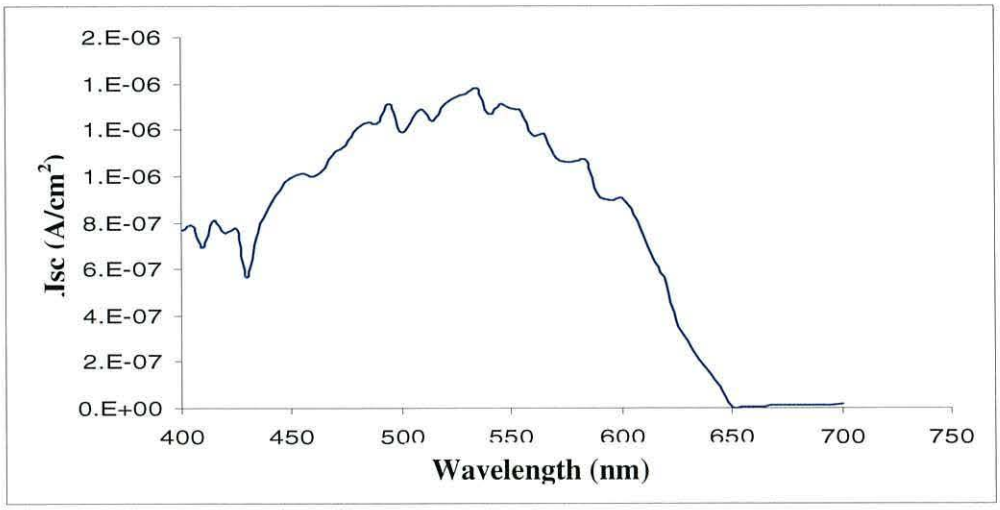

Figure 6.8 *Short circuit current density Jsc of DLSC produced from batch A as function of wavelength.*

Figure 6.9 shows the effect of light intensity on the J-V characteristics of the batch A DLSC. The current increases from 0.01 to 0.36mA/cm^2 at -1V as the light intensity increases, a consequence of increased charge generation. At high forward bias, increasing the light intensity has little effect on the forward current, confirming that photoconduction in the bulk semiconductor is small.

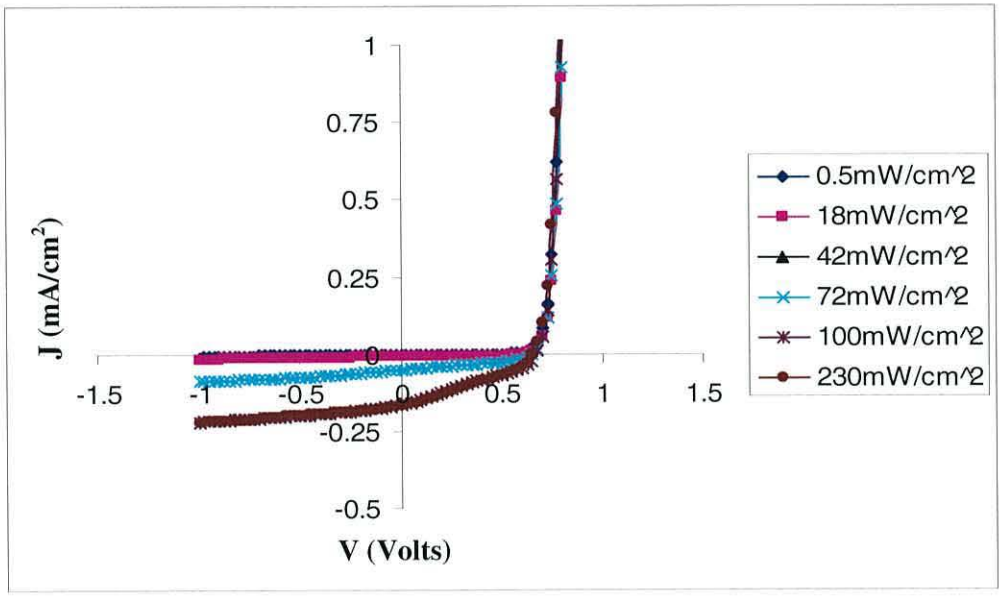

Figure 6.9 *Effect of the light intensity on the I-V characteristics of DLSCs.*

The effect of light intensity on Jsc is plotted for a batch A device in figure 6.10. The relationship between the short circuit current density and the light intensity is reported to be of the form [7].

$$J_{SC} \alpha I_{in}^{n} \qquad (6.2)$$

where I_{in} is the incident light intensity, n a factor whose value is determined by the nature of exciton recombination in the device. From the plot in figure 6.10, we estimated that n~0.88.

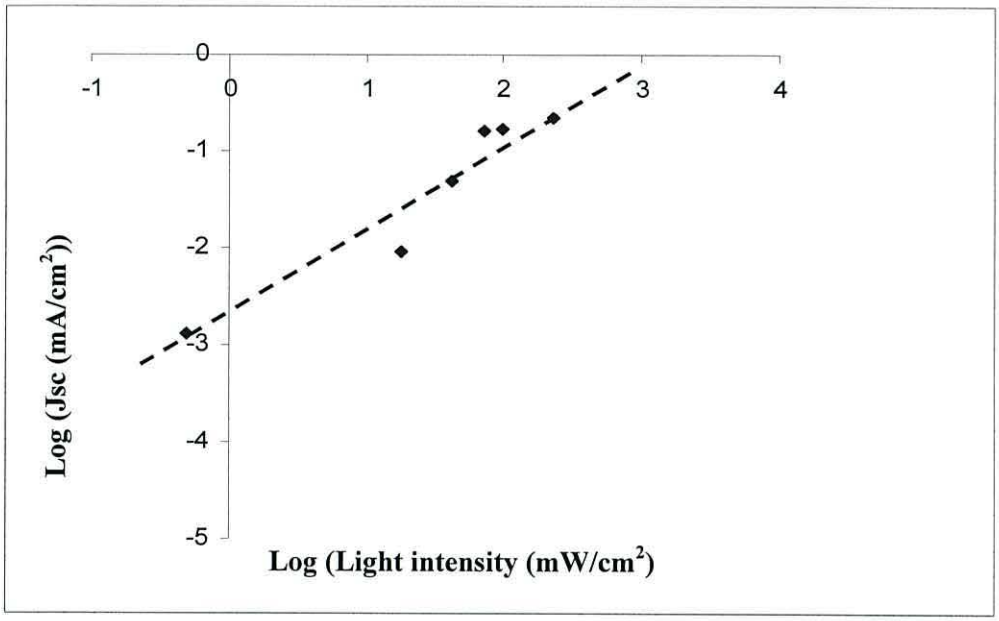

Figure 6.10 *Dependence of Voc on incident light intensity for a TLSC.*

Figure 6.11 shows the variation of Voc with incident light intensity. For low light intensity, Voc was initially ~0.5V then increased to reach 0.675V at 100mW/cm^2. However, as the light intensity increased to 230 mW/cm^2 a slight decrease occurred to 0.65V.

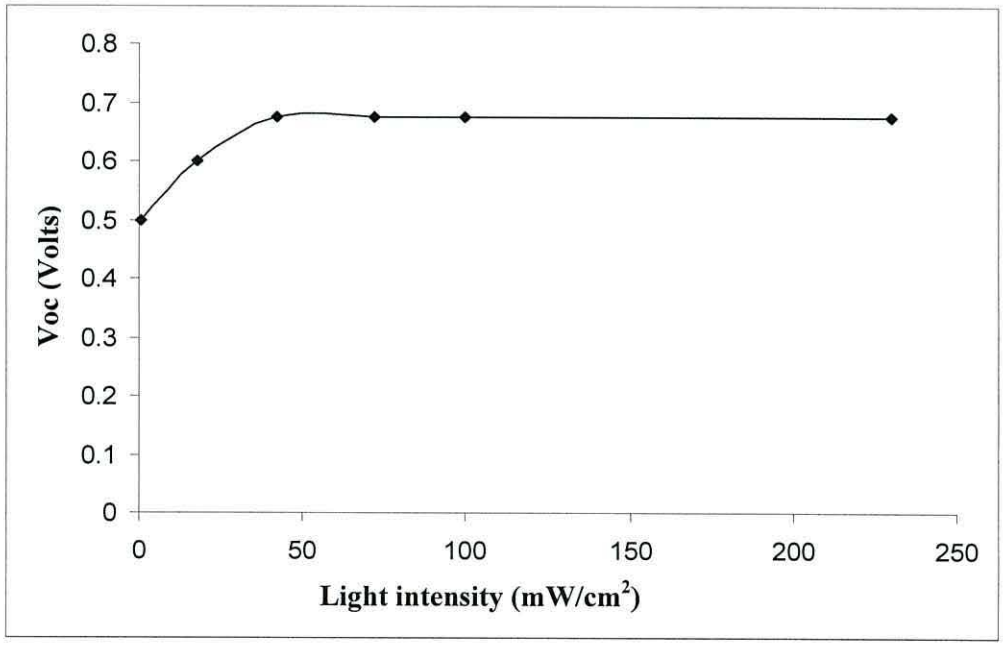

Figure 6.11 *Dependence of Voc on incident light intensity for a DLSCs.*

6.2.2 Discussion

The properties of the interface between polymer hole conductors and nc-TiO_2 have attracted much attention. The discussion has focused on the existence or otherwise of a depletion region at the interface between, for example, P3HT and nc-TiO_2. The possibility is also discussed of band bending in the TiO_2 grain. Our measurements were made in air, the oxygen component of which is known to dope P3HT [8]. Hence, alignment of the Fermi levels in the P3HT and nc-TiO_2 would be expected to lead to the creation of a space-charge region (depletion region) at the interface between nc-TiO_2 and P3HT. Thus, the photovoltaic effect in devices does not depend on the difference in work function between the top electrode and quasi-Fermi level of the TiO_2. An electric field is created at the interface within the depletion region in P3HT which plays the main role in exciton dissociation. This view is supported by the diode –like behaviour of the DLSCs.

Section 6.3 where measurements under vacuum will be reported and Chapter 8 which presents results of AC measurements on DLSCs provide further evidence in support of the existence of depletion region at the interface between nc-TiO_2 and P3HT. Following Watanabe [9] an energy band diagram for the DLSC which indicates a depletion region at the TiO_2/P3HT interface is given like figure 6.12. The HOMO and LUMO of P3HT were reported to be ~3eV and ~4.9eV respectively [10]. These values agree with the optical energy gap (~2ev) for P3HT. The gold (Au) electrode results only in a small contact potential difference between it and P3HT: the contact is essentially Ohmic [11]. The conduction and valence bands of nc-TiO_2 are ~4eV and 7.2eV respectively. The bottom electrode, $SnO_2:F$, acts as a metal of work function ~4.5eV and makes an Ohmic contact with the nc- layers (see section 3.2.1)

In air, the nc-TiO_2 and P3HT were doped with atmospheric impurities causing a shift in their Fermi levels. The Fermi level goes up for nc-TiO_2 and down for P3HT so that both become more conductive. After contact (see figure 6.11), a built in potential of 0.8V appears at the interface from the diffusion of electrons from nc-TiO_2 to P3HT and the diffusion of holes from P3HT to nc-TiO_2. This leads to an alignment of the Fermi levels, and the creation of a depletion region at the interface between nc-TiO_2 and P3HT, resulting in a bending of the energy bands in both nc-

TiO_2 and P3HT. In the dark, the forward and reverse bias currents are controlled by the depletion region. Under forward bias, the potential barrier is reduced thus enhancing hole diffusion from P3HT into the nc-TiO_2 and electron diffusion from TiO_2 into P3HT. Under reverse bias, the current is low and virtually independent of voltage applied to the device. In a conventional diode, the reverse current arises from the drift of minority carriers across the junction and a similar process is likely to be occurring here.

The dark currents in batch A devices were higher than for batch B devices, presumably reflecting the different morphologies of the two types of nc-TiO_2. These differences can give rise to a number of different effects e.g. differences in bulk resistance, differences in the penetration of P3HT and it has also been suggested [3] that there could be differences in the wetting properties of nc-TiO_2 by P3HT. These factors are discussed further in chapter 7. The lower forward current in the batch B devices could be explained, therefore, by any or all of these mechanisms. The higher turn-on voltage of batch B devices could also arise from a higher bulk resistance - part of the applied voltage appears across this resistance. The lower reverse currents most likely reflect a reduced of contact area in batch B devices suggesting poorer penetration of P3HT. Under illumination, the device exhibits similar characteristics to a photodiode except with free electrons and holes created by dissociation of excitons in the field of the depletion region. The open circuit voltage will be limited to some maximum value determined by the built in potential ~0.8V, although this may be reduced by the presence of an interfacial dipole layer. The short circuit current density will be limited by bulk resistance and recombination at the interface.

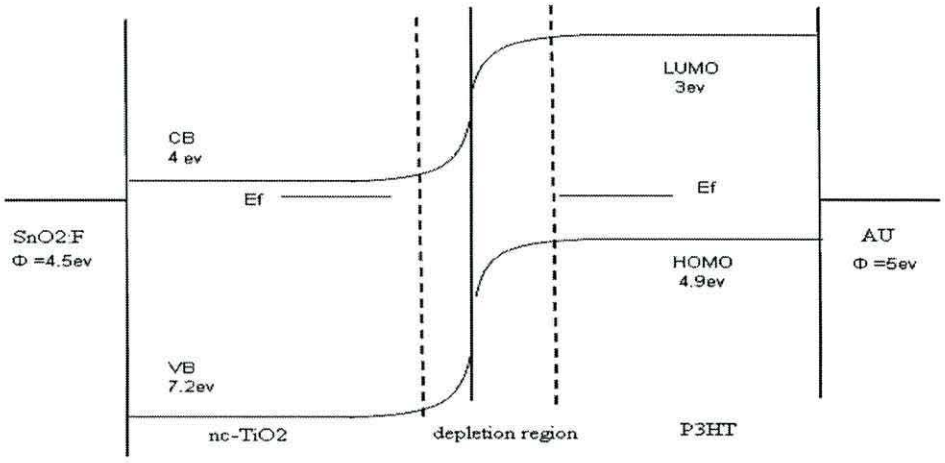

Figure 6.12 *Schematic energy level diagram of a nc-TiO_2P3HT DLSCs.*

In section 6.2.1, figure 6.5, it was shown that the displacement current $C\frac{dV}{dt}$ was significant at higher voltage sweep rate and in detailed studies of the dark I-V behavior should be avoided by sweeping at lower sweep rates. However, when it is present it can be used to advantage to obtain an estimate of the device capacitance. Thus from figure 6.5 where the displacement current is $\sim 1.39\times10^{-4}\,A/cm^2$ in a device of radius ~2 nm when the sweep rate is 25mV/s, then C is estimated to be $\sim 1.39\times10^{-7}\,F$. This is much larger than expected based on the device geometry. This point will be taken up again in chapter 8 where the dependence of capacitance on frequency and applied voltage is discussed. Under illumination, the displacement current is negligibly small compared to the total device current and so has no influence on the measurements of Jsc and Voc.

The external quantum efficiency (EQE) mirrored the absorption spectrum of the nc-TiO_2 /P3HT bi- layer i.e. approximately constant for the range λ <550 nm but decreasing to zero at $\lambda \sim$ 650 00.nm. The low efficiency is attributed to poor contact between nc-TiO_2 and P3HT which leads to a reduction in exciton dissociation [3] and increase the series resistance (see equation 2.14)

Light intensity was seen to affect the measured values of Voc and Jsc. The value of Jsc increased with increased light intensity through an increased generation rate. Equation 2.14 shows also that Jsc increases when the value of Rs decreases. This can occur through increased photoconductivity in the semiconductor by increasing the light intensity. However, the value of Jsc was almost constant for a light intensity of more than $72mW/cm^2$ which is similar to reports in [12]. This is due to the fact that the P3HT has a poor contact or adhesion with nc-TiO_2. This will be verified through comparison with nc-TiO_2 /dye/P3HT solar cells. The plot of log Jsc versus light intensity yields an almost linear relation with n equal to 0.88 indicating the presence of a bimolecular recombination process. The Voc of DLSCs increase from 0.45 to 0.7 V when the light intensity increased from $1mW/cm^2$ to $72mW/cm^2$. This is attributed to an increase in the photo generated current in the devices. From equation 2.11 it is seen that to maintain $I_{out} = 0$ requires Voc to increase.

6.3 Electrical Measurements in Vacuum

6.3.1 DC Characteristics of DLSCs

This section presents the DC characteristics of DLSCs produced from batches A and B when measured in high (10^{-5} torr) and low (10^{-1} torr) vacuum. Figure 6.13 shows that the turn-on voltage for the device when tested in the dark has decreased from 0.6V to 0.1V.Figure 6.14 shows a semi-logarithmic plot of a typical current density versus voltage (J-V) characteristic of DLSCs (batch A) in the dark under high vacuum and in air for comparison. The dark current at high forward bias (+1V) decreases by some 6 orders of magnitude in vacuum. In reverse bias, the current decreases by about 2 orders of magnitude, resulting in a slight reversal of the rectification. Under vacuum, the minimum value of the current was observed close to zero bias rather than at 0.2V, indicating a much reduced displacement current.

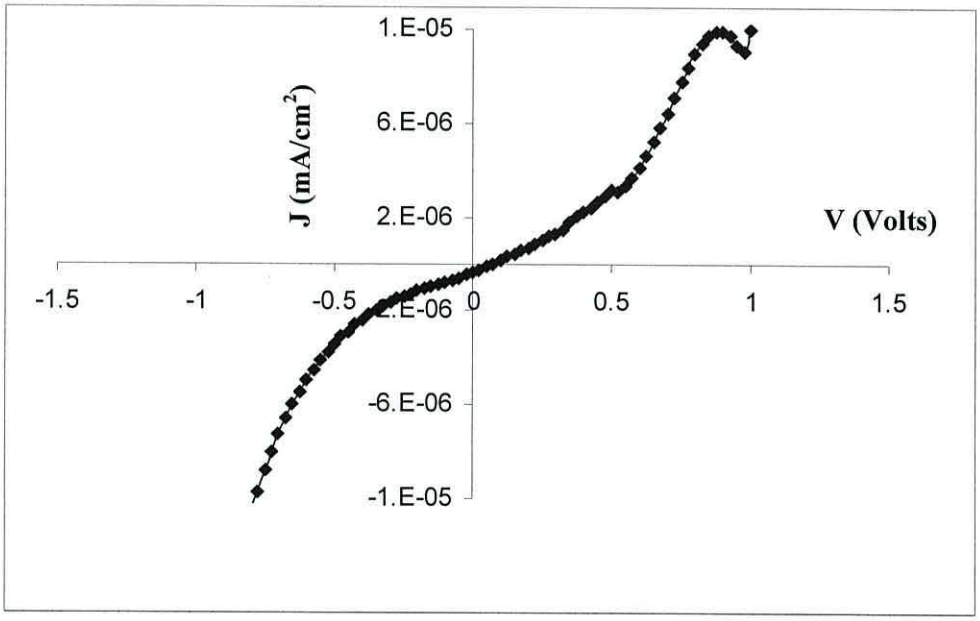

Figure 6.13 *J-V characteristics of DLSCs produced from batch A tested in the dark under high vacuum.*

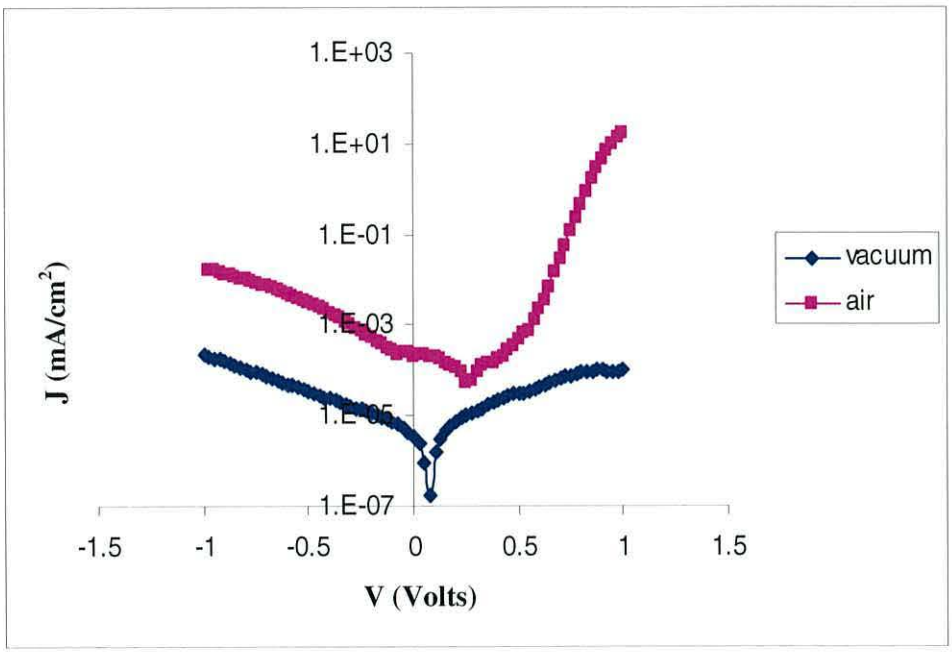

Figure 6.14 *Log J-V characteristics of DLSCs produced from batch A.*

Figure 6.15 shows the difference in current density versus voltage (J-V) characteristic of DLSCs from batch A under illumination in air and in vacuum. In contrast to illumination in the air, the device exhibits no photovoltaic behavior under vacuum. Furthermore, the characteristics are essentially symmetrical with device current some 4 to 5 orders greater than in the dark. The reverse current, under vacuum are an order of magnitude greater under illumination compared with illumination in air.

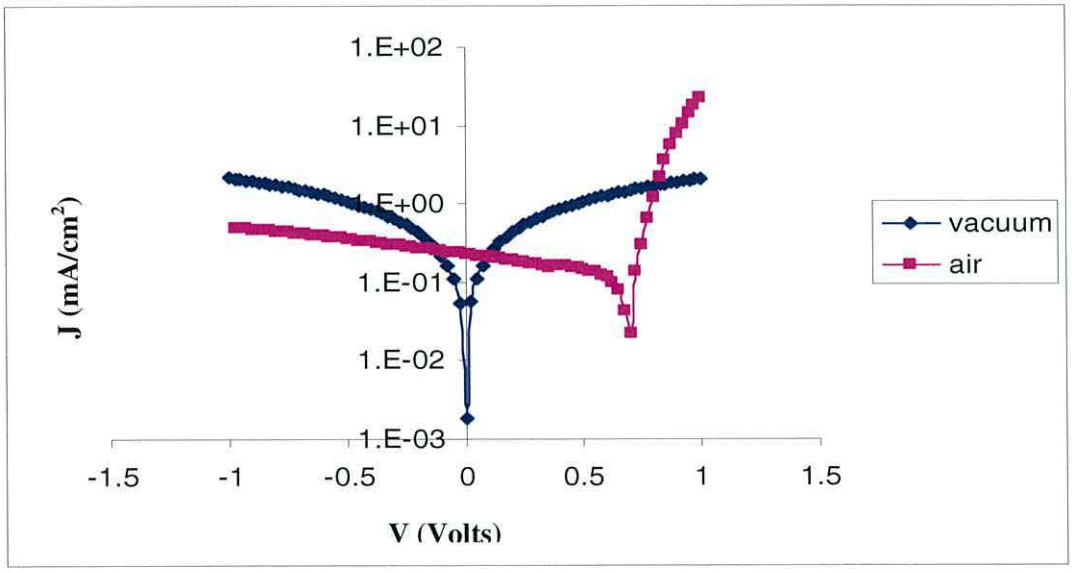

Figure 6.15 *Comparison of log J-V characteristics of DLSCs produced from batch A when illuminated with halogen lamp.*

Figure 6.16 shows that the J-V curve under illumination in vacuum is linear with the forward bias current equal to the reverse bias current which is consistent with photoconductivity in the bulk semiconductor.

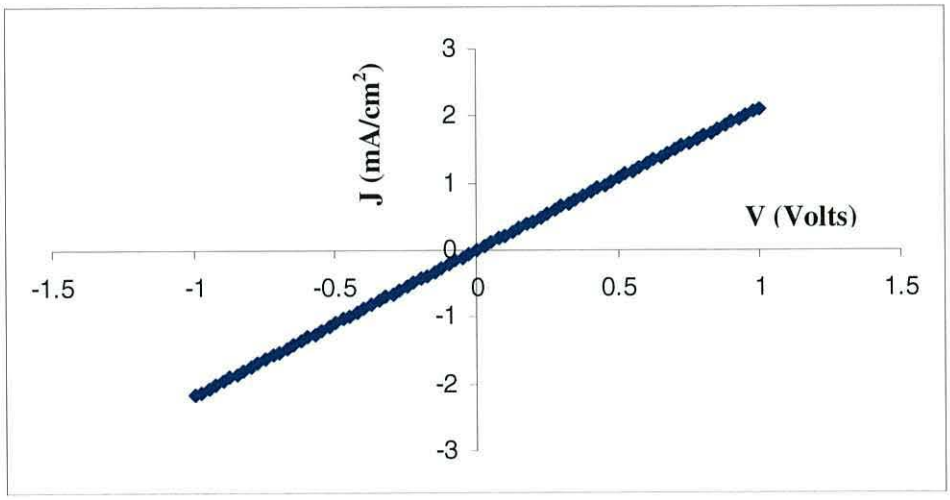

Figure 6.16 *J-V characteristics of DLSCs produced from batch A the light under high vacuum.*

Similar results were obtained for DLSCs from batch B when the devices were tested in vacuum with regard to the decrease of the dark current in vacuum, absence of photovoltaic effect, the reduction of turn–on voltage and the increase of photocurrent (see figures 6.17- 6.20).

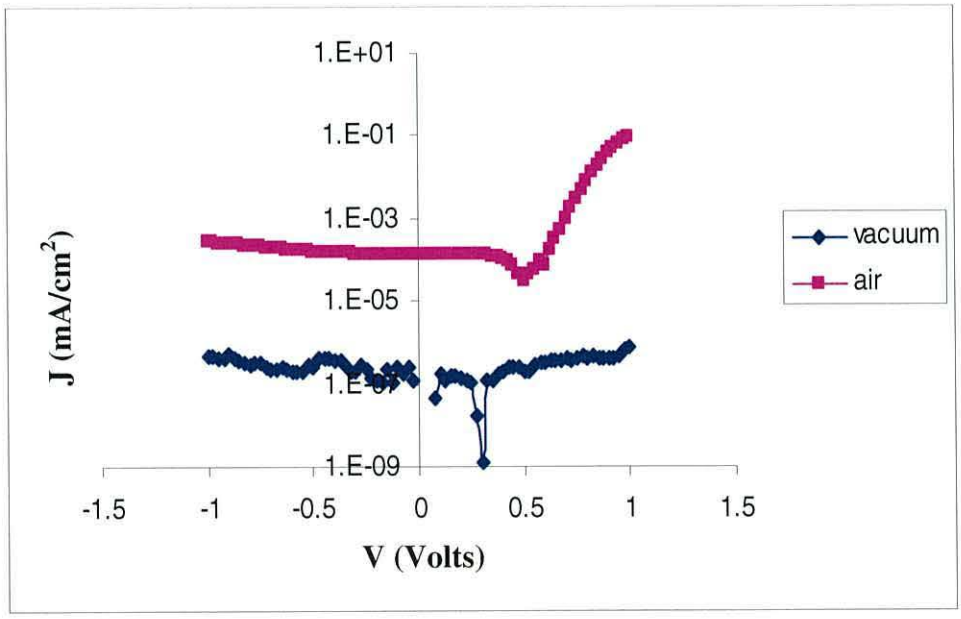

Figure 6.17 *Comparsion of* log *J-V characteristics of DLSCs produced from batch B in when measured in air and in vacuum.*

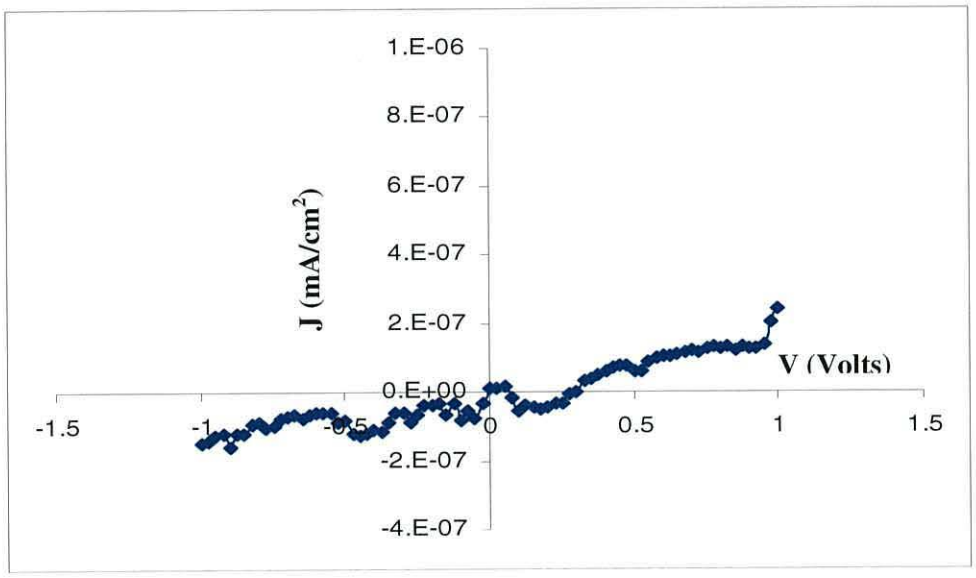

Figure 6.18 *J-V characteristics of DLSCs produced from batch A tested in the dark under high vacuum.*

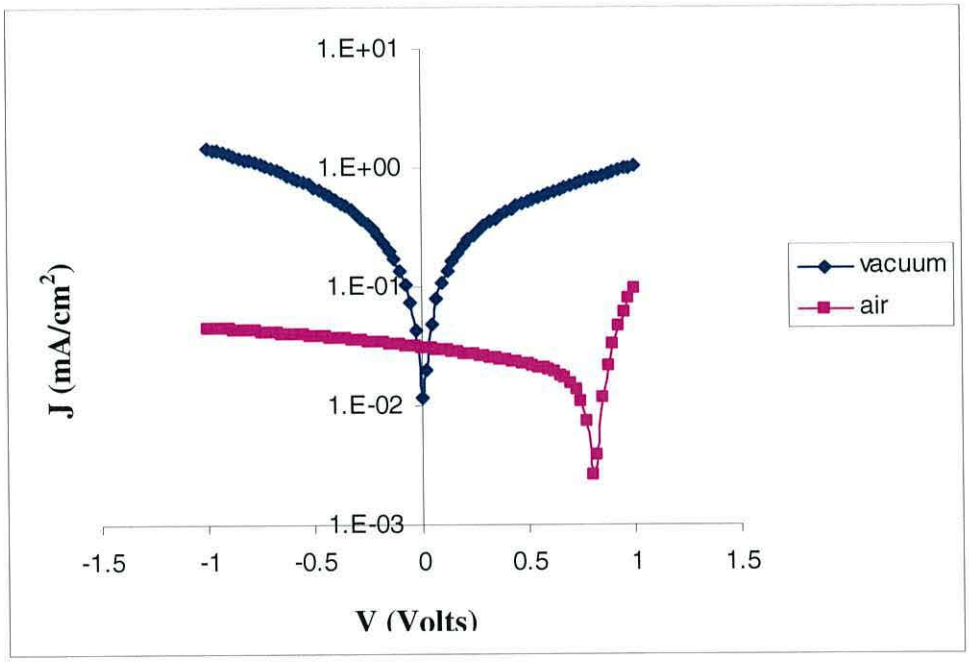

Figure 6.19 *Comparison of log J-V characteristics of DLSCs produced from batch A when illuminated with halogen lamp.*

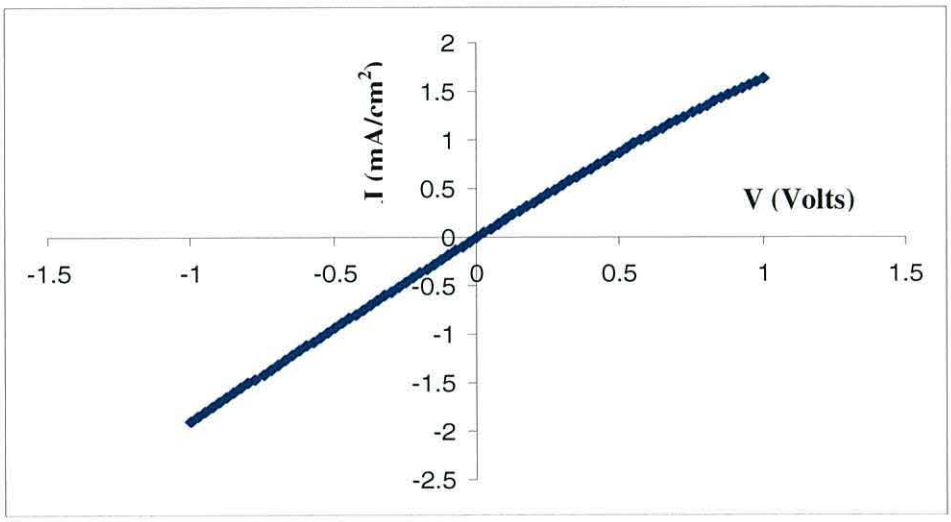

Figure 6.20 *J-V characteristics of DLSCs produced from batch B when illuminated.*

Figure 6.21 shows the loss of photovoltaic behavior and the growth of photoconduction with time in a DLSC from batch B when illuminated at 72 mW/cm^2 in a low vacuum. Voc was ~ 0.675V when the device had been illuminated for 30 seconds, but decreased to 0.3V and 0.125V after illumination for 120s and 210s respectively (Figure 6.22).

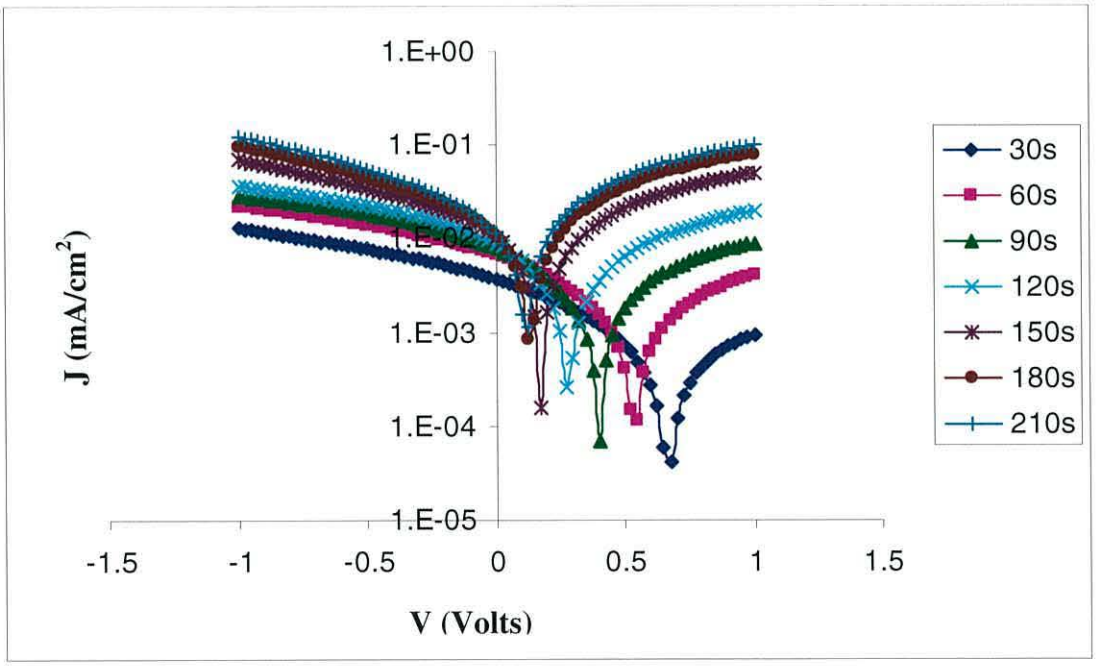

Figure 6.21 *J-V characteristics of DLSCs produced from batch B under low vacuum after illuminating the device for different length of time.*

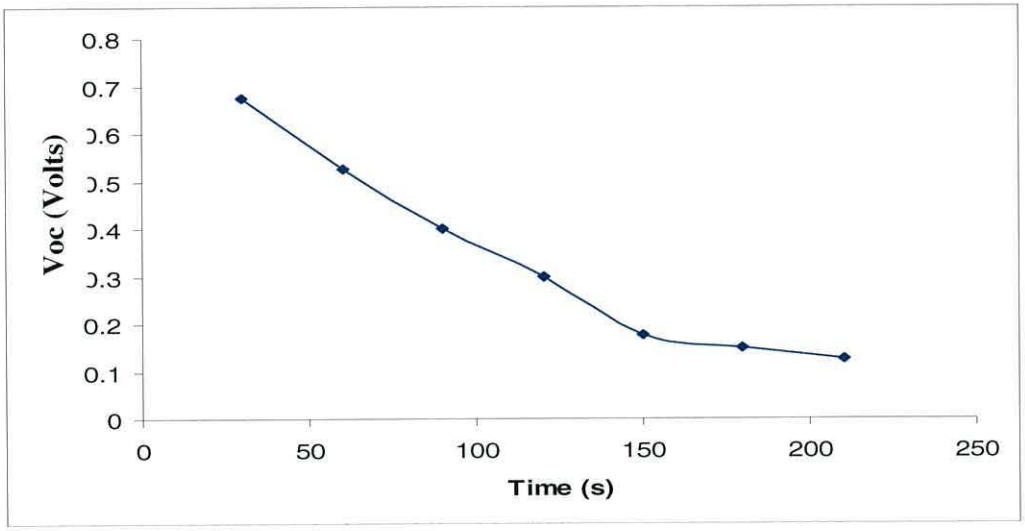

Figure 6.22 *Change in Voc of a DLSC produced from batch B while illuminating the device in a low vacuum.*

Figure 6.23 shows that both light and ambient- induced changes occur in the J-V properties of a DLSC from batch B. Initially I-V measurements on the DLSC were made in the dark. Then, the DLSC was illuminated and the I-V measurement repeated which took 10s. The device was then measured in the dark immediately after terminating the illumination. Finally, I-V measurements were made in the dark after introducing air into the chamber.

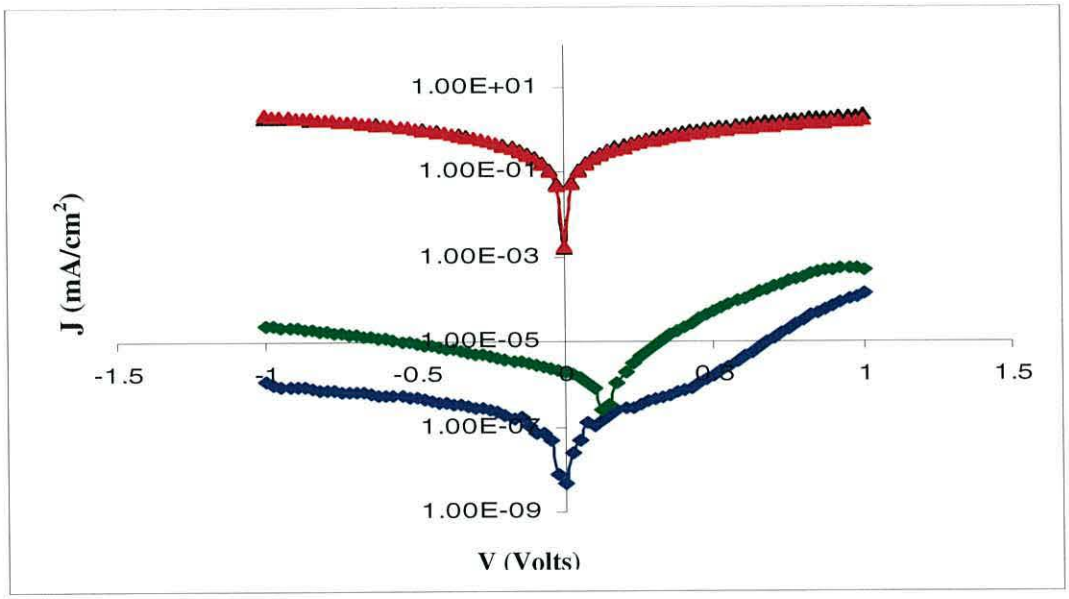

Figure 6.23 *I V characteristic of DLSCs produced from batch B under different condition: Initial dark current under vacuum (blue curve), under illumination in vacuum (dark curve),dark current in vacuum immediately after illumination (red curve) and dark current in air after illumination in vacuum (green curve).*

Figure 6.20 reveals that the dark current was very low under high vacuum and increases by around 5 orders of magnitude under illumination. After illuminating for 5s, the dark current measured subsequently remained high but decreased over time. Figure 6.24 shows the dark current decay at reverse bias with data points obtained every 5s. As can be seen, the dark current decreased from 0.4 to 1.5 $\times 10^{-5}$ mA/cm^2 over 500s.

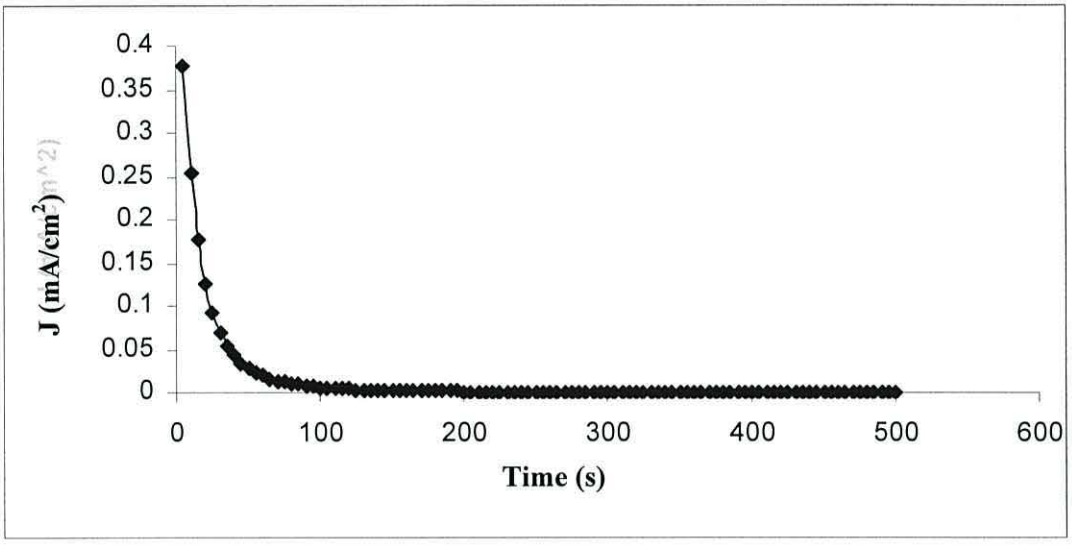

Figure 6.24 *Decaying dark current of batch B DLSCsdevice in vacuum after illuminating underr high vacuum*

Figure 6.25 shows the photocurrent of a DLSC from batch B measured in the air as a function of time. The results shown in the figure were obtained during two consecutive periods of illumination separated by a period of darkness. The photocurrent increased for a few seconds, reached a maximum value, then slightly decreased for hundreds of seconds. In the dark period, the photocurrent decreased within a few seconds. In the second stage of illumination, the photocurrent was higher than the photocurrent in the first stage as shown in the figure.

Figure 6.26 shows the photocurrent of a DLSC from batch B measured under high vacuum and high light intensity. Unlike the case for air, the photocurrent continues to increase during illumination, showing no sign of saturating. During the second period of illumination, the higher photoconductivity achieved during the initial period of illumination was maintained and then exceed

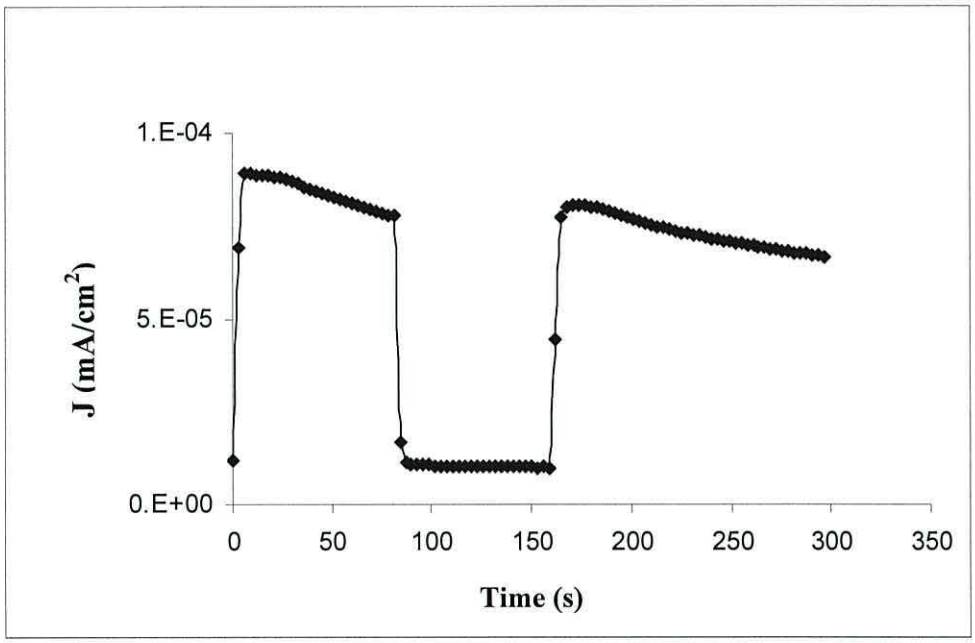

Figure 6.25 *Photocurrent for DLSCs produced from batch B illuminated at high light intensity in air. The light was switched off after about 90s and on again after a period of 90s.*

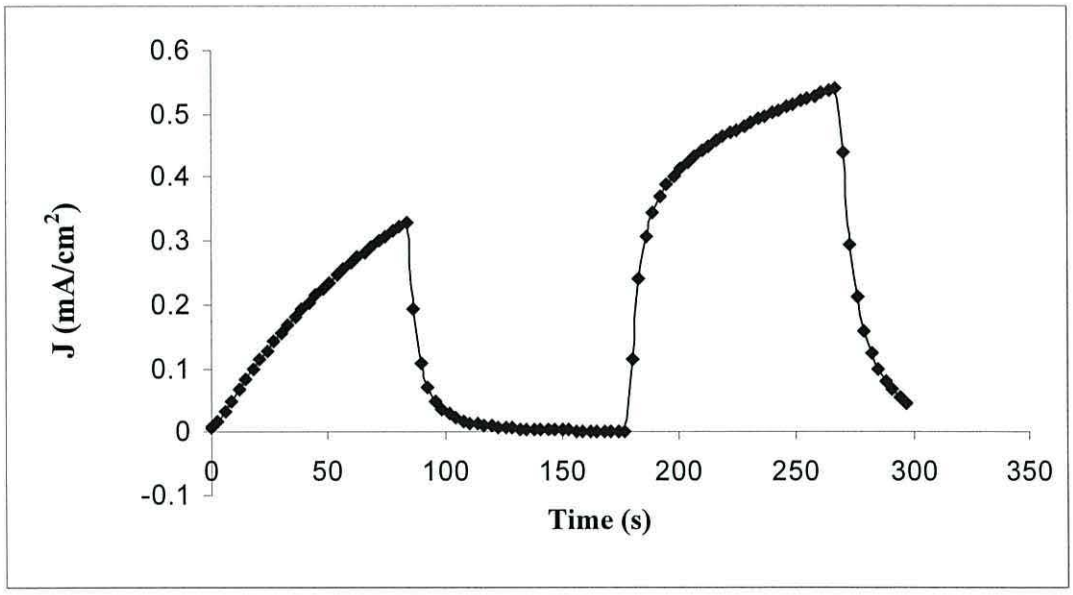

Figure 6.26 *Photocurrent for DLSCs produced from batch B illuminated at high light intensity in vacuum. The light was switched off after about 90s and on again after a period of 90s.*

6.3.2 Discussion

The properties of DLSCs have been shown to be sensitive to the ambient condition. Based on the J-V plot and literature evidence, these devices behave as a p-n junction. The position of the Fermi level in P3HT depends on the doping density which is related to the oxygen concentration in the P3HT film. The electrical properties of surface states of nc-TiO_2 are changeable with the existence of oxygen and water vapor. The dark current for double layer solar cells in vacuum was low because of the decrease in the conductivity of P3HT and nc-TiO_2 resulting from the absence of atmospheric oxygen and water vapor. For nc-TiO_2, this occurs when the Ti^{3+} state was formed from absorbing water vapor and P3HT when the oxygen concentration was low.

The decrease in the values of the dark current and turn–on voltage in DLSCs were also accompanied by a reduction of Voc. In vacuum, the band bending of P3HT decreases as a result of extraction of oxygen. The band bending and conductivity of nc-TiO_2 are dependent on impurities adsorbed on the surface as mentioned in the literature. Thus, the band bending of nc-TiO_2 was presumably dominated by the position of the Fermi level of P3HT and the formation of defect states which then affect the Voc of the DLSCs by reducing the band bending of nc-TiO_2 and P3HT until the depletion region disappears.

In air, the photocurrent is dominated by recombination at the interface. Under vacuum, the loss of photovoltaic behavior suggests that the photocurrent is dominated by transport through the bulk region of the device. From figure 6.24 the increasing current with time, suggests that trap states are becoming filled during the irradiation. Furthermore, the rapid rises to higher current during exposure indicates a long trapping time.

According to Walauble and Karsa [9] ,the dark current decreased when the solar cell was exposed to air from which they concluded that oxygen doping had a minor effect on the decrease in Voc under vacuum. However, the results presented in figure 6.23 demonstrate that this may be a false conclusion. Here it is seen that the dark current measured under vacuum immediately after illumination was high but decreased with time (figure 6.24). When air was introduced into the chamber a further decrease was observed, consistent with Walauble results [9]. However, figure 6.17 and 6.14 show that with no previous exposure to light and the dark current is

significantly lower under vacuum than in air. Additionally, under vacuum no rectification was observed. Together with capacitance –voltage measurements (chapter 8) we conclude that oxygen and other defects have a major effect on device performance

6.4 Summary

We have fabricated DLSCs based on the P3HT/nc – TiO_2 multilayer structure from two batches of sol-gel: A and B. The DLSCs produced from batch A exhibit better performance compared to DLSCs produced from batch B. This is due to the difference in nc-TiO_2 film morphology produced from the two batches. The DLSCs produced from batch A have efficiency of ~0.09%, Voc ~0.675V, and Jsc ~0.3mA/cm^2. The dark current was also affected by the morphology of nc-TiO_2. We also noticed an increase in the series resistance, in batch B therefore, the devices fabricated from the two batches have different turn-on voltages.

A p-n junction is formed between the nc-TiO_2 and P3HT because of differences in their Fermi levels. Therefore, the electric field formed at the interface between nc-TiO_2 and P3HT plays an important role in the process of exciton separation. The External Quantum Efficiency (EQE) of DLSCs was ~2% which was very low compared to the EQE of MEH/PPV/nc-TiO_2 solar cells. The charges generated by light in DLSCs were found to be limited by penetration and bad adhesion of P3HT into nc-TiO_2.

We also showed in this chapter the effect of atmosphere on the performance of DLSC. In vacuum, the dark current decreased, the photovoltaic behavior was lost so that Voc=0. Under illumination, significant photoconduction occurred. After illumination, the dark current is high initially and takes a time to decay. The higher dark current observed in vacuum after illumination decreases when air enters the vacuum chamber.

6.5 References

1. C. D. Grant, A. M. Schwartzberg, G. P. Smested, J.Kowalik, L. M. Tolbert, and J. Z. Zhang, *Synthetic Metals*, **132,** 197, (2003).
2. M. Y. Song, K. J. Kim, D. Y. Kim, *Solar Energy Materials and Solar Cells*, **85,** 31,(2005).
3. D. Gebeyehu, C. J. Brabec, F. Padinger, T. Fromherz, and S. Spiekermann, N. Vlachopoulos,F. Kienberger, H. Schindler and N. S. Sariciftci, *Synthetic Metals* **121**, 1549 (2001).
4. A. Watanabe, and A. Kasuya, *Thin Solid Film*, **483,** 358, (2005).
5. M. Wang, and Wang, *Solar Energy Material and solar cells,* **91,** 1782, (2002)
6. A. J. Breeze, Z. Schlesinger, and S.A. Carter, *Physical Reviews B.* **64**,125205, (2000),
7. U. Mengesha, T. Yoannes, *Solar Enery Materials and Solar Cells*, **90**, 3508, (2006) .
8. D. B. A. Rep, A. F. Morpurgo, T. M. Klapwijk, *Organic Electronics*, **4**, 201, (2003).
9. A. Watanabe, A. Kasuya, *Thin Solid Films*, **483**, 358, (2005).
10. P. Ravirajan. A. M. Peiro, M. K. Naseeruddin, M. Grätzal, D. D. Bradley, J. R. Durrant, and J. Nelson, *Journal of Physical Chemistry B,* **110** . 7635 (2006).
11. G. Gustafsson, O. Inganäs, M. Sundberg, C. Sevesosn, *Synthetic Metals*, **41,** 499, (1999)
12. A. F, Nogueira, M. A. D, Paoli, *Solar Energy Materials and Solar Cells,* **61,** 135, (2000).

Chapter 7
Electrical Characteristics of Three Layer TiO_2 Solar Cells (TLSCs)

7. 1 Introduction

In chapter 5, we described the preparation of nc-TiO_2 films from two batches of TiO_2 sol-gel. Despite nominally identical preparation conditions, the films had different morphology, topography and particle size. This was attributed to the difference in the composition of the TiO_2 sol-gel in the two cases.

Twenty five P3HT/dye/nc-TiO_2 solar cells described here as Three Layer Solar Cells (TLSCs) were fabricated from the two batches. The current–voltage (I-V) characteristics of these devices were measured under different conditions both in the dark and under illumination with a halogen lamp. The main variables were light

intensity, temperature, irradiation time and device age. The external quantum efficiency was measured for the TLSCs to extract the conversion efficiency at AM1.5. The effect of vacuum on solar cells parameters was investigated and compared with the results obtained from experimenting in the air.

7.2 Electrical Measurements in the Air

7.2.1 DC Characteristics of TLSCs

The I-V characteristic of the TLSC batch A was measured as described in section (4.3) by applying a voltage to the gold electrode, starting at +1V and incrementing in steps of 0.025 up to -1V. Figure 7.1 is a linear plot of the typical current density versus voltage (J-V) characteristic of the cell. Figure 7.2 shows the same data plotted in semi logarithmic form to enhance the low current regime. The first point of interest is the strong rectification observed in the dark ~3000 at $1 \pm 1V$. This is partly achieved by a low reverse current, which is smaller than observed in batch A DLSCs.

Under forward bias in the dark, the device starts to conduct strongly at a turn-on voltage ~0.65V. Under illumination with a halogen lamp ($72mW/cm^2$), the device produced an open circuit voltage, Voc, ~0.73V a short circuit current density, Jsc, ~$2.3mA/cm^2$ and a fill factor, FF, 49%. The power conversion efficiency from equation (2.17) under the experimental conditions was 1.1% and so lower than observed with dye-sensitized nc-TiO_2 /electrolyte solar cells, which have much higher Jsc. DLSC and TLSC produced from batch A have the same value of turn on-voltage and differ from each other with regard to the value of Voc by ~ 0.1V. They significantly differ from each other with regard to the value of short circuit current density which is an order of magnitudes greater in the TLSCs.

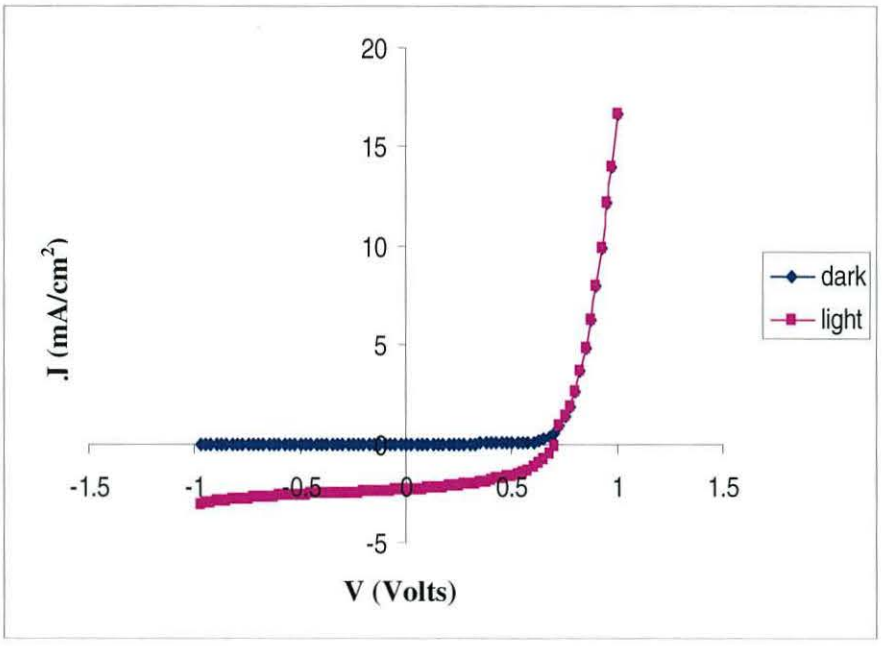

Figure 7.1 *J-V characteristics of a TLSCs produced from batch A.*

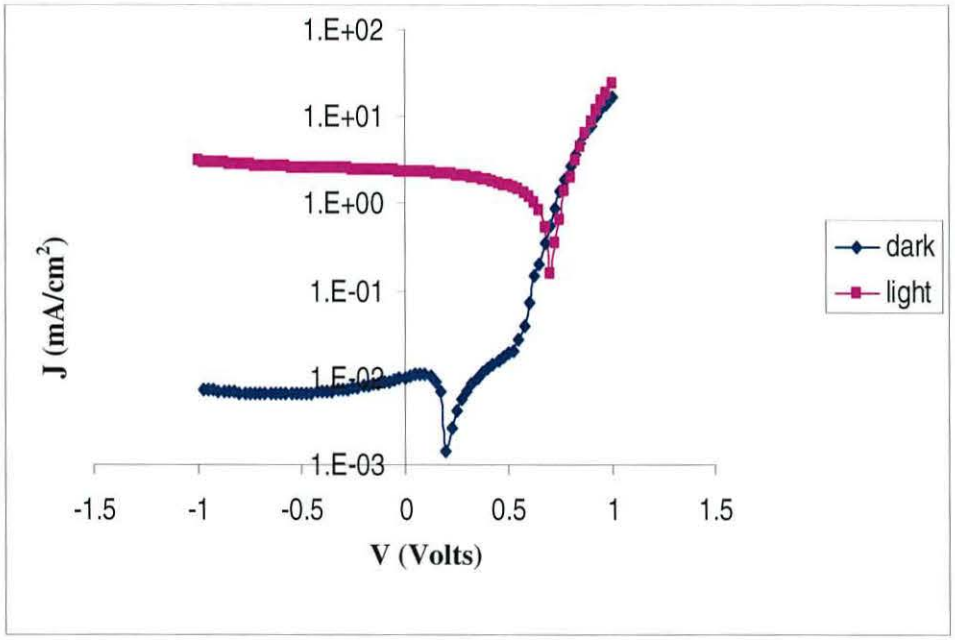

Figure 7.2 *Log J-V characteristics of a TLSCs produced from batch A. The data is the same as in figure 7.1.*

The I-V characteristics for batch B TLSCs are shown in linear form in figure 7.3 and semi logarithmic form in figure 7.4. The dark rectification ratio at ±1V was 500 and so much lower than observed in batch A TLSCs. The forward current in the dark is significantly lower in batch B TLSCs, resulting in a large apparent turn-on voltage ~0.8V in the linear plot of figure 7.3. This behaviour is consistent with the presence of a series resistance in the device. Under illumination, this cell generated an open circuit voltage, Voc~0.9V, and short circuit current density, Jsc, 0.23 mW/cm^2 and fill factor of 34% leading to a power conversion efficiency of 0.2%. These parameters are similar to those quoted for P3OT/dye/nc-TiO_2 solar cells[1]. Comparing the parameters of batch B DLSCs with batch B TLSCs, there is only a slight difference in Voc and turn on voltage of only 0.03V. However, Jsc of batch B DLSCs was very lower than Jsc of batch B TLSCs.

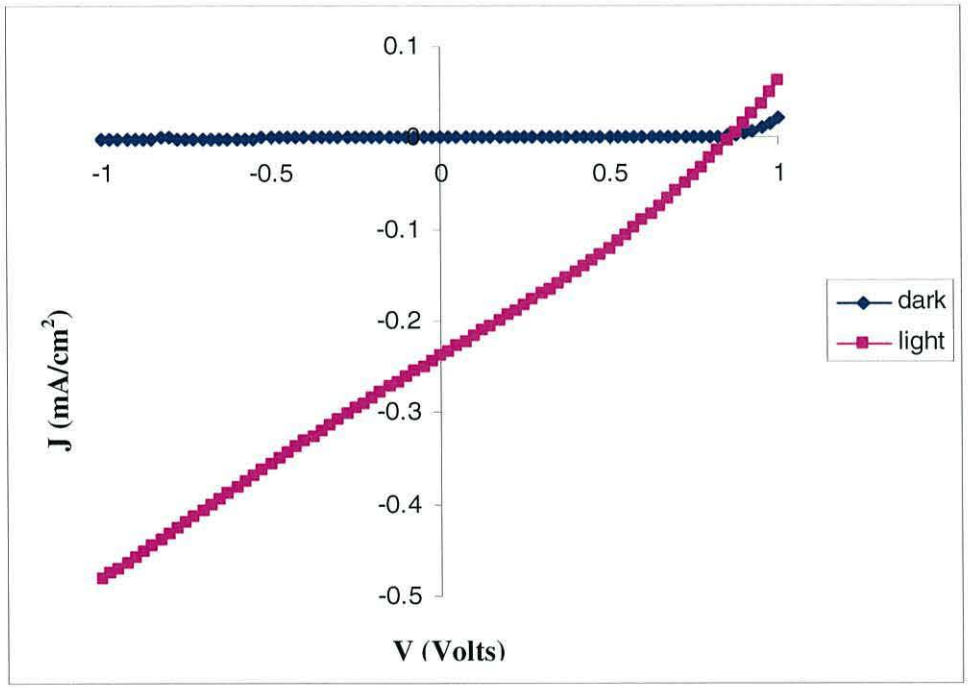

Figure 7.3 *J-V characteristics of a TLSCs produced from batch B.*

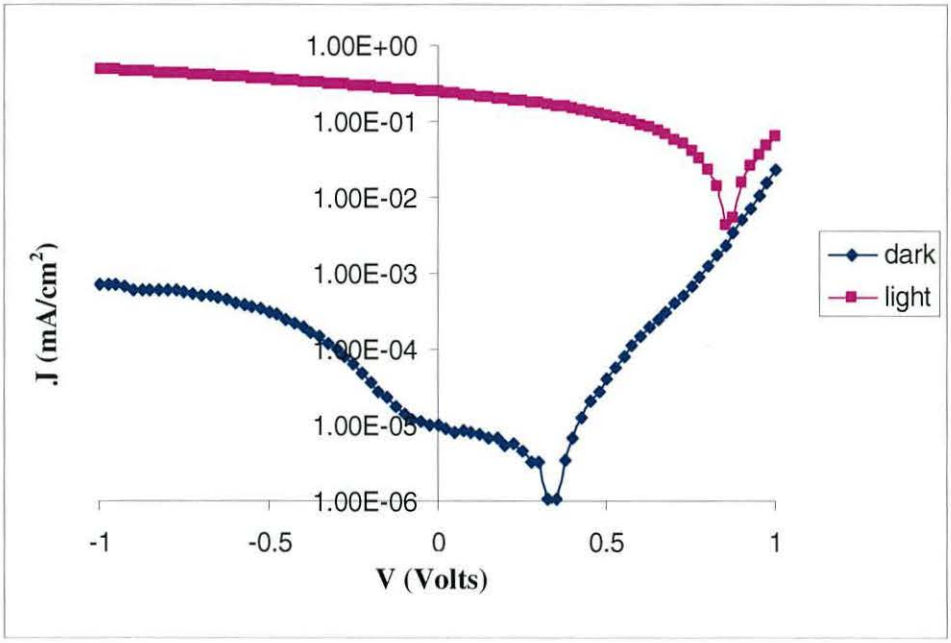

Figure 7.4 *Log J-V characteristics of a TLSCs produced from batch B The data is the same as in figure 7.3.*

In total 25 devices from batch A and from batch B were investigated in detail and their properties collected in table 7.1 which gives the mean and standard deviations of Jsc, Voc, FF and η_e for the devices. As can be seen, the differences observed between the two devices in figure 7.1 and 7.4 are statistically significant and characteristic of the two batches.

Parameter	**Batch A**	**Batch B**
J_{SC} (mA/cm^2)	2.3±0.006	0.23±0.0006
V_{OC} (V)	0.725±0.02	0.88 ±0.18
FF (%)	43.5 ±3.8	34 ±4.4
η_e (%)	1±0.08	0.2 ±0.01

Table 7.1: *Mean and standard deviations of the short circuit current density, J_{SC}, open-circuit voltage, V_{OC}, fill factor, FF, power conversion efficiency, and η_e for the devices produced from batches A and B.*

The information is displayed as histograms in figure 7.5 to show the full range of behavior observed in the two batches of TLSCs. The better performance of batch A TLSCs is clearly confirmed by the higher efficiencies observed in figure 7.5d.

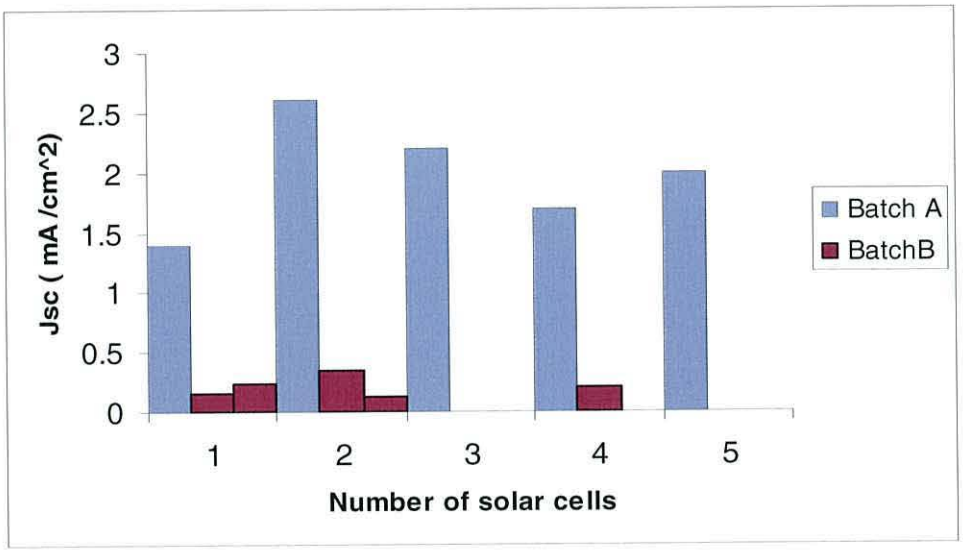

Figure 7.5(a) *Histogram of Jsc distribution obtained for 25 solar cells produced on different substrate.*

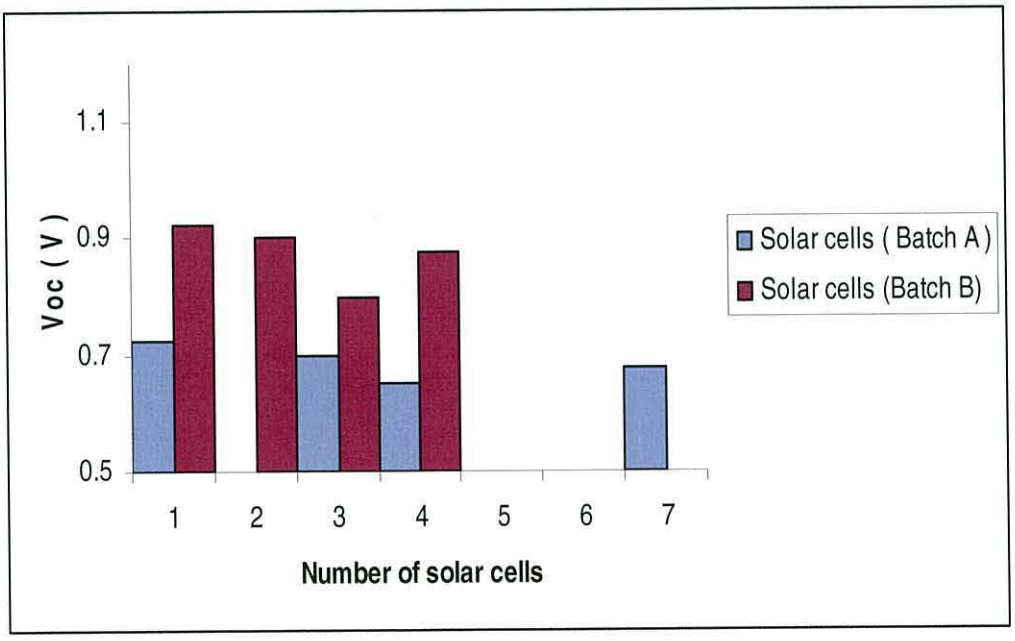

Figure7.5(b) *Histogram of Voc distribution obtained for 25 solar cells produced on different substrates.*

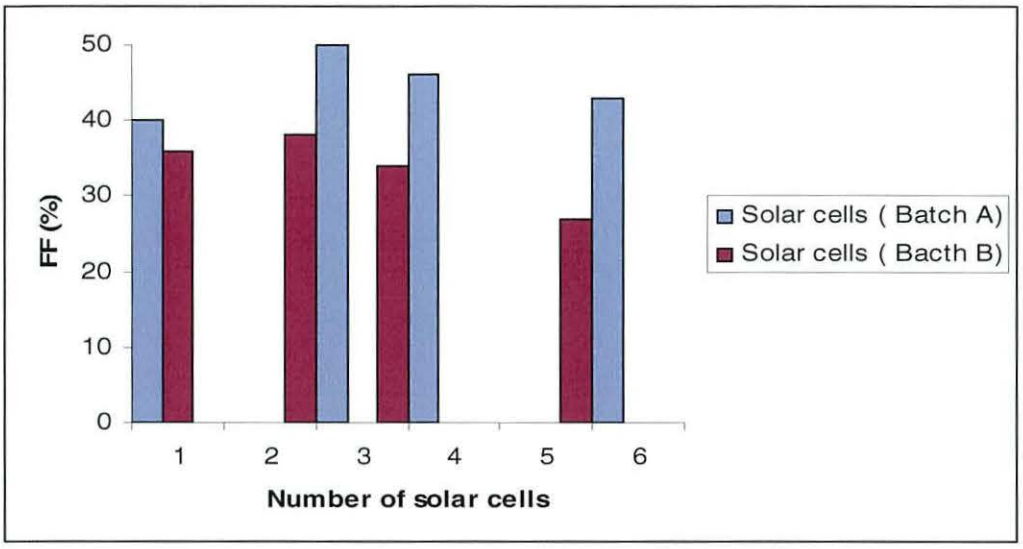

Figure7.5*(c) Histogram of FF distribution obtained for 25 solar cells produced on different substrates.*

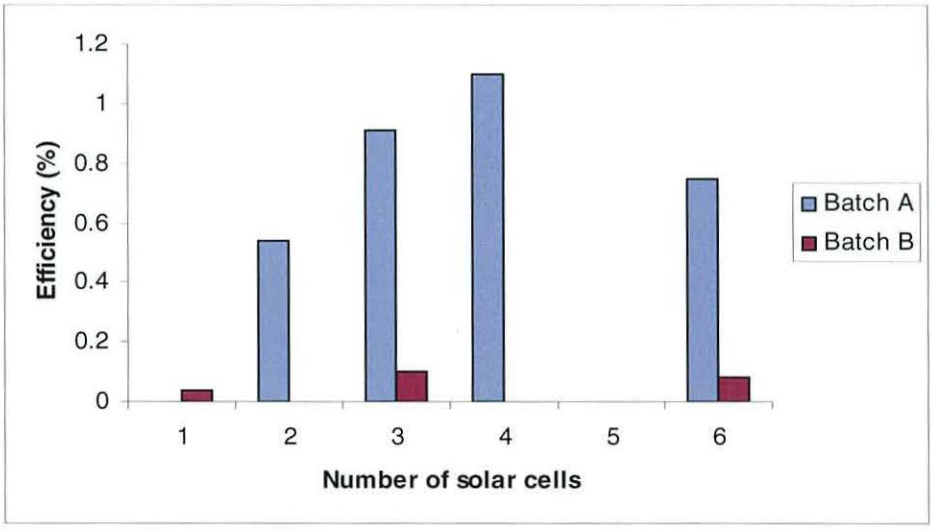

Figure7.5*(d) Histogram of Efficiency distribution obtained for 25 solar cells produced on different substrates.*

7.2.2 Optical Absorption of Materials used for Constructing Batch A TLSCs

The UV-visible absorption spectra of the materials used for constructing the batch A solar cells are given in figure 7.6. The absorption edge of the nc-TiO_2 film is ~ 420 nm but after soaking in the dye solution, the absorption edge shifts to ~600nm with a peak occurring at 520 nm as result of dye absorption. So the dye layer absorbs in the same range as P3HT. When P3HT was spin coated onto the dye-coated nc-TiO_2 the resulting composite showed good absorption over the range 600nm down to 350nm. It shows an increase of absorbance compared with the dye/nc-TiO_2 film in the visible region. The absorbance of nc-TiO_2/dye/P3HT was higher than the absorbance of P3HT/nc-TiO_2 indicating a difference in light harvesting between batch A DLSCs and TLSCs.

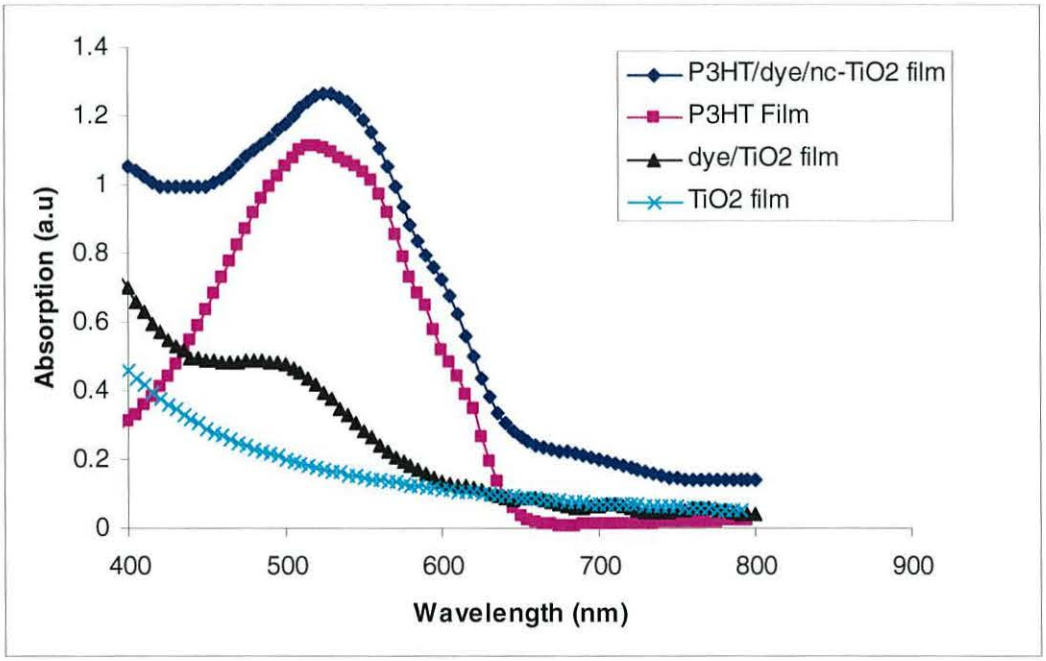

Figure 7.6 *The optical absorption of a P3HT film and nc- TiO_2 dye/nc- TiO_2 , P3HT/dye/nc- TiO_2 films.deposited deposited on glass substrate and compact TiO_2 /SnO2 /glass substrate.*

7.2.3 External Quantum Efficiency of Batch A TLSCs

The External Quantum Efficiency (EQE) for a typical device was obtained by measuring the zero-bias photocurrent as a function of wavelength, λ (Figure 7.7). The value of EQE varied between 11% and 16% for the wavelength ranges from 380nm to 580nm. The wavelength dependence of the EQE and the absorption spectrum of the batch A TLSCs were similar and results from the absorption of the light in the P3HT and dye layer. The EQE of TLSCs is higher than achieved in non-dye-sensitized TiO_2-polymer solar cells employing thinner TiO_2 layer [2] and polymers with greater hole mobility [3]. Following Wienk et al [4] and others, we estimated the short-circuit current density J_{SC} of batch A TLSC under solar conditions by numerically integrating the overlap of the EQE plot with the solar AM1.5 spectrum using equation (2.23)

In figure 7.8 we plot the contribution Jsc (λ) to the total current at each wavelength. The integral is determined from the area enclosed by the plot leading to Jsc=2mA/cm^2. Multiplying this value of Jsc with Voc=0.735V and Fill Factor of 0.49 yields a calculated efficiency ~0.69% for batch A TLSCs for simulated solar cells conditions which is a amongst the highest efficiency values so far reported for dye-sensitized solar cells based on nc-TiO_2 and poly(3-alkylthiophene) [1, 5].

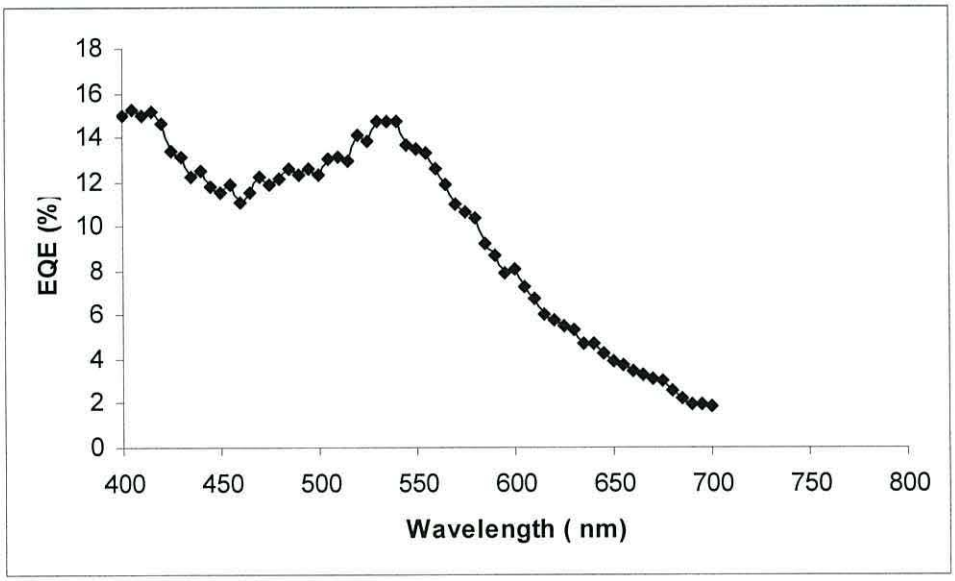

Figure 7.7 *External quantum efficiency of TLSCs produced from batch A.*

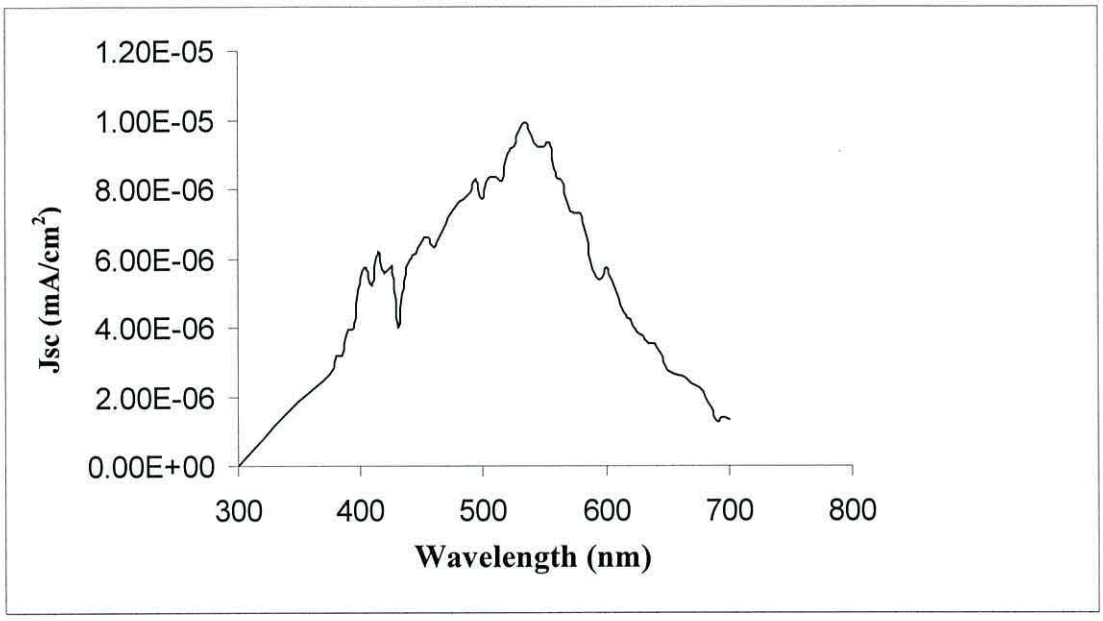

Figure 7.8 *Short circuit current density Jsc of a TLSCs produced from batch A as function of wavelength.*

7.2.4 Discussion

Before explaining the difference in efficiency of TLSCs produced from the two batches, we need to consider the energy levels of the materials used to construct the devices. The optical properties of batch A TLSCs discussed in this chapter are readily explained by drawing on the energy diagrams presented by [6]. Such a diagram is presented in figure 7.9. Relative to the vacuum level, the conduction and valence bands of the nc-TiO_2 are believed to lie at ~ -4eV and -7.2eV respectively giving an energy gap of 3.2eV close to that determined by STS (section 5.3.4). The HOMO and LUMO levels for P3HT are at -3eV and -4.9eV respectively, yielding an optical gap of 1.9eV, which is again consistent with the optical absorption edge of P3HT seen in figure 7.6. The HOMO and LUMO levels of the dye will depend on its molecular structure, with Gebeyehu et al. [1] placing them at ~ -5.5 eV and ~-3.8eV. The LUMO of the dye is intermediate between the LUMO of P3HT and the nc-TiO_2 conduction band. Also, the HOMO of the dye is intermediate between the HOMO of P3HT and the nc-TiO_2 valence band. The high work function of gold, ~5.1eV, ensures a good Ohmic contact for holes from the P3HT, while the lower work function of the SnO_2:F contact (4.5eV) ensures facile electron transport to and from the bottom contact.

We showed in chapter 6 that in the absence of sensitizing dye, the P3HT/nc-TiO_2 interface appeared to have an associated depletion region, suggesting that band bending occurs in one or both sides of the interface. However, the dye affects on band bending by creating new states in the band gap of nc-TiO_2. This is confirmed when water vapor was adsorbed on the nc-TiO_2 surface creating defect sites (OH). In addition, there was no direct contact between the nc-TiO_2 and P3HT because of the intermediate dye layer. Therefore, band bending at the interface may be ignored in this case .That was observed by using AC measurements (see chapter 8)

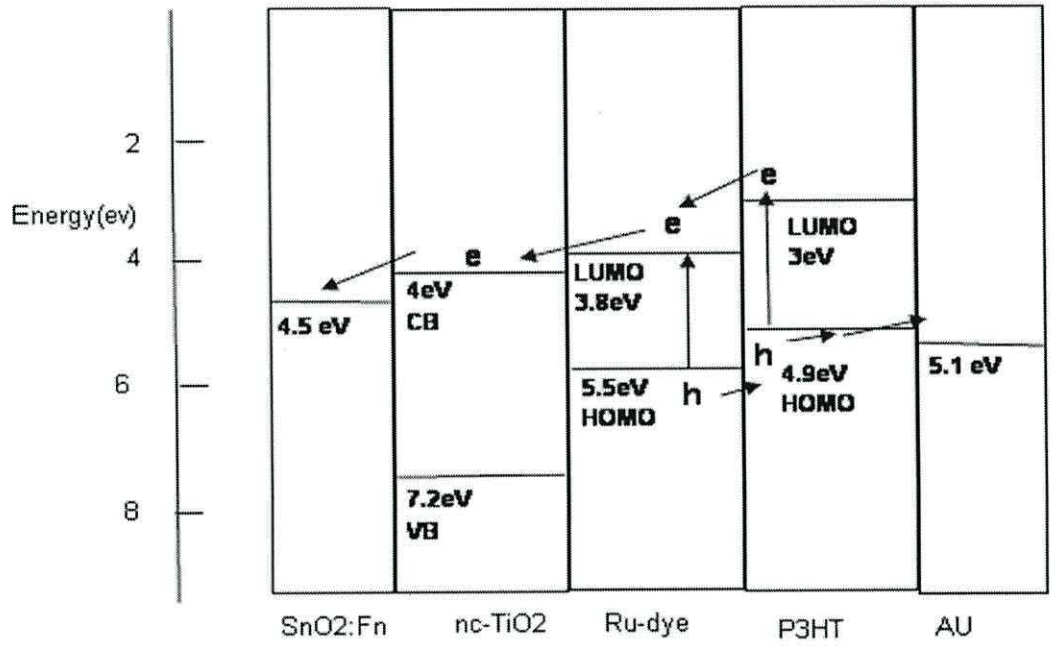

Figure 7.9 *Illustration of the energy level diagram for TLSCs with formation of charges passing through junction. These charges were transported to the electrode giving the external current.*

In the dark, the IV characteristics show that our solar cells behave as an ideal diode with good rectification. Under forward bias conditions, holes are injected into the HOMO of P3HT from the gold electrode. Also, electrons are injected from the bottom electrode into the conduction band of nc-TiO_2 film. Thus, the forward current would be expected to be high because the injection of charge carriers from the electrodes to P3HT is energetically favored. Under reverse bias, electron injection from the gold electrode to the LUMO of P3HT and holes from SnO_2:F to the

conduction band of nc-TiO_2 are not favored. This interpretation of course only applies because we assume no band bending at the P3HT/nc-TiO_2 interface because it is suppressed by the intermediate dye layer. The dark current passing through the P3HT/dye/nc-TiO_2 interface is dominated by transport across this interface. The photogeneration process relies on photon absorption by both the dye and P3HT. The excitons generated close to the interface will dissociate. Electrons from the P3HT and/or dye will transfer to the conduction band of the nc-TiO_2. Holes generated in the P3HT together with those released into P3HT in order to regenerate the dye are transported to the gold electrode

As indicated in Chapter 3, Voc is expected to correspond to the energy difference between the conduction band of nc-TiO_2 and the HOMO of the hole conductor. However, there is much discussion as to the applicability of this rule of thumb. In our case the batch A cells gave Voc ~ 0.73V while Voc for batch B was ~ 0.88V. This difference, we can attribute to differences Rsh through consideration of equation 2.13. The Rsh of TLSCs produced from batch B and A were estimated by using slope of J-V curve at Voc. The batch A TLSCs has a lower Rsh in comparison with Rsh of batch B TLSCs. This might depend on the quality of the contact between dye/nc-TiO_2 and P3HTwhich is affected by the morphology of nc-TiO_2 and the interfacial area at junction.

The difference in short circuit current density of TLSCs is attributed to a difference in the series resistance of these devices (see equation 2.14), which is confirmed from an estimate of the slop of the I-V current at Jsc (Figure 7.1 and 7.3). This difference depends on the morphology of nc-TiO_2 produced from batch B which affects the efficiency of devices. The have sharply pointed of batch A nc-TiO_2 allows better penetration and pore-filling by P3HT and dye. This is confirmed by estimating the interfacial area in TLSCs using capacitance measurements (see chapter 8). This arguments agrees with results published in 2005 [7] by Menda et al. He reported that not only complete interfacial contact, achieved by complete wetting of the TiO_2 surface is essential but also the complete filling of pores is crucial for high efficiency cells. This appears in the TLSCs produced from batch B where the topographical feature of nc-TiO_2 film is round and smooth. In this case, where pores are not completely filled with the hole-conductor, the path for the electrons to reach the bottom electrode is longer. As more hole-conductor material is found in the

nanopores, a shorter pathway for electrons to the SnO_2:F electrode becomes available.

However, the good penetration of P3HT was not the only factor given a high short circuit current density in TLSC (batch A). The dye also plays an important role to reducing: a)the recombination process of excitons at the junction, b) improving adhesion between P3HT and nc-TiO_2, c) increasing the wetting area between them, and d) increasing harvesting of light falling on the device. Thus, the performance of TLSCs (batch A) is better than the DLSCs (batch A). This result agrees with the device by Gebeyehu [1] but our in TLSCs the small series résistance is much lower than in their devices.

Finally, the TiO_2/dye/P3HT heterojunction is also expected to control the dark I-V characteristics of the respective devices. Thus the reduction from batch A to batch B in the voltage required to observe the onset of forward current in the dark may be explained by a reduction in the series resistance of the nc-TiO_2 layer and improved penetration of P3HT. The reduction in the onset-voltage for forward conduction observed for batch A, will inevitably reduce V_{OC} since, to a first approximation, V_{OC} is the voltage at which the photo-induced current equals the dark forward current.

7.3 The Effect of Ambient Conditions on Batch A TLSCs

Ambient conditions are known to affect the performance of solar cells. In the following, we report the effect of temperature and irradiation conditions on the solar cells produced from batch A.

7.3.1 Temperature Dependence of Solar Cells Parameters

This section examines the effect of temperature on solar cell parameters. Figure 7.10 shows the current-voltage characteristics of devices fabricated from batch A as a function of temperature. As seen both Jsc and Voc decrease with increasing temperature. The actual dependences on temperature are shown in figure 7.11 and 7.12 from which it is seen that Voc remains relatively constant at ~0.7V until ~ 330K when it decreases to ~0.43V at 397K. In addition, the slope of the I-V curve in the third quadrant also decreases which can be attributed to a decrease in the shunt resistance Rsh. Furthermore, in the first quadrant of the I-V plot, there was an initial

small increase in the slope of the curve as the temperature increased but it then decreased as the temperature continued to increase.

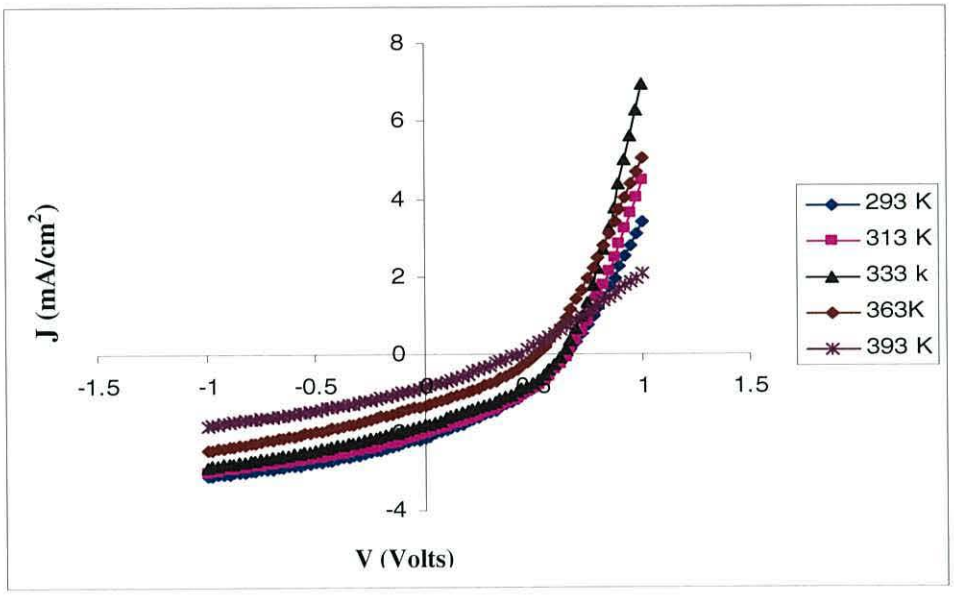

Figure 7.10 *I-V characteristics of TLSCs produced from batch A under illumination plotted as function of temperature.*

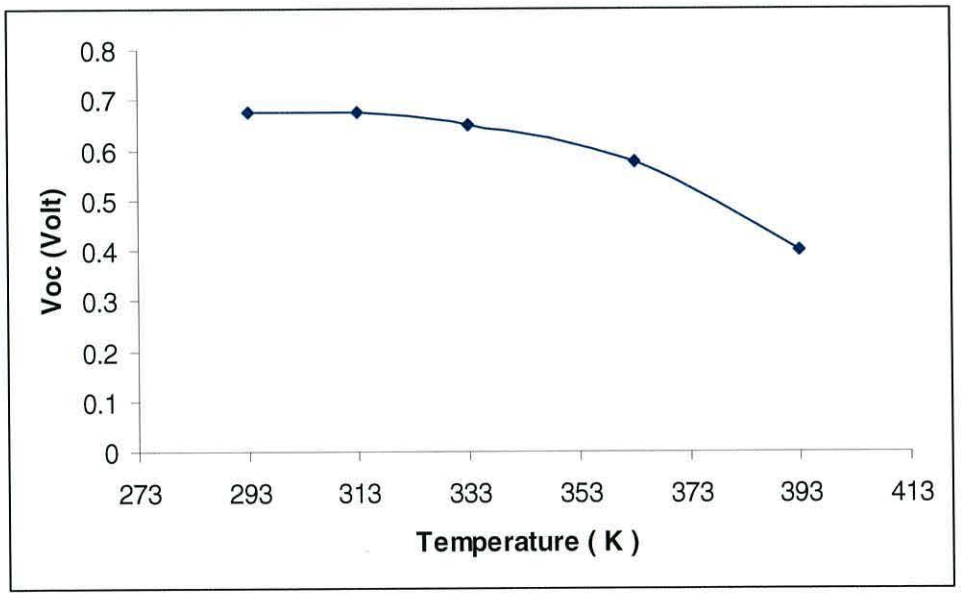

Figure 7.11 *The variation of Voc with temperature for a TLSC produced from batch A.*

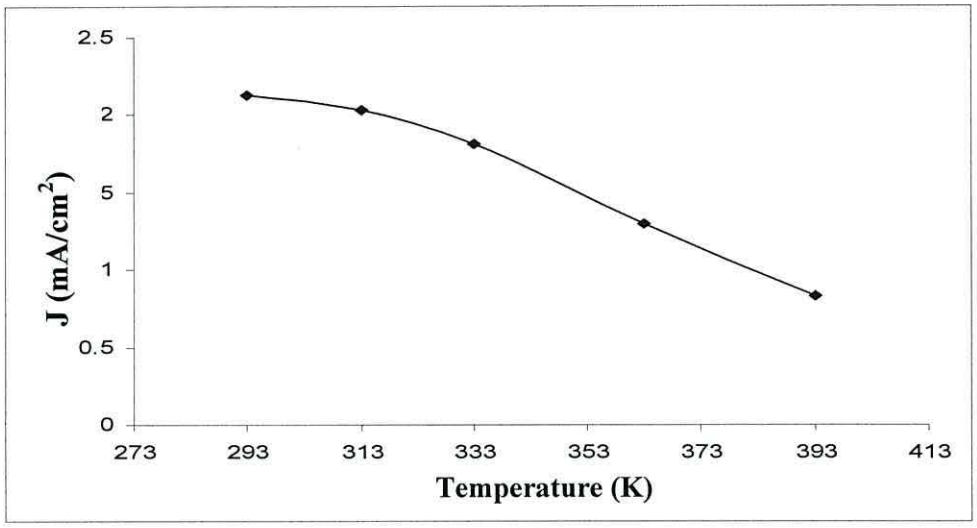

Figure 7.12 *The variation of Jsc with temperature for a TLSCs produced from batch A of TLSCs produced from batch A with temperature.*

7.3.2 Stability of Solar Cells during Irradiation

The stability of batch A TLSCs solar cells under illumination with a halogen lamp was monitored over a period of time. The values of Voc and Jsc were recorded while the device was subjected to light of intensity 230 mW/cm^2. The results are shown in figure 7.13 and 7.14. Following an initial small decrease both the short circuit current density and open circuit voltage remained almost constant during 4800 seconds of irradiation. In total, Jsc decreased by 0.5mA/cm^2 during illumination while Voc decreased by ~ 0.18V.

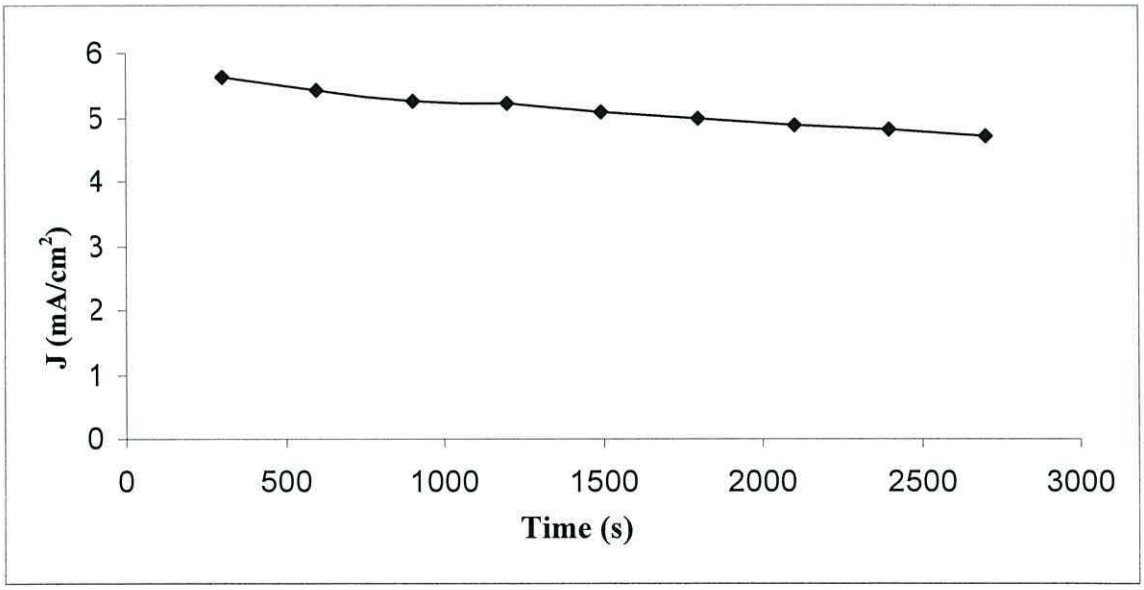

Figure 7.13 *Jsc as function of photo irradiation time for TLSCs produced from batch A.*

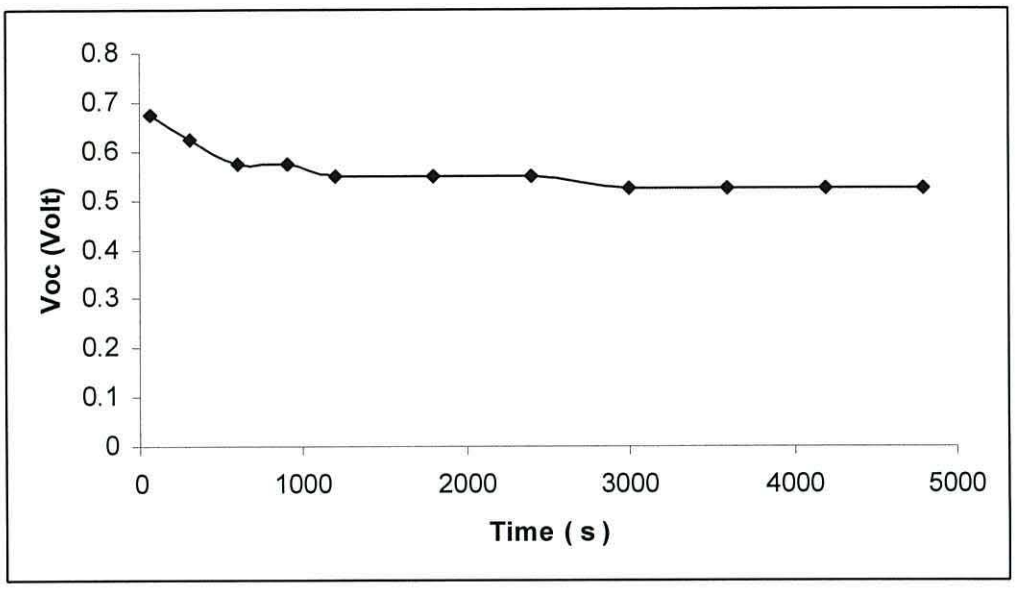

Figure 7.14 *Voc as function of photo irradiation time for TLSCs produced from batch A.*

Following this initial test, different pixels on the same device substrate were tested on four further occasions over a period of twenty days. It is necessary to mention here though that in between tests solar cells were stored in air in the dark. Figures 7.15 and 7.16 show the resulting changes in Jsc and Voc under 72 mW/cm^2 light intensity . As can be seen, the device exhibits good stability with Jsc increasing slightly for 10 days but decreasing slowly therefore. Voc on the other hand, decreases slowly over the same period.

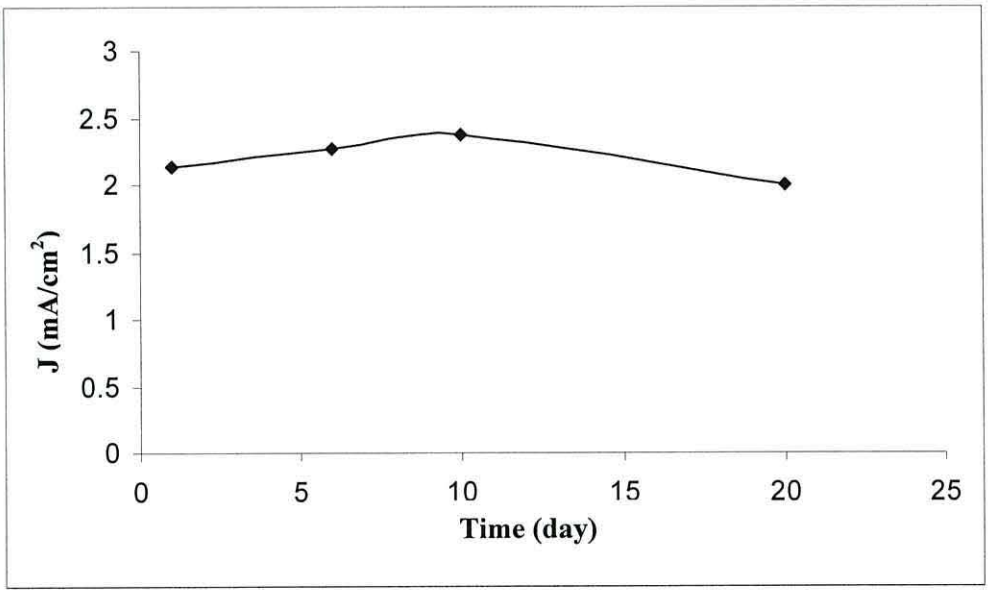

Figure 7.15 *Jsc as a function of solar cells age time for TLSCs produced from batch A.*

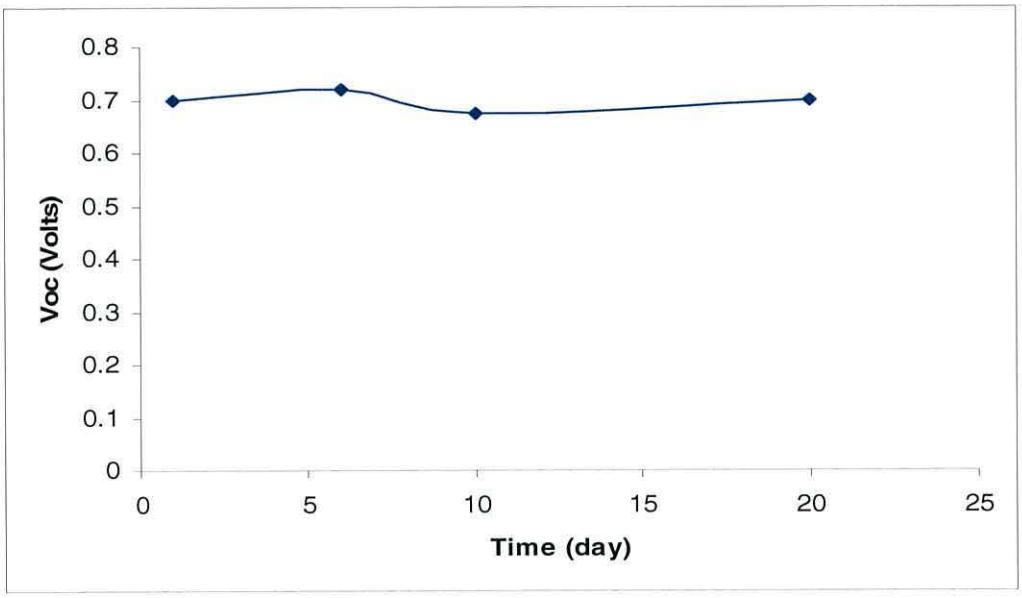

Figure 7.16 *Voc as a function of solar cell age time a TLSC produced from batch A.*

Although noting the effect at time on Voc and Jsc are important for establishing the operating limits of the device, of greater significance is the output power. This is shown in figure 7.17 where the output power is plotted as a function of the forward voltage applied to the device. Over the first 6 days, the output power increased slightly to 0.8mW/cm^2 reflecting the increase in Jsc. The maximum output power then decreased reaching 0.45mW/cm^2 after 20 days.

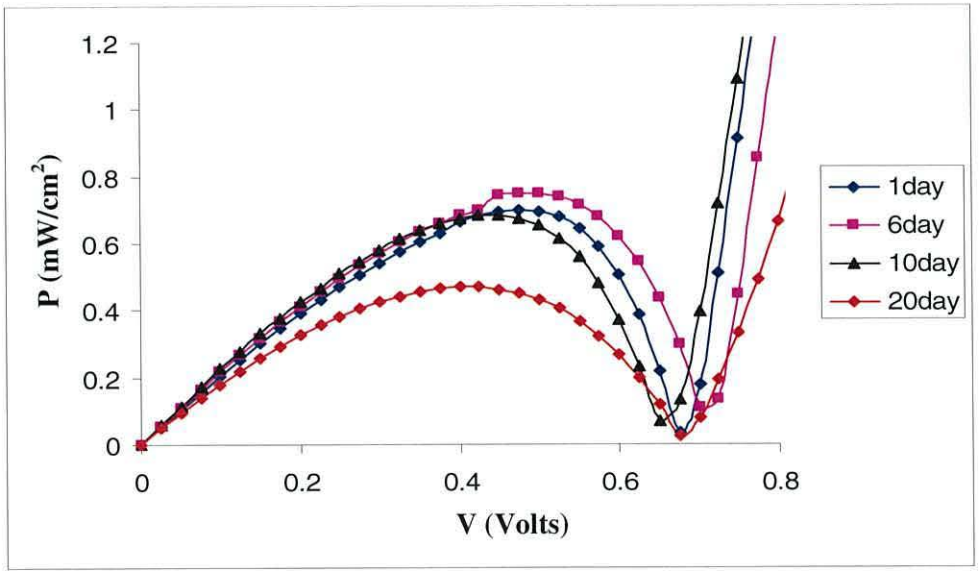

Figure 7.17 *The output power versus voltage of age time for TLSC produced from batch A.*

7.3.3 The Effect of Light Intensity on Solar Cells Parameters

The effect of light intensity on the operation of a batch A TLSCs was studied by varying the light intensity falling on the solar cells from 0.7 to 230 mW/cm^2. Figure 7.18 shows the current density as a function of applied voltage at various values of light intensity. As expected, the current increases with light intensity from 0.05 to 5.7 mA/cm^2. This is due to the increase in charge generation as the light intensity increases. However, this increase is accompanied by changes in the slope of the plot in the first and third quadrant. From the analysis in section 2.3.2, we explain these by changes in the series and shunt resistance in the equivalent circuit of device.

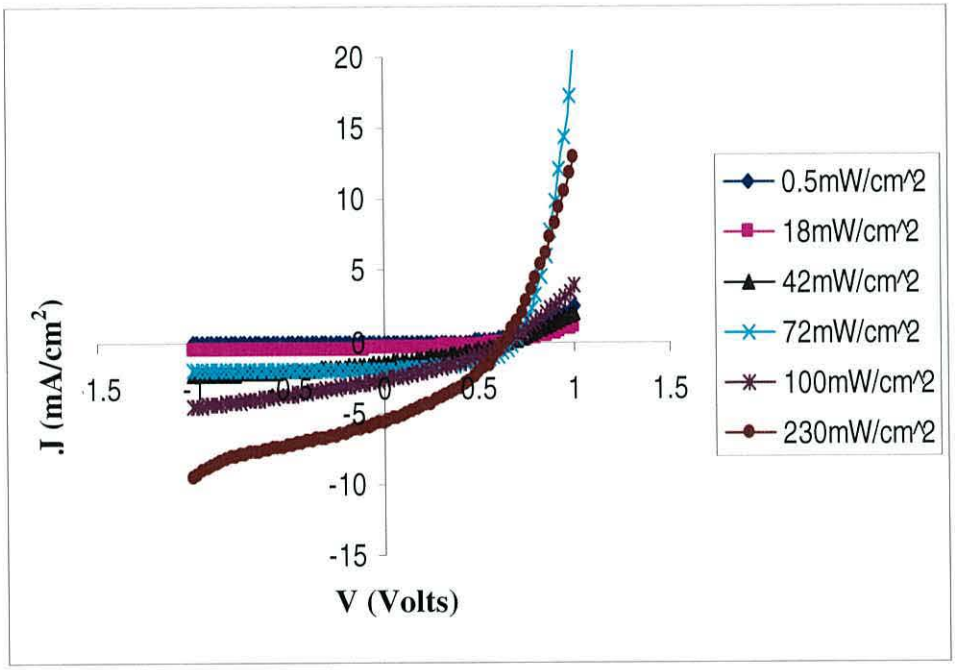

Figure 7.18 *Effect of the light intensity on the I-V characteristics of TLSCs produced from batch A.*

Figure 7.19 shows a log plot of current density versus light intensity. The slope of the plot is ~0.9 indicating that bimolecular recombination of excitons occurs in the bulk and interface regions of the device (see equation (6.2))

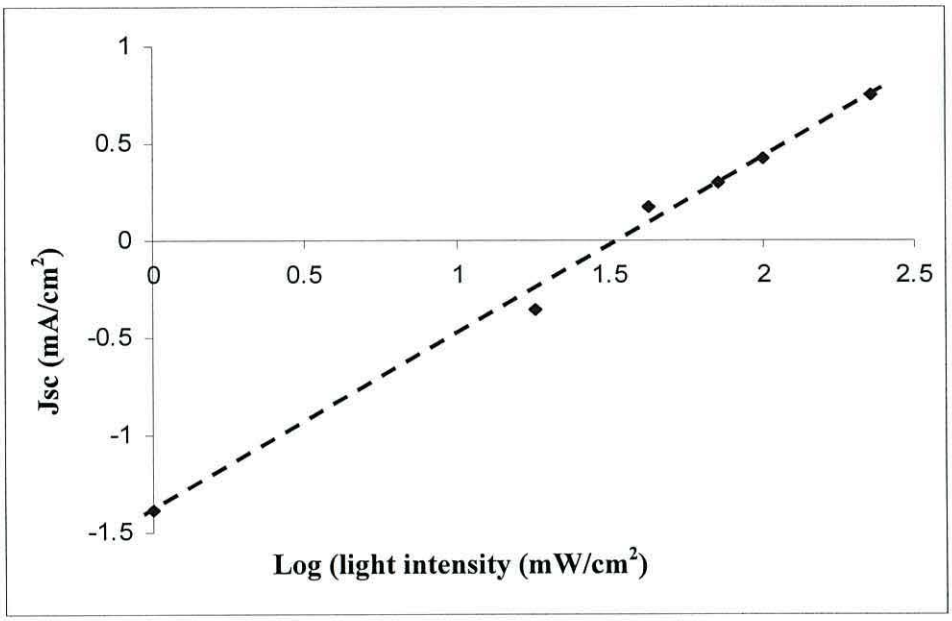

Figure 7.19 *Dependence of Jsc on incident light intensity for a TLSCs produced from batch A.*

Figure 7.20 shows that the Voc is also dependent on the light intensity. For low light intensity, Voc was low but then increased to reach 0.7 V at 100 mW/cm^2. However, when the light intensity was increased to 230 mW/cm^2, Voc decreased slightly to 0.65V.

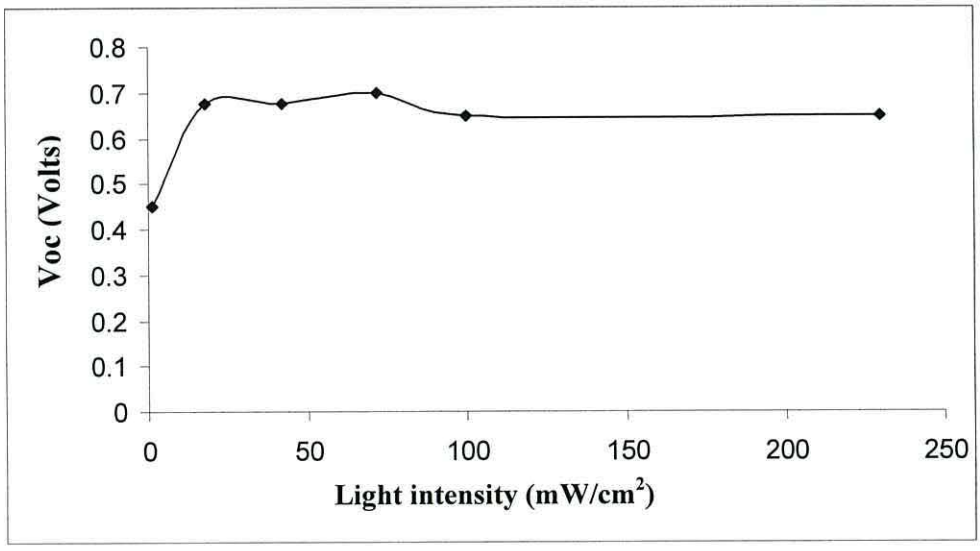

Figure 7.20 *Dependence of Voc on incident light intensity for TLSC produced from batch A.*

7.3.4 Discussion

A number of researchers have been trying to investigate the effect of temperature on polymer/dye/ nc-TiO_2 solar cells [27, 28]. From equation 2.13 and 2.11, Voc is seen to be affected by the photogenerated charges (denoted by Ig) and the recombination of photogenerated charges (denoted by R_{sh}). Increasing temperature increases the mobility of charge carriers and reduces the series resistance in the bulk region. If this assumption is applied and the recombination of photogenerated charges was unchanged with temperature, Voc should have increased with temperature to maintain open circuit condition i.e. I_{OUT} =0. This was not observed in our results and also contradicts the result in [8]. Therefore, we consider that the recombination of photogenerated charges must also increase with increase in temperature i.e. a reduction occurs in R_{sh} as seen in figure 7.12. The relation between Voc of a dye/ nc-TiO_2 / solid state-hole conductor and the recombination of photogenerated charges is given [9] by

$$Voc = \frac{KT}{q} \ln\left[\frac{J_p}{qSN_c}\right] + \frac{E_c - E_F}{q} \qquad (7.1)$$

where S is the interface recombination velocity, N_c is the effective density of states in the conduction band of the TiO_2. In [9] the thermal activation energy of the solar cells was calculated by multiplying elementary charge (q) with the value of Voc obtained at T= 0 K.

Thus by extrapolating to T=0K (Figure 7.21), the thermal activation energy, Ea, of the TLSCs was estimated to be ~1.3eV. This value is supposed to depend on the HOMO of P3HT and the conduction band of nc-TiO_2. However, the difference between the LUMO of P3HT and conduction band of nc-TiO2 was 0.9eV. The difference may be caused by the NCS group of the Ru dye absorbed on nc-TiO_2 surface which might contribute around 0.4eV in thermal activation energy by forming a surface dipole on nc-TiO_2 [8]. Additionally, the Fermi level of P3HT is affected by temperature which may also lead to an increase in the thermal activation

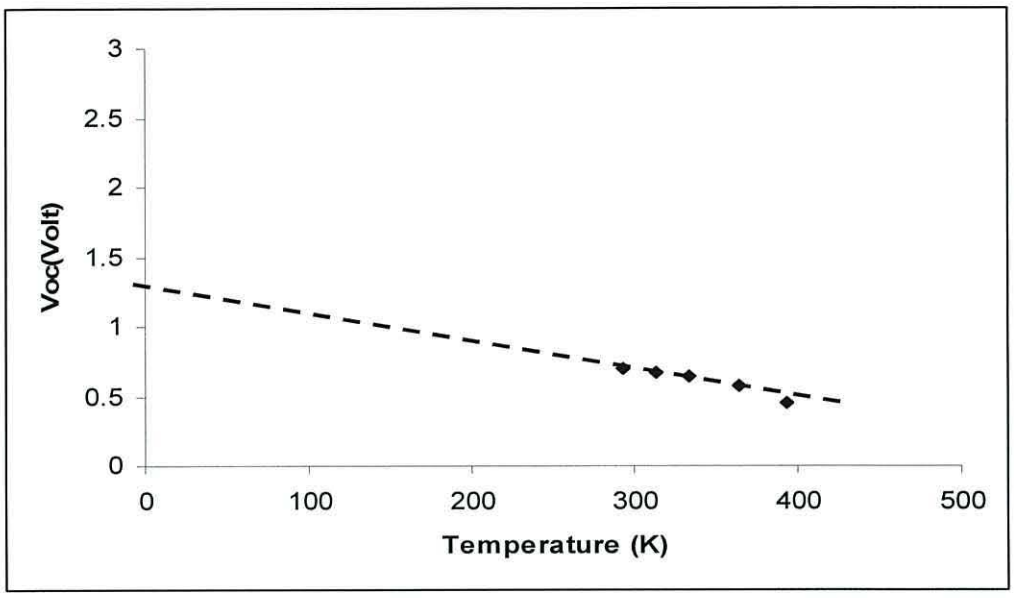

Figure 7.21 *Open circuit voltage versus temperature of TLSCs produced from batch A after extrapolation of Voc values. The curve is intercepted Y axis at 1.3eV where the temperature is zero.*

The increase in temperature also improves the conductivity of P3HT which will decrease Rs. However, there was no indication of improvement in the value of Jsc when the temperature increased from 293K to 333 K. This is attributed to the strong effect of the temperature on Voc. Thus, the decrease in Jsc when the Voc decreased from 0.7V to 0.45V was caused a shift in the I-V curve as the temperature increased.

The deterioration in TLSCs performance under continuous irradiation is mentioned in [10]. The Jsc of TLSCs increased in the first few seconds of irradiation then it started to decrease slowly over a few thousand seconds. This is due to filling of traps or defects at the interface produced by absorbed oxygen and water vapor on the $nc-TiO_2$ surface. This leads to an increase in the Jsc in the first few seconds. However, these defects were unlimited and regenerated from absorbing oxygen, so that, the Jsc decreased after the first seconds of illumination. The Voc of the TLSCs decreased in the first few seconds also as a result of traps filling (defects) at the interface as explained in section 6.3.2

When TLSCs were tested over a period of 20 days, the change in Jsc and Voc were relatively small. However, the maximum output power decreased to almost half the maximum observed value observed after 6 days. Although the TLSC were stored in the dark between measurements, they were, nevertheless, exposed to the

atmosphere. We assume therefore that the degradation in performance was due to the oxygen and/or atmosphere moisture affecting at the interface properties between dye/ nc-TiO_2 and P3HT.

We have also shown that Voc and Jsc are affected by light intensity. In the absence of other effects, increased light intensity is expected to increase both Voc and Jsc through an increased generation rate (equations 2.11 and 2.13). Also this may occur due to decrease in the series resistance seen in figure 7.20. On the other hand, this causes an increase in the recombination process and reduces the charge life time which has an effect on Voc. The results show that Voc of the TLSCs increases with an increase in light intensity which indicates that the photogenerated rate is higher than the recombination rate. This latter was also observed in batch A DLSCs where the Voc and Jsc increased with an increase in light intensity. Unlike Jsc of TLSCs, the value of Jsc for DLSCs was constant when the light intensity increased above $72mW/cm^2$. This was attributed to the poor wetting of the $nc-TiO_2$ particles by the P3HT in DLSCs leading to an increase of resistance. For TLSCs, the dye layer between P3HT and nc-TIO2 reduced the resistance across the device by improving the contact between them

7.4 Electrical Measurements in the Vacuum

7.4.1 DC characteristics of Batch A TLSCs

The current–voltage (I-V) characteristics of solar cells were also studied under vacuum. Figure 7.22 is a semi-logarithmic plot of current density versus voltage (J-V) for a typical batch A TLSCs. Under high vacuum (10^{-5} torr), the dark currents in reverse bias are some two orders of magnitude less than in air. In forward bias, the differences are even larger. Under high vacuum, the forward current remains small and the device shows only limited rectification. Under illumination, the device behaved as a photoconductor with both Voc and Jsc equal to zero (Figure 7.22).
This phenomenon was also observed in batch A DLSCs and batch B DLSCs.

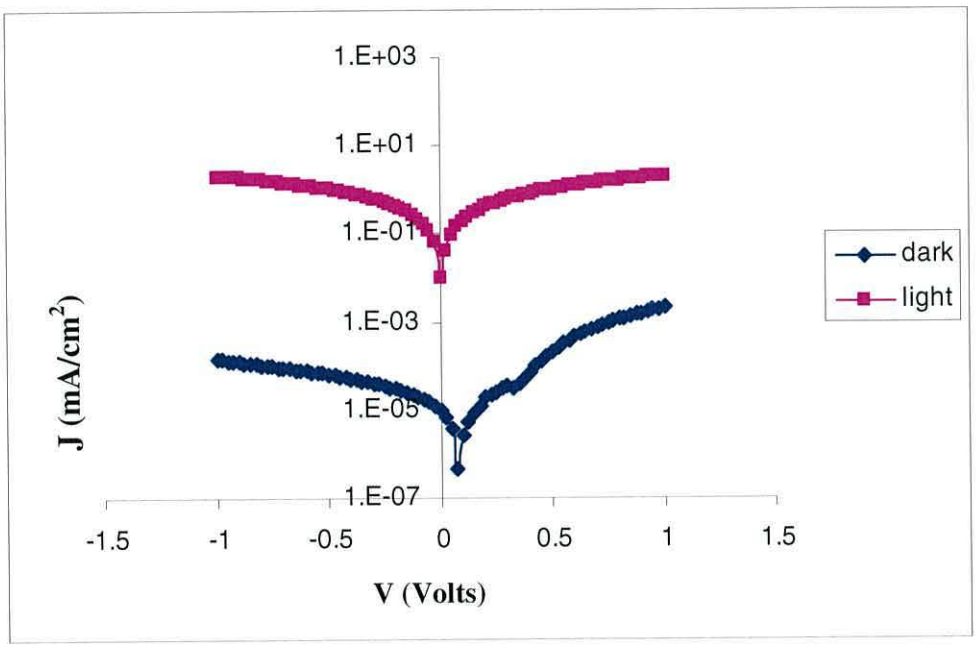

Figure 7.22 *Log J-V characteristics of TLSCs produced from batch A in high vacuum.*

Figure 7.23 shows that the photocurrent depends linearly on voltage under forward bias and reverse bias conditions. The turn on-voltage of batch A TLSCs in high vacuum was decreased from 0.6V in air to 0.2V in high vacuum in dark (Figure7.24).

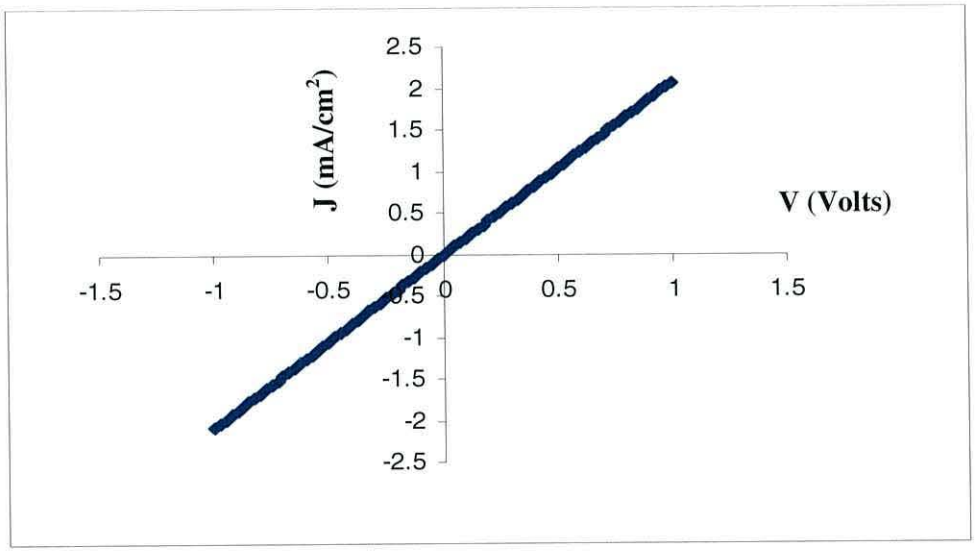

Figure 7.23 *J-V characteristics of TLSCs produced from batch A in the high vacuum in light.*

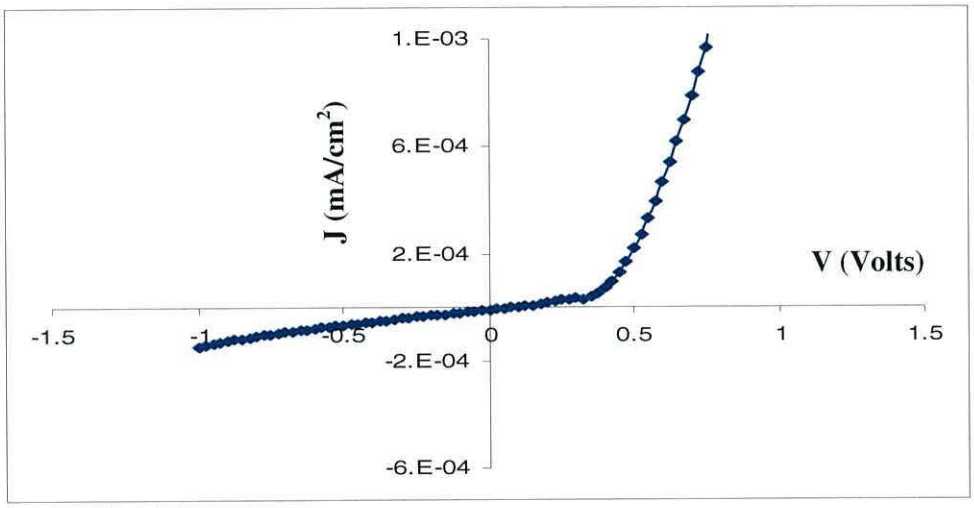

Figure 7.24 *J-V characteristics of TLSCs produced from batch A in the high vacuum in dark.*

7.4.2 DC Characteristics of Batch B TLSCs

DC measurements were also made on batch B TLSCs under high vacuum (10^{-5} torr) gave surprising results compared to batch A TLSCs and batch A and B DLSCs. The batch B TLSCs behaved as a solar cell under high vacuum. Figure 7.25 shows the semi-log plot of current density versus voltage (J-V) characteristic of a typical batch B TLSC. In the dark, the current was smaller than when the device was tested in the air (Figure 7.3). The rectification ratio was less than 10 at ±1 V. However, under illumination, the device produced a short circuit current density of ~0.45 mA/cm^2 and an open circuit voltage of ~ 0.8V

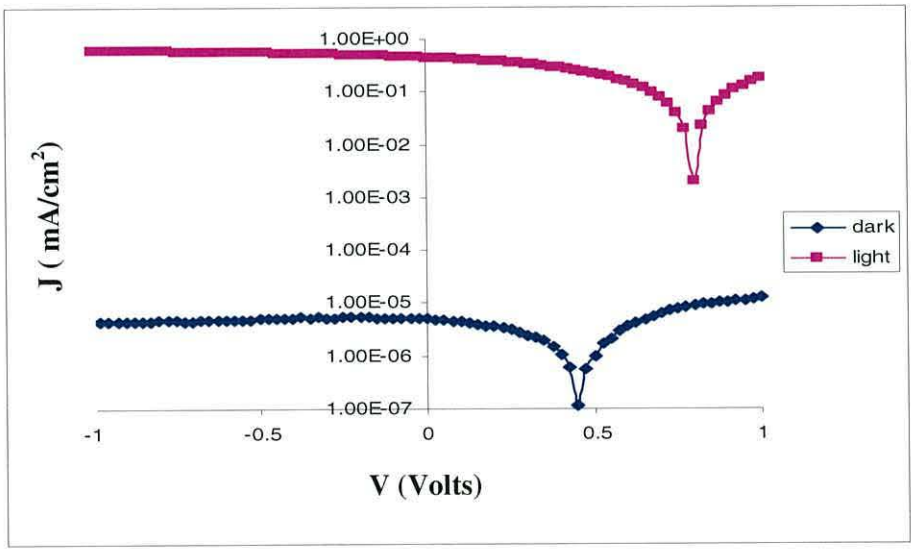

Figure 7.25 *Log J-V characteristics of TLSCs produced from batch B in high vacuum.*

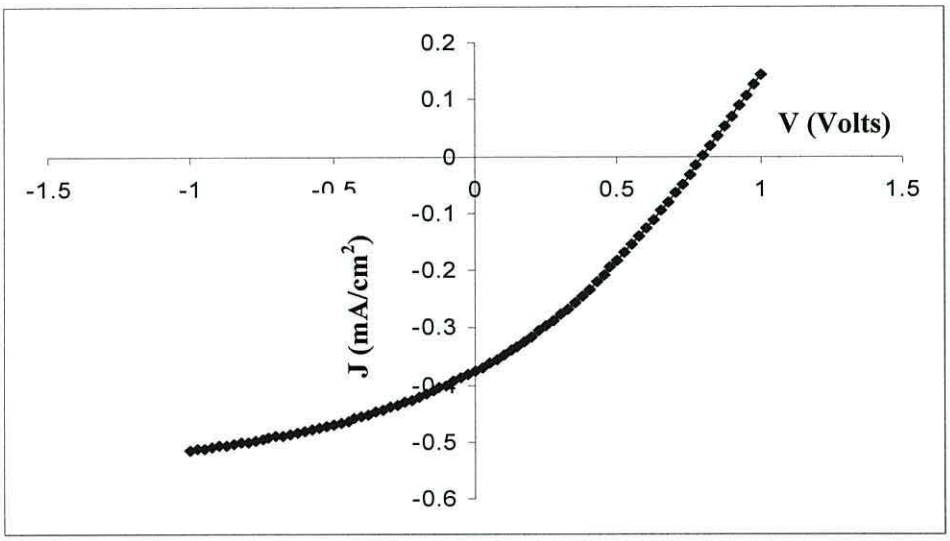

Figure 7.26 *Log J-V characteristics of TLSCs produced from batch B in high vacuum and in the light.*

Figure 7.27 shows a typical current density versus voltage (J-V) characteristic of batch B TLSCs under high vacuum in the dark. The turn-on voltage of the device was ~0.55 V and was accompanied with a decrease in the value of Voc (from 0.9 to 0.8V).

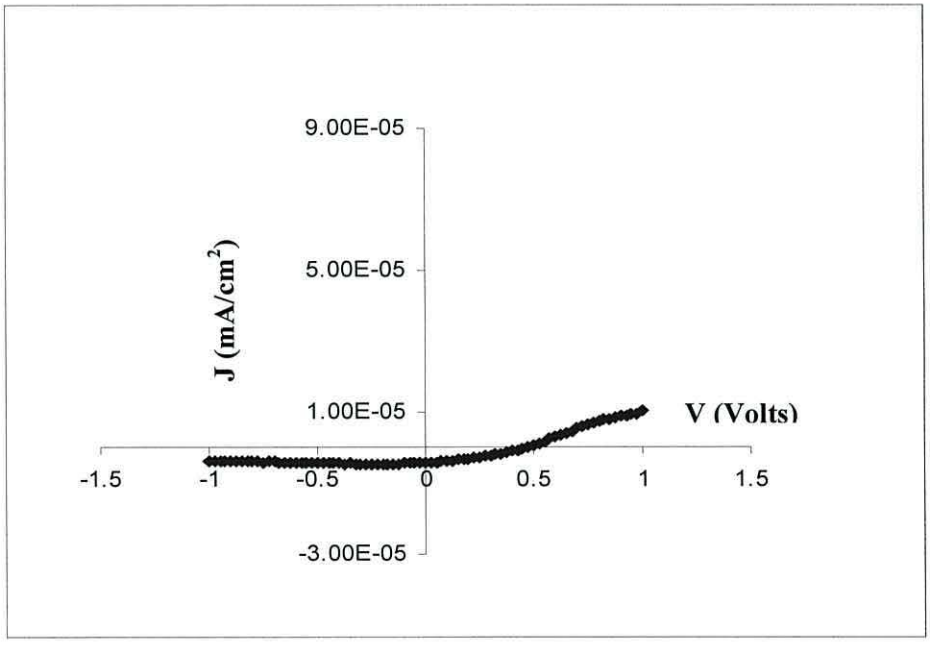

Figure 7.27 *Log J-V characteristics of TLSC produced batch B in high vacuum in the dark.*

7.4.3 Discussion

TLSCs produced from the two batches of sol gel gave interesting results when measured under high vacuum. Both the dark current and turn-on voltage decreased under vacuum. This is related to the decrease in the conductivity of both the nc-TiO_2 and P3HT. However, with dye layer absorbed on the nc-TiO_2 surface, the photovoltaic effect was not expected to depend on vacuum as in DLSCs. For batch A TLSCs, the Voc was zero and the current increased due to the photoconductivity process. This appears to contradict the supposed effect of the dye layer. However, it has been mentioned in the literature that the dye layer might not cover all of the nc-TiO_2 so that the hole conductor can make direct contact with the nc-TiO_2 [6]. This will increase the recombination process so that the device exhibits p-n junction characteristics. Two processes now cause the photocurrent generation. The first process leads to a photocurrent from a depletion region at the interface between P3HT and nc-TiO_2. The second process leads to a photovoltaic behaviour controlled by the dye. Since the photocurrent produced in depletion region (photoconduction process) was higher than the current produced from photovoltaic effect, the value of Voc will decrease under vacuum

For batch B TLSCs, the device was working as a solar cell despite being in vacuum. This is attributed to the poor penetration of P3HT through which forms a thin layer on the top of nc-TiO_2. The dye separated the nc-TiO_2 and P3HT and prevented any contact between them. We found that the Voc was ~0.8 V and Jsc was $0.45mA/cm^2$ in vacuum bigger that the results found in air. In this case, we believe that only a small area of contact is present between P3HT and $nc-TiO_2$ i.e. most of the interface area was covered with dye .

7.5 Summary

The results obtained from experimenting with the TLSCs (batches A and B) are explained based on the difference of morphology and surface contact between P3HT and dye/ nc-TiO_2. The device showing the better performance was investigated under different conditions. The external quantum efficiency of the TLSCs was found to be ~14% and used to extract the value of Jsc at AM 1.5 solar which was $2mA/cm^2$. The effect of the light intensity, stability, and the age of the device were also investigated

for batch A TLSCs. The thermal activation energy was ~1.3eV. The ambient effect on TLSCs was studied and compared with DLSCs. The photovoltaic effect of batch A TLSCs was dependent on the ambient condition. In contrast, the photovoltaic effect of batch B TLSCs was independent of the ambient condition and exhibits solar cells characteristics in high vacuum and in air.

7.6 References

1. D. Gebeyehu, C. J. Brabec, F. Padinger, T. Fromherz, and S. Spiekermann, N. Vlachopoulos,F. Kienberger, H. Schindler and N. S. Sariciftci, *Synthetic Metals,* **121**, 1549 (2001).
2. M. Coakley , and M. D. McGehee, *Applied Physics Letters*, **83,** 3380, (2003.)
3. J. Breeze, Z. Schlesinger, S. A. Carter and P. J. Brock, *Physical Reviews B.* 64, 125205, (2001).
4. M. M. Wienk, M. P. Struijk and R. A. J. Janssen, *Chemical Physics Letters*, 422, 488, (2006).
5. Y. Wang, K. Yang, X. wang, R. Nagarajan, L. A. Samuelson, J. Kumar, *Organic Electronics*, **7**, 546, (2006).
6. P. Ravirajan. A. M. Peiro, M. K. Naseeruddin, M. Grätzal, D. D. Bradley, J. R. Durrant, and J. Nelson, *Journal of Physical Chemistry B,* **110** .7635, (2006).
7. L. S. Menda,and M. Grätzel, *Thin Solid Film*, **500**, 296, (2006).
8. H. J. Snaith, L. S. Mende, and M. Grtäzel, *Physical Reviews B*, **74,** 045306, (2006)
9. G. Kron, T. Egerter, J. H. Werner, and U. Rau, *Journal of Physical Chemistry B*, **107**, 3556, (2003)
10. W. A. Daud, and M. Turner, *Reactive and Functional Polymers*, **66**, 13, (2006)

Chapter 8

AC Measurements on Double Layer and Three Layer Solar Cells

8.1 Introduction

This chapter presents AC admittance measurements for Double Layer Solar Cells (DLSCs) and Three Layer Solar Cells (TLSCs). The measurements were conducted to obtain information about the interfacial properties of the cells, particularly to investigate the different TiO_2 sol-gels but also to determine the effect of the dye on the interface. The AC measurements were undertaken by following the procedures described in Chapter 5 with a DC voltage applied to the SnO_2:F electrode ranging from 1V to -1V. Thus, the devices were driven into forward bias when negative voltage was applied to the SnO_2:F electrode.

8.2 Dielectric in Time Dependent Fields

To understand the behaviour of a heterojunction solar cell it is useful to consider the behaviour of polar dielectric in an alternating electric field. If a small sinusoidal voltage of angular frequency ω is applied to a parallel plate capacitor filled with such a material then the capacitance, C, is given by

$$C = \frac{\varepsilon_r \varepsilon_o A}{d} \tag{8.1}$$

Where ε_r is the relative permittivity of the dielectric, ε_o the permittivity of free space, A the place area and d the plate separation.

When measured over a wide range of frequencies from 10^2 to 10^{10} Hz, ε_r shows a strong frequency dependence, see figure 8.1.

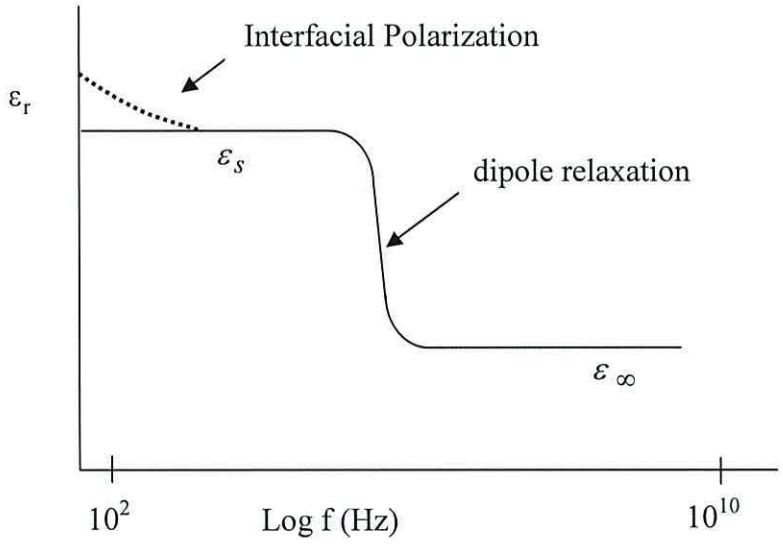

Figure 8.1 *Frequency dependence of* ε_r *for a polar dielectric. The dotted curve shows the effect of interfacial polarization.*

At low frequencies ε_r is essentially constant and equal to ε_s the static or low-frequency dielectric constant. As the frequency increase and permanent dipoles in the dielectric cease to be able to follow the voltage, then dispersion occurs and ε_r decrease to ε_∞, the high frequency dielectric constant, which reflects induced polarization corresponding to atomic and electron displacements in the alternating electric field. Also shown dotted at low frequency is a possible contribution from

interfacial polarization. In our solar cells, this is an important contribution for interfaces formed between the components of devices.

8.2.1 Interfacial polarization (Maxwell –Wagner Effect)

In a homogenous dielectric with conductivity σ and permittivity ε, the current density of the system is determined using Maxwell's equation

$$J = \sigma E + \varepsilon \frac{dE}{dt} \tag{8.2}$$

where E is the electric field. For an alternating applied voltage $V=V_O e^{j\omega t}$ and since $E=\frac{V}{d}$, equation (8.2) may be written as

$$J = j\omega \left(\varepsilon - j\frac{\sigma}{\omega}\right)\frac{V}{d}. \tag{8.3}$$

Hence the capacitor may be represented by a complex capacitance per unit area, C^*, where

$$C^* = \frac{\varepsilon - j\frac{\sigma}{\omega}}{d}. \tag{8.4}$$

If the capacitor consists of two different materials, they may be characterized by their thickness (d_1,d_2), conductivity (σ_1,σ_2) and permittivity (ε_1,ε_2) (Figure 8.2).

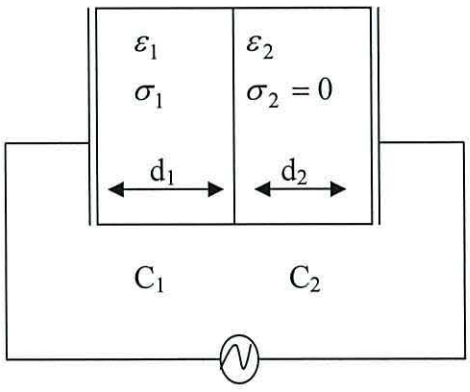

Figure 8.2 *An inhomogenous capacitor formed from two different dielectrics.*

The two materials will have capacitances C_1 and C_2 in series and if $\sigma_2 = 0$, then

$$C_1 = \frac{\varepsilon_1 - j\frac{\sigma}{\omega}}{d} \tag{8.5}$$

and

$$C_2 = \frac{\varepsilon_2}{d_2} \tag{8.6}$$

so that the total capacitance C_T is given by

$$C_T^* = \frac{C_1 C_2}{C_1 + C_2} = \frac{\varepsilon_T^*}{d_1 + d_2} \tag{8.7}$$

where ε_T^* is the apparent complex permittivity.

The apparent permittivity ε_T^* is given by

$$\varepsilon_T^* = \frac{(\varepsilon_1 - j\frac{\sigma}{\omega})\varepsilon_2}{(\varepsilon_1 - j\frac{\sigma}{\omega})f_2 + \varepsilon_2 f_1} \tag{8.8}$$

where $f_1 = \frac{d_1}{d_1 + d_2}$ and $f_2 = \frac{d_2}{d_1 + d_2}$

When $\omega \to 0$, $\varepsilon_T^* \to \varepsilon_S$, the apparent value of the static permittivity

$$\varepsilon_S = \frac{\varepsilon_2}{f_2}. \tag{8.9}$$

When $\omega \to \infty$, $\varepsilon_T^* \to \varepsilon_\infty$, the apparent value of the high frequency permitivity

$$\varepsilon_\infty = \frac{\varepsilon_2 \varepsilon_1}{\varepsilon_1 f_2 + \varepsilon_2 f_1}. \tag{8.10}$$

By substitution it can be shown that

$$\frac{\varepsilon_T^* - \varepsilon_\infty}{\varepsilon_S - \varepsilon_\infty} = \frac{-j\frac{\sigma}{\omega}}{\varepsilon_1 f_2 + \varepsilon_2 f_1 - j\frac{\sigma}{\omega} f_2} \tag{8.11}$$

or

$$\frac{\varepsilon_T^* - \varepsilon_\infty}{\varepsilon_S - \varepsilon_\infty} = \frac{1}{1 + j\omega\tau} \tag{8.12}$$

where $\tau = \frac{\varepsilon_1 f_2 + \varepsilon_2 f_1}{\sigma f_2}$. Here τ is the relaxation time of the double-layer capacitor structure. Rearranging equation (8.12) then yields

$$\varepsilon_T{}^* = \varepsilon_\infty + \frac{\varepsilon_S - \varepsilon_\infty}{1 + j\omega\tau} \tag{8.13}$$

or

$$\varepsilon_T{}^* = \varepsilon_\infty + \frac{\varepsilon_S - \varepsilon_\infty}{1+\omega^2\tau^2} - \frac{j\omega\tau(\varepsilon_s - \varepsilon_\infty)}{1+\omega^2\tau^2}. \tag{8.14}$$

Equation (8.14) may be simplified to

$$\varepsilon_T{}^* = \varepsilon' - j\varepsilon'' \tag{8.15}$$

where the real part

$$\varepsilon' = \varepsilon_\infty + \frac{\varepsilon_S - \varepsilon_\infty}{1+\omega^2\tau^2} \tag{8.16}$$

And the imaginary part

$$\varepsilon'' = \frac{\omega\tau(\varepsilon_s - \varepsilon_\infty)}{1+\omega^2\tau^2}. \tag{8.17}$$

These represent exactly the format of the Debye equation for a single relaxation time process and show that ε' and ε'' are frequency dependent (Figure 8.3).

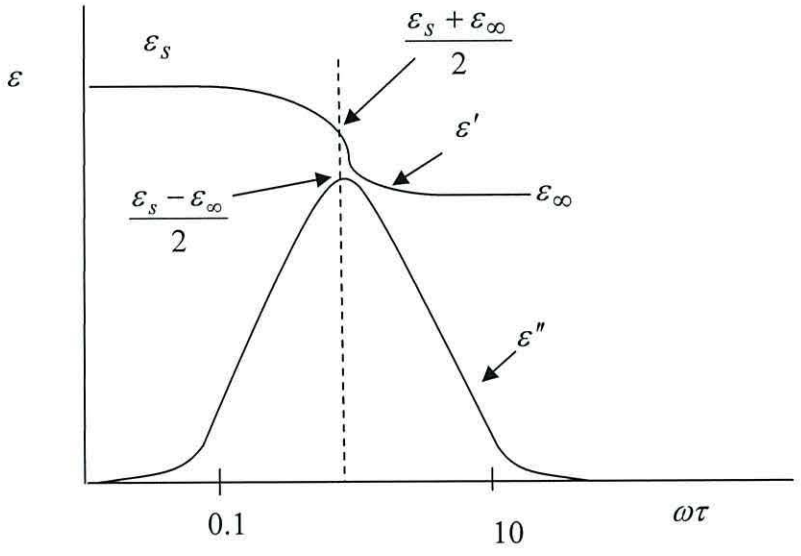

Figure 8.3 *Relaxation spectrum of the inhomogenous capacitor.*

The Debye equation can be rearranged to eliminate ω, yielding

$$(\varepsilon'(\omega) - \frac{\varepsilon_s + \varepsilon_\infty}{2})^2 + (\varepsilon''(\omega))^2 = \frac{1}{4}(\varepsilon'' - \varepsilon_\infty)^2 . \qquad (8.18)$$

This is an equation for a circle when $\varepsilon''(\omega)$ is plotted against $\varepsilon'(\omega)$. Such a plot (figure 8.5) is known as a Cole-Cole plot.

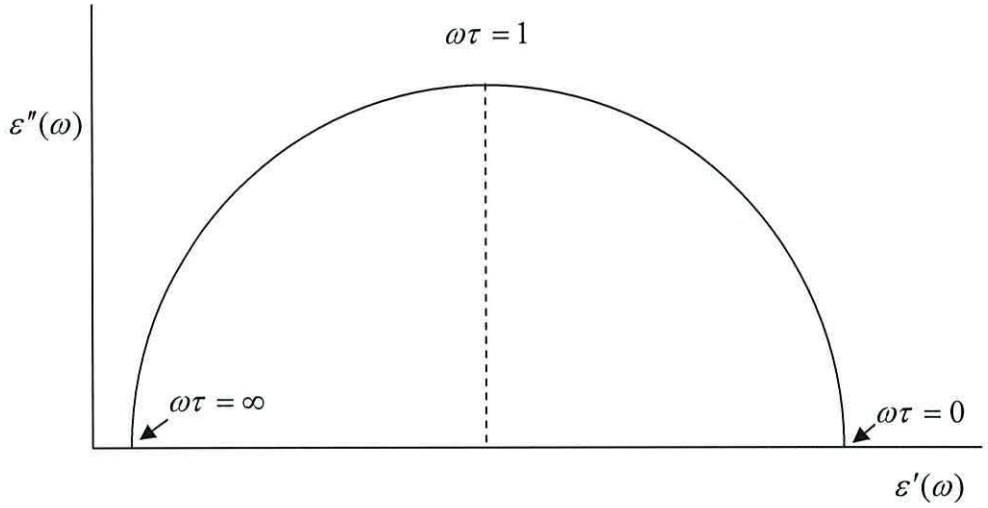

Figure 8.4 *A Cole-Cole plot of* $\varepsilon''(\omega)$ *versus* $\varepsilon'(\omega)$ *of a single relaxation time process .*

If there are two semicircles in the Cole –Cole plot, then this provides evidence of two process occurring in the device (Figure 8.5.

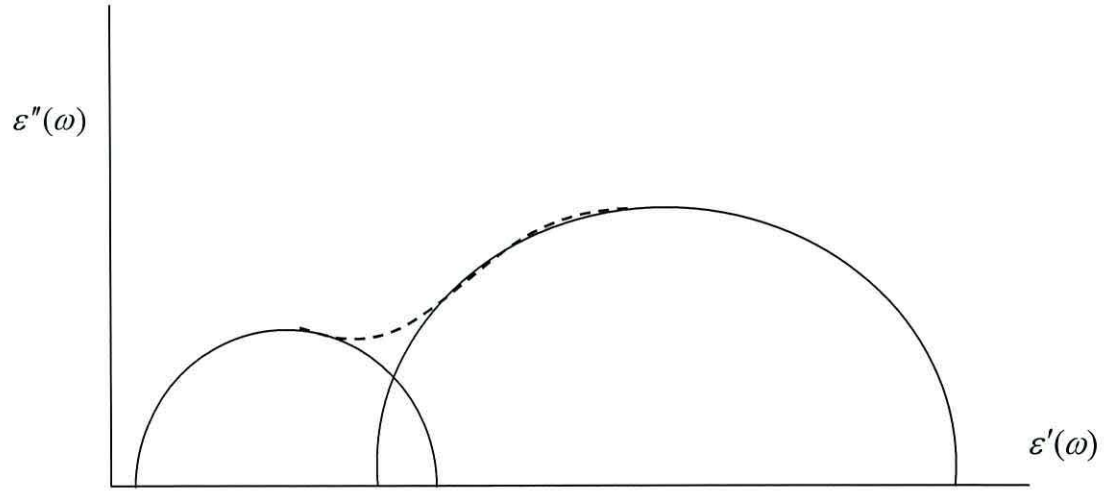

Figure 8.5 *Cole-Cole plot of* $\varepsilon''(\omega)$ *versus* $\varepsilon'(\omega)$ *with two process occurring in the device.*

In an interpenetrating system such as a bulk heterojunction solar cell, then the simple two-layer model breaks down and the device is likely to be characterized by a distribution of relaxation times. By analogy with polar dielectrics with a distribution of relation times we may now write the complex permittivity $\varepsilon_T{}^*$ as

$$\varepsilon_T{}^* = \varepsilon_\infty + \frac{\varepsilon_S - \varepsilon_\infty}{1 + j\omega\tau^{(1-\alpha)}} \tag{8.19}$$

where α is a parameter describing the distribution. When α =0 the single relaxation time response is recovered. When 0<α <1, the effect of the distribution of relaxation times is to broaden and flatten the Cole-Cole plot as shown in figure 8.6.

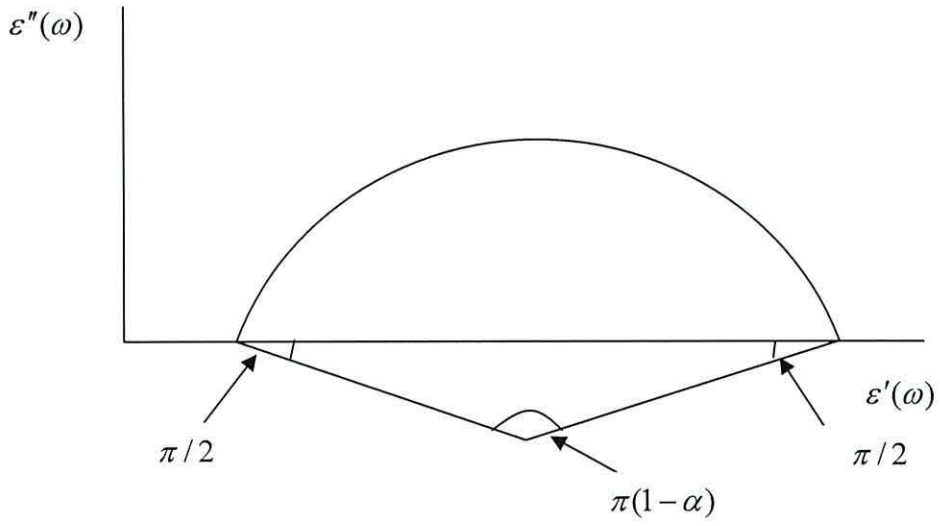

Figure 8.6 *The effect of the distribution of relaxation time on the Cole-Cole plot.*

8.3 AC Measurements in the Air

8.3.1 AC Measurements on Batch A DLSCs in the Air

Figure 8.7 shows the capacitance versus frequency characteristics of DLSCs (batch A) as a function of the applied voltage. At high frequency (0.1MHz), the capacitance was ~188 pF and almost constant as the applied voltage increased. The low frequency capacitance was over 3 orders of magnitude greater and dependent on the voltage applied to the device. For an applied voltage of 0V, the capacitance measured at 1Hz was 156nF and increased to 448 nF at -0.4V therefore remaining constant for further increases in forward bias.

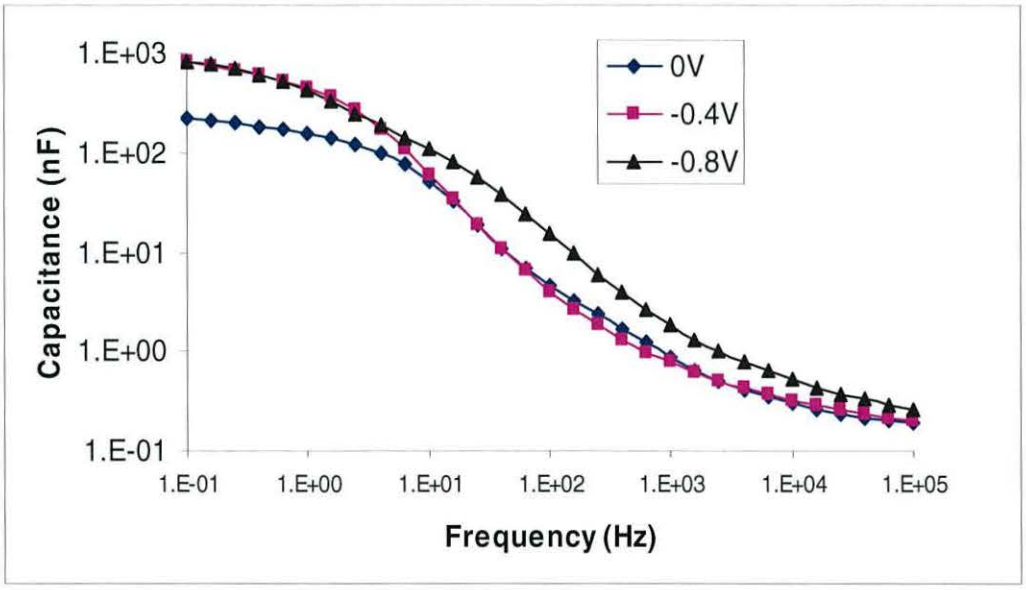

Figure 8.7 *Logarithmic plot of capacitance versus frequency characteristics of DLSCs (batch A) for different voltages applied to the SnO_2:F electrode.*

Figure 8.8 shows the loss-frequency relationship for a DLSC from batch A with different voltages applied to the SnO_2:F electrode. With -0.8V applied, the loss at 0.1MHz was ~290pF, but increasing, following a law of the form $\omega^{-0.83}$, to ~1300nF at 1Hz. Similar behavior was observed for ~ 0.4V and 0V expect that at low frequency the loss appears to become almost constant.

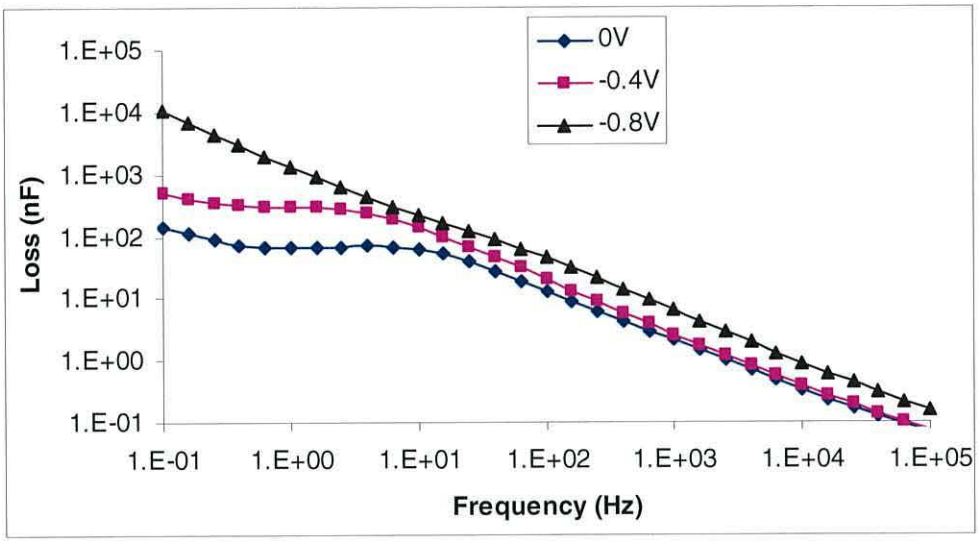

Figure 8.8 *Logarithmic plot of loss versus frequency characteristics of DLSC (batch A).*

In figures 8.9 to 8.11, the results presented in figure 8.1 and 8.2 are replotted as Cole-Cole plots. Figure 8.9 shows a clear dispersion between about 1Hz and 100Hz, corresponding to the region of almost constant loss in figure 8.8. At low frequency, a second process is observed which suggest additional dispersion although the almost constant capacitance in this region suggests that it arises from a DC loss in the device. This view is reinforced in figure 8.10 and 8.11 where application of a forward voltage increases this component significantly. At the highest frequencies (Figure 8.12), there is a tendency for the plots to converge at a capacitance of 188pF, which corresponds to the device thickness.

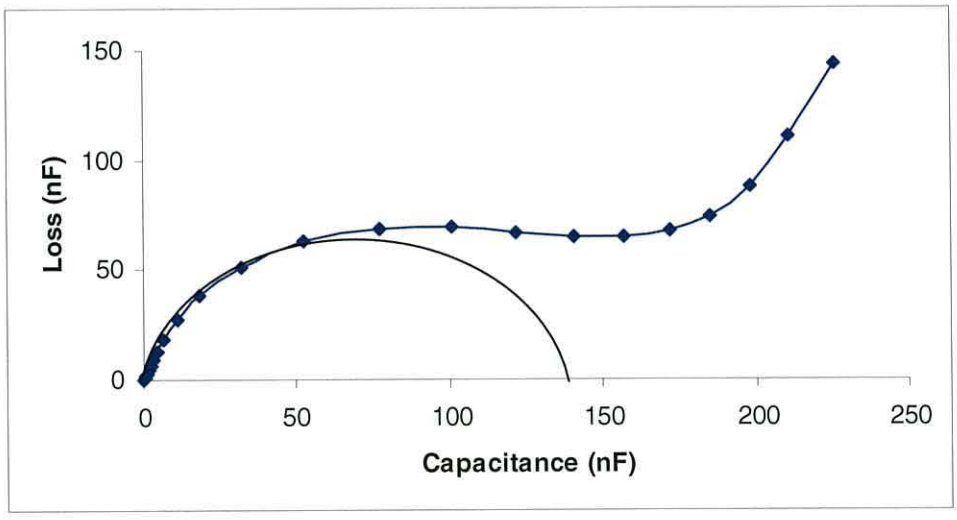

Figure 8.9 *Loss versus capacitance characteristics of DLSC (batch A) at 0V bias voltage.*

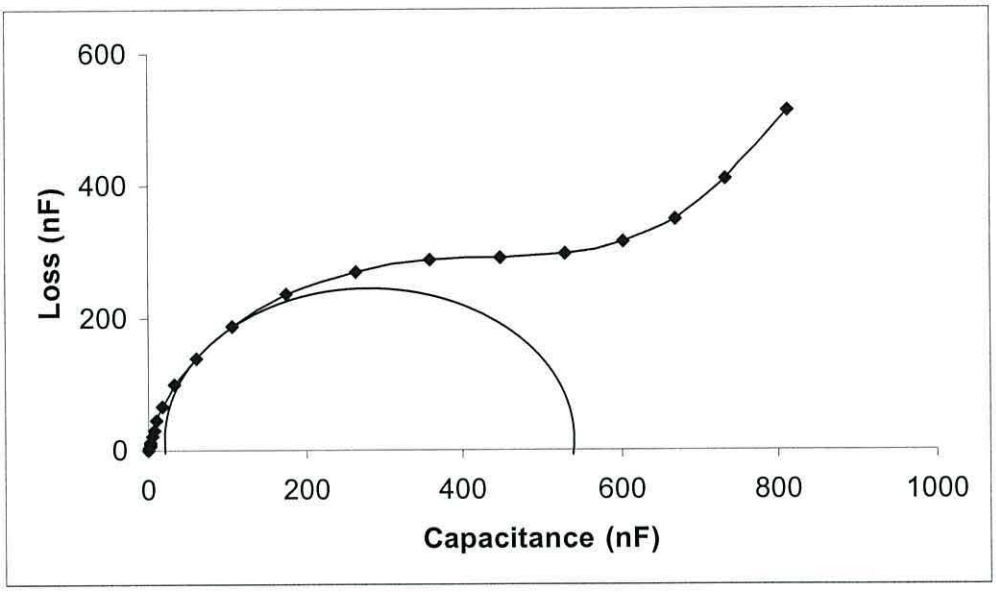

Figure 8.10 *Loss versus capacitance characteristics (Cole-Cole) of DLSC (batch A) at -0.4V bias voltage.*

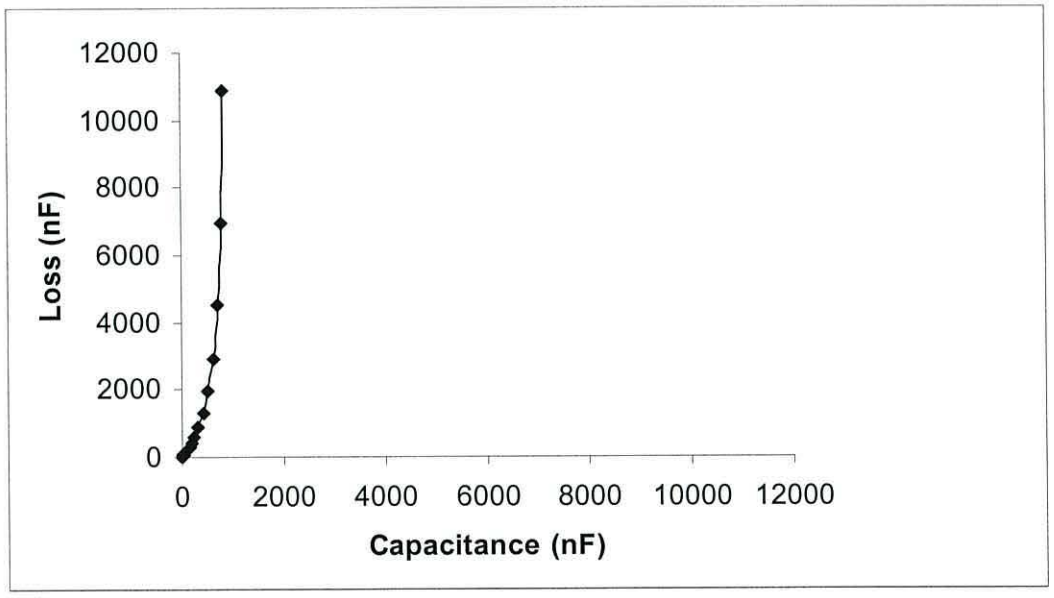

Figure 8.11 *Loss versus capacitance characteristics (Cole-Cole) of DLSC (batch A) at -0.8V bias voltage.*

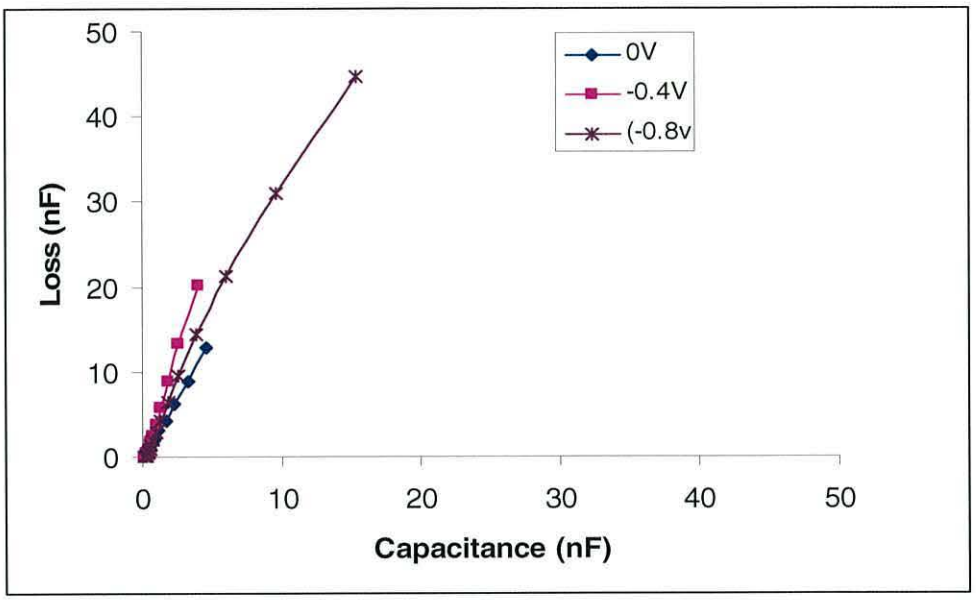

Figure 8.12 *Cole-Cle plot of DLSC (batch A) at different voltage bias. the data from figure 8.3 to8.5 but restricted to the frequency range 100Hz to 100Khz.*

The capacitance-voltage (C-V) characteristics of DLSCs from batch A were also measured at two different frequencies, namely 10 KHz and 1 Hz. The results are shown in figures 8.13 and 8.14 respectively. As can be seen, capacitance was virtually independent of the applied voltage when the device was under reverse bias, but increased rapidly at -0.6V at high frequency and at -0.2V for the lower frequency. In both cases, this capacitance passes through a maximum and decreases rapidly for further increase in forward bias.

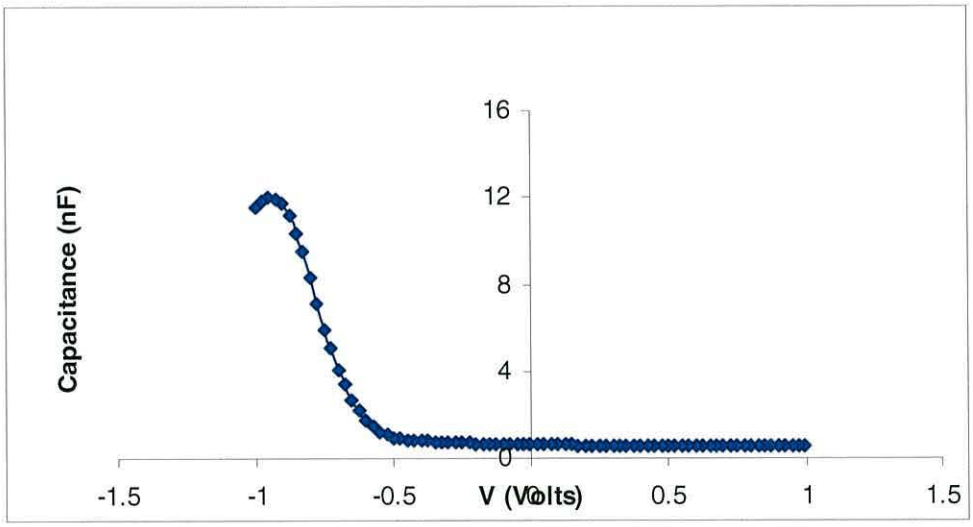

Figure 8.13 *Capacitance-voltage characteristics of DLSC (batch A) at 10KHz.*

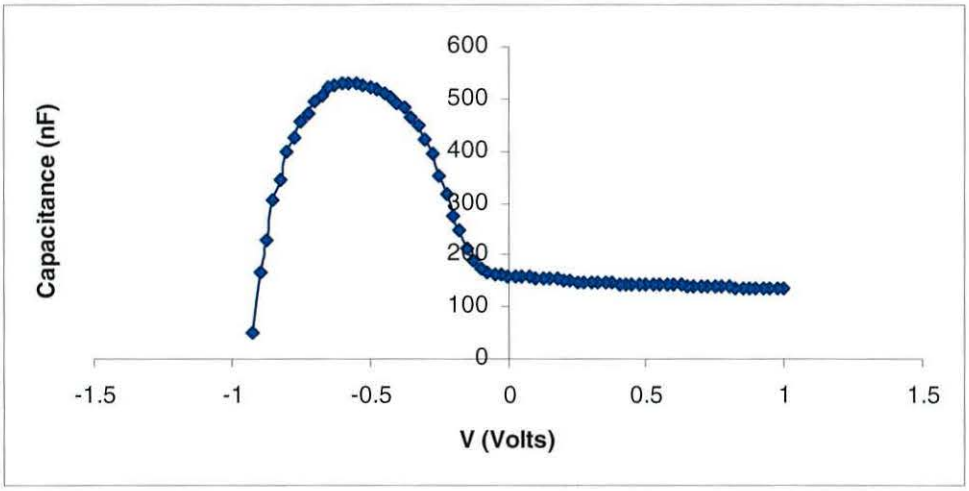

Figure 8.14 *Capacitance-voltage characteristics of DLSC (batch A) at 1Hz.*

Apart from showing smaller capacitance values at low frequency and lower loss over the whole frequency range, the general behavior of batch B devices was similar to these of batch A. There is a small but gradual decrease of capacitance from 0.1Hz to ~10Hz followed by a more rapid decrease to an almost constant value at 0.1MHz (see figure 8.15). The loss-frequency plot (figure 8.10) shows an underlying process following a law of the form $\omega^{-0.75}$ and very similar therefore to batch A DLSC. Superimposed on this background is a loss peak centraed at ~10Hz. As for batch A DLSC (figure 8.7) the loss with 0V and -0.4V applied appears to become constant at the lowest frequencies.

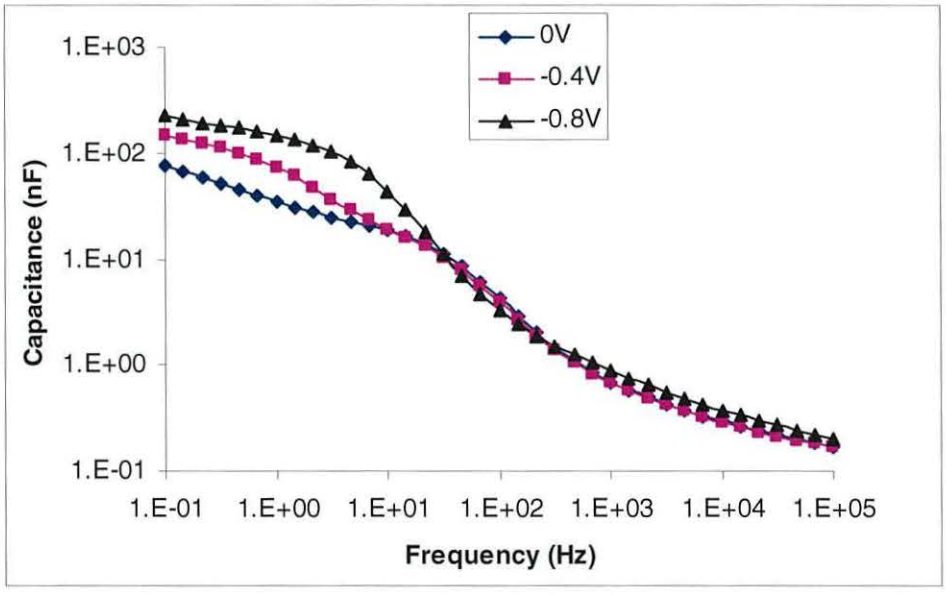

Figure 8.15 *Logarithmic plot of capacitance versus frequency characteristics of DLSC (batch B) for different voltage applied to the SnO_2:F electrode.*

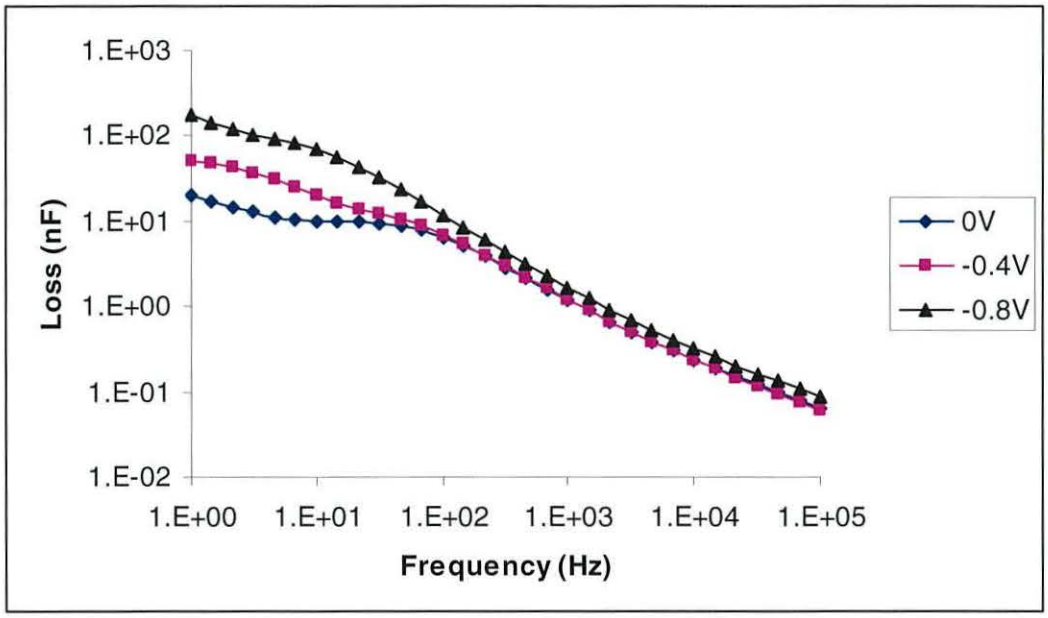

Figure 8.16 *Logarithmic plot of loss versus frequency characteristics of DLSC (batch B).*

Interestingly, the Cole-Cole plots in figure 8.17 and 8.18 suggest two possible relaxation processes in addition to DC loss at the lowest frequencies. As for batch A DLSCs, the DC loss process with -0.8V applied swamps the relaxation processes (Figure 8.19)

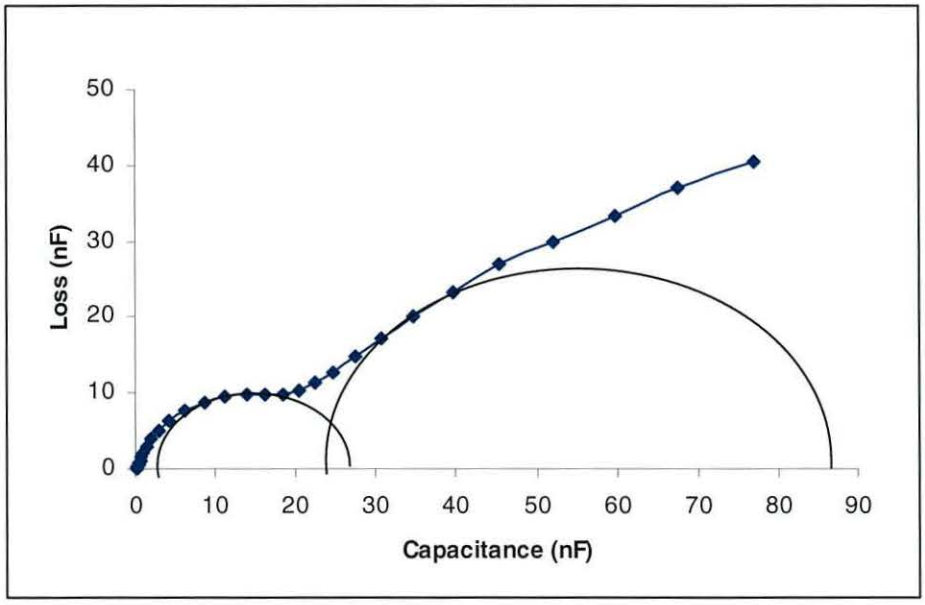

Figure 8.17 *Loss versus capacitance characteristics of DLSC produced from batch B at 0V bias voltage.*

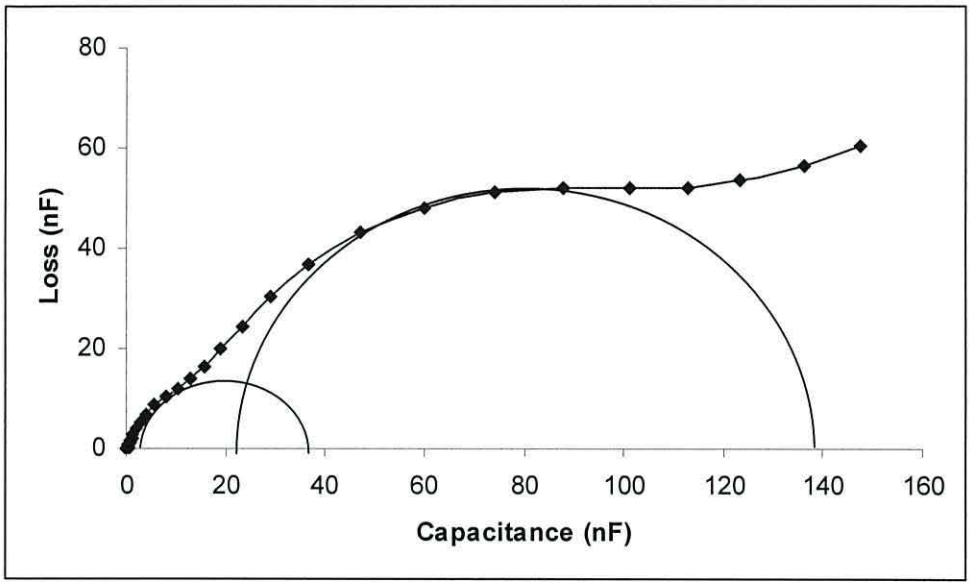

Figure 8.18 *Loss versus capacitance characteristics of DLSC produced from batch B at -0.4V bias voltage.*

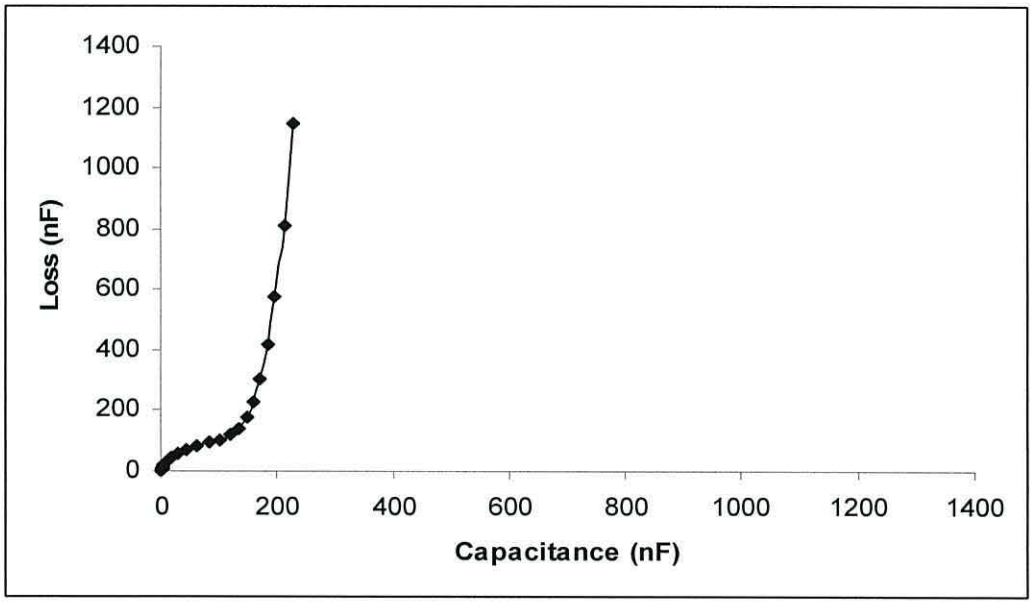

Figure 8.19 *Loss versus capacitance characteristics of DLSC produced from batch B at -0.8V bias voltage.*

Figure 8.20 shows the data from figures 8.17 to 8.19 but restricted to the frequency range 100Hz to 100KH from, which the convergent to identical behavior is clearly observed

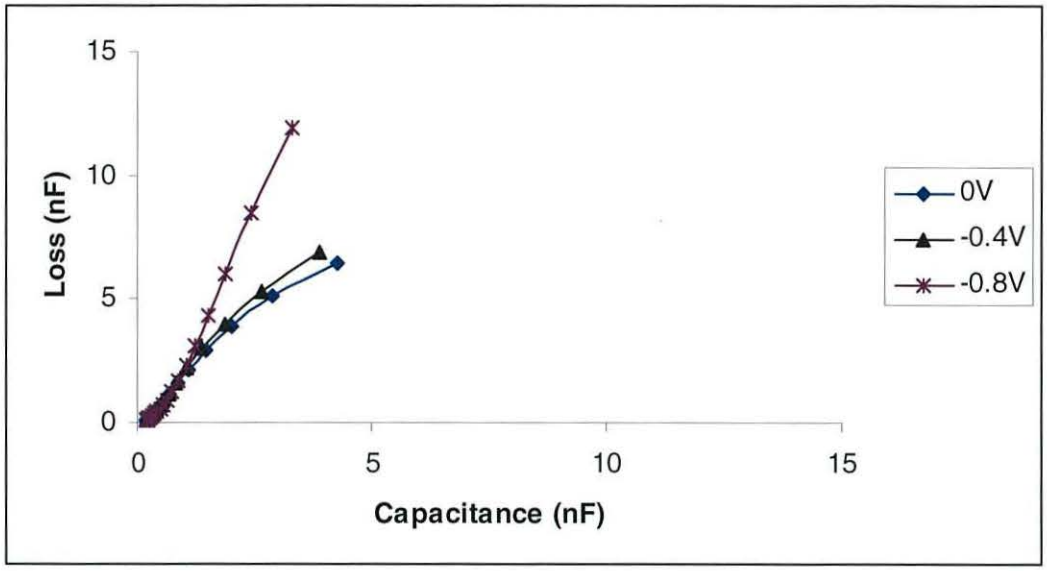

Figure 8.20 *Loss versus capacitance data from figure 8.11 to 8.13 but restricted to the frequency range 100Hz to 100 KHz.*

Figures 8.21 and 8.22 give the C-V characteristics of a batch B DLSCs device at frequencies of 10 KHz and 1 Hz respectively. Contrary to the batch A device, the capacitance measured at 10KHz was almost constant over the whole voltage range from forward to reverse bias. At 1Hz, the previously observed behaviour is seen .i.e constant capacitance in reverse bias, a rapid increase to maximum in forward bias followed by a decreasing capacitance as the forward voltage is increased further.

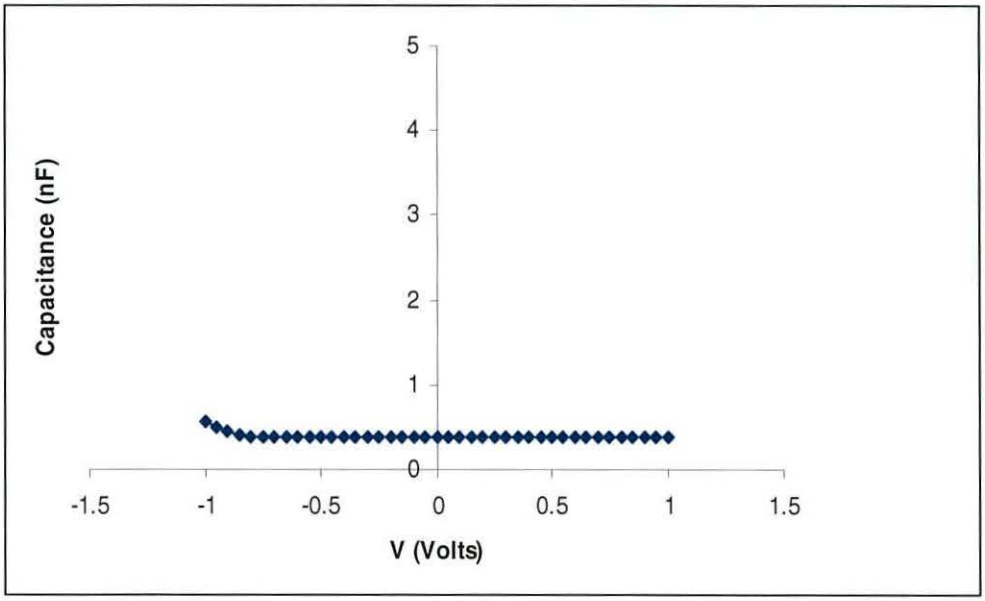

Figure 8.21 *Capacitance-voltage characteristics of DLSC (batch B) at a frequency of 10KHz.*

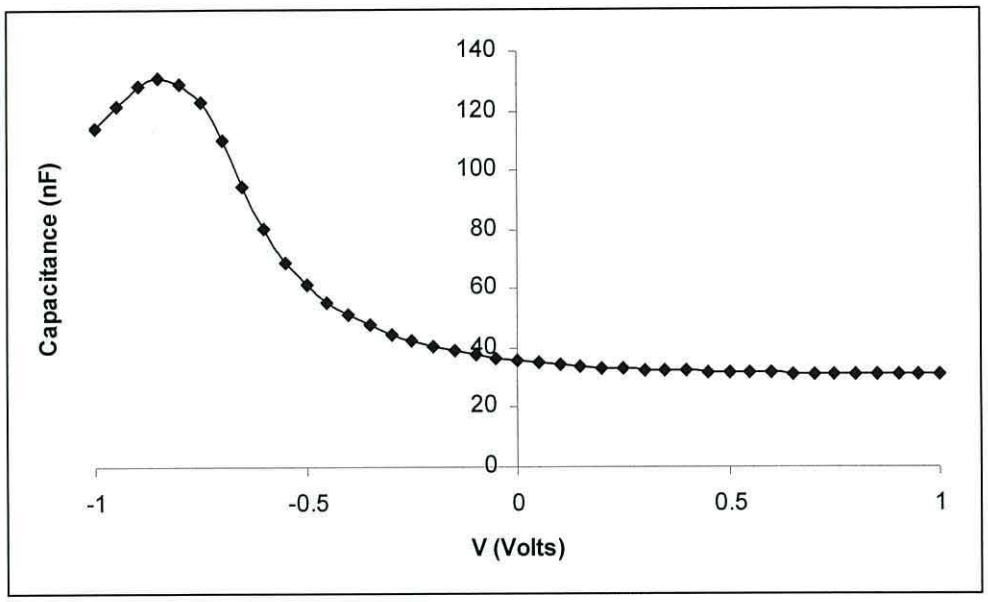

Figure 8.22 *Capacitance-voltage characteristics of DLSC (batch B) at a frequency of 1Hz.*

8.3.2 AC Measurements on Three Layer Solar Cells in the Air

Figure 8.23 shows capacitance versus frequency characterization of a TLSC (batch A) as a function of the voltage applied to the SnO_2:F electrode. For an applied voltage of 0V, the high frequency capacitance was ~189pF for a frequency of 0.1MHz which is similar to the high frequency capacitance of a DLSC (batch A). However, comparing figure 8.7 and figure 8.23 the high frequency capacitance of the TLSC (batch A) was more strongly dependent on the applied voltage, especially at frequencies below 0.1MHz. However, there was an increase in the low frequency capacitance compared to DLSCs as follows:

1- For an applied voltage of 0V, the capacitance of DLSC at 1Hz was ~157 nF in contrast to 42nF for TLSC produced from batch A.
2- For an applied voltage of -0.8V, the low frequency capacitance of TLSCs at 1Hz was ~3340nF and hence significantly greater than ~471nF for DLSCs batch A.

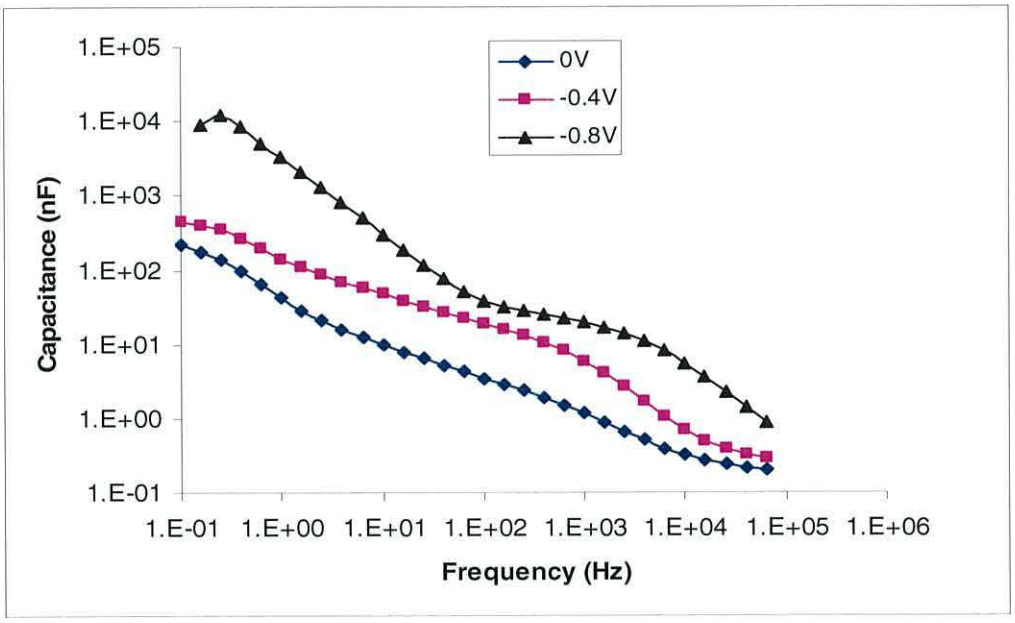

Figure 8.23 *Logarithmic plot of capacitance versus frequency characteristics of TLSC (batch A) for different voltage applied to the SnO_2:F electrode.*

Figure 8.24 shows the loss–frequency characteristics of the TLSCs (batch A) with different bias voltages applied to the SnO_2:F electrode. At 0.1 MHz, the loss showed stronger voltage dependence in the TLSC compared with the DLSC (batch A). At 1Hz, this dependence was much more marked. The loss in the TLSCs increased by more than 3 orders of magnitude to ~ 2.2 $\times 10^4$ nF for an applied voltage of -0.8V.

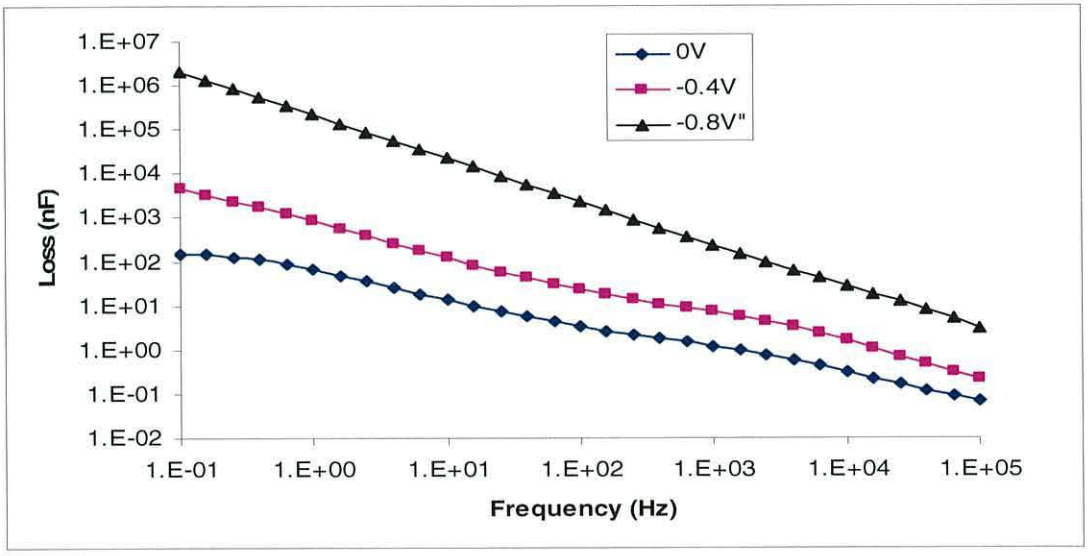

Figure 8.24 *Logarithmic plot of loss versus frequency characteristics of TLSC (batch A) for different voltage applied to the SnO_2:F electrode.*

Figures 8.25, 8.26, and 8.27 show the Cole-Cole plots for the TLSCs (batch A) with a different applied voltages. At zero bias, while there is evidence for a relaxation process, this is not so clear as for the DLSC. Here the DC loss is already beginning to dominate the dispersion and clearly does so when the voltage applied was increased from 0V to -0.4V and -0.8V.

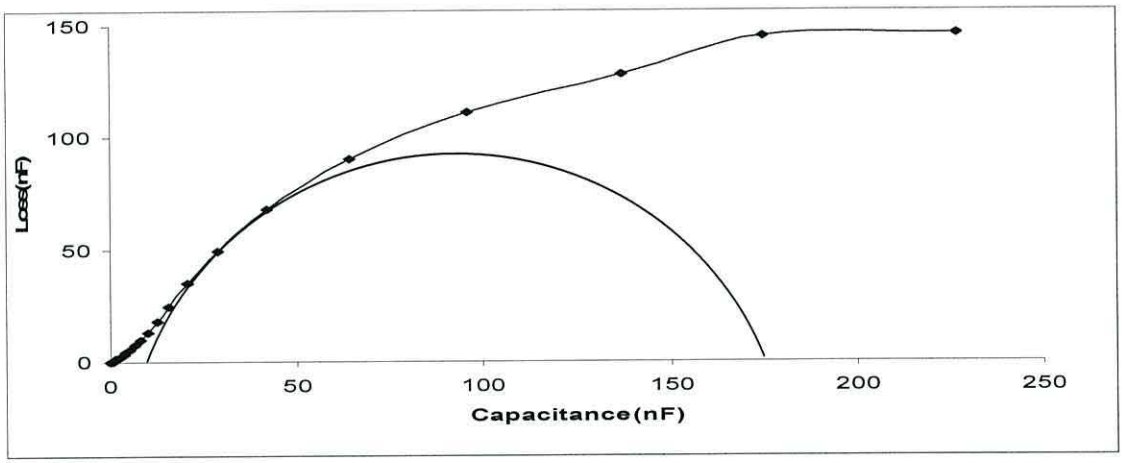

Figure 8.25 *Loss versus capacitance characteristics (Cole-Cole plot) of TLSC produced from batch A at 0V bias voltage.*

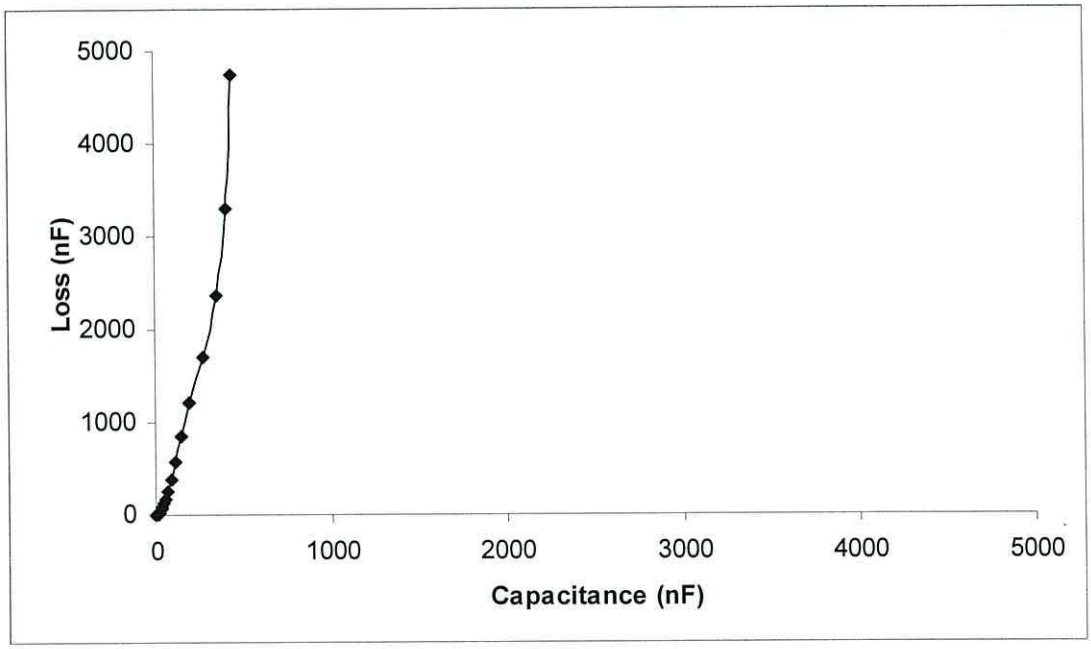

Figure 8.26 *Loss versus capacitance characteristics (Cole-Cole plot) of TLSC produced from batch A at -0.4V bias voltage.*

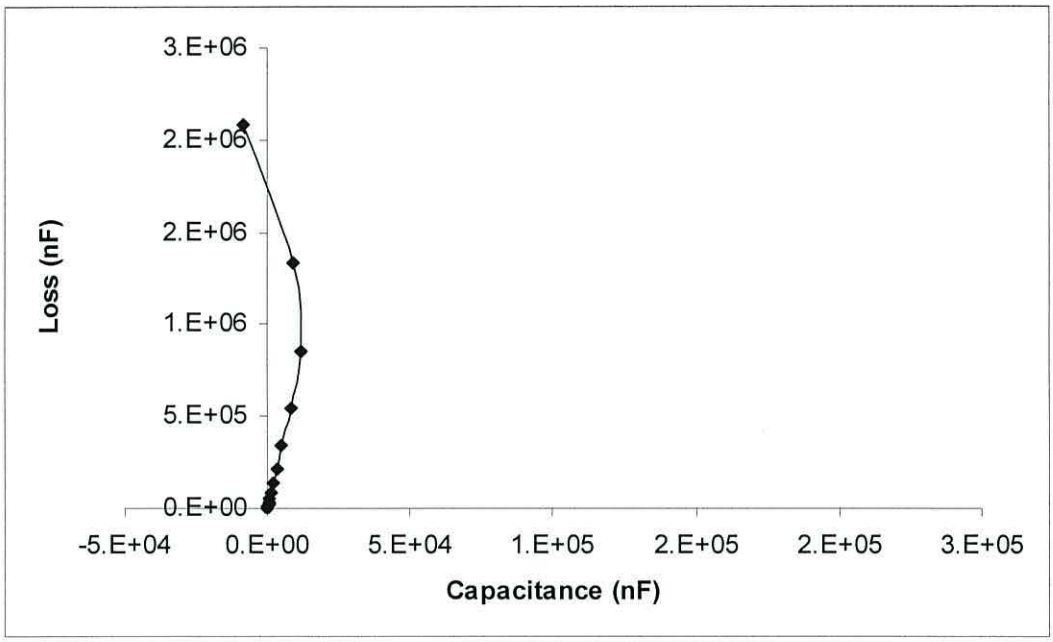

Figure 8.27 *Loss versus capacitance characteristics (Cole-Cole plot) of the TLSC produced from batch A at -0.8V bias voltage.*

Figure 8.28 shows the C-V characteristic of a TLSC at a frequency of 10KHz. The capacitance was independent of the applied voltage when the device was in reverse bias, but increased rapidly to a maximum value in forward bias as seen in the DLSCs (figure 8.9). Interestingly in the TLSC, the maximum capacitance reached was lower than in DLSCs batch A (~4 nF compared to 13 nF) and occurred at a lower voltage -0.85V.

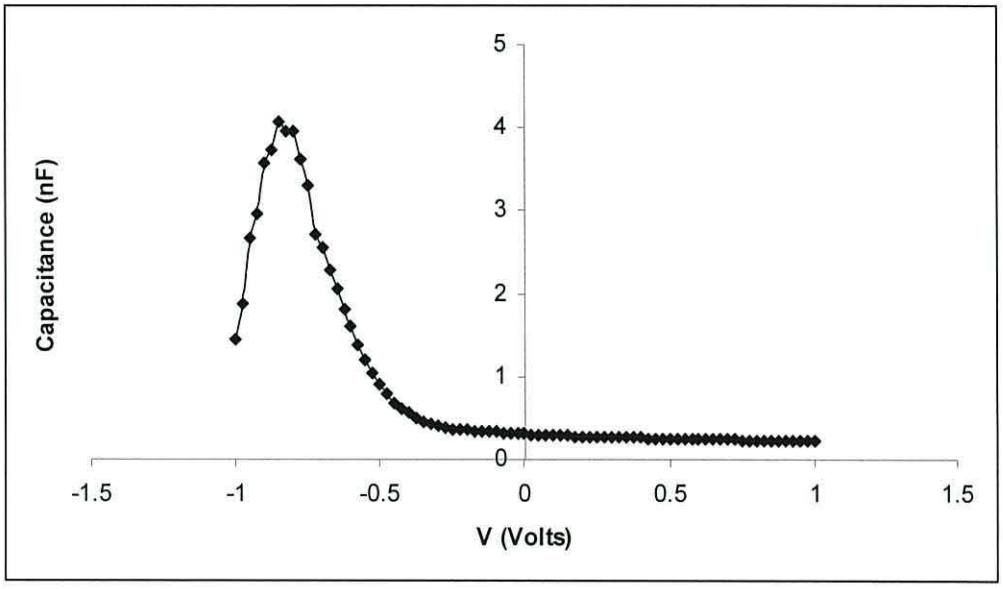

Figure 8.28 *Capacitance-voltage characteristics of the TLSC at 10KHz.*

Capacitance-voltage measurements on a TLSC at 1Hz (figure 8.29) showed a steadily increasing capacitance for increasing forward bias, reaching 1600nF at 0.5V and much higher, therefore, than observed in DLSC under corresponding conditions.

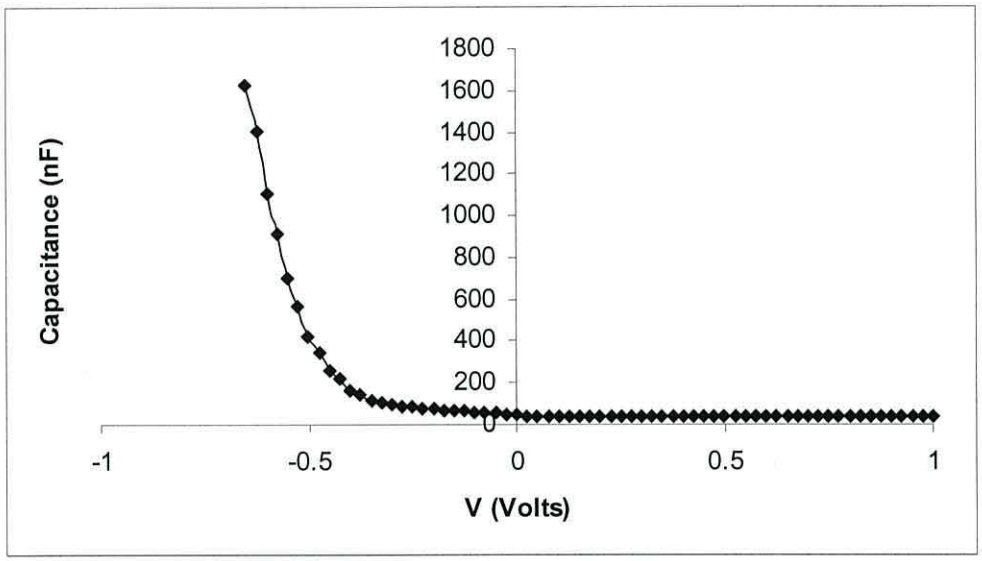

Figure 8.29 *Capacitance-voltage characteristics of TLSC at 1Hz.*

Figure 8.30 shows the capacitance–frequency characteristics of the TLSCs (batch B) with different voltages applied to the SnO_2:F electrode. The high frequency capacitance of TLSC (batch B) was ~140 pF close to the high frequency capacitance of DLSCs (batch B) and is determined by the thickness of nc – TiO_2 layer. Thus, the high frequency capacitance of TLSC (batch B) was lower than TLSC (batch A). Additionally, the high frequency capacitance of TLSC (batch B) was independent of the voltage applied to the device.

The frequency dependence of capacitance in TLSC (batch B) is different to that for TLSC (batch A) and DLSC (batch B) as follows:

- At low frequency and an applied voltage of 0V, the capacitance of TLSC (batch B) was lower than for TLSC (batch A) and DLSCs (batch B).
- The capacitance of TLSC (batch B) was almost independent of applied voltage., unlike TLSC (batch A) and DLSCs (batch B).

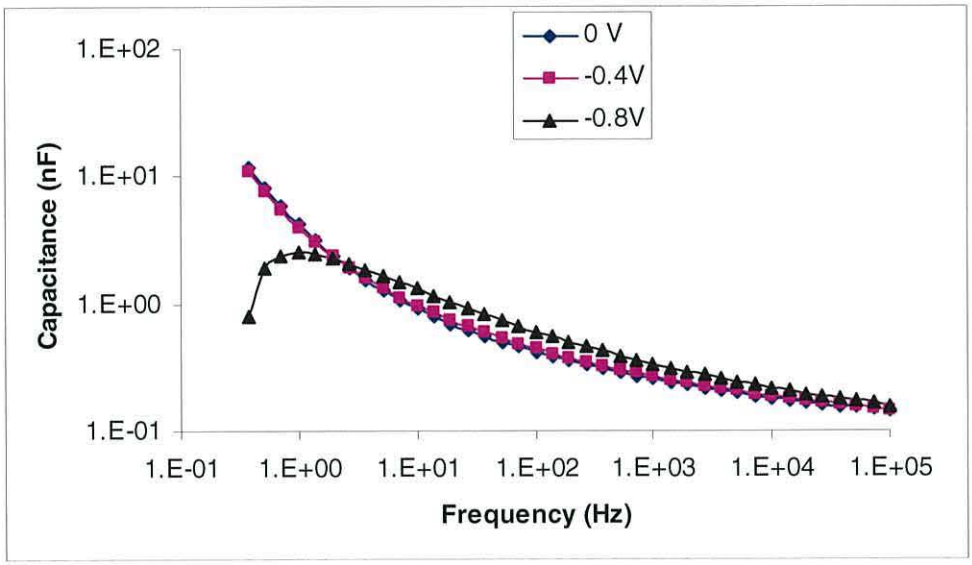

Figure 8.30 *Capacitance-frequency characteristics of TLSC (batch B) under forward bias condition.*

Figure 8.31 shows the loss–frequency characteristics of the TLSCs produced from batch B. Again there is an underlying $\omega^{-0.7}$ dependence but this time the voltage dependence is relatively weak. The low frequency loss were 0nF, 14nF, and 40nF for applied voltages of 0V,-0.4V and -0.8V respectively. The low frequency loss was also lower than that observed in DLSC from batch A and much lower than for the TLSCs from batch A under the same conditions. The frequency dispersion in the TLSCs from batch B occurs below 10Hz, the lowest value of any of the devices tested.

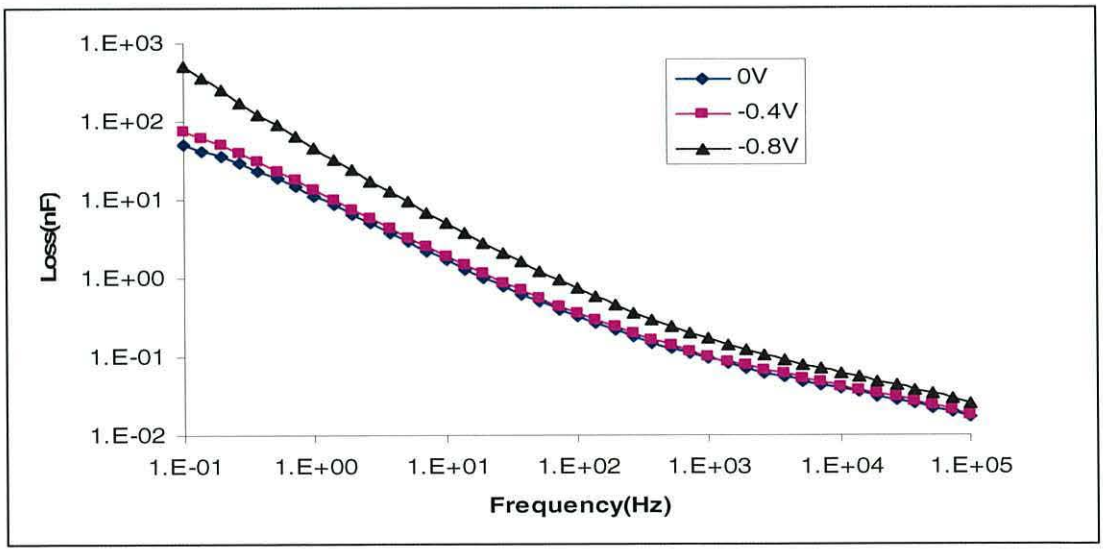

Figure 8.31 *Logarithmic plot of loss versus frequency characteristics of TLSC.*

The Cole–Cole plot for TLSCs (batch B) shows only partial dispersion (figure 8.32). The relaxation frequency of the dispersion occurred at a frequency below 1Hz.

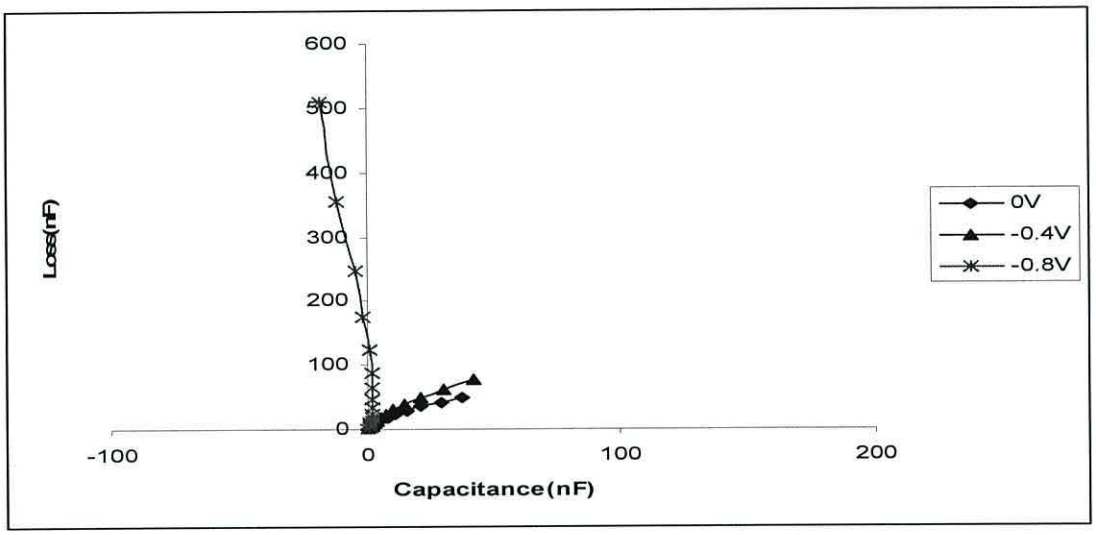

Figure 8.32 *Loss versus capacitance characteristics of TLSC produced from batch B at -0.8, -0.4, -0.2 V bias voltage.*

Figure 8.33 shows the capacitance–voltage characteristics of a TLSC from batch B measured at 10KHz. The capacitance was virtually constant over the whole voltage range, increasing only slightly as the forward voltage increased. This was different to the C-V results for DLSCs (batch A) and TLSCs (batch A) which showed a much stronger dependence on applied voltage. Similar results were also obtained for the capacitance-voltage characteristics of batch B TLSCs at 1Hz (Figure 8.34). The capacitance was essentially independent of the applied voltage except for a small increase in forward bias followed by a rapid decrease.

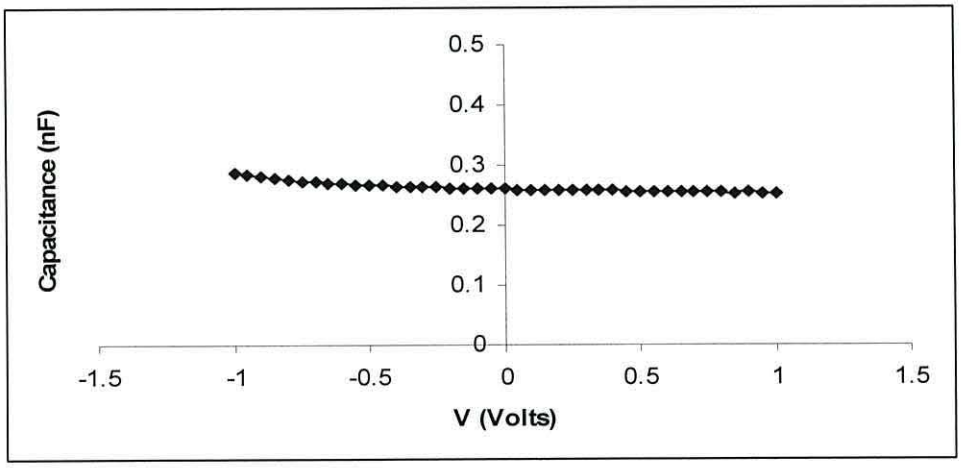

Figure 8.33 *Capacitance-voltage characteristics of TLSC at 10kHz .*

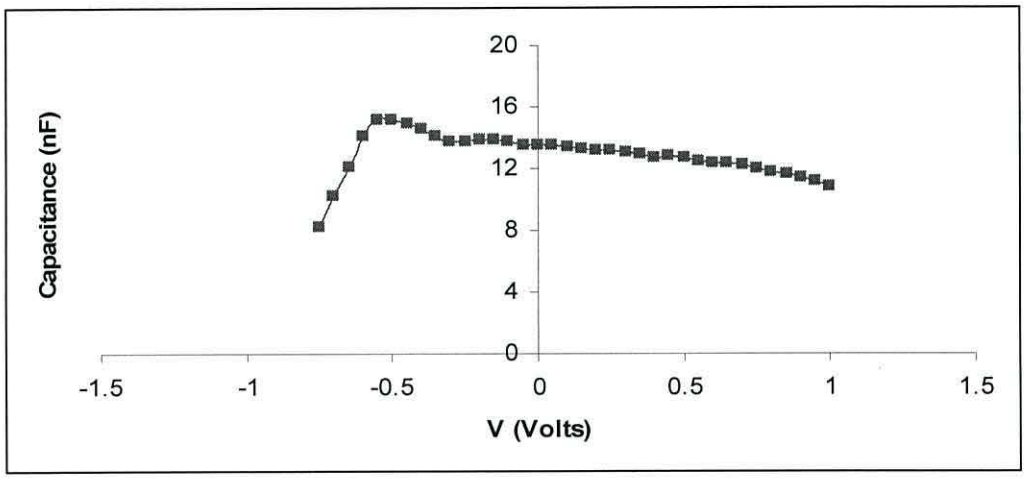

Figure 8.34 *Capacitance-voltage characteristics of TLSC at 1Hz.*

8.3.3 Discussion

The results of the AC measurements on DLSCs and TLSCs will be analyzed by defining an Equivalent Circuit (EC) for each of them. In chapter 2, we introduced a basic AC model of a Schottky diode for a p-type organic semiconductor sandwiched between two metals. Such a model may apply to our devices after adding additional elements to suit our devices. This approach is acceptable since the hole conductor in the solar cell studies in this work was the p-type organic semiconductor, P3HT, which forms a p-n junction with the n-type semiconductor, nc-TiO_2. Figure 8.35 shows an AC model of our DLSC and TLSC taking into consideration that the dye attached to the nc – TiO_2 surface is a part of the nc-TiO_2.

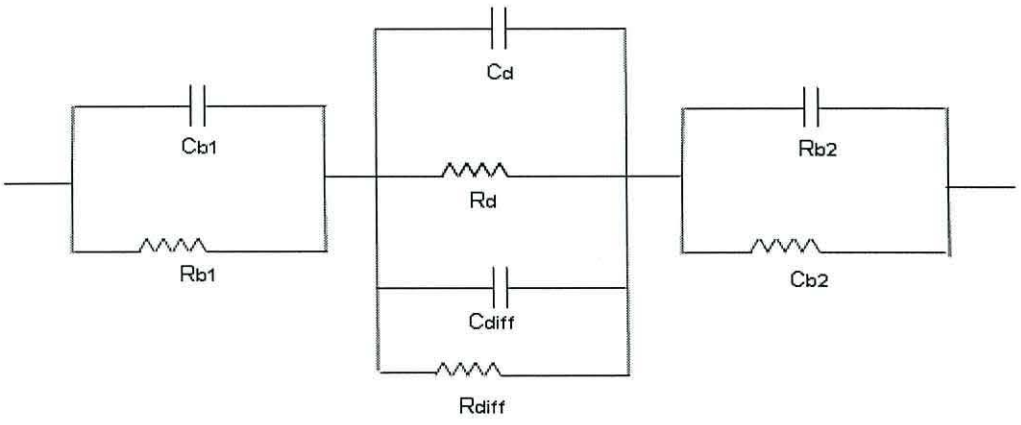

Figure 8.35 *Equivalent circuits of a DLSC and TLSC fabricated in this work.*

The symbols in figure 8.29 are as follows:

- C_{b1} and R_{b1} represent the capacitance and the resistance respectively of the bulk region of P3HT.
- C_{b2} and R_{b2} represent the capacitance and the resistance respectively of the bulk region of nc-TiO_2.
- C_d and R_d represent the capacitance and the resistance respectively of the depletion region formed at the P3HT/nc – TiO_2 interface .
- C_{diff} represents the diffusion capacitance arising from storage of minority charge carriers close to junction when the device is under high forward bias.
- R_{diff} represents the transport of charge across the junction in forward bias.

The high frequency capacitance of TLSCs and DLSCs does not change as the voltage applied to the device changes. This capacitance is dominated by the smallest of the series capacitances i.e. the bulk capacitances in the circuit of figure 8.29. This is because the total capacitance C_{total} is expressed by

$$\frac{1}{C_{total}} = \frac{1}{C_{b1}} + \frac{1}{C_{b2}} + \frac{1}{C_j} . \qquad (8.20)$$

C_j is the capacitance of the junction and arises from the depletion region capacitance and diffusion capacitance i.e.

$$C_j = C_{deple} + C_{diff} . \qquad (8.21)$$

At 0.1MHz, the junction capacitance is almost equal to the depletion region capacitance. The diffusion capacitance is small since the minority charge carriers cannot follow the ac signal [1]. Equation 8.1 can then be rewritten

$$\frac{1}{C_{total}} = \frac{1}{C_{b1}} + \frac{1}{C_{b2}} + \frac{1}{C_d} \qquad (8.22)$$

Also, since the depletion region is expected to be thin, especially in forward bias, then, the total capacitance of the device at 0.1MHz 188pF is dominated by bulk

region capacitance for the composite P3HT and nc – TiO_2 with the latter having the main influence. From the standard equation for the capacitance of a parallel – plate capacitor and assuming an area of $3x10^{-6}m^2$, and a thickness of $1.9\mu m$, we estimated an effective relative permittivity of 15 for the nc-TiO_2 layer in the DLSCs and TLSCs from batch A sol gel. For DLSCs and TLSCs from batch B, the measured capacitance at 0.1MHz was 140pF and when coupled to the greater thickness ~ 2.1 nm, the effective relative permittivity of the nc – TiO_2 layer was estimated to be 11. These values are close to the effective relative permittivity of titanium oxide film reported in [2, 3].

The section 8.2 and equivalent circuit in figure 8.29 readily explains the dispersion in capacitance as the frequency decreases. Now the transport of carriers through the bulk region can follow the small single voltage, so that C_{b1} and C_{b2} can be shunted by R_{b1} and R_{b2} and the measured capacitance becomes equal to the junction capacitance. At zero applied voltage and for reverse bias, this capacitance is equal to the depletion capacitance and decrease with increasing reverse bias. With forward voltage applied, the diffusion capacitance becomes important. Since the capacitance is proportional to the dc current flowing, it grows exponentially with increasing forward voltage; this will lead to an increase in capacitance at low frequency.

Finally, the maximum and subsequent decrease in capacitance as the forward voltage increases, probably arise initially from the shunting effect of a decreasing R_{diff} and C_{diff}. The continuing decrease and eventual sign reverse points to significant phase lag arising between the signal voltage and the carrier response at the junction. The more detailed differences between the different batches and different devices can be ascribed to different in bulk resistance (thickness, morphology), and especially to differences in the conditions at the junction. The latter will include difference in effective junction area, the influence dye on the depletion region and the fraction of the interface coated in the dye.

8.4 AC Measurements on Solar Cells Vacuum

8.4.1 Double Layers Solar Cells

Figure 8.36 shows capacitance–voltage (C-V) plots of DLSCs fabricated from batches A and B tested in the dark under high vacuum(10^{-5}). At 10KHz, the capacitance was independent of the voltage applied to the SnO_2:F electrode. The values of the capacitances for each device were 0.143nF and 0.092nF for batches A and B respectively.

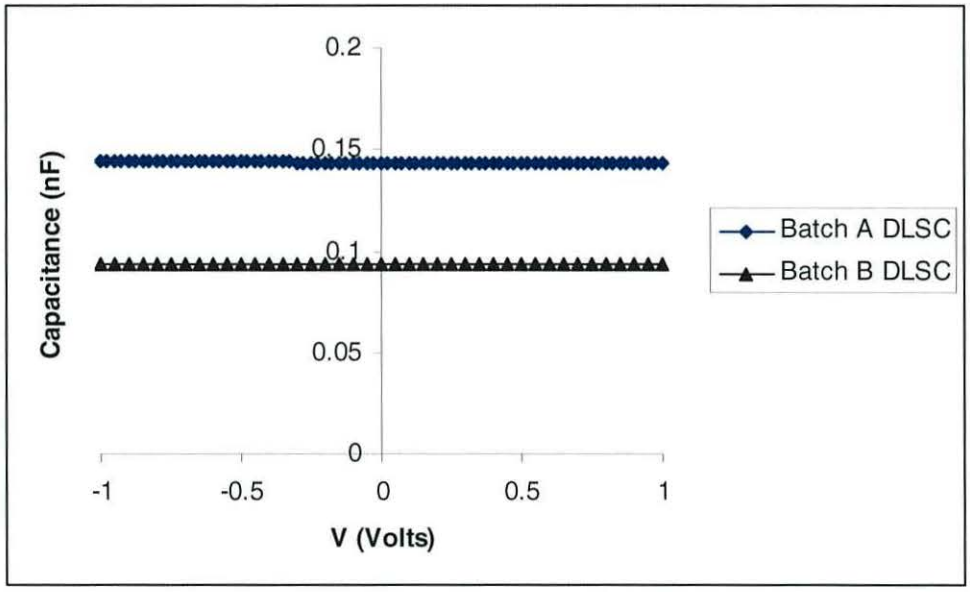

Figure 8.36 *Capacitance-voltage characteristics of DLSC (B, A) at 10kHz.*

Figure 8.37 shows C-V plots of the same devices at a frequency of 1Hz. The capacitance of the batch B device was again constant with bias voltage. For DLSC batch A, however, the capacitance decreased slightly in reverse bias. It is clear that the capacitance of DLSCs tested in the air is much higher than when tested in vacuum.

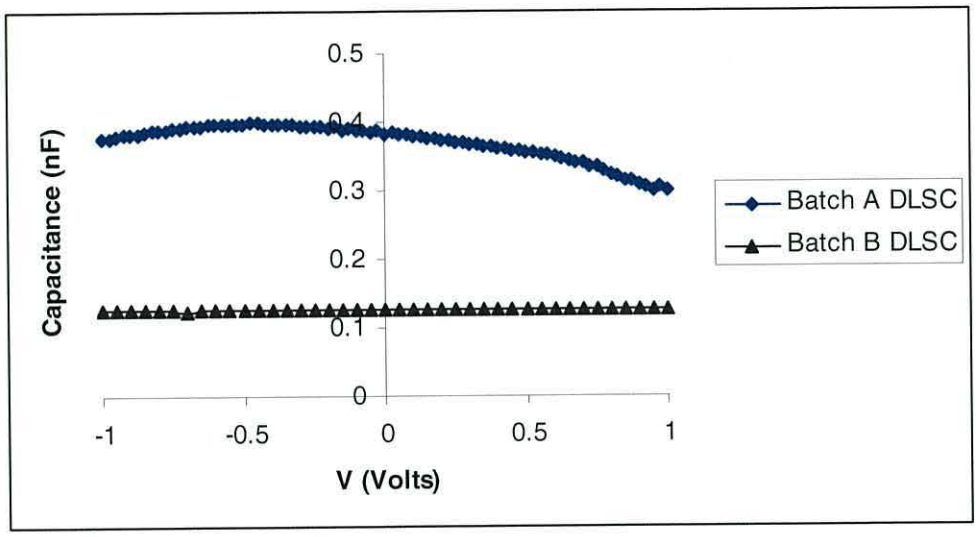

Figure 8.37 *Capacitance-voltage characteristics of DLSC (B, A) at 1Hz.*

Finally, the frequency dependence of DLSCs from batches A and B measured under high vacuum are shown in figures 8.38 and 8.39. The high frequency capacitance of DLSCs from batches A and B were independent of applied voltage, and similar in value to that obtained in air. Under vacuum, the low frequency capacitance was also independent of forward bias voltage with very much reduced dispersion.

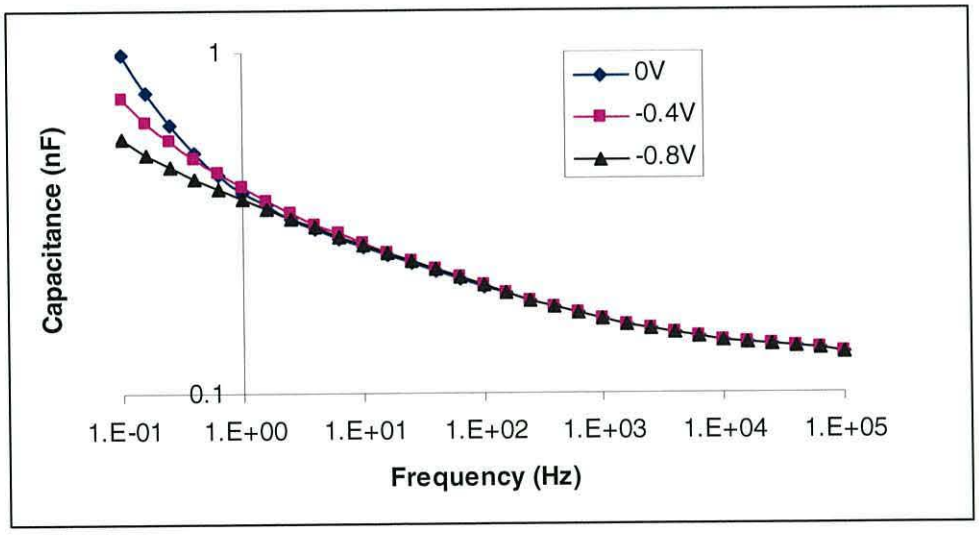

Figure 8.38 *Capacitance-frequency characteristics DLSC (A) under forward bias condition.*

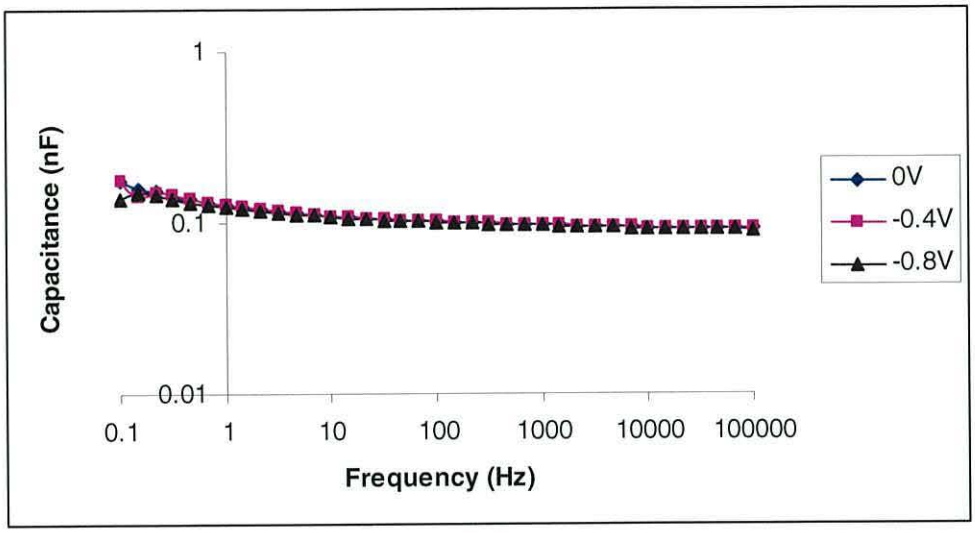

Figure 8.39 *Capacitance-frequency characteristics of DLSCs (B) under forward bias condition.*

8.4.2 Three Layers Solar Cells

Vacuum AC measurements were also performed on the TLSCs from batches A and B sol gel**.** Figure 8.40 shows that at 10KHz the capacitance of both devices are equal and independent of the applied voltage. This is similar to results obtained with DLSCs in vacuum. In all cases, therefore, the high frequency capacitance is independent of voltage and consistent with values dominated by the bulk capacitance of the device. At low frequency, the capacitance of a batch B device is still independent of voltage (see figure 8.35) while the batch A device shows a behavior reminiscent of that seen in figure 8.28.

Figure 8.42 shows the frequency dependence of the capacitance of a batch A TLSCs under vacuum. Confirming the data in figures 8.40 and 8.41 the capacitance is independent of applied voltage except at the lowest frequencies, where the capacitance decreases rapidly at a frequency dependent on the applied voltage, even becoming negative. This effect probably arises from the same mechanism that causes the downturn in capacitance seen at high forward bias in all devices. Assuming we may neglect experimental artifacts (possibly due to high DC conduction), the effect must be related to significant phase difference between the applied signal voltage and the carrier response in the device.

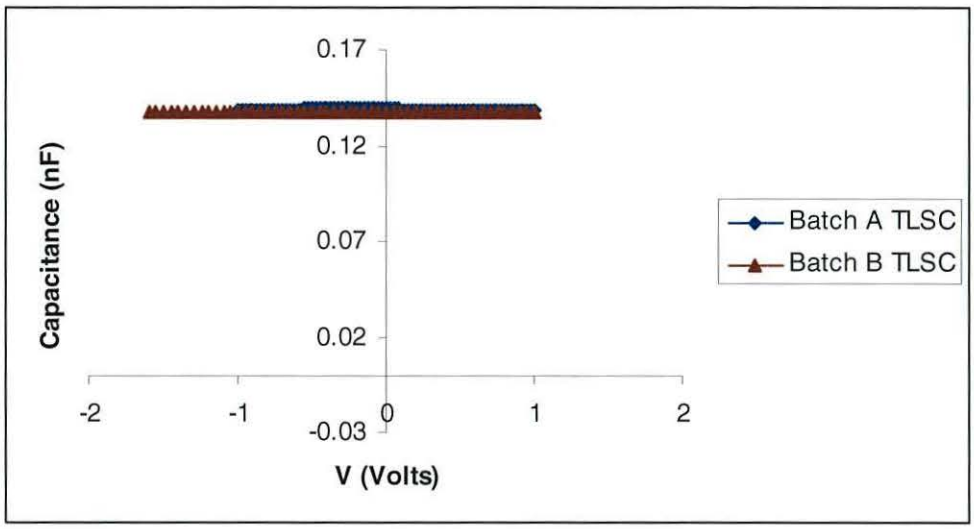

Figure 8.40 *Capacitance-voltage characteristics of TLSC (B,A) at 10KHz.*

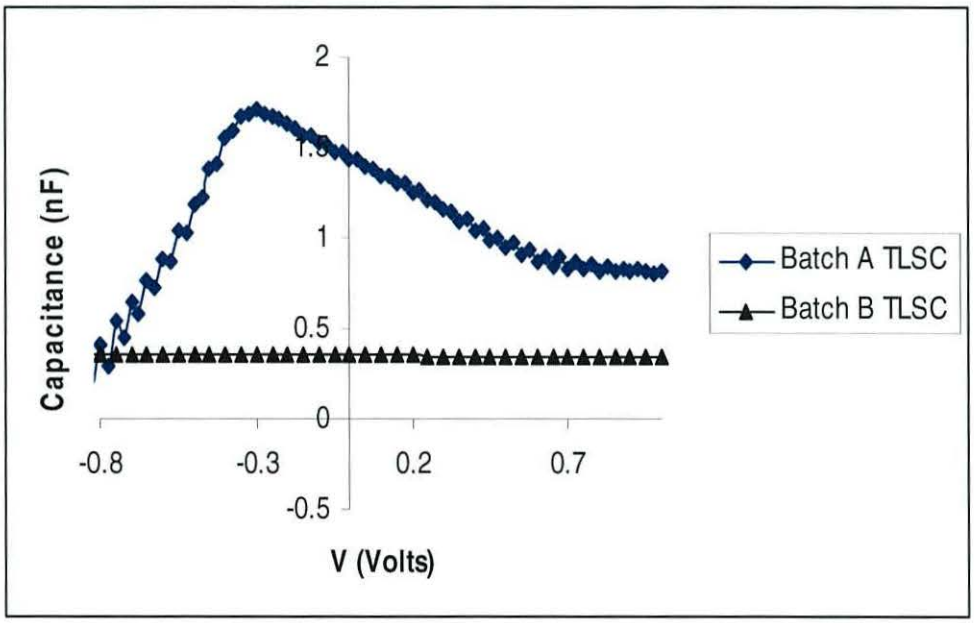

Figure 8.41 *Capacitance-voltage characteristics of TLSC (B,A) at 1Hz.*

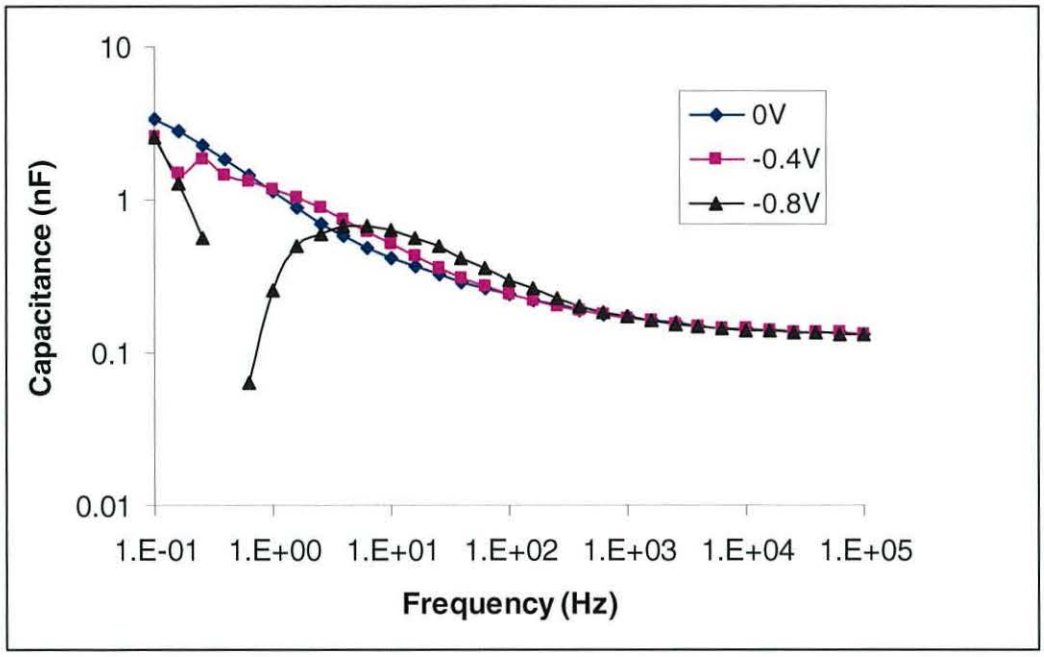

Figure 8.42 *Capacitance-frequency characteristics of TLSC (A) under forward bias condition.*

8.4.3 Discussion

Under vacuum, the voltage–dependence of capacitance was almost completely lost. Only at the lowest frequency was any difference observed mainly in the TLSCs. At high frequency, in all cases, the measured capacitance corresponded to the geometric capacitance of the cell and determined, therefore, by the device thickness. As the frequency was lowered the capacitance of both devices increased. However, for the DLSCs, the decrease was significantly smaller than observed for the TLSCs (batch A). For both devices types the increases were smaller than measured in air.

It is known that ambient oxygen can dope P3HT [4]. Thus on reducing the oxygen dopant concentration under vacuum, the conductivity of the polymer will be lower, leading to an increase in the polymer bulk resistance. This is turn will lead to a reduction in the relaxation frequency of the equivalent circuit in figure 8.29 and a shift of the dispersion of lower frequencies, possibly outside the measurements range (as for the DLCSs). This also comes for reduction of nc-TiO_2 conductivity which is very low in vacuum. It is also known that oxygen doping significantly changes the flat band voltage of metal/insulator/semiconductor (MIS) diodes from 0.1 vaccum to

1V after oxygen exposure [5]. Such an effect could arise from electrostatic charging of insulator/semiconductor interface or from a shift in the Fermi level of the polymer. One or both effects are likely to occur here, also especially in the case of the DLSCs. Under vacuum, reducing the oxygen concentration doping will be accompanied by a shift in the Fermi level of P3HT from near the HOMO levels closer toward mid-gap. The Fermi level and band bending of the nc-TiO_2 may also depend on the concentration of impurities atmosphere Therefore, the reduced contact potential between polymer and nc-TiO_2 could then result in the loss of the depletion region.

8.5 Summary

The C-V and C-f characteristics of DLSCs and TLSCs from batches A and B sol-gel have been investigated under different ambient conditions. A simple equivalent circuit is used to describe the device behavior. Based on this circuit, the observed similarity in the values of capacitance measured at high frequency is readily explained as the bulk capacitance dominated by the $nc-TiO_2$ layer. As frequency decreases, the bulk resistance of $nc-TiO_2$ and the P3HT will shunt the bulk capacitance, so that the measured capacitance increases rapidly to a value determined by the junction capacitance. Differences between the various devices types at low frequency may now be explained by the presences of a depletion region in air e.g. DLSC and the presences of dye layer in TLSCs.

At moderate frequency, in forward bias, the depletion capacitance dominates the diffusion capacitance owing to the short recombination time of carriers. At low frequency diffusion capacitance dominates. In the case of TLSC, behavior consistent with partial coverage of nc-TiO2 by the dye was observed.

8.6 References

1. M. L. Lucia, J. L. H. Hernandez, C. Leon, and I. Mártil, *European journal of physics,* **14**, 86, (1993).
2. B. Arvan, A. Khakifirooz, R. Tarighar, S. Mohazdeh, A. Goodarzi, E. A. Soleimani, and E. Arzi, *Material Science and Engineering B*, **15,** 17. (2004).
3. F. Jin, H. Tong, L. sSjem, K. Wang, and P.K. chu, *Material Chemistry and Physics,* **10,** 31, (2006).
4. E. J. Meijer, C. Detcheverry, P. J. Baesjou, E. V. Veenendaal, and D. M. d. Leeuw, T. M. Klapwijk, *Journal of Applied Phyiscs*, **93**, 4831, (2003).
5. E. J. Meijer, A. V. G. Manghus, B. H. Huisman, G. W. tHooft, D. M. de Leeuw, T. M. Klapwijk, *Synthetic Metals*, **142,** 53, (2004).

Chapter 9

Conclusions and Further Work

9.1 Conclusion

The work described in this thesis was concerned with investigating the properties of bulk heterojunction solar cells based on nc-TiO_2, an n-type semiconductor, and poly (3-hexylthiphene), a p –type semiconductor. The basic device was termed Double Layer Solar Cells (DLSCs). When the nc-TiO_2 was sensitized with ruthenium dye, the device was termed Three Layer Solar Cells (TLSCs).

Inclusion of the dye improved significantly the power conversion efficiency of the solar cells. The average efficiency of TLSCs from batch A was found to be 0.85% with the best devices having an efficiency of 1.1 % using halogen lamp. Not surprisingly, TLSCs also display the highest EQE for this class of device, 16%<EQE<11% for the wavelength range 380 nm to 580 nm. When the EQE was integrated with the AM 1.5 solar spectrum, the short-circuit current density of TLSCs was estimated to be ~ 2mA/cm^2 and be close to experimental values using illumination (72mW/cm^2) from halogen lamp. The AM 1.5 power conversion efficiency of TLSC was calculated and found to be around ~ 0.69% from the Voc ~ 0.735V, and fill factor ~ 0.49 and Jsc ~ 2mA/cm^2. The obtained power conversion efficiency of TLSCs from batch A is amongst the highest value found by the researchers in this field.

The corresponding performance figures for TLSCs from batch B were open circuit voltage ~ 0.9V, short circuit current density ~0.23mW/cm^2, and power conversion efficiency ~ 0.2 using halogen lamp. The performance of batch A DLSCs was much worse. Efficiency were, Jsc ~ 0.22mW/cm^2, and Voc ~0.68V. Again batch B devices performed worse than those from batch A.

An important finding of this work was the key role played by the morphology of the nc-TiO_2 layer produced from the two batches of sol-gel. This is not surprising perhaps since the penetration of dye and P3HT into the nc-TiO_2 layer must be related to the structure of the layer. What was surprising here was the significant differences in morphology and topography of the layer produced from the two batches of sol-gel

using the same sintering protocol. Although the final layer thicknesses were similar, 1.9μm for batch A and 2.1 μm for batch B, the former led to columnar-like structure (rms roughness= 21 nm), while the latter retained its particle-like structure and had a smoother surface (rms roughness =12 nm). We presume the columnar structure of batch A material encourages better penetration of the dye and P3HT into the nc-TiO_2.

Furthermore, the SEM images revealed that batch A nc-TiO_2 made an intimate contact with the underlying compact, while for batch B a clear boundary existed suggesting a poorer contact between the two layer, Clearly, improved penetration and better contact between layer is expected to improve device efficiency through an increase in effective area for photon collection and reduced internal series resistances

XRD measurements confirmed that nc-TiO_2 from both batches was in the required antase phase. Interestingly, the grain size in batch A was ~ 25 nm but only ~ 19 nm in batch B. This suggests that electron transport in batch A nc-TiO_2 is likely to be easier i.e. reduced bulk resistance.

Literature reports have suggested that the morphology of nc-TiO_2 layer is dependent on the composition of the starting sol-gel. Hence thermo-gravimetric analysis of the two batches was undertaken to investigate this possibility and indeed differences were found. Batch A had a smaller solid content and a higher solvent content than batch B.

In addition, to morphological differences, STS measurements indicate significant differences in the surface electronic properties ofnc-TiO_2 films. While both had optical band gap of 3.4 eV, the electronic band gap of Batch A as deduced by STS, was 3.3eV while that of batch B was much lower, 2.6 eV indicating the existence of surface states in the band gap.

A previously–reported, simple equivalent circuit model of solar cells was used to explain detailed differences observed between devices. Apart from the obvious factor such as the effective interfacial area which governs the generated photocurrent, it is also important to recognize the influence of (a) the bulk series resistance which limits the short- circuit current and (b) the interface properties which determine the recombination of dissociation excitons (represented by a shunt resistance) and the turn-on voltage of the diode formed at the heterojunction which limit Voc. The turn–on voltage and shunt resistance for TLSCs and DLSCs (batch A)

were lower than when we experimented with TLSCs and DLSCs (batch B). So there has been a different Voc produced in these devices

Further measurements on batch A TLSCs showed that Jsc and Voc increased with the increase of light intensity from 0.7mW/cm^2. But the Voc was unchanged when the light intensity was above 72mW/cm^2. Both Jsc and Voc showed good long term stability during 5000 seconds of irradiation at room temperature using halogen lamp. Additionally, the values of Jsc and Voc changed slightly even when the device was tested during different occasions in twenty days. However, the maximum output power (P_{max}) of the device decreased after twenty. The Voc decreased with the increase of the temperature. This was expected because the increase in thermal energy will increase the probability of exciton dissociation (the Rsh will decrease).

When the device was placed under vacuum interesting changes were observed. The dark currents of DLSCs fell markedly and rectification was lost. Under illumination, the photovoltaic behavior was lost but the devices were strongly photo conductive. This was attributed to the loss of the depletion region at the nc-TiO_2/P3HT heterojunction resulting from the loss of oxygen dopant in the P3HT and the loss of defects species at the surface of TiO_2. The two batches of TLSCs behaved differently to each other. For batch A, again the dark current decreased and both rectification and photovoltaic behaviour was lost. Batch B TLSCs were found to retain their photovoltaic properties under vacuum. In the latter case, we argue that the dye must have coated the whole of nc-TiO_2 surface and that the depletion region , if present, was not controlling factor. For batch A only limited dye coverage may have been achieved so that much device of the device behaved as a DLSC in vacuum However, it is vital to mention that the dye cover big area of nc-TiO_2 in batch A TLSCs unlike in batch B TLSCs. Thus there is a difference in size of contact area between P3HT and nc-TiO_2. That might lead to form direct contact between P3HT and nc-TiO2 in batch A TLSCs and act as DLSC in vacuum

There is much discussion in the literature about the origin of the photovoltaic effect. If it is due to the pressure of a depletion region, then AC measurements should provide information supporting evidence, In Chapter 8, small signal voltage measurements are reported for batches (A ,B) DLSCs and TLSCs both in air and under vacuum. In all cases, at the highest frequencies, the measured capacitance was low and determined by the geometric capacitance of the device i.e. the thickness of

the nc-TiO_2 layer. As the frequency decreased, capacitance increased by several orders of magnitude in some cases. A series parallel equivalent circuit model was used to explain the results. At low frequencies, series resistance shunts the bulk resistance so that the measured capacitance is now closer to that of the junction. For reverse and small forward bias in DLSCs and batch A TLSCs, the junction capacitance in air is dominated by the depletion capacitance whiles high forward voltages the diffusion capacitance was dominated. The low–frequency capacitance of batch A devices was higher than batch B devices pointing to an increased interfacial area and/or high bulk series resistance. The diffusion capacitance of batch A TLSCs was higher than for batch A DLSCs reflecting the enhance forward current in the dye –sensitized devices.

Under vacuum, the capacitance of batch A DLSC, TLSC and batch B DLSC were independent of voltage and showed only limited frequency-dependence.

9.2 Future Work

The investigations to date have highlighted a number of areas where further work could usefully be undertaken. These are listed below.

1. The hole mobility in P3HT is low. Some work has already reported polymers with higher hole mobilities, e.g. MEH-PPV and PA-PPV, which have been used instead of P3HT. Other approaches at reducing the series resistance posed by the polymer hole conductor is to incorporate carbon nano tubes and other fullerenes such as C_{60} butyric acid menthyl ester (PCBM) to enhance charge transport through the polymer layer.
2. Studies could be undertaken to improve the penetration of the polymer into the nc-TiO_2 layer. For example, the layer could be soaked in a dilute solution of P3HT prior to spin-coating the final P3HT layer.
3. Other approaches could include investigating the composition of the starting sol-gel of especial interest here would be the development of a low-temperature method for preparing anatase nc-TiO_2 that would be suited to flexible plastic substrate.

4. Other oxides with higher electron mobilities could be investigated. Some work in this area has already been undertaken for example using ZnO.
5. Finally, little work has been reported on the AC properties of solar cells. The present studies have shown that there is much information to be obtained from such studies. A more detailed investigation would be justified and improved equivalent circuit models development.